NTNU – Trondheim
Norwegian University of
Science and Technology

Integration of Geophysical Interpretation Methods Applied in the Perdido Fold Belt

Juan Carlos Flores Zamora

Petroleum Geosciences
Submission date: June 2013
Supervisor: Egil Tjåland, IPT

Norwegian University of Science and Technology
Department of Petroleum Engineering and Applied Geophysics

NTNU - Trondheim
Norwegian University of
Science and Technology

Integration of Geophysical Interpretation Methods Applied in the Perdido Fold Belt Area.

A thesis
Submitted to the Graduate Faculty
in partial fulfillment of the requirements for the Degree of
MASTERS OF SCIENCE

by

Juan Carlos Flores Zamora

Petroleum Geosciences
Submission date: June 2013
Supervisor: Egil Tjaland, IPT

Norwegian University of Science and Technology
Department of Petroleum Engineering and Applied Geophysics

ACKNOWLEDGMENTS

I would like to thank to God who gave me the strength, faith and encouragement to work every day with the same motivation and happiness.

Also I would like to thank to my Mother Cataline and Brothers Arturo, Denise, Carmen and Erick who always have given me support and encouragement to work hard and never leave my goals. To my friend Aracely for her support, advice and love during this new experience in my life.

I would like to give my appreciation and acknowledge to my supervisor Dr. Egil Tjaland for his guidance, tutelage, and for share his experience during the development of my thesis project. Also I would like to thank to Dr. Martin Landro for all his facilities and support during all my studies in the NTNU.

I acknowledge to my PEMEX Advisor, M.S. Victor Mercado for all his compromise, advices, feedbacks and support along of all my master development.

I would like to give my sincerely thanks to PEMEX for give all the facilities and support to develop this master program, as well as CONACYT, SENER, BANOBRAS and all the persons involve in this process especially to: Antonio Escalera Alcocer, José Trinidad Martinez Vázquez, Arturo Escamilla, Jose Robles Nolasco, Guadalupe Bernabe Martínez, Carlos Rosas Lara, Sergio Paz López, Cesar Aguilar Campos, Ericka Coral Carmona Castañon, Rafael Ramos Palmeros, Pablo Arturo Gomez Duran, y Ana Rosa Parrilla Puente.

ABSTRACT

Today, with discoveries of the fields Great White, Baha, Trident and Tobago in U.S portion and the recent drilling of wells Trion-1 and Supremus-1 in Mexican waters, have established the Perdido fold belt in the Gulf of Mexico as a significant potential petroleum province in its initial stages of evaluation. This area according with studies realized so far, shows an important potential of reservoirs associated with extra-light crude oil, however to explore, delimitate, characterize and produce these resources is necessary the implementation of the most modern technology of interpretation, drilling and development.

In this work, I considered one of the new wells discovered in the Mexican portion into the Perdido Fold Belt system, where the main target of this project is establish and delimitate the probable and possible extension of hydrocarbons associated with such well. To develop this, first was carried out the seismic interpretation of area of study, and thus establish all the geological setting associated to the reservoir. Although most of Perdido Fold Belt structures usually are anticlines of great magnitude, experiences obtained in U.S wells has showed that hydrocarbon distribution is most related with the presence of stratigraphic traps associated with submarine fans and channels systems that often shows a response of amplitude below of seismic resolution, making their definition and interpretation more complex. So this type of traps in the Mexican portion also was evident during the interpretation of this project, which was characterized by two types of traps: one structural characterized by a set of high amplitude anomalies limited by normal fault blocks and other stratigraphic interpreted as a system of submarine channels with medium to high amplitude produced as a result of depositional system of Northern and Northwest Gulf of Mexico. Hence, an AVO analysis has been proposed as part of this project allowing calibrate the amplitude anomalies identified in the reservoirs and understand their relationship with the type of fluids associated to the reservoir and lithological changes, being possible to derive two types of hydrocarbons in each reservoir; one associated to gas and other to oil.

Once obtained the AVO analysis results, the LMR and EI seismic inversion were performed, where the main goal of this was to complement the AVO analysis and therefore,

reduce the uncertainties associated to the amplitude anomalies identified and their relationship with the reservoir conditions. With this analysis was possible to establish and define not only the reservoir rock distribution, but also the areas associated with higher hydrocarbon saturation and water saturation characterized by low and high values of Lamnda-rho and Elastic Impedance respectively. In addition of establish the seismic properties response associates to each stratigraphic unit interpreted in this area. Thereby, reducing the geological risk and delimiting and identifying new potential areas to contain hydrocarbons.

TABLE OF CONTENT

LIST OF FIGURES

LIST OF TABLES

I. INTRODUCTION

Today with the increase in demand of new discoveries and delimitation of oil fields in areas already discovered, the oil industry has developed new techniques of acquisition and seismic data processing, which have guided to implementation of new concepts, models and innovative interpretation tools, such as the AVO and the seismic Inversion.

The AVO analysis is a methodology of processing and interpretation where its main target is the identification of fluids and lithological characterization. The basis of this methodology is the physical model of reflectivity depends on the variations of three properties: compressional velocity (*Vp*), shear velocity (*Vs*) and density (ρ).

On the other hand, the seismic Inversion method is based in the convolutional model which attempt to reverse this model by removing the wavelet effect, resulting in *P* and *S* impedance in the subsurface which can be translated to lithology and porosity.

In the last years, the AVO and the inversion theories has been treated as individual methodologies, however with their implementation in areas with different geology and different reservoir characteristic has been highlighted that every one of these methods have their own limitations. While the AVO has the inability to distinguish between fizz water and hydrocarbon saturation, the inversions methods tend to be simplistic and limited by the lack of wavelet definition.

An alternative to solve such problems is to combine both methodologies through of the LMR (Lambda-Mhu-Rho) inversion, which is an inversion method based in the Lames's elastic parameters in the form $\lambda\rho$ and $\mu\rho$. Goodway et al. (1997). Hence it may be possible to use the result from the AVO to be applied later in the inversion method LMR, such as the fluid factor attribute (*Rp-Rs* reflectivity), which may be used as input to estimate the acoustic impedance or the conditioning of gathers during the AVO analysis to extract the wavelet to different angles.

Other alternative to combine AVO data with seismic inversion is the method of Elastic Impedance developed by P.Conolly of BP in 1999, which uses angle stacks for a range of

incident angles for the inversion. Often this method is used in near angle stack or far angle stack for a well, that allow see if there are AVO effects which could indicate the presence of hydrocarbons.

This thesis work is focused in the AVO and seismic inversion analysis together with seismic interpretation results obtained in one deep water prospect located at 226 Km off coast of Tamaulipas and 39 Km south in the border between Mexico and US into the Perdido Fold Belt area (Figure 1), which is characterized geologically by an anticline cored by autochthonous salt with targets into upper Oligocene. These targets show high amplitude anomalies associated with oil and gas saturated sands, which were deposited in facies of turbidites and channel systems in environments of talud and proximal basin.

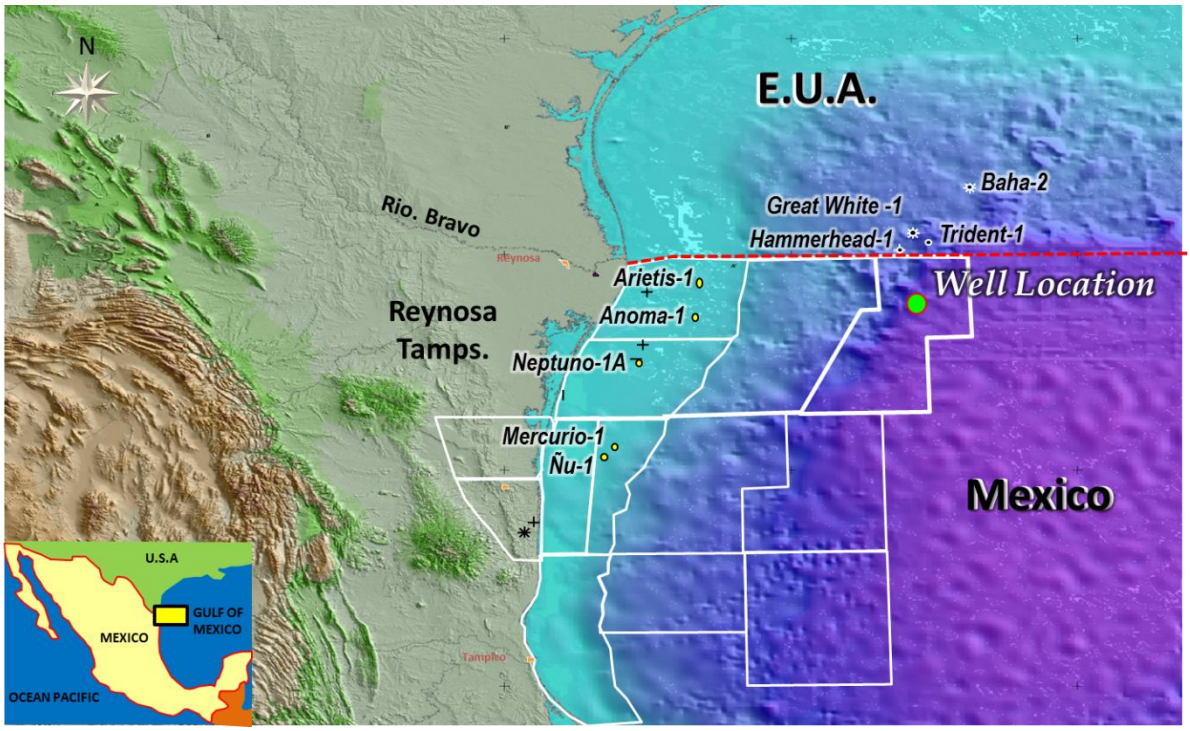

***Figure 1**. Location Map of area of study, regarding the strategic exploration blocks by PEMEX in the North Gulf of Mexico. Taken and modified from Study of Plays, PEMEX 2009.*

In this thesis work, I begin by reviewing the structural and stratigraphic geological setting of the Perdido Fold Belt Area (chapter 2), followed by the seismic interpretation around of well location, taking into account the main events of deformation and structural styles associated, as well as the definition of trap and deposit system in the target intervals

(Chapter 3). After, I perform a log modeling to identify the main types of fluids associated with my reservoir, to later by using the AVO analysis to define their distribution and their relationship with the amplitude response (Chapter 4). Finally, I perform a LMR inversion and Elastic Impedance Inversion to reinforce my AVO results and derive a set of sections and maps of properties associated with my reservoir (Chapter 6).

1.1. Problem Statement

Because this a project located in wildcat areas, exist little information of wells and geological analogues available, which can support both geological models and reservoir condition during the exploration, delimitation and development of leads and fields in this area. Therefore, I address this project to solve two main problems:

- The evolution of Perdido Fold Belt is related by several steps and deformations events, where the halokinetic process (salt withdrawal), shale tectonics, gravitational systems (extension – contraction), and shortening within the salt canopies are associated with the development of faults and compressional structures basinward that dominates the area, which makes difficult the identification of the main events of deformation and interpretation of extensional events produced as result of the later deformation.
- Although most of Perdido Fold Belt structures usually are anticlines of great magnitude, experiences obtained in US wells has showed that hydrocarbon distribution is most related with the presence of stratigraphic traps, associated with turbidites, submarine fans and channels systems that often shows a response of amplitude below of seismic resolution, making their definition and interpretation more complex.

1.2. Previous Studies

Today, still has not been performed any AVO and seismic inversion study in the Perdido Fold Belt area in Mexican waters that can contribute significantly in the prediction and characterization of possible sand reservoirs identified in the area of study, due it is an wildcat area where the well information is little available. However, there are regional

studies of Plays and Prospects which have allowed the definition and understanding of structural, stratigraphic and sedimentary framework in this area. Into of these studies we can mention the study of Plays “Turbidite - Halokinetic” performed in 2003 by PEMEX, which allowed the definition two of main plays tested by American wells in the Perdido Fold Belt area in Mexican waters. Being possible the trap definition and distribution of reservoir rock by implementation of regional mapping and analysis of spectral decomposition respectively. In this project also was integrated the results of sampling of piston core in the seabed, showing the presence of oil in almost all the structural alignment of Perdido Fold Belt in Mexican waters. Other important study performed in this area, was the collaboration study Pemex – Shell performed in 2005. This study allowed define the Lower Eocene Wilcox as one of most potential plays into the Perdido Fold Belt in Mexican territory, by analysis of the petroleum system and taking into account the results obtained by wells (Trident, Baha, Hammerhead and Great white) in US. Finally, other study that is important to mention is the study of plays performed in 2008 “Integral Megacube Perdido”, which defined the Play Oligocene Frio as other potential play into the Perdido Fold Belt in Mexican waters. This study allowed the definition of sand sheets and submarine fans and channels of high amplitude as main facies associated to the distribution of rock reservoir. In addition of identification of fault bend folds and fault propagation folds with shallow detachment as a new trap system into the Perdido fold belt.

1.3. Objectives

- Establish and define the geological model associated to the prospect, taking into account the different geological events and systems of deposit.
- Identify and define the type of hydrocarbons associates to the reservoir and its relationship with the amplitude and log responses.
- Characterize and delimit the probable and possible extension of hydrocarbons, taking into account their geological properties and their relationship with the type of fluids and lithological changes.

II. GEOLOGICAL SETTINGS

2.1. Regional Geology Description in Perdido Fold Belt

The Perdido Fold Belt (PFB), is located in the Northeast Gulf of Mexico (Figure 2) in water depths between 2 - 3 Km. It is a deep water salt tectonic contractional structures and it occupies the 60-70 km wide region limit of the autochthonous Middle Jurassic Louann Salt and the allochthonous Sigsbee Salt Canopy [Peel et al., 1995; Hall, 2002; Rowan et al., 2004].

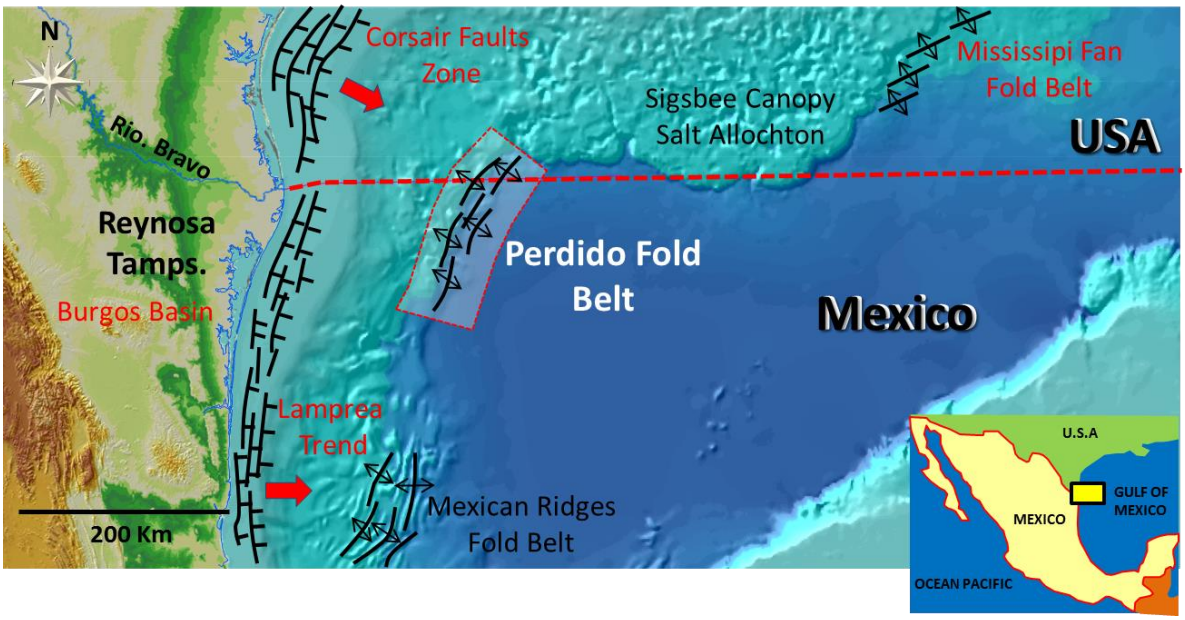

***Figure 2**. Location Map of Perdido Fold Belt, showing the Cenozoic fold belts and extensional system in shallow waters (platform). Taken and modified from Study of Plays, PEMEX 2008.*

The folds and trust structures related in Perdido Fold Belt are interpreted as result of gravity spreading of sedimentary layers detaching over a substratum that is interpreted as evaporites or overpressure shale, which has produced a linked system (extension-contraction) domain. The folds and trust structures vary in structural style, overburden thickness, overburden composition, location and timing of the deformation [Peel et al., 1995; Hall, 2002; Rowan et al., 2004].

The figures 3 and 4 show two structural profiles located in the Northern Gulf of Mexico into the Mexican waters, where is possible interpret the characteristic folds in PFB and their landward continuation beneath of allochthonous Sigsbee Salt Canopy (figure 3), which may vary from 10-20 Km [Peel et al. 1995; Hall, 2002; Rowan et al. 2004] to 100 Km [Radovich et al. 2007] and its structural geometry basinward.

The cross sections depicted in the figure 3 shows how the folds in PFB have a set of angular folds with wavelength around of 10 Km and seaward dipping fold envelop of 5 degrees [Rowan et al. 2000]. As is shown in the profile, the dip tilts the entire fold belt as a result of the seaward tapering of the underlying salt wedge. The tilts of the fold belt decreasing to 1-2° in the distal 15-20 Km, leading a bend in the fold envelope [Rowan et al. 2000].

The folds interpreted in PFB are highly symmetric, sometimes leaning landward or seaward with NNE-SSW direction, where the main age of deformation is interpreted belongs to upper Oligocene. However some recently studies has interpreted that the deformation continues till the recent [PEMEX et al. 2008]. This area is characterized by having mainly kink bands structures [Carmelo and Benson et al. 2006], although also has been interpreted the presence of salt walls, pop-up structures, fault bend folds and fault propagation folds in the south portion [PEMEX, et al. 2008] (figure 4).

Another feature that is evident in the Perdido Fold Belt structures is the presence of salt inflation underlying all the tilted pre-kinematic sequences (figures 3 and 4), which is interpreted occurred after deposition of these sedimentary layers and after or during their deformation [Trudgill et al. 1999]. The cause and timing of inflation of salt detachment layer is still disputed for several authors. Trudgill et al. (1999), suggest a post shortening early Pliocene salt inflation generated by the load of the seaward extruding Sigsbee Canopy. Rowan et al. (2000), interpret that the salt inflation occurred immediately after of the main folding phase of Perdido Fold Belt. Waller et al. (2007), points out that a significant amount of salt inflation could result as product of salt being squeezed out of the narrowing anticlines and from the sinking synclines, due that the distal synclines are below

their regional datum even after restoration [Rowan et al. 2000; Waller et al. 2007], which implies a net deflation of salt occurred underneath the distal end of the fold belt. Finally some studies interpret that the salt inflation could be the result of para-authocthonous movement of salt, as product of the gravitational pushing and sedimentary loading landward [PEMEX et al. 2009].

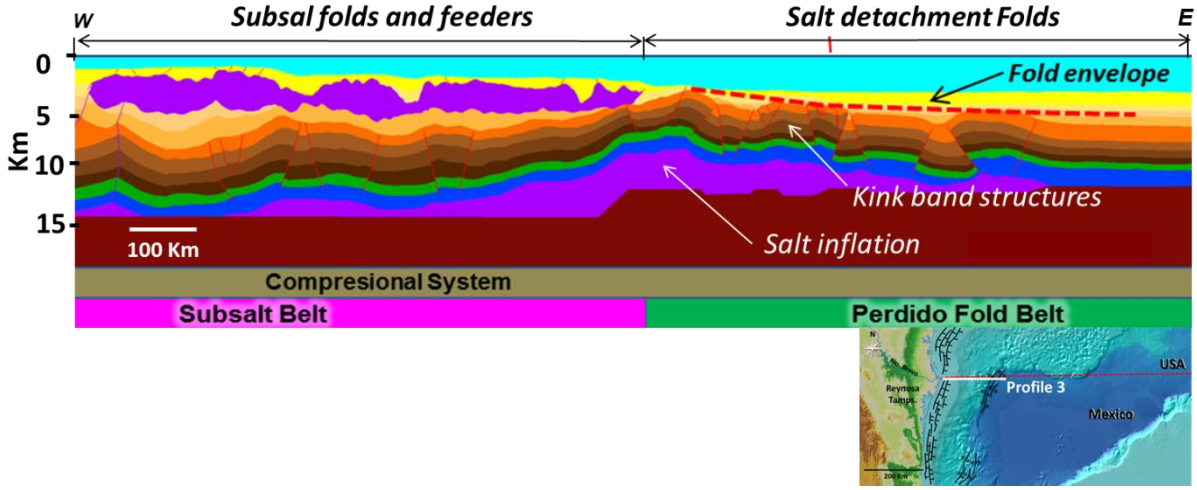

***Figure 3**. Structural profile of the Northwestern portion Gulf of Mexico, showing the main structural domains in Perdido Fold Belt into Mexican waters, characterized by kink band structures and salt inflation Taken and modified from Interegional Study of Salt Tectonics, PEMEX 2009.*

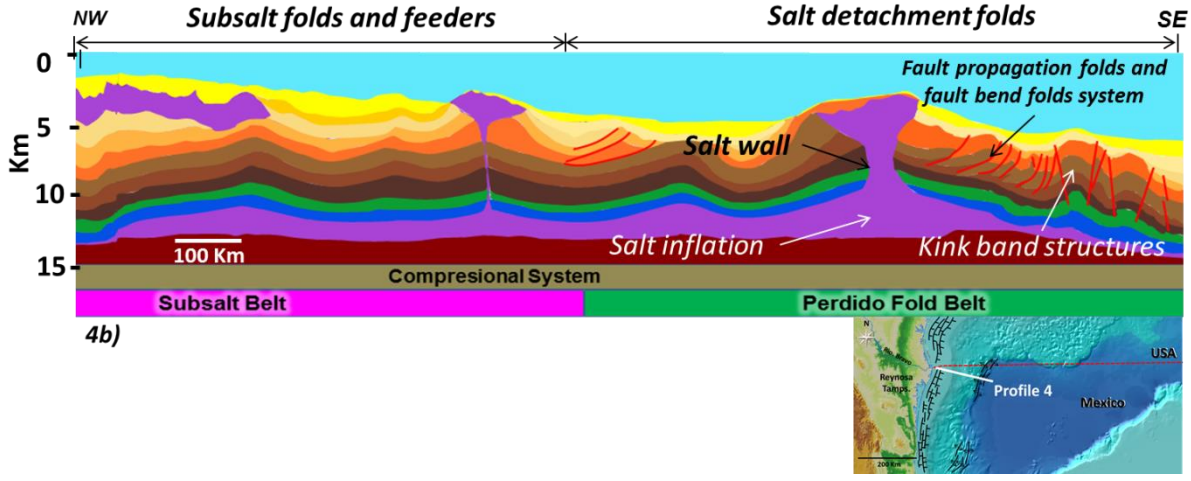

***Figure 4**. Structural profile of the Northwestern portion Gulf of Mexico, showing the main structural domains in Perdido Fold Belt into Mexican waters, characterized by kink band structures, salt inflation, fault propagation folds and fault bend folds with shallow detachment, as well as by salt walls. Taken and modified from Study of plays, PEMEX 2010.*

2.2. Stratigraphy and Depositional System

In the north Gulf of Mexico the stratigraphic column has been controlled by the incorporation of geology information proportioned by wells drilled both in the US and Mexican portion, where in base of regional stratigraphic and structural interpretation has been able to identify and delimit the units with more hydrocarbons potential. The stratigraphic column drilled by the Trident-1, Great White-1, Baha-2, Hammerhead, Silver Tip and Tobago wells, control in the U.S waters the stratigraphic column from the Pliocene to Cretaceous, while that in the continental platform into Mexican waters the Anoma-1, Arietis-1, Mercurio-1 and Ñu-1 wells, give the control of the stratigraphic units from the Lower Miocene until recent [PEMEX et al. 2009]. The figure 5 shows the representative stratigraphic column of the area highlighting the plays more important in this project.

The Perdido fold Belt involves the autochthonous Middle Jurassic (Callovian) Louann Salt and its overburden, as well as the emplacement of allochthonous salt in sequences of Upper Oligocene - Lower Miocene. The stratigraphy beneath the autochthonous salt is largely unknown. Presumably, synrift continental clastics may occur above rifted basement. These strata possibly would be equivalent to the Triassic Eagle Mills Formation found onshore in the subsurface of southern Arkansas, east Texas, and west-central Mississippi [Salvador, 1991].

Immediately overlying the salt is a sequence interpreted to consist of shallow-marine carbonates changing upward into deep-marine carbonates and shales [the Challenger unit of Shaub et al. 1984]. This abrupt change from shallow-marine to deep marine deposits reflects the rapid subsidence of the basin associated with the start of thermal subsidence [Winker and Buffler, 1988]. The overlying Paleogene section is interpreted to consist of hemipelagic strata and possibly coarser grained turbidite systems derived from the major shelf-edge delta systems to the northwest in the Texas/Rio Bravo region [Galloway, 1989; Fiduk et al. in press].

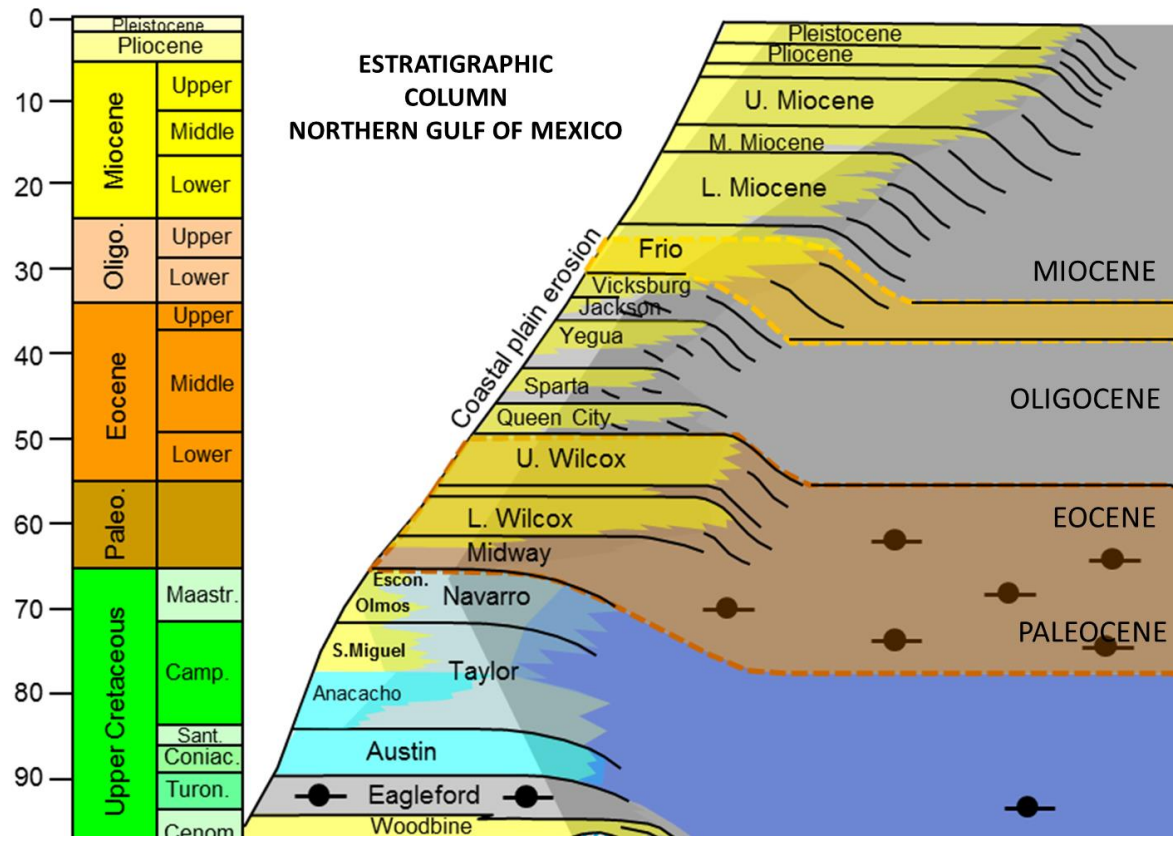

Figure 5*. Stratigraphic column of northern Gulf of Mexico. Taken and modified from Study of Plays, PEMEX 2009.*

The top of the preserved Eocene strata represents the approximate boundary between pre-kinematic and syn-kinematic strata. The lower Oligocene interval represents the time where the main phase of deformation occurred across the fold belt. Earlier deformation is present on some structures, whereas later periods of minor fold growth are observed. The post-kinematic upper Oligocene and younger strata in the Perdido fold belt are represented by units that infill the synclinal areas and gradually onlap the anticlinal structures before finally burying the folds. Toward the subsalt area the stratigraphic units are affected by the emplacement of allochthonous salt, which is more present in sequences of Lower Miocene and reducing toward upper Oligocene. However, there are some diapirs continuing their emplacement until the Pliocene-Pleistocene affecting the sea bottom [PEMEX et al. 2009].

In almost all the history of the tertiary sequence, the Rio Bravo has been a strong sediment supplier toward the basin covering the zones of Delta del Bravo, Subsalt zone and Perdido Fold Belt. The sediments related are characterized by showing a composition lithic and quartz. The big presence of lithic sediments point it out that the source in the continent had a strong influence to produce these sediments traveled long distances toward deeper waters, not ruling out the presence of other contributors in the south [PEMEX et al. 2009]. The figure 6 shows a map with the main sources of sediment supply in the Northern Gulf of Mexico.

In the eastern portion the sediment composition tend to be richer in quartz, which point it out that these sediments were transported by the system of rivers Trinity, Houston and Corsair, where the presence of lithic sediments is reduced. In the Perdido Fold Belt has been realized several studies to determine the main sources and distribution of sediments basinward, thereby has been interpreted that most of the sedimentation is controlled by submarine fans and channels systems distributed along of the different geological layers and where the Rio Bravo and others rivers systems located southward play an important role in the sand distribution basinward [PEMEX et at. 2011] (figure 7).

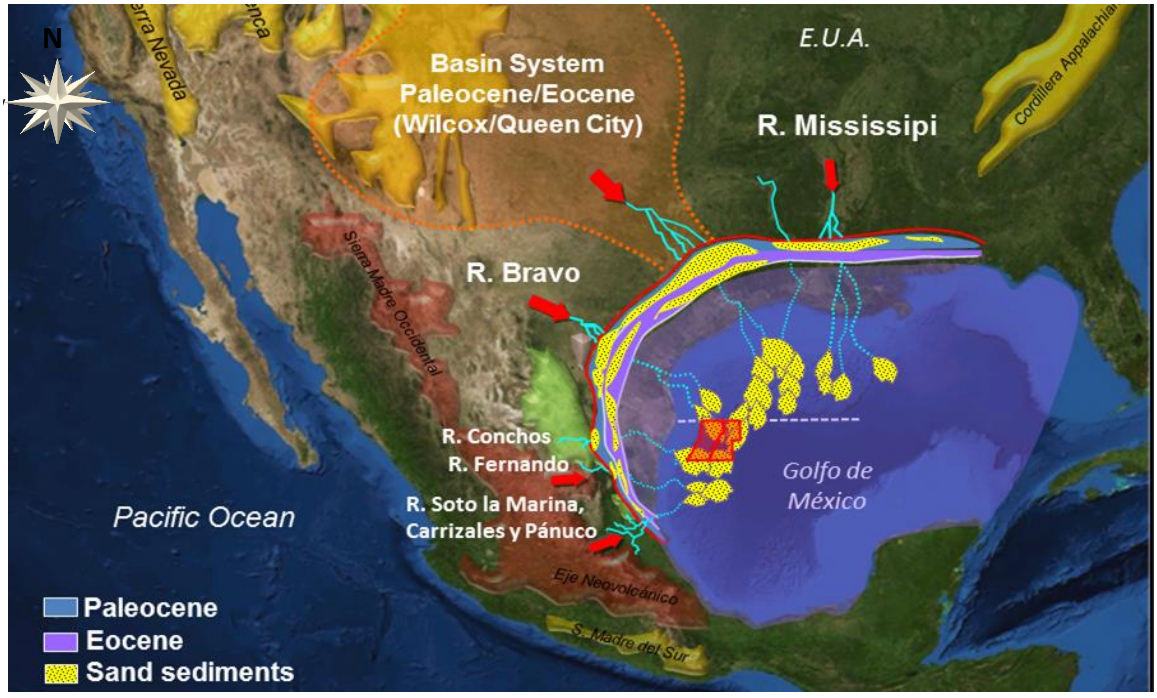

***Figure 6**. Main sources of sediment supply in the Northern Gulf of Mexico. Taken and modified from Study of Plays, PEMEX 2010*

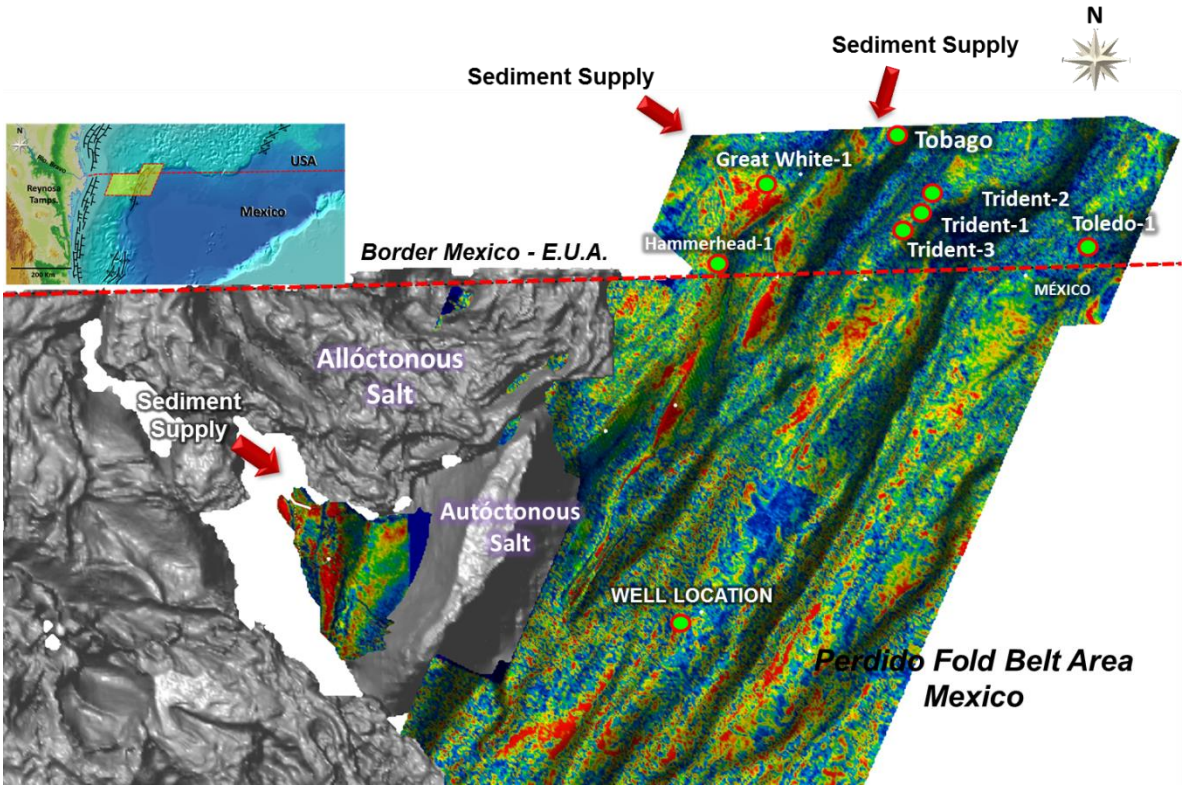

Figure7. *RMS amplitude map extracted into the Lower Eocene, showing the channels and submarine fans systems in Perdido Fold Belt. Taken and Modified from Study of Plays, PEMEX 2011.*

The wells drilling in the Northwestern portion Gulf of Mexico both in U.S waters and Mexican waters have proportioned important information for the quality of reservoir rock. In the wells drilled in the Mexican portion (Delta del Bravo area) were realized petrophysical, petrographycal and ternary diagrams analysis to determine the mineral component, as well as the interpretation of thin sections and calculus of porosity and permeability of data directly from the well in sands of Lower Miocene.

According with the result of petrophysical and petrographycal analysis from the Mexican wells, the porosities vary from 4 to 26 % while the permeabilities vary from 0.004 to 178 mD. The main porosity interpreted is inter-granular, while the second porosity is given by microfractures and grain dissolution (feldspard and bioclats) [Study of Plays PEMEX et al. 2008]. The reservoir rock quality is interpreted as fine grains of Litharenite and greywackes

and clay matrix. The quartz is the main component identified, which is defined by a microcrystalline shape, sub-rounded and well sorted [Study of Plays PEMEX et al. 2008] (figure 8).

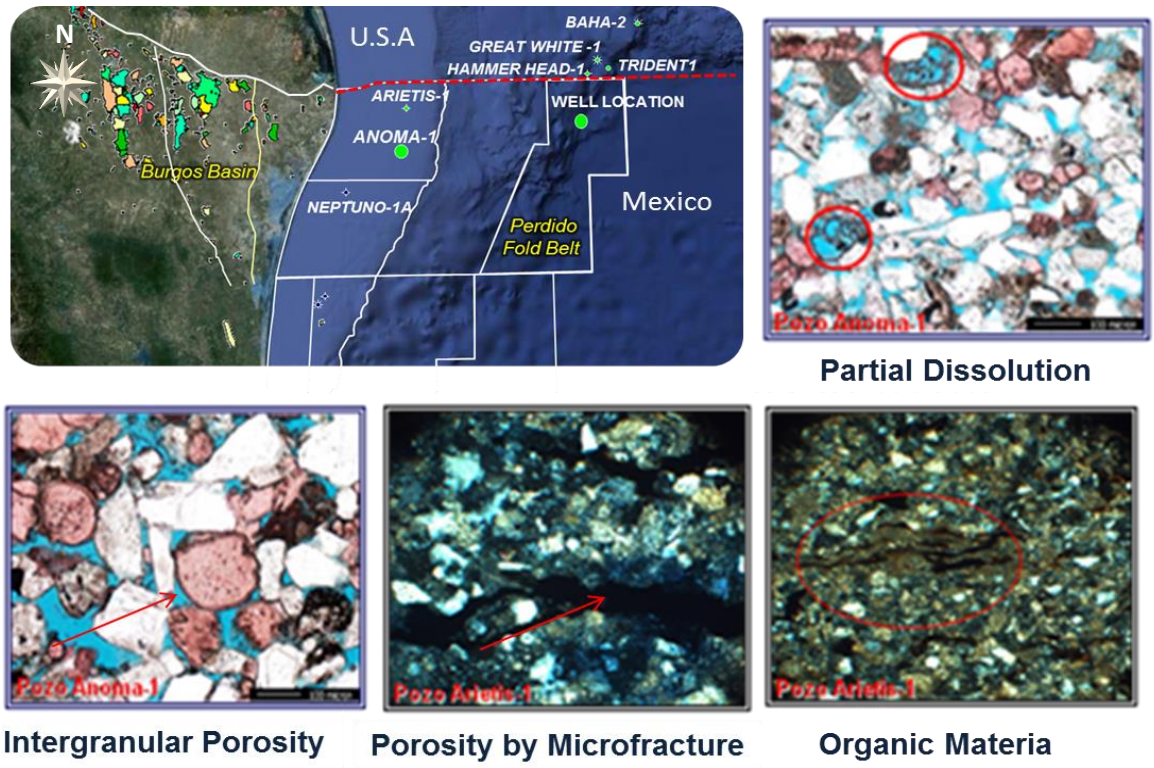

***Figure 8**. Thin sections interpreted in the Anoma-1 well, showing the reservoir rock quality and the mineral components. Taken and modified from Study of Plays, PEMEX 2008.*

The analysis of thin sections realized in the Perdido Fold Belt (Baha-2 well) into the Lower Eocene Wilcox formation, shows a strong quartz component and rock fragments, showing partial dissolution in the lithic and reduced quartz overgrowth [Study of Plays PEMEX et al. 2008]. This formation also shows clean sands with reduced clay matrix and showing a good inter-granular porosity (27%) (figure 9). On the other hand, the Oligocene Frio formation is represented by an inter-granular porosity poorly sorted (24%), which is constituted by quartz components, volcanic glass and carbonate fragments with permeability varies from 24 to 40 mD [Study of Plays PEMEX et al. 2009].

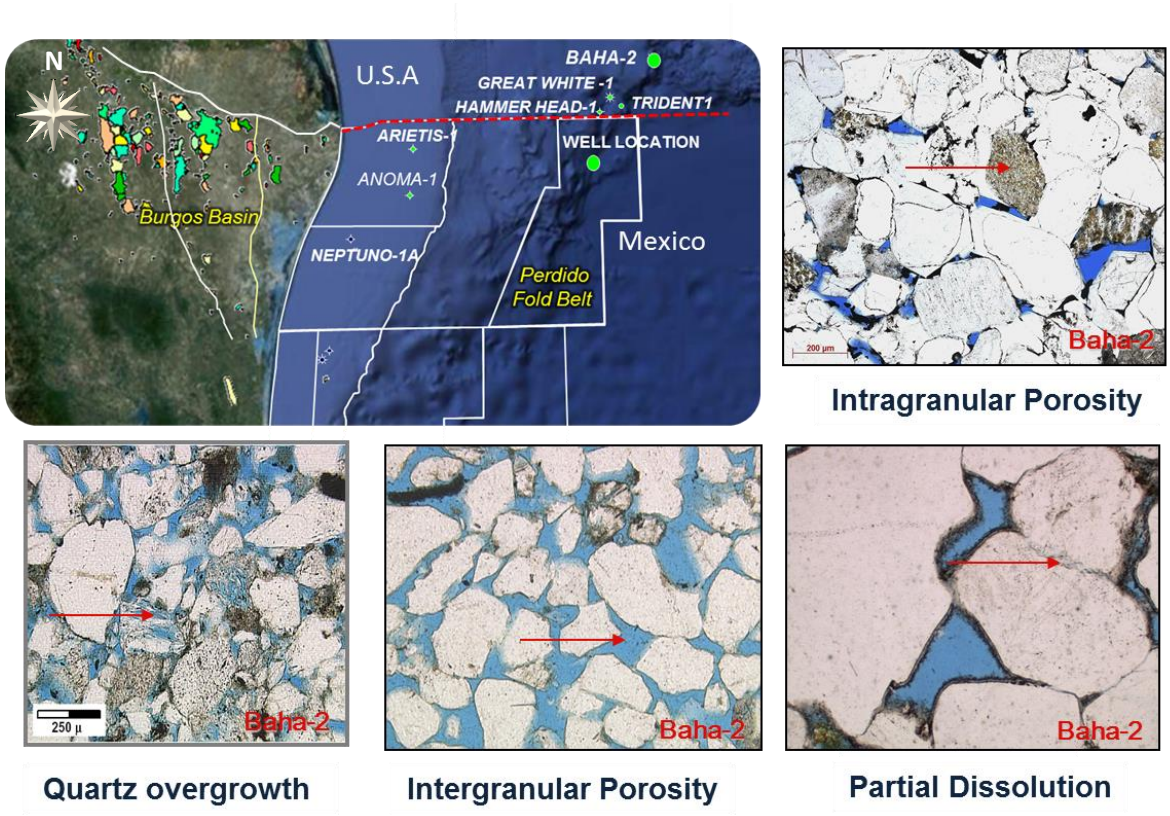

***Figure 9**. Thin sections, showing the reservoir rock quality and the mineral components interpreted in the Baha-2 well. Taken and modified from Study of Plays, PEMEX 2008.*

2.3. Geological and Production Analogues

Today in the Perdido Fold Belt, several U.S companies independent and operators participate in the concessions that the U.S government provide for the exploration and production of hydrocarbons, highlighting three of the most important companies as Chevron-Texaco, Shell and BP, which control around 70% of exploration in Gulf of Mexico [Wood Mackenzie, May 2003]. The analogue fields more important in the Perdido Fold Belt closer to Mexican waters, taking into account the structural alignment, depositional system and hydrocarbons associated are: Great white-1, Trident-1, Baha-2 and Jack-1, which have reserves per field ranging between 300 to 15,000 billion barrels of oil (40 °AP) and associated gas. The water depths for these fields vary from 2,400 m to 2,950 m, where has been able to drill vertical depths until 6,300 m. [Wood Mackenzie, May 2003].

BAHA

In November 1994, the companies Shell, Amoco, Mobil and Texaco built a co-participation company to drill one well, where every company had contiguous blocks ("Brachiosaurus", "Anaconda", "HI-C" and "Alfa Centaury" respectively), thereby the project was called Baha, according with the initials of each block. Thus, the first well drilled in Perdido Fold Belt area was the Baha-1 (April of 1996), with a water depth of 2,322 m. Baha was originally identified as a large, deep, sub-salt prospect with spanned up to 9 blocks in central Alaminos Canyon. The Cretaceous limestone the main objective was estimated to have a reserve potential in excess of 1 billion boe, while the secondary objectives were identified within Eocene and Jurassic sediments. However owing to small drilling margins (difference between pore pressure and fracture gradient) a great number of casing run were required in the upper hole section, so the well was abandoned in the top of Lower Eocene Wilcox, even when it had found 3 m with hydrocarbons impregnation [Wood Mackenzie, May 2003].

Later in the 2000 years was drilled the well Baha-2 (figure 10), with a water depth of 2,374 m and located only at 5 m Northeast from Baha-1. This well had as main targets the deeper Cretaceous and Jurassic, and as secondary objectives the shallow section into the Lower Eocene Wilcox, which had been drilled originaly by the Baha well. This well had two side-tracks with water depths 4,989 and 5841 meters respectively. The Baha-2 drilled the Lower Eocene Wilcox formation (showing low hydrocarbons saturation and poor permeability), Cretaceous (showing low characteristic to be consider reservoir rock) and Jurasic. So this well was evaluated as non-commercial production well and marginal reserves no higher than 150 MMbo [Mackenzie, May 2003].

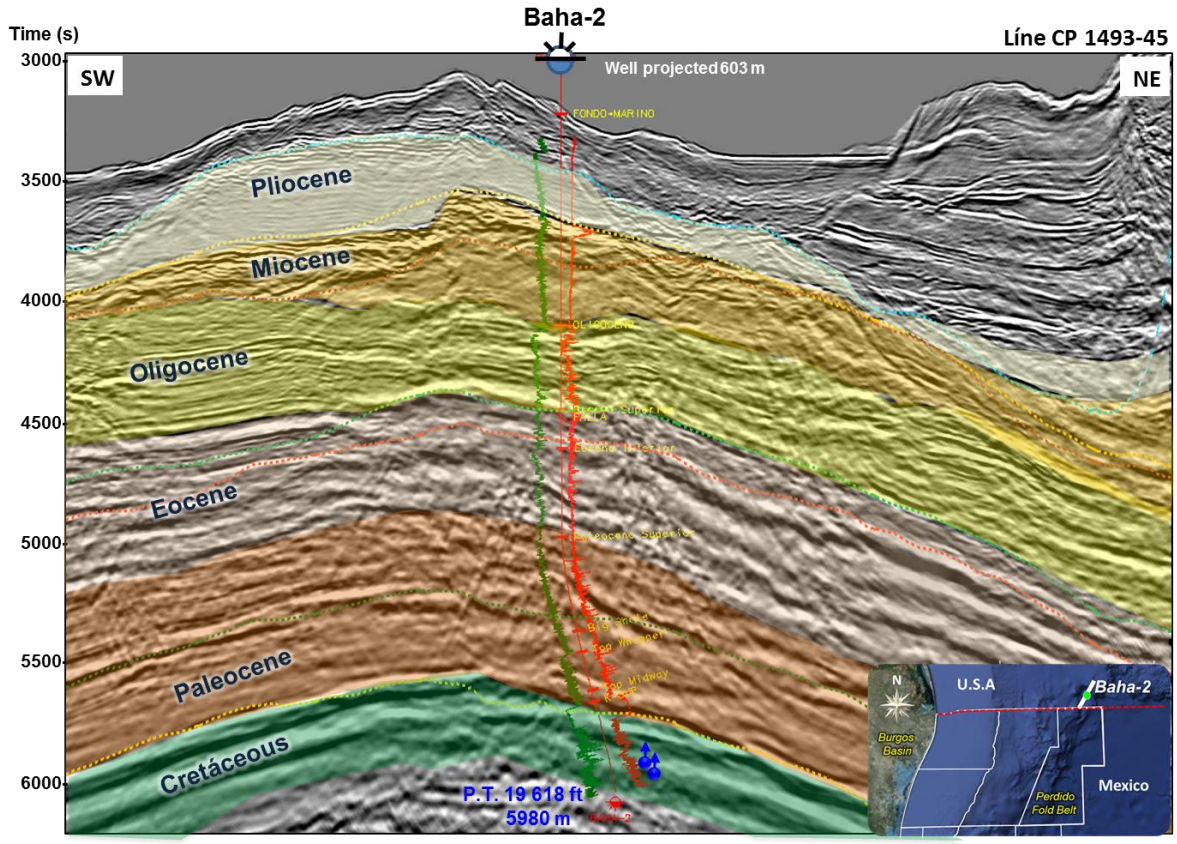

***Figure 10**. Stratigraphic column drilled by the well Baha-2, which was evaluated as non-commercial well due its poor reservoir rock qualities and low hydrocarbon presence. Taken and modified from Study of Plays PEMEX, 2011.*

TRIDENT FIELD

The Trident-1 field is located into an ultra-deep waters zone in the Alaminos Canyon area, approximately six kilometers Northern from the border between Mexico and US and 10 kilometers Southeast from Great White field. This field consists of seven blocks: AC 860, 861, 903, 904, 905, 947 and 948. The common block ownership was shared as: Unocal (59.50% and operator), Chevron Texaco (15.00%), Ocean (12.75%), ENI (12.75%) and ENI picking up the 4.25% by courtesy of ENI in August 2001, so Trident was drilled in 2001, with a water depth of 2,970 m and total depth of 6,246 m (figure 11) [Wood Mackenzie, May 2003].

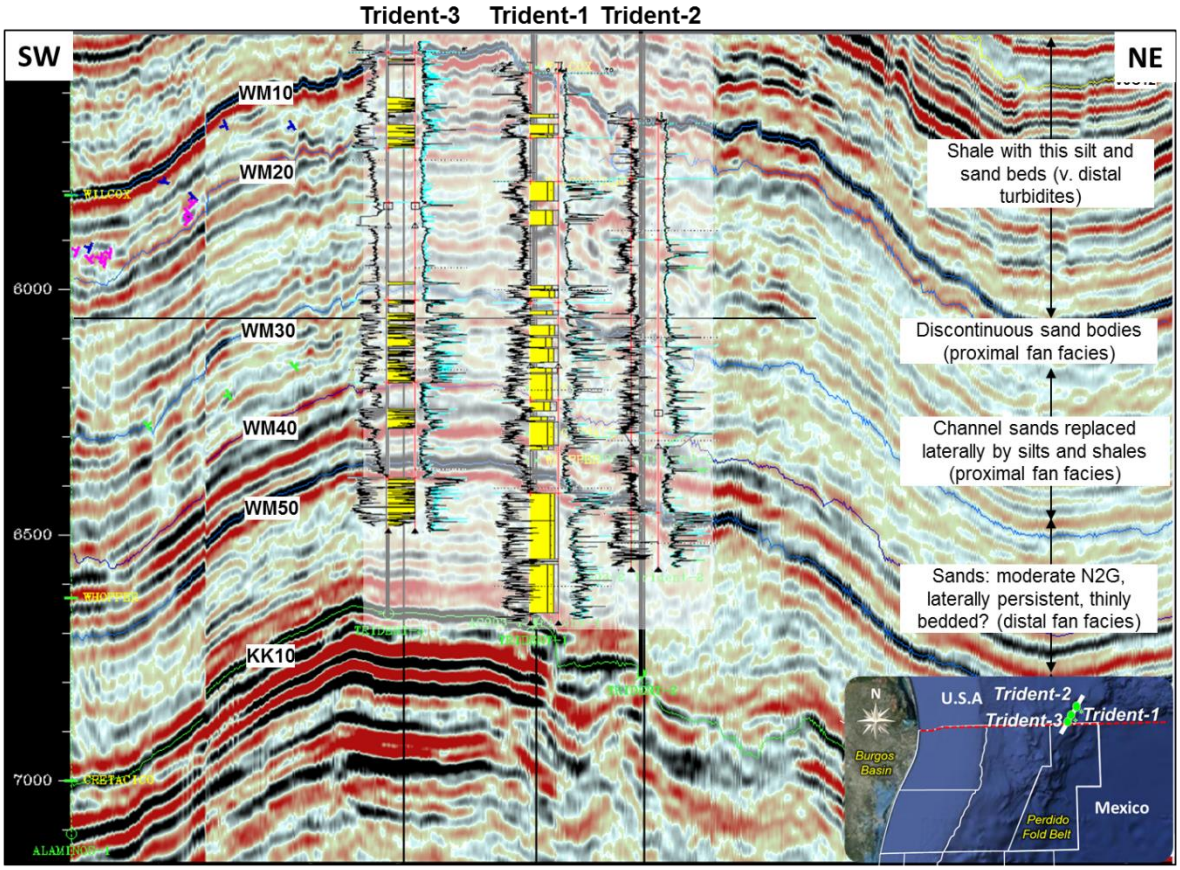

Figure 11. *Well correlation in the Trident field, showing the presence of reservoir rock into the tertiary formation Lower Eocene Wilcox and Upper Paleocene Whopper. Taken and modified from Study of Plays PEMEX, 2008.*

Later were drilled two delimiter wells, one located at North with water depth of 2,965 m, which was evaluated as successful due it confirmed the continuity of the field to the North. Originally, Trident was estimated to comprise a large accumulation of oil and associated gas. Although the reserves has not been fully evaluated, initial estimates suggest recoverable reserves ranging between 200 – 400 mmboe. However, it has assumed an ultimate recovery around 250 mmboe, dividing 210 mmbbl with high quality oil (40° API) and 230 bcf of associated gas and a gas/oil ratio (RGA) around of 1,100 m^3/m^3 [Wood Mackenzie, May 2003].

GREAT WHITE FIELD

The Great White field is located South in the Alaminos Canyon area (approximately 10 kilometers North of the border between Mexico and U.S and 10 kilometers Northwestern of Trident field. This field includes six blocks: 813, 814, 857, 858, 900 and 901. This field covers an area of 163 square kilometers, being the operators companies responsible from this field Shell (33.34% and operator), BP (33.33%) and Chevron Texaco (33.33%) [Wood Mackenzie, May 2003].

The well Great White-1 was drilled in 2002, with a water depth of 2,437 meters and total vertical depth of 4,116 meters. Later was drilled a Side Track in the same 2002 reaching a total vertical depth of 6,067 meters. Additionally, were drilled two delimiter wells with a water depth of 2,452 meters. Great White is believed to comprise a potentially large accumulation of oil and associated gas. Initial evaluation suggests that the reserves could be ranging between 300 – 1,000 mmboe. However, it has estimated recoverable reserves around of 700 mmboe of high quality oil (40° API) into the Lower Eocene Wilcox formation, dividing 550 mmbbl of oil and 850 bcf of associated gas. (figure 12) [Wood Mackenzie, May 2003].

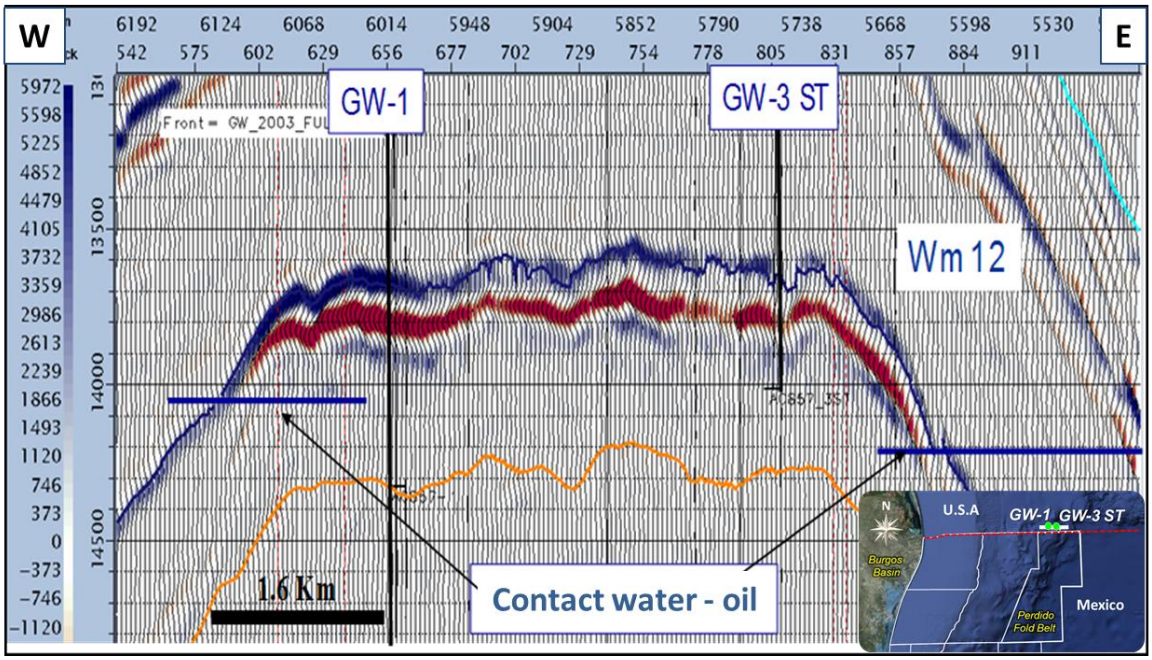

Figure 12*. Well correlation in the Great White field, showing the producer interval of oil into the Lower Eocene Wilcox formation. Taken and modified from Study of Plays PEMEX, 2008.*

2.4. Potential Plays in Perdido Fold Belt

The information derived from wells drilled in U.S waters, has been useful to correlate and try to predict the reservoir rock quality in Mexican waters, so in base of Baha-2, Trident-1 and Great White has been possible establish three main plays with hydrocarbon potential: 1) Upper Oligocene (Frio formation), 2) Lower Eocene (Wilcox formation), and 3) Paleocene (Whopper formation).

Play Lower Oligocene (Frio Fm.)

Source rock: Shaly-Carbonated rocks deposited in a suboxic environment during the Upper Jurasic (Oxfordian-Tithonian), no ruling out the possible presence of shally-carbonted rocks of Barremian-Turonian and Eocene.

Reservoir Rock: Turbiditic sands characterized by channel facies deposited in talud and proximal basins environments, with porosity ranges from 13 to 28 % and net thickness from 10 m to 110 m.

Seal Rock: Shaly sequences mixed with some sands, compactness affected by intense faulting and low compactness, which could represent the main risk in this play.

Trap: This play is characterized by the presence of anticlines with closer in four directions, closer against faults and stratigraphic traps mainly channels.

Play Lower Eocene (Wilcox Fm.)

Source rock: Shaly-Carbonated rocks deposited in a suboxic environment during the Upper Jurasic (Oxfordian-Tithonian), no ruling out the possible presence of shally-carbonted rocks of Barremian-Turonian and Eocene.

Reservoir Rock: Turbiditic sands characterized by channels and laminar facies, associated to Wilcox formation deposited in talud and basin environments, with porosity ranges from 16 to 28 % and net thickness from 20 m to 140 m.

Trap: Characterized by the presence of big anticlines with closer in four directions, closer against faults and stratigraphic traps mainly submarines basin floor fan, channel systems and sheet sands.

Seal: The seal in this play is represented by shaly sequences deposited above of the Wilcox formation, which shows a wide extension and thickness until 110 meters. This seal in some zones shows the presence of small sand bodies.

Play Whopper

Source rock: Shaly-Carbonated rocks deposited in a suboxic environment during the Upper Jurasic (Oxfordian-Tithonian), no ruling out the possible presence of shally-carbonted rocks of Barremian-Turonian and Eocene.

Reservoir Rock: Turbiditic sands characterized mainly by laminar and lobular facies, associated to the Wilcox formation (Upper Paleocene) deposited in basin environments, with porosity ranges from 12 to 18 % and net thickness from 45 m to 150 m.

Trap: Characterized by the presence of big anticlines with closer in four directions, closer against faults and stratigraphic traps mainly basin floor fans and sheet sands.

Seal: The seal in this play is represented by shaly sequences deposited above of the Wilcox formation, which shows a wide extension and thickness until 150 meters, such as the Big Shale unit which was cut by the Trident well. This seal shows in some areas intercalations of thin layers of sand.

III. SEISMIC INTERPRETATION

The seismic interpretation performed in this thesis work, was performed in a prospect, which is located in the Northern Gulf of Mexico (see figure 1) into the deep water compressional system of Perdido Fold Belt. This prospect is considered as an important opportunity in the strategic scheme of PEMEX in the searching and exploration of deep water prospects that can incorporate new hydrocarbon reserves in Mexico.

The Perdido Fold Belt is a geological complex area, where several steps and deformations events, halokinethic process (salt withdrawal), shale tectonics, gravitational systems (extension – contraction), and shortening within the salt canopies are associated with the development of reverse faults and compressional structures that dominates the area.

The Perdido Fold Belt also is characterized to be in ultra-deep water zone where to explore and characterize this area, has been necessary implement new techniques of acquisition and seismic data processing that oil industry has developed recently. These techniques also have guided to the implementation of new concepts, models and innovative interpretation tools, such as: advanced seismic attributes, application of new concepts of structural geology and salt tectonic, AVO and seismic inversion analysis, etc. So, this progress has enabled to have a better stratigraphic and structural understanding in this area, so today is possible to identify and propose new geological models with hydrocarbon potential.

The Interpretation sequence performed in this project, starts with the analysis of seismic data (revision of seismic acquisition parameters and sequence process), followed by the calibration of the seismic - borehole by implementation of a synthetic seismogram, understanding of structural geology involved in the area by using variance attributes, faults interpretation and developing of a simple structural evolution model in the main structure. In addition, by implementing of conventional amplitude attributes and by using horizons and seismic attribute volumes flattened was possible to obtain an understanding of deposit system.

3.1. Seismic Acquisition Parameter and Data Processing

3.1.1. Seismic Acquisition

In 2002, PEP (for its acronyms in Spanish “Pemex Exploration y Produccion") realized a 3D seismic acquisition called Maximo3D, which covers an area of 2600 Km^2, being its main target to reduce the geological uncertainty by densification and improved image in the subsurface. The Maximo3D survey is located in Northern Gulf of Mexico in the limit of the exclusive economic zones between Mexico and U.S and 130 nautical miles eastern Tamaulipas cost with waters depth varies between 2,382 m to 3,438 m (figure 13).

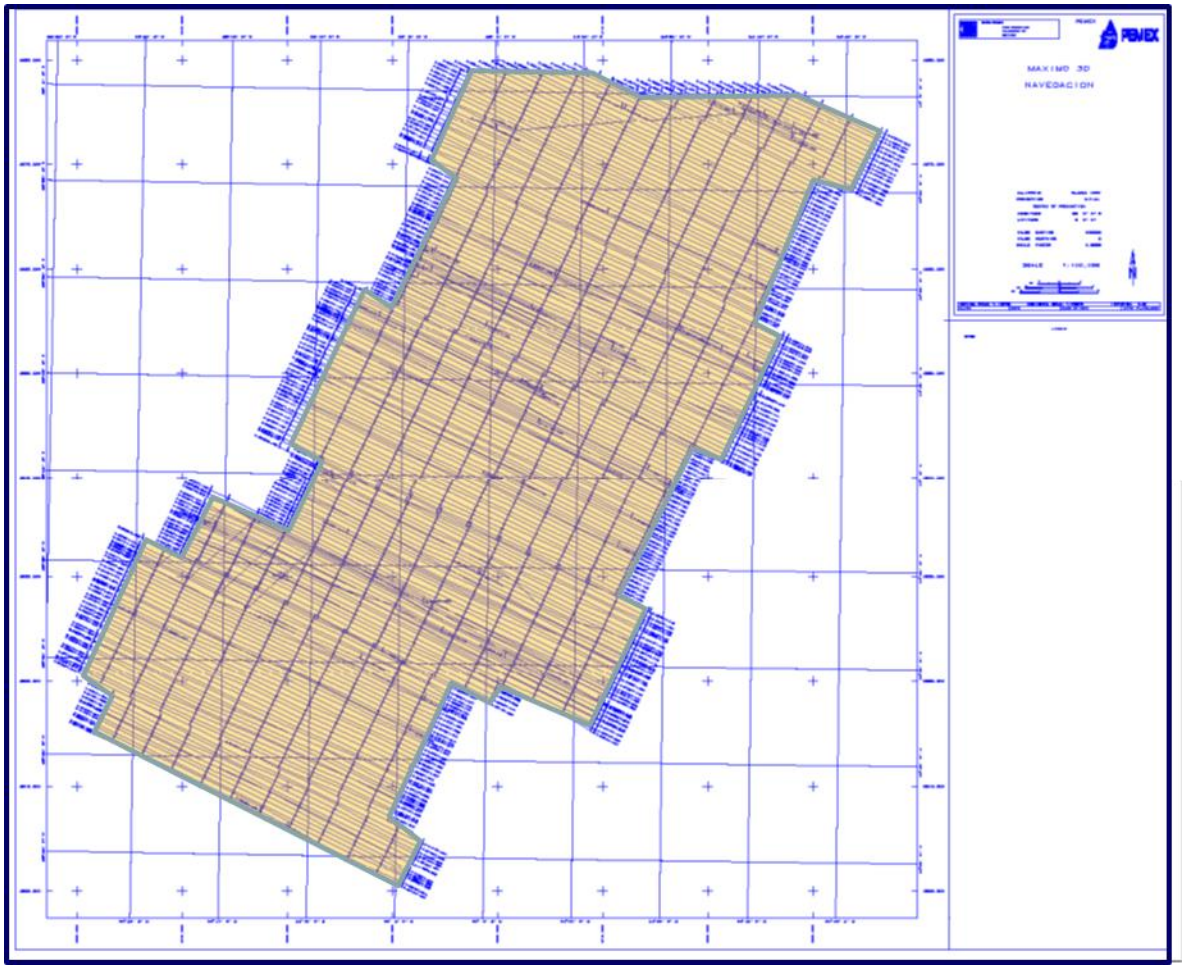

Figure 13*. Base Map of Maximo3D survey, showing the geometry and orientation of the seismic sources implemented during the seismic acquisition. Taken and modified from PEMEX, 2002.*

This seismic acquisition was performed by WesternGeco Company by using navigation lines oriented in direction 296° - 115°, and average longitude of 28,091 Km. This study was

performed by the Western Patriot ship by using a standard shooting pattern. The streamers configuration was implemented with 6 Thompson Marconi cables with longitude of 7,200 m and crosslines separation of 600 m, located at 8 meters depth. Every cable consisted of 288 channels considering a distance between groups of 25 m. The source configuration consisted of a pair of sources of 300 cubic inches each one, and crossline separation of 80 m. The sources were operated to a water depth of 6 m and shot in an alternated pattern (flip-flop) every 31.25 m or 62.5 m by source. Every source consisted of 4 sub-arrays of 750 cubic inches each one, separated by a crossline distance of 6 m. This array generated a total fold of 57, starting from North to South [PEMEX et al. 2002] (figure 14).

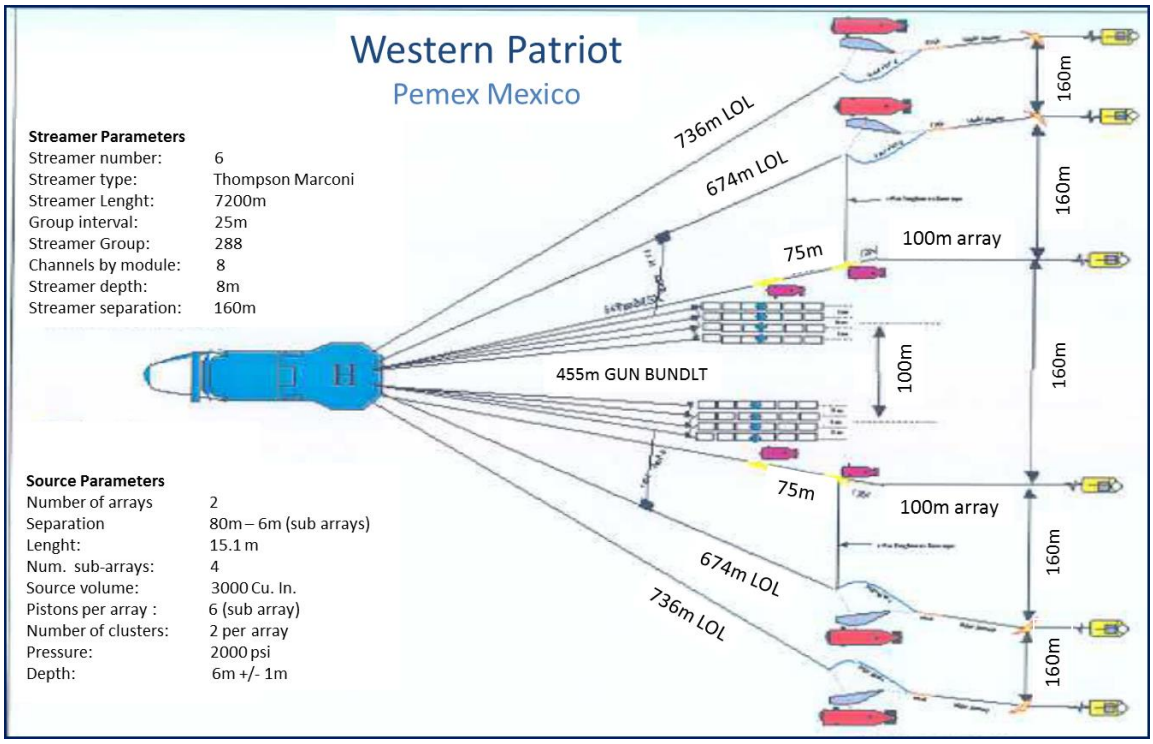

Figure 14*. Streamer towing configuration, showing the sources pattern and streamers array implemented during the seismic acquisition of the seismic volume Maximo 3D. Taken and modified from PEMEX, 2002.*

This study was performed to PEMEX with exploration objectives. The target depth of this 3D seismic survey was focused between 4,500 m and 5,200 m, with two travel time between 1 to 2 seconds. The geological target was both structural and stratigraphic taking into account a normal deposition of siliciclastic and carbonated sediments [PEMEX et al. 2002].

3.1.2. Data Processing

The 3D Maximo surveys that covers 3000 square kilometers of area was processed in two steps: the first step consisted to process the data acquired onboard, which generated a Post-stack seismic migration volume and the second and final version, a volume of seismic migration Pre-stack, which was processed by PEMEX in the CNPS (for its acronyms in Spanish "Centro Nacional de Procesado Sísmico") processing center (figure 15).

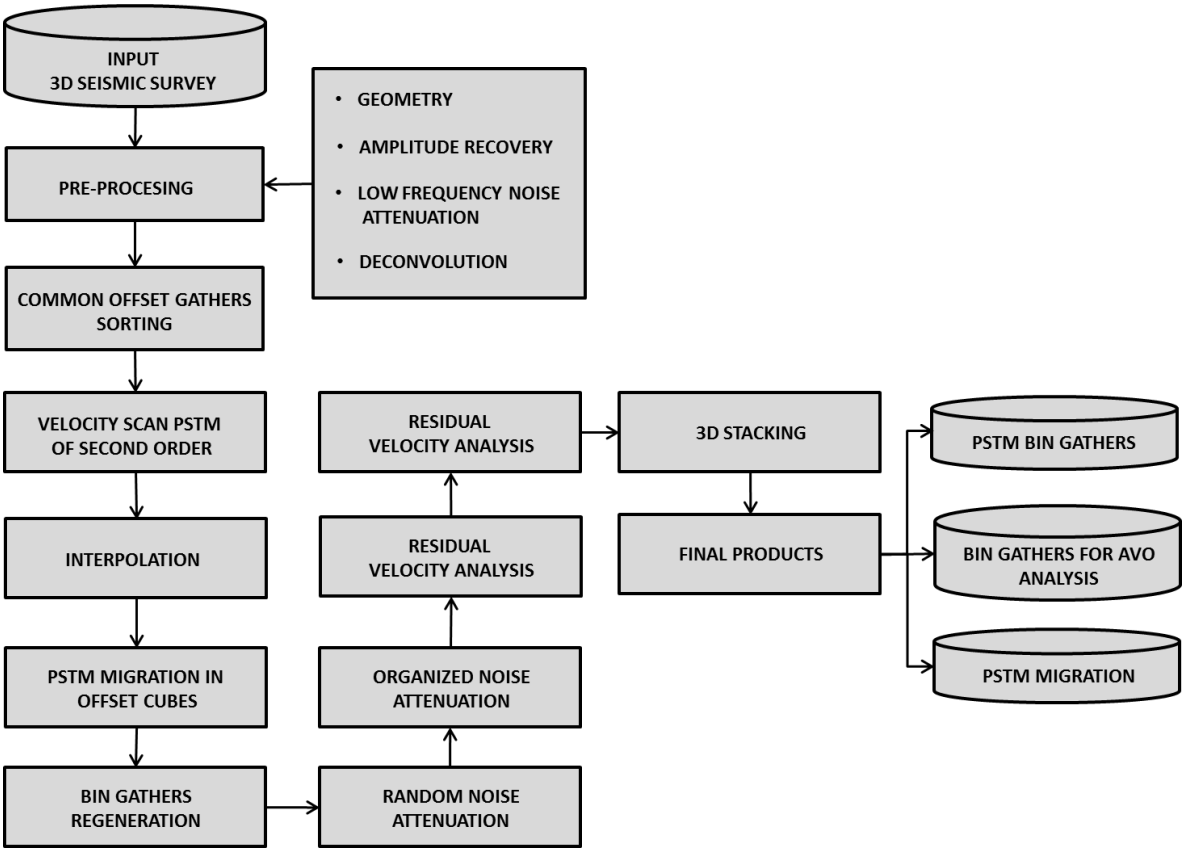

Figure 15*. Diagram showing the data processing flow applied in the seismic Maximo 3D survey, which was the first 3D seismic survey developed for PEMEX in deep waters in the CNPS (for its acronyms in Spanish "Centro Nacional de Procesado Sísmico") data processing center. Taken and modified from Study of Plays PEMEX, 2008.*

The seismic survey Maximo 3D was processed taking into account both geological and geophysical targets. Since the geological point of view, it had as primary goal to define the geometry and continuity of anticline structures in the Perdido Fold Belt with the purpose to

increase the reliability during the risk evaluation and volumetric estimation. In addition, define the fault patterns and their trajectory which affect the anticline structures, thereby to reduce the geological risk.

Since the geophysical point of view, the primary targets were, obtain a reliable seismic image of subsurface (considering both tertiary and Mesozoic objectives), enabling a high quality seismic interpretation both structural and stratigraphic. In addition, obtain a reliable seismic information, enabling the amplitude anomalies identification (bright spots, flat spots, polarity changes, dim spots), as well as CDP (common deep point) gathers and velocity models, which allow the implementation of advanced studies in the future: pore prediction, depth migration and special processes (AVO and seismic inversion).

The data processing of the seismic Maximo 3D survey, constituted the first 3D seismic project processed by the CNPS in Mexico. This project involved the using of intense compute resources, besides the use of trained people to perform such process. The constant interaction with the UEAP (for its acronyms in Spanish "Unidad Especializada de Aguas Profundas") seismic interpreters was necessary also, mainly during the velocity model construction and seismic migration.

3.2. Database Integration

To perform the seismic interpretation in this work, first was necessary the construction of a database to integrate all the geological and seismic information available, that consisted in a 3D seismic volume (Maximo 3D), well logs, seismic horizons, seismic gathers, and software of seismic interpretation and AVO-Seismic Inversion analysis (Table 1). The seismic and well information was proportioned by PEMEX, which is owner and delivered all permissions to perform this thesis work. While that, software used was the Petrel version 2011 and Geoview (Hampson & Russell) version CE8/R4.4.1, proportioned by the NTNU as support all student who develop their Master or PhD program in this institution.

Seismic Information		
Type of Seismic	**Volume (Km^2)**	**Format**
CDP Gathers in time	80	SEG-Y
PSTM migration	80	SEG-Y
Geophysical logs		
Type of log	**Segment (mts)**	**Format**
Caliper	2232-4466	Ascii
Gamma Ray	2233-4465	Ascii
Resistivity	2232-4466	Ascii
Density	2232-4466	Ascii
Sonic Compresional	2232-4466	Ascii
Sonic Shear	2232-4466	Ascii
Neutron	2232-4466	Ascii
Check Shot	0-7500	Ascii
Surfaces		
Horizon	**Version**	**Format**
Sea bottom	Time	Ascii
Oligocene Frio 14	Time	Ascii
Oligocene Frio 20 Top	Time	Ascii
Oligocene Frio 20 base	Time	Ascii
Oligocene Frio 26	Time	Ascii
Oligocene Frio 30	Time	Ascii
Oligocene Frio 31	Time	Ascii
Software		
Program		**Version**
Hampson-Russel		CE8/R4 4.1 2010
Petrel		2011

Table 1*. Database integrated for the Seismic Interpretation and AVO and Seismic Inversion Analysis*

3.3. Seismic Interpretation Methodology

The Seismic interpretation realized in this project was performed following three main objectives: 1) understand and interpret the trap geometry, taking into account all the geological events and their faults system associated, 2) obtain a reliable sedimentary and stratigraphic model, that allows the mapping of reservoir rock distribution and associated stratigraphic trap and 3) identify and interpret the distribution of amplitude anomalies associated to possible hydrocarbons presence and reservoir rock. . In addition, obtain a key geological model for the AVO and seismic inversion analysis. This required to follow an interpretation workflow (figure 16), which helped to achieve such targets.

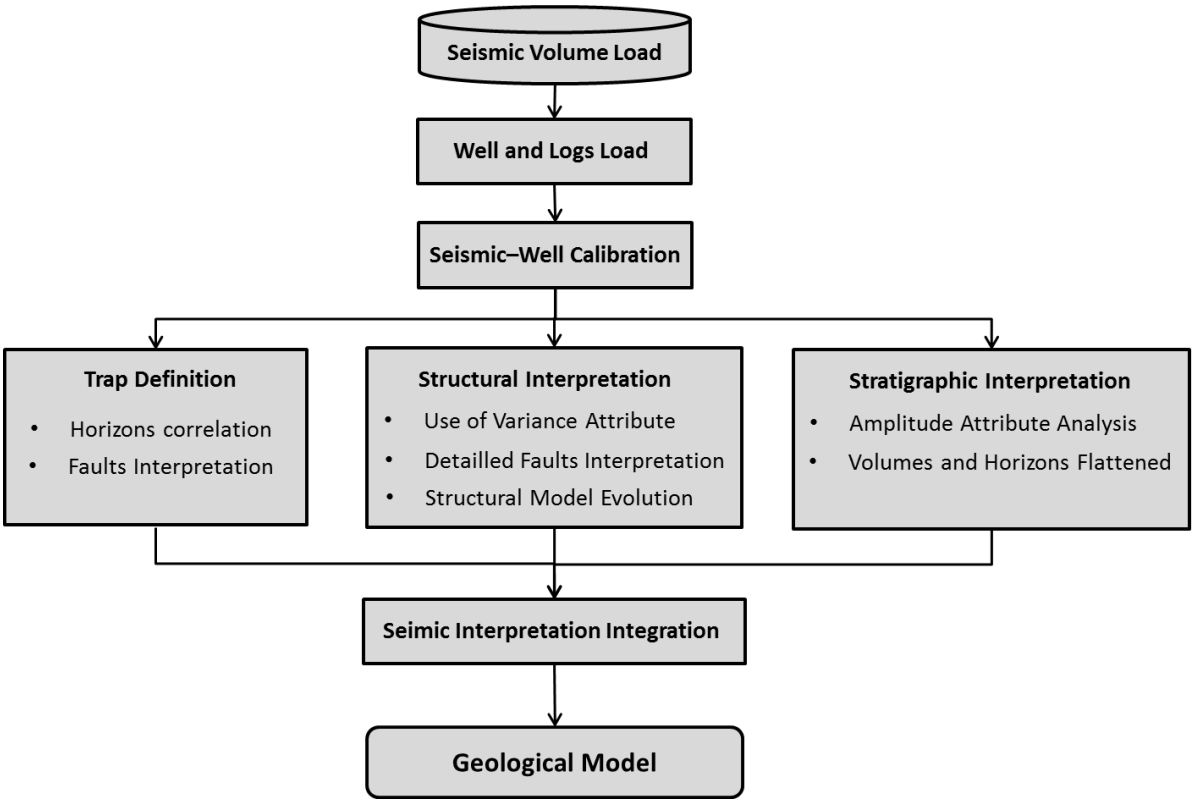

***Figure 16**. Seismic interpretation workflow performed to obtain the optimal geological model for the subsequent AVO and seismic inversion analysis.*

3.4. Seismic –Well Calibration (Well tie)

Once loaded the seismic survey and well logs related to the prospect, the next step was to do the seismic – well calibration. To do this, was necessary the development of a synthetic seismogram. The synthetic seismogram developed in this project basically involved three main steps: 1) sonic well log calibration, 2) seismic wavelet extraction and 3) the performance of synthetic seismogram.

The sonic log calibration was done by using a checkshot function derived directly from the well drilled. The target of this step is to quantify the accuracy that exists between the sonic log and the TZ function, which is measured by a drift curve. The difference in time between the checkshot and drift curve is a residual drift curve. The closer it is to zero, the sonic log match better with the checkshot. If the residual drift curve does not deviate from the zero

line, it means that the log times are fully consistent with checkshot times and the drift curve will coincide with the checkshot points (figure 17).

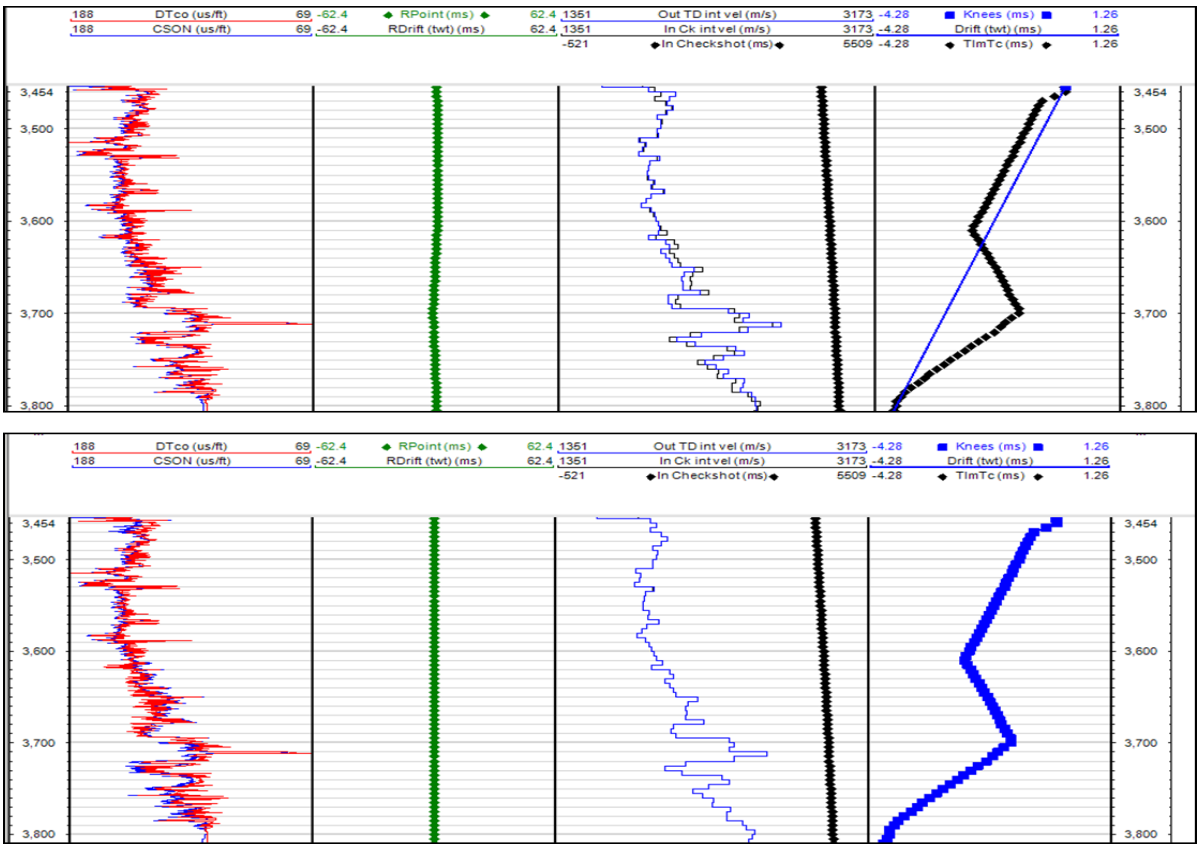

Figure 17*.Sonic log calibration before and after to do the drift correction.*

The sonic log and the checkshot function in this prospect, showed a good match due drift curve is very close to zero, being the interval approximately between 3610 – 3780 where the mismatch is higher (around of 4-5 ms), however it is considered still low.

After of develop the sonic log calibration, the next step was the wavelet extraction to be implemented later in the synthetic seismogram construction. In this case was extracted a wavelet directly from the seismic around the well (figure 18). It wavelet showed a negative minimum phase, and dominant frequency between 18 – 40 Hz. Thereby, was possible to see that the wavelet extracted showed a good percent of predictability (above 60 percent), it means a good relationship between the reflection coefficient series and the seismic around

of well position, taking into account the lag time, inline-crossline positions and wavelet phase.

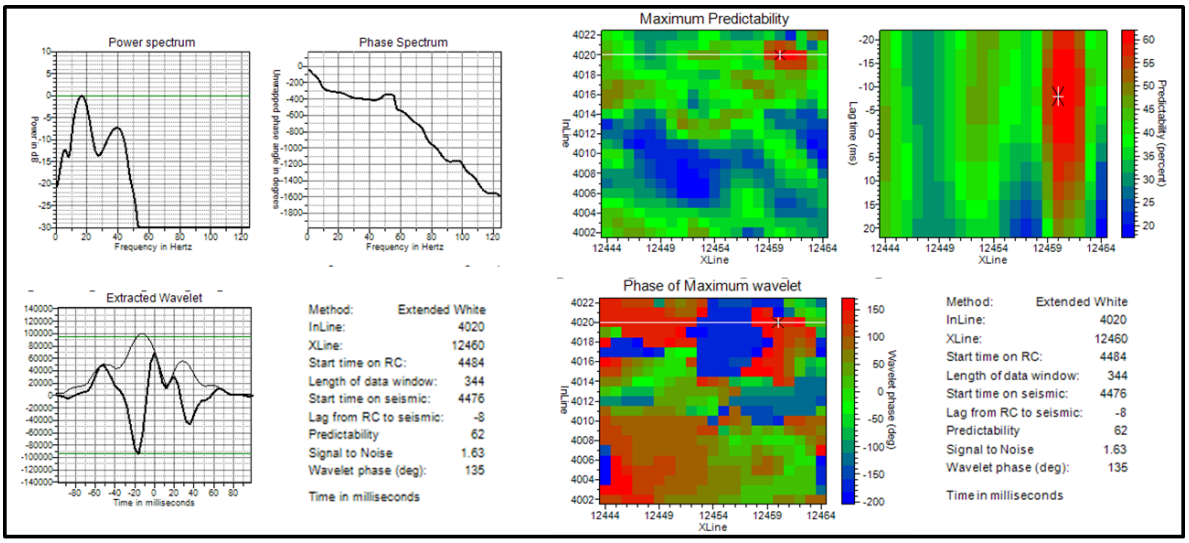

***Figure 18**. Characteristics of the seismic wavelet extracted from seismic around the well, showing a good percent of predictability to be performed in the synthetic seismogram construction.*

Once calibrated the sonic log correctly and extracted the best wavelet around of the well, the synthetic seismogram construction was executed. The synthetic seismogram construction was performed by using the convolutional model. The basic assumption is that a stacking seismic trace for a given location can be represented as a convolution between a representative wavelet and a series of reflection coefficient representing the layers of subsurface, which can be expressed as:

$$y(t) = w(t) * f(t) \tag{1}$$

Where:

$y(t)$ = Recorded seismic signal

$w(t)$ = Input signal (wavelet)

$f(t)$ = The impulse response of the Earth

To carry out the estimation of coefficient reflection, first was necessary to calculate the acoustic impedance of different layers in the subsurface by using the density and sonic logs.

The mathematical expression for a reflection coefficient in function of acoustic impedance is represented by:

$$RC = \frac{Z_i - Z_{i-1}}{Z_z + Z_{i-1}} \tag{2}$$

Where:

RC = Reflection coefficients

Z_i = Acoustic Impedance

The resultant synthetic seismogram performed in this project showed a good match with the seismic surrounded (figures 19 and 20). Thereby, could be interpreted that the seismic information corresponds a seismic American polarity with minimum phase.

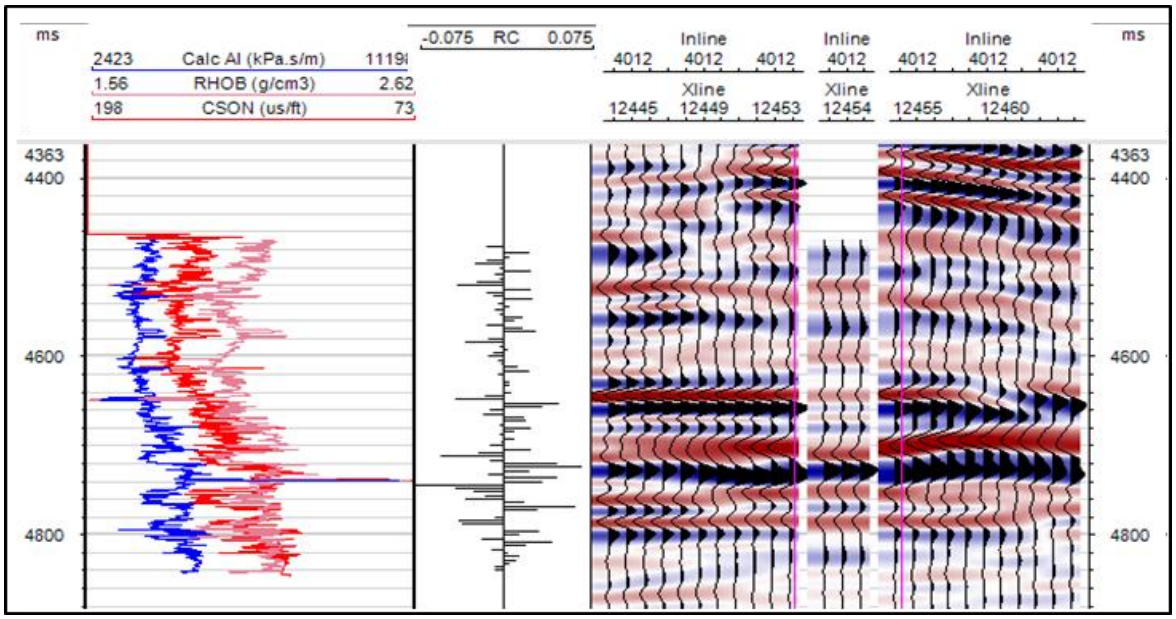

***Figure 19**, Synthetic seismogram obtained from the reflection series and wavelet extracted directly from the seismic, showing a good match with seismic around the well.*

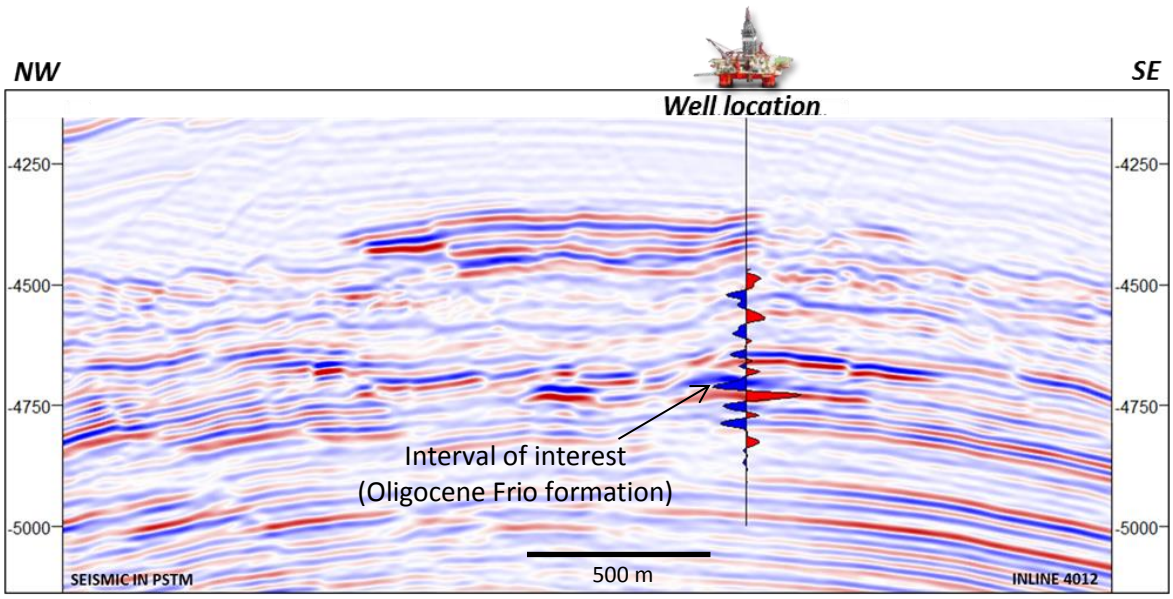

***Figure 20**. Synthetic seismogram performed in the well location, showing a good match between the reflective series associated to the Oligocene Frio formation and the seismic line 4012 (well location).*

3.5. Structural - Stratigraphic interpretation

Once calibrated the seismic data with the wellbore correctly, I proceeded to the trap interpretation. To do this, first was necessary to establish the targets to follow, which were derived for the information proportioned by the well. This well, as previously was described drilled a structure which belongs to the compressional system of Perdido Fold Belt with a water depth 2,900 m and total depth of 4000 m. The well had as main targets to evaluate a geological play characterized by a set of shallow anomalies and sands interval into the Miocene and Oligocene Frio formations, which had already been drilled and tested in near areas for the Trident-1 and Great White-1 wells in U.S, identifying the presence of hydrocarbons saturation and distribution of reservoir rock in the Oligocene Frio formation.

This borehole, showed three manifestations of gas and oil into the Oligocene Frio formation, which were analyzed petrophysically, thereby were identified two potential intervals of gas and oil, due in these intervals the well showed the presence of reservoir rock with good porosity and permeability (see appendix 1). Taking into account these evaluations, were established three targets to be studied: Oligocene Frio 14, Oligocene Frio

20, and Oligocene Frio 26. The figure 21 depicts a seismic line across of well, showing the geological characteristic and intervals of interest into the Oligocene Frio formation drilled by this well.

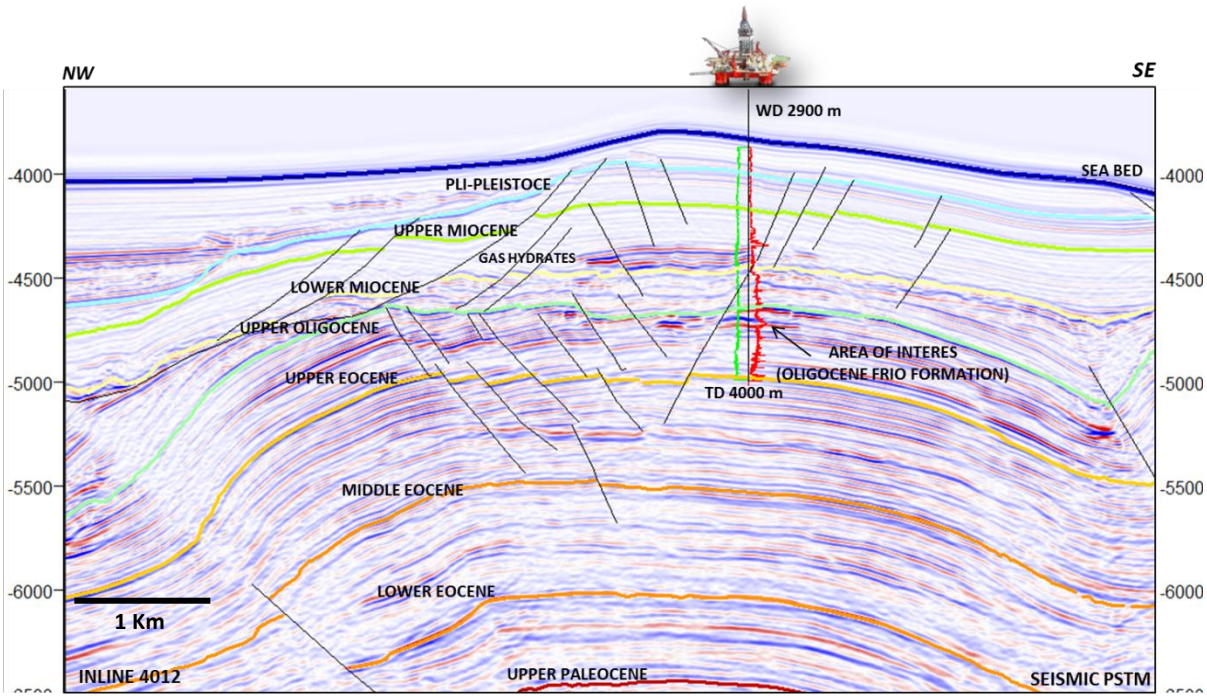

***Figure 21**. Seismic section across of well, showing the amplitude anomalies associated with the hydrocarbon presence and distribution of reservoir rock interpreted in this area.*

The interpretation model proposed in the inline 4012 (figure 21), is related with a structure generated by compression with Jurassic Salt detachment. This structure is associated with a salt anticline structure (by its definition in salt tectonics), due it shows an elongated geometry cored by authocthonous salt and limited by reverse faults in both flanks of the structure. The syn-kinematic deposits show that this structure could have been formed during the Upper Oligocene-Lower Miocene. Although also is evident that the deformation continues till the recent, due Plio-Pleistocene and the sea bottom present a late deformation (figure 22). Others events that also are evident in this area is the linked system (extension – contraction) in shallow sediments (Miocene-Pliocene), mainly in the west flank of structure (figure 23) which could has been produced by the instability of sediments as a result of late deformation. On the other hand, is possible to interpret a regional unconformity in the Upper Oligocene-Lower Miocene, which could confirms that during this period occurred the maximum deformation.

Other important features interpreted in this area, is the presence of normal faults in the top of the structure. These normal faults system, is assumed were generated by gravitational collapse during the main deformation of the structure.

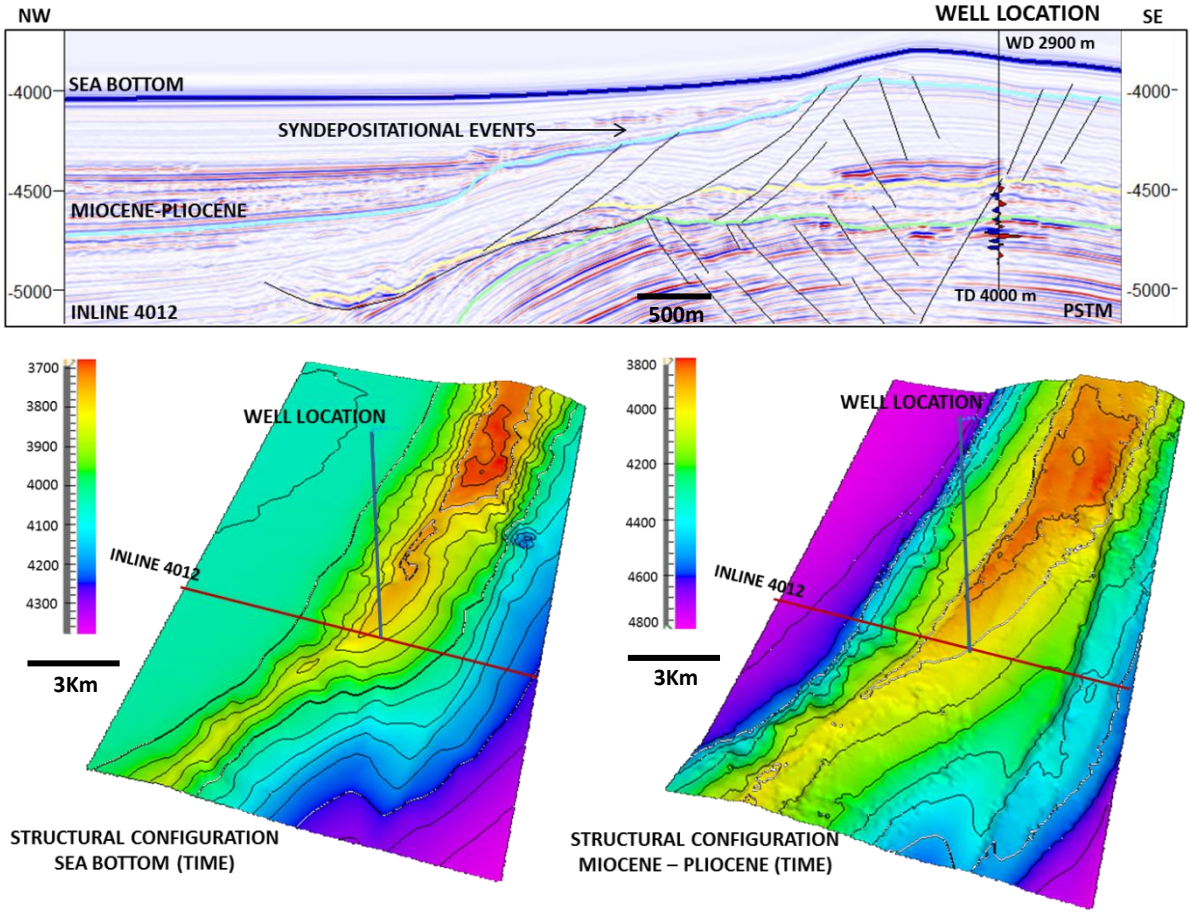

***Figure 22**. Shallow seismic line (inline 4012) and structural configuration performed in the sea bottom and Pliocene-Miocene events, where is possible to observe the late deformation occurred during this period of time, as a product of the gravitational linked-system (extension – contraction) actually occurring in the Northern Gulf of Mexico.*

The figure 24, shows a time slice at 5028 ms, where the variance attribute has been applied. Hence, is possible to observe the fault patterns associated with the main deformation occurred during the Upper Oligocene – Lower Miocene. This normal faults system were generated as product of gravitational collapse in the crest of the structures because of intense folding, which adopted a concentric geometry possibly due at different rate of sedimentation, producing a faster displacement basinward in zones where the sediment supply is bigger. Another possibility could be the difference in thickness of salt located in

the core of the structure, which may be producing a faster displacement basinward in zones where the salt thickness is bigger and therefore causing less displacement in areas where the salt thickness is reduced. The normal faults system has in the North flank of the structure an orientation NW-SE, becoming more N-S towards center, while in the south flank these change their orientation in direction almost W-E.

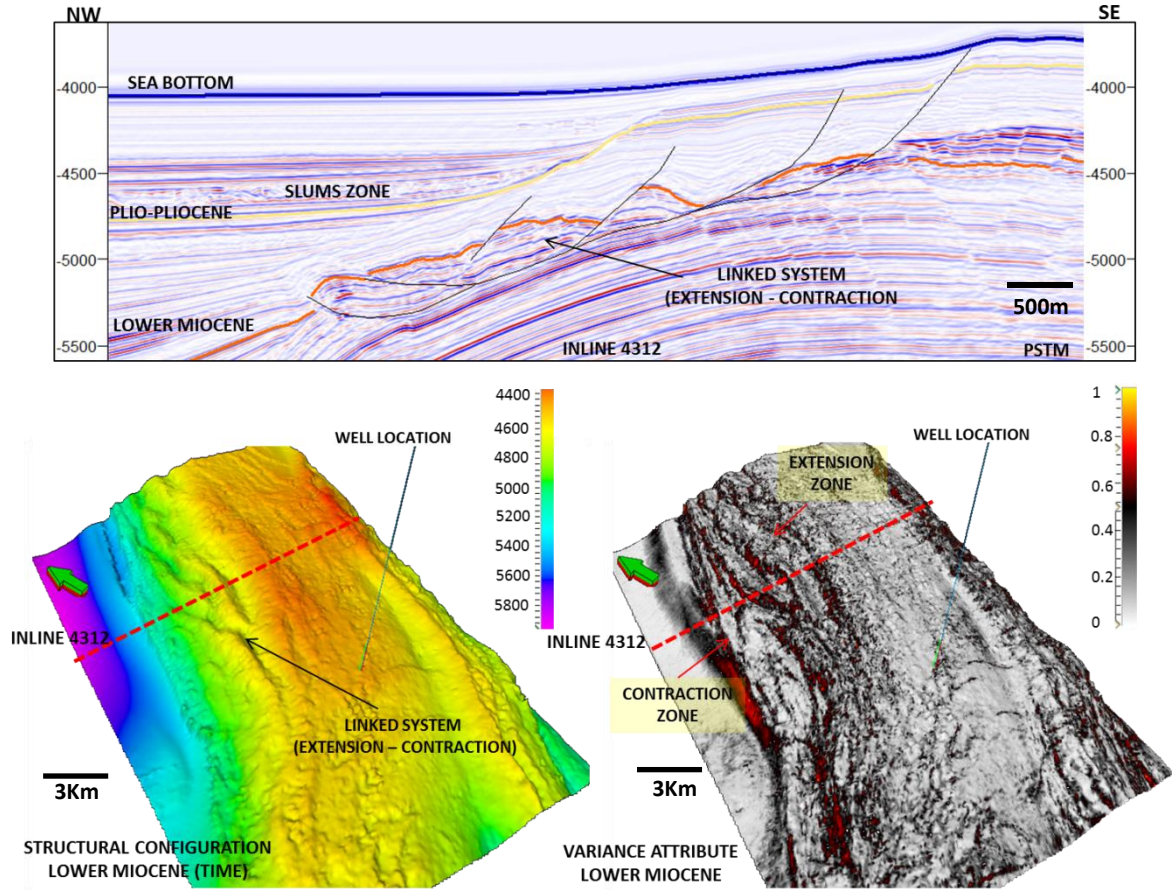

***Figure 23**. Seismic line (4312), structural configuration performed in the lower Miocene and variance attribute (extracted in the lower Miocene), showing the shallow linked system (extension – contraction) interpreted in the western flank of the structure. In this figure is possible to see how the variance attribute helps to distinguish between the extension zone from the contraction area, due it highlights in red color the normal fault planes.*

The figure 25 shows a time slice at 4340 ms, where the attribute of variance has been applied. Thereby, is possible to interpret a set of normal faults produced by gravitational collapse on the crest of the structures. In the center of the structure we can observe that the orientation of faults is NNE-SSW, however in the North and South flanks of the structure

we can see how the orientation change NNW-SSE and NE-SW respectively, producing a concentric fault system along of the structure. This could point out that the structure continues having a late deformation due to gravitational pushing basinward, such it was interpreted during the first period of deformation (Upper Oligocene- Lower Miocene). Other geological feature that is possible to interpret is the presence of a gravitational sliding in opposite direction to the basin. This could be originated due that during the late deformation were deposited very loose sediments (sediments of talud), which generated an instability zone in the center of the structure and possibly induced the sliding down of sediments, producing a slump zones and a shallow linked – system overlying the top of Oligocene.

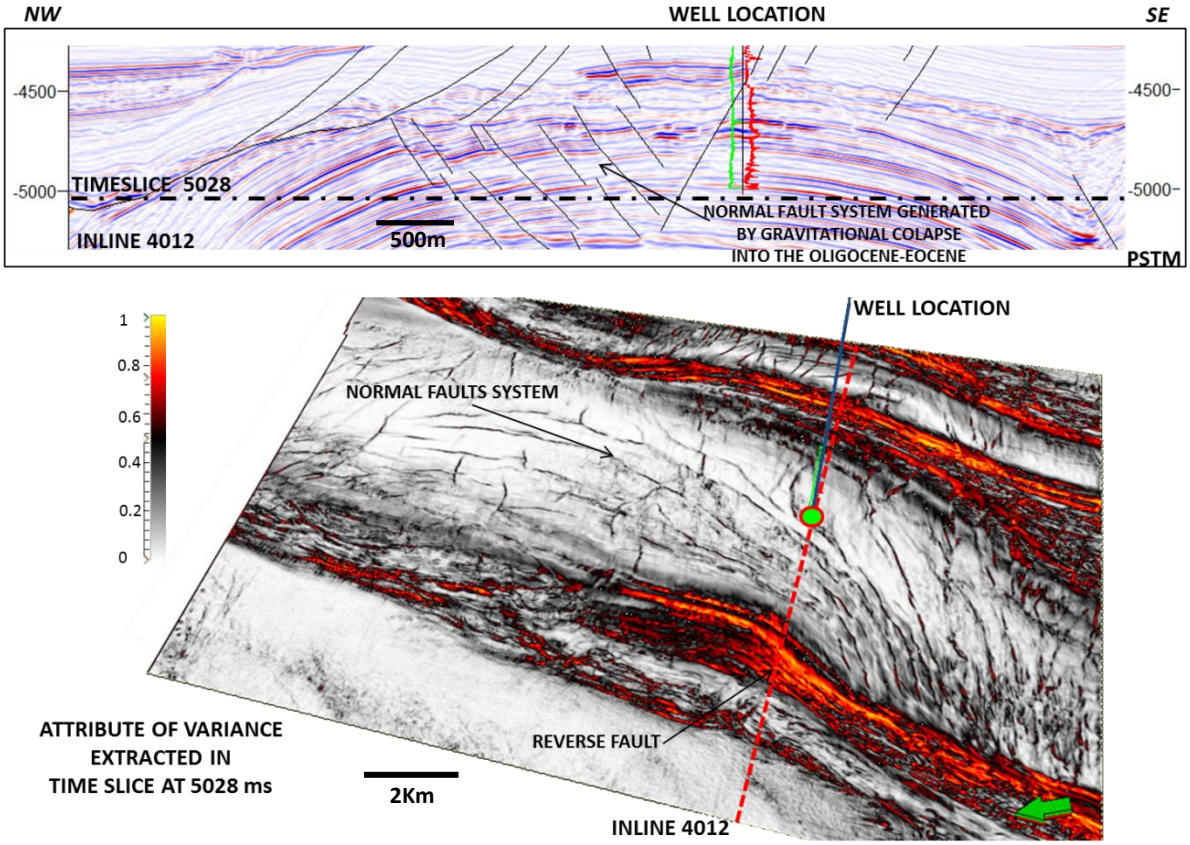

Figure 24*. Seismic section (inline 4012) and attribute variance extracted over the time slice at 5028 ms, showing the normal faults system generated by gravitational collapse, as product of the intense folding in the top of the structures. In this figure is evident how the normal faults system has a concentric pattern being more evident in the south, due they change almost in E-W direction.*

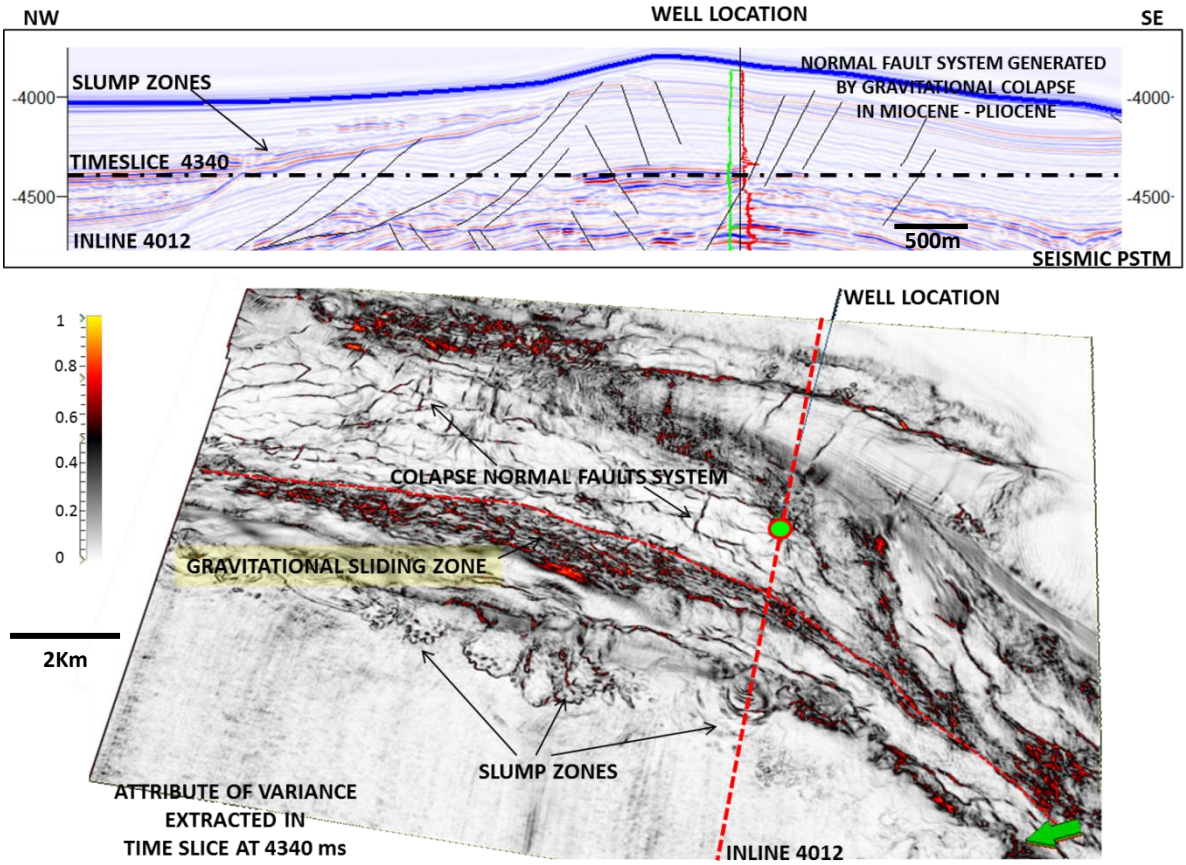

Figure 25*. Seismic section (4012) and time slice at 4340 ms with seismic variance attribute, showing the concentric geometry of collapse normal faults in the crest of the structure. In this figure also is evident the gravitational sliding and slumps zone produced as product of instability of sediments as a result of the late deformation (Pliocene – Miocene).*

Other feature that also is evident into the Miocene – Pliocene sequences, is the presence of a high amplitude anomaly just below of the possible presence of methane hydrates. This type of bodies according with the theory, is a crystalline solid consisting of gas molecules, usually methane surrounded by a cage of water molecules [Dr. William Dilon, U.S Geological Survey]. It looks very similar to water ice, although the physical behavior is different, due these when enter in contact with fire will burn as hydrocarbons. The methane hydrates are stable in floor sediments at water depth greater than 300 meters where the high pressure and low temperature are present [Dr. William Dilon, U.S Geological Survey].

The figure 26 shows the geometry and distribution of anomalies below of methane hydrates interpreted in this project. The anomalies in the North portion present a thickness increment

and wider distribution in both sides, as well as the presence of a set of sediments onlaping against anomalies, which produce a contrast in the seismic reflection represented by a negative seismic response (trough) compared with the positive seismic response (pick) of the seabed, (figure27). In the center of structure these bodies are narrower and with a medium thickness, while the southern portion these become thinner, being in some places displaced and cut by the presence of normal faults.

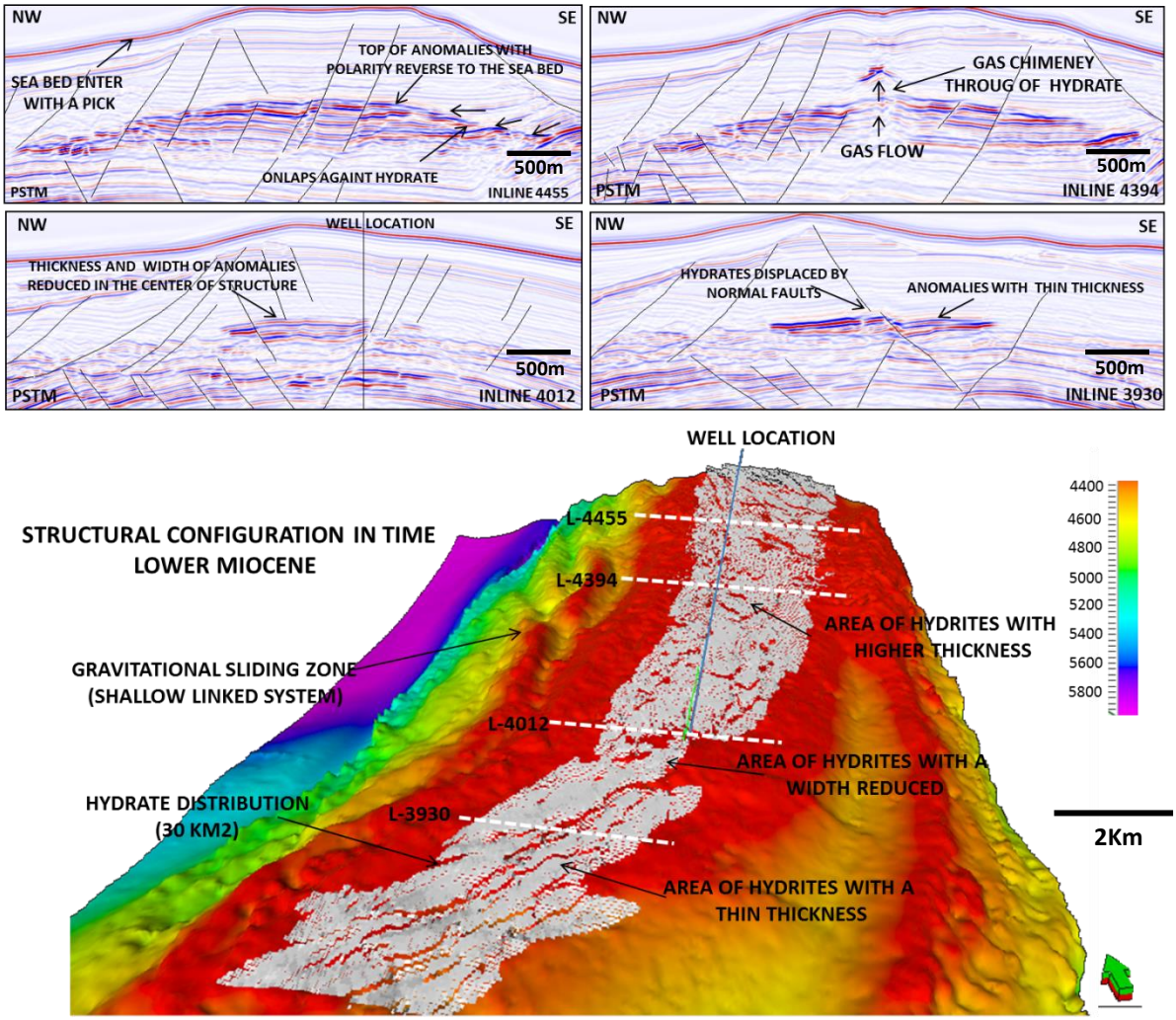

Figure 26*. Seismic lines, structural configuration (Lower Miocene) and geobody showing the geometry and distribution of amplitude anomalies below of methane hydrates interpreted into the Miocene sequences*

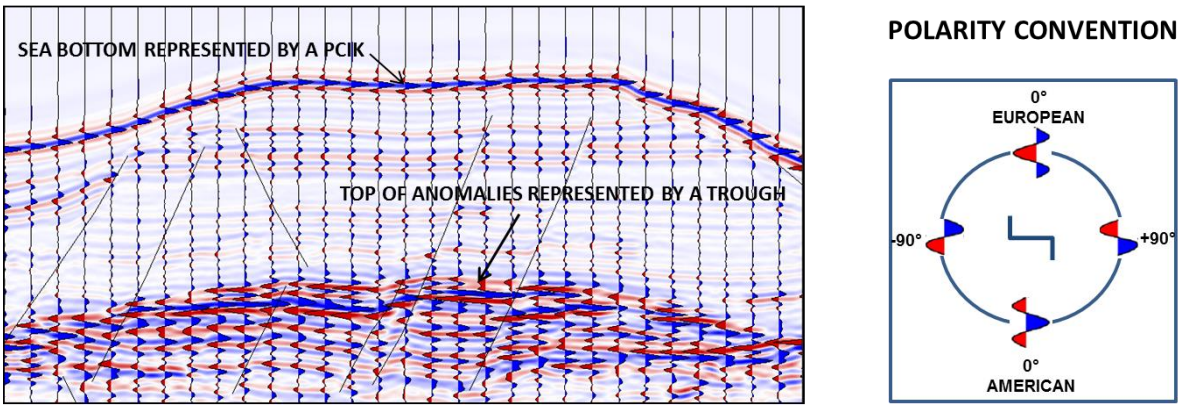

***Figure 27**. Seismic line showing the seismic response associated to the sea bottom and top of hydrates, where is evident the change of polarity between them.*

From the seismic responses interpreted both sea bottom and top of the anomalies, I may deduct that the amplitude related with the anomalies zone could be associated with a low acoustic impedance zone taking into account the international polarity convention (figure 27), due these show a negative reflection coefficient. Thereby, that may be possible the free gas presence underlying the hydrates zone, having as evidence also the presence a chimney of gas located in the northern portion of structure (figure 26). This decreasing in the acoustic impedance in the anomalies zone also may is pointing out the presence of methane hydrates compacted, which may be working as a solid material producing this contrast.

Once realized the structural interpretation in the area and defined the main deformation events involved in the structure, the next step was to perform the stratigraphic interpretation. This was done taking account the seismic horizons interpreted in the interval of interest: Oligocene Frio 14, Oligocene Frio 20 and Oligocene Frio 26 (Figure 28).

Therefore, considering these horizons I performed a set of amplitude extractions by using of flattened volumes, with the main target to identify anomalies related to the reservoir rock distribution and areas associated with the possible presence of hydrocarbons. This technique was used to define stratigraphic features in more detail, even below of seismic resolution, because this removes the structural effect leaving the events as if they had been deposited in flat layers. The figure 29 shows the workflow implemented to carry out the stratigraphic interpretation by using of flattened volumes.

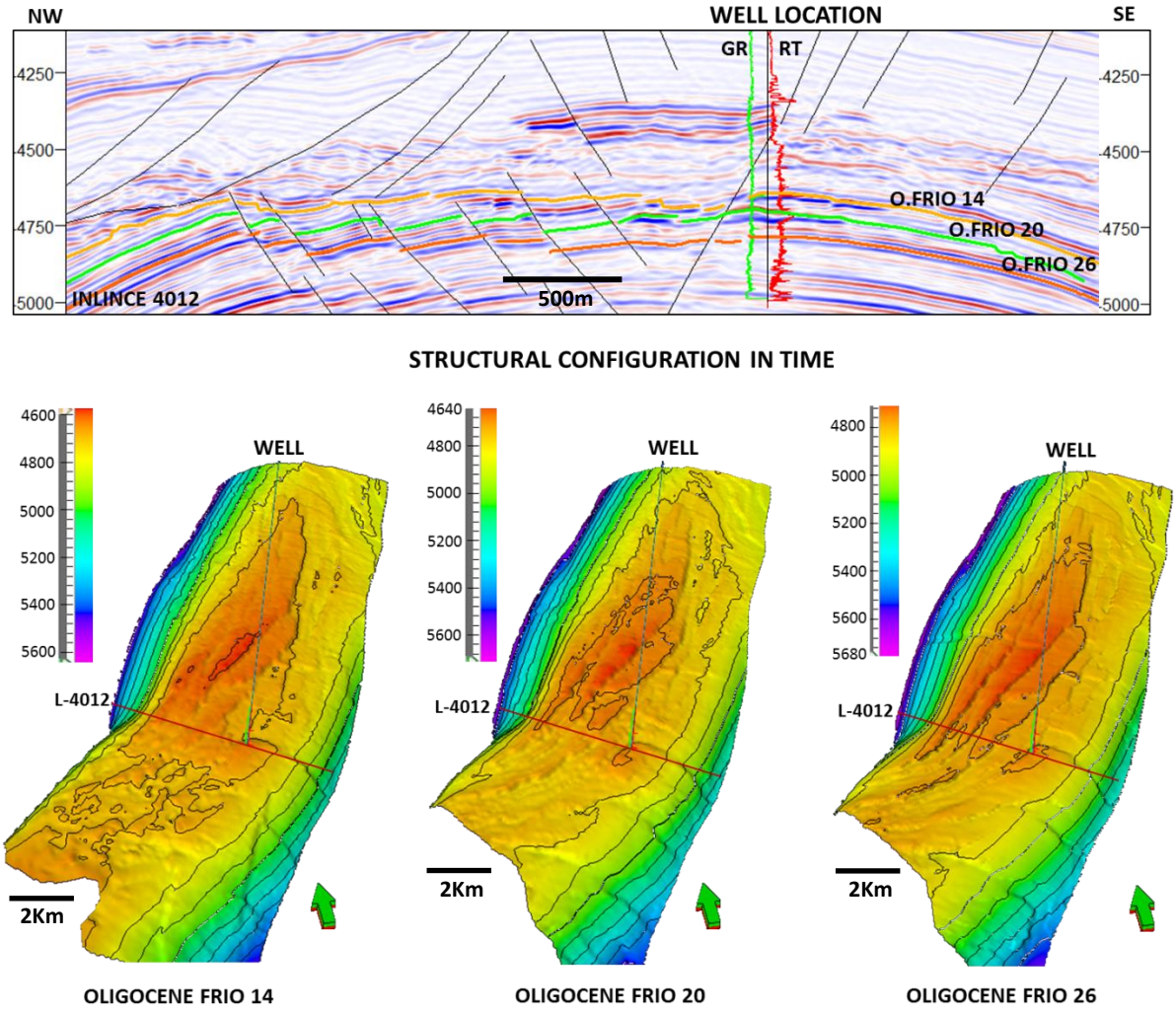

Figure 28. *Structural configuration of Oligocene Frio-14, Oligocene Frio-20 and Oligocene Frio 26, which correspond to every one of the main targets to be analyze in this project. Taking into account the sands interval and hydrocarbon presence identified by the well.*

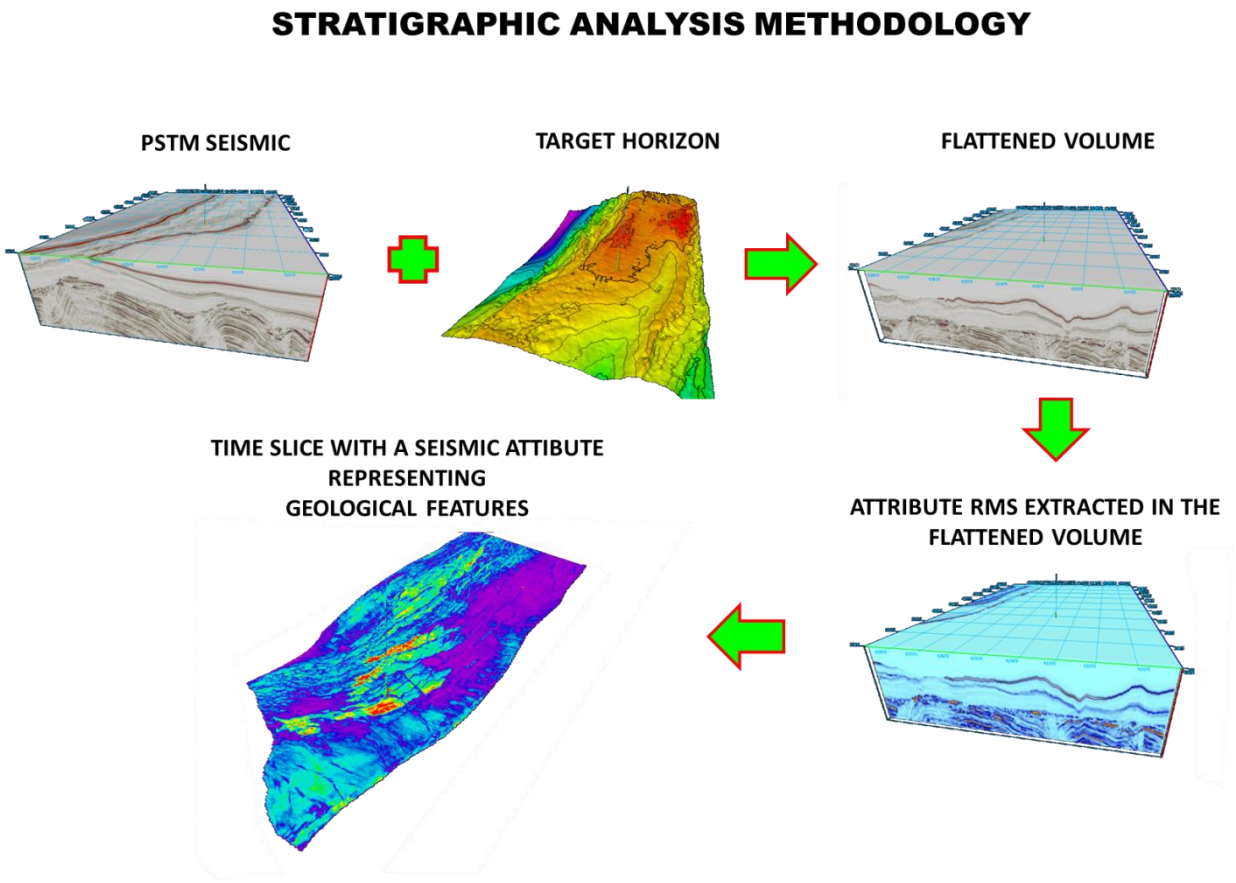

***Figure 29**. Workflow implemented to carry out the stratigraphic interpretation in the area of study, taking into account the technique of flattened volumes.*

As shown in the work flow depicted in the figure 29, to perform the attribute of flattened volume, first was considered as input the conventional seismic migration volume, which was flattened by using a target horizon. Once flattened the input seismic volume, the amplitude extraction along all volume was performed, in this case corresponded to RMS attribute. Later were created a set of time slices along of the interval of interest to identify stratigraphic features. The figure 30 shows the result of flattened seismic volume applied in the horizon Oligocene Frio 14. Thereby, I could interpret a set of high amplitude anomalies distributed in the top of the structure, where also is evident how these anomalies are cut by a normal faults system. From these amplitude anomalies, I also interpret they belong a set of turbiditic sediments deposited in talud facies and proximal basin zones, taking into account their geometry and distribution, as well the stratigraphic and sedimentary information of analogues fields.

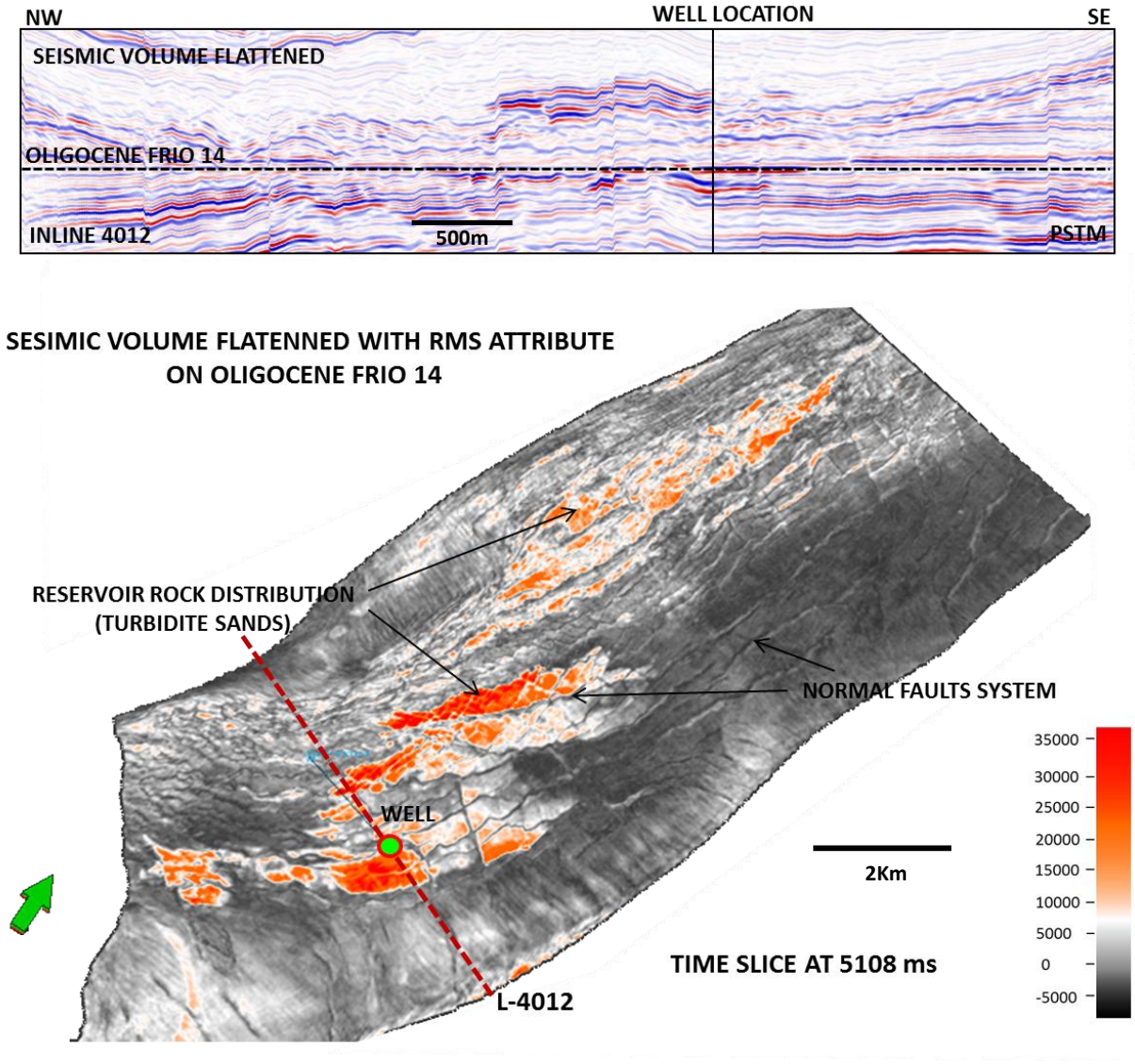

Figure 30. *Seismic section flattened, and seismic volume flattened with a RMS attribute, considering the Oligocene Frio 14 as target horizon. Thereby, is possible to interpret the normal faults pattern and distribution of reservoir rock along of the structure. In this figure also is evident some areas with higher amplitude anomalies, which may be related with to the possible presence of fluids.*

The figure 31, show the result of the seismic volume flattened with the RMS attribute applied in the Oligocene Frio 20. Hence, I could interpret once more the normal faults system generated by gravitational collapse in the crest of the structure, but the reservoir rock distribution now is bit different to that interpreted in the Oligocen Frio 14. In this interval is evident the presence of sinuous channels crossing across the structure in

direction W-E and NW-SE. These channel system show from medium to high amplitude, which I interpret as submarine channels of low energy, due these present a high sinuosity, which could point out that their source of supply could be far away, so a possibility could be associated with the Rio Bravo, considering their orientation and distribution basinward.

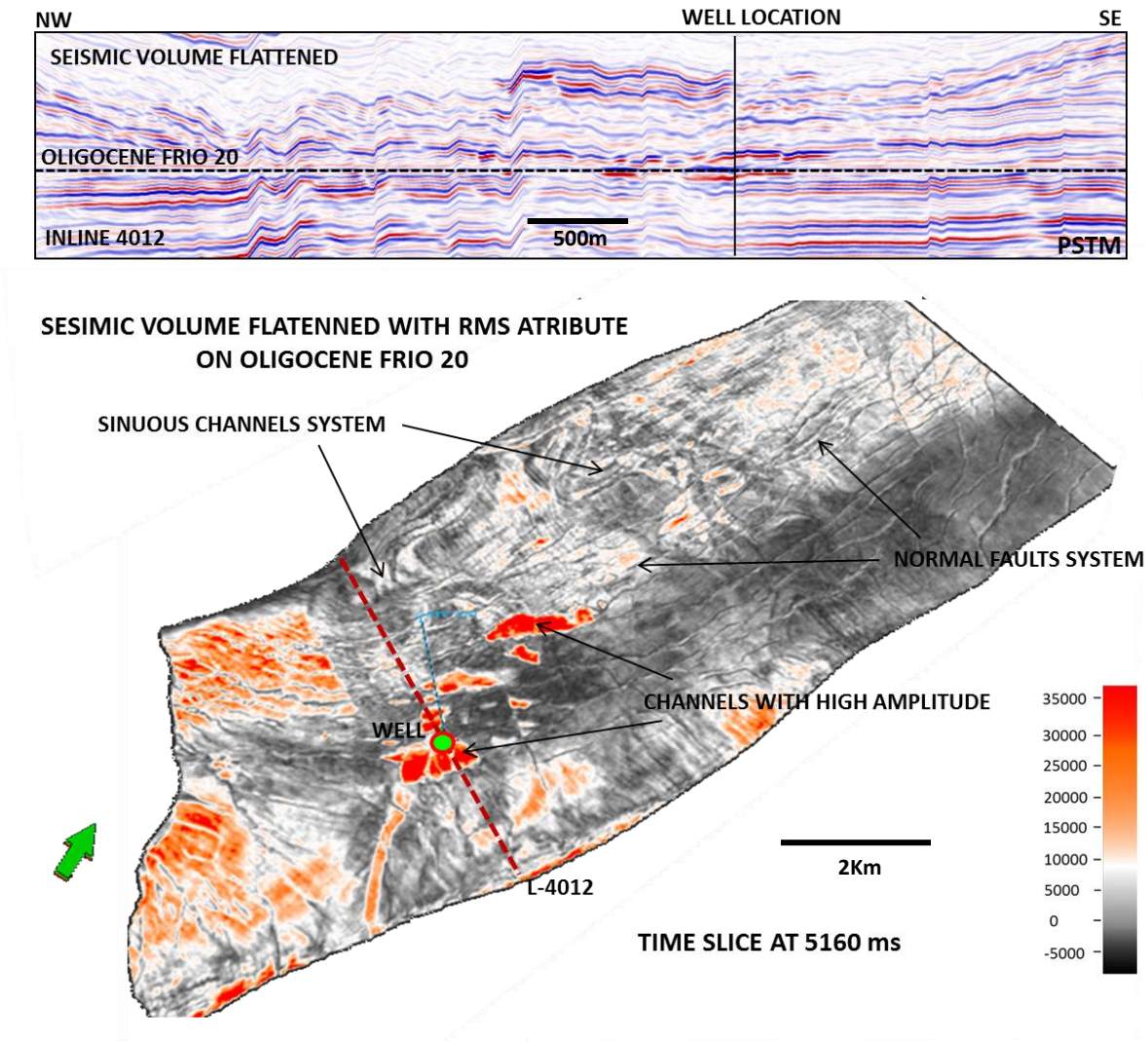

Figure 31. *Seismic section flattened and seismic volume flattened with a RMS attribute, considering the Oligocene Frio 20 as reference, showing the normal faults system and the distribution of submarine channels along of the structure.*

The figure 32 shows the result of the seismic volume flattened with the RMS attribute, taking into account the Oligocene Frio 26 as reference. From this figure I interpret once more the normal fault system generated by gravitational collapse, which were subsequently

deformed by a gravitational pushing basinward in the upper layers. Thereby, also I could interpret a set of high amplitude anomalies aligned in direction NNE-SSW in the west flank of structure, which were interpreted as sand sheets or turbiditic deposit in talud facies or proximal basin zones. These amplitudes are cut by an erosional channel in the center of the structure. So, according with its characteristic, this channel may be interpreted as a submarine channel of high energy due it shows a geometry very straight but probably very shaly, because it shows also a very low amplitude response.

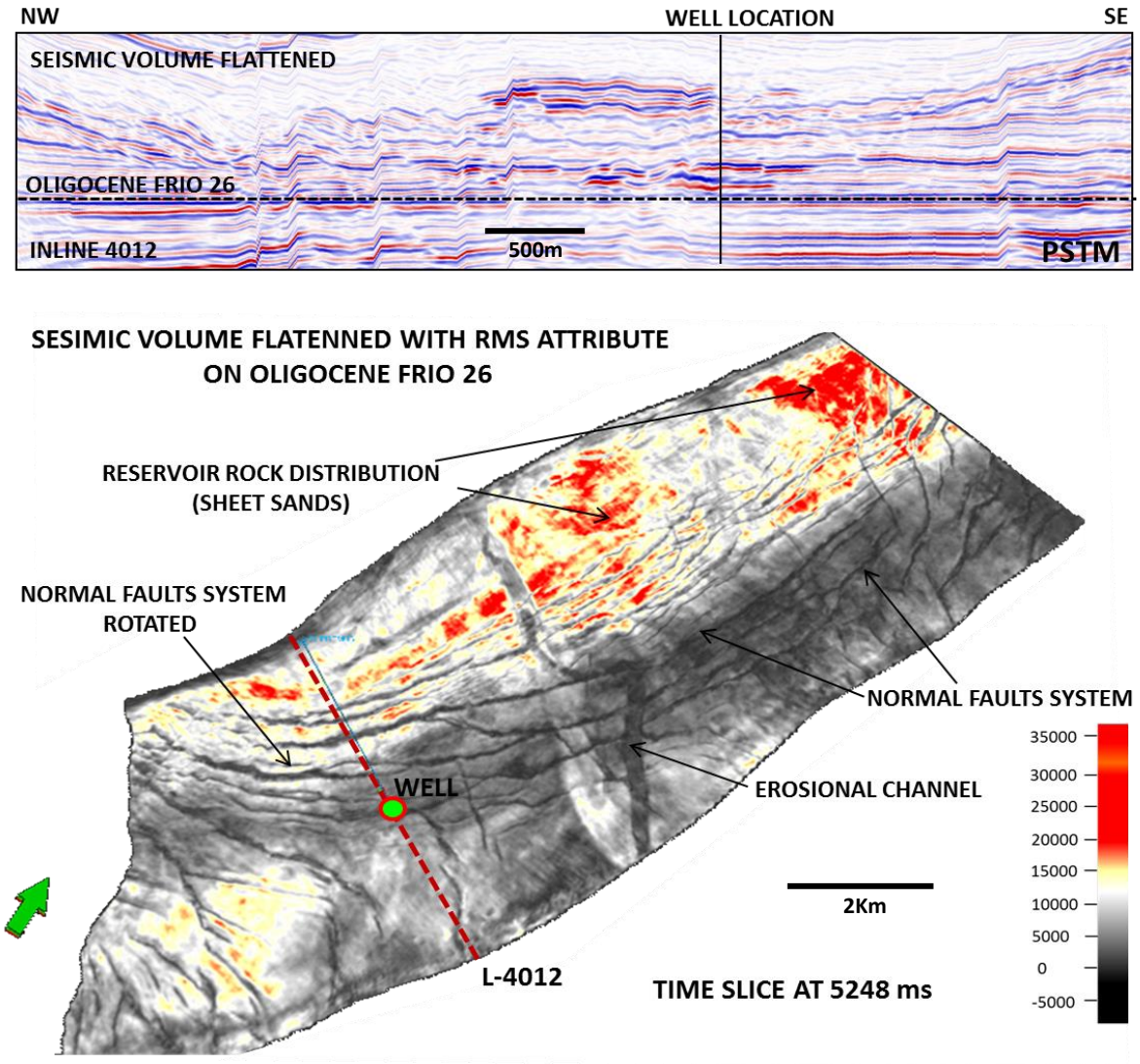

***Figure 32**. Seismic section flattened and seismic volume flattened with a RMS attribute in the Oligocene Frio 26, showing collapse normal faults system and high amplitude anomalies associated to reservoir rock distribution in the west portion of the structure.*

3.6. Discussion and Results

From the regional structural analysis performed in this work, I can define that the age of deformation related with the main structure could be interpreted as Upper Oligocene – Lower Miocene. One evidence of this is the presence of syn-kinematic deposits in the flanks of the structure. Other evidence is the presence of a regional erosional surface in this interval, which suggests that in this period of geological time was when occurred the stronger deformation.

Towards younger layers, I could interpret a set of sediments with medium amplitude and medium frequency associated with sediment no consolidated, which I interpret were deposited during a reduction of sea level (talud), causing a mixture between continental sediments and marine sediments. The combination between these materials and late deformation, generated a shallow linked system (extension – contraction) in the upper west flank of the structure, which has its detachment in the clay sediments deposited on the top of Oligocene.

Overlying the lower Miocene sediments other geological feature important is the presence of a high amplitude anomaly, which I interpret is generated by the presence of a hydrate of methane. The interpretation done in the anomalies below of methane hydrates showed that these have different behaviors and characteristics along of structure. In the northern portion the anomalies are wider and thicker, showing in some portions the presence of gas chimneys that cross it vertically. In the center of the structure, the anomalies become thinner and narrower and towards the south it becomes very thin and displaced by local normal faults.

In the more recent layers (Pliocene – Recent), I could interpret that the structure continues having a recent deformation, because the sea bottom and sediments deposited in the Pliocene show a gentle structuration, in addition of the presence of syn-kinematics deposits in their flanks. Into Pliocene sequences, the early deformation generated a gravitational sliding (slumps), mainly in the west portion of the structure possibly related with deposit of loose material during that geological period of time.

From the stratigraphic analysis realized in every one of the target horizons I could observe that the trap is related with an anticline structure limited by reverse faults in the flanks. Its top is characterized by normal fault systems generated by a gravitational collapse as a product of the intense folding. The normal faults system also shows a secondary deformation which generated these faults adopted a concentric geometry. This secondary deformation I suggest was created as a result of the gravitational pushing basinward derived of the instability zone landward (platform) and by the big amount of sediments supplied by the rivers system in land.

The amplitude distribution identified in each one of the targets has different geometry and characteristics. The Oligocene Frio 14 shows a set of amplitude anomalies related with a turbiditic sediments deposited in facies of talud, which in most of them tend to be truncated by normal faults. From the amplitude anomalies identified in this objective, I could observe that some of these anomalies (mainly in the center of the structure) show a very high amplitude response, which could be associated with the presence of fluids.

The Oligocene Frio 20 showed stratigraphic features a bit different compared with the Oligocene Frio 14. Because it shows a set of submarine channels with orientations almost W-E, which suggest that the Rio Bravo could be the main sediment supplier, taking into account the geometry and orientation of channels. These channels showed a medium and high amplitude response with a very high sinuosity, which point out that these may be interpret as channels of low energy, so its source for the time of deposition could has been located far away. The channels system identified in the Oligocene Frio 20 also showed toward the center of structure a very high amplitude which may point out the fluid presence. On the other hand, the Oligocene Frio 26 shows a set of amplitude anomalies from medium and high amplitude aligned in direction NNW – SSE and separated in parallel direction by the normal faults system. These amplitude anomalies also are cut in perpendicular direction by the presence of a channel toward the center of structure. The low amplitude response and the straight geometry showed by the channel may point out that it could be related with an erosional channel of high energy.

IV. AVO ANALYSIS

4.1. Description and Methodology

In the last years, the seismic reflection technique has become one of the most important tools for the oil industry, identifying and indicating potential areas to drill and find hydrocarbons. Today with the new advances in seismic acquisition, data processing and interpretation now is possible to use seismic traces to interpret more than just reflectors by their shape and position. Most of the seismic pulses reflected from the subsurface can be used and interpreted to derive a depositional model in the subsurface, the rock type or even the nature of pore fluid. So under this wide range of possibilities has been developed some innovative interpretation tools such as the AVO. The AVO analysis is widely used in the oil industry for the hydrocarbon detection, mainly in areas where the amplitude anomalies are present. Hence that AVO also can give information about of lithology and fluid parameter, due the seismic amplitude are affected by the variations in the physical properties in the limits of the reservoirs.

In areas of complex geology and deep waters such as Perdido Fold Belt, one of the main targets not only is to define the structure nature and reservoir rock distribution but also try to predict the possible areas where could be the largest hydrocarbon accumulation, and thus try to reduce the geological risk before drilling. Thereby, that I will use the AVO analysis as additional interpretation tool to define the areas with major potential to contain hydrocarbons, taking into account the structural and stratigraphic geological model derived in the chapter II. Where I could define the geometry of the trap and its geological events associated, as well as the depositional system characterized by turbiditic deposits and submarine channels, which showed high amplitude with possibility to be associated to the presence of hydrocarbons.

The methodology of AVO analysis that I use in this work, is that proposed by Hampson & Russell in February of 2010 (figure 33), which start with the preparation of seismic gathers, followed by a log modeling considering different fluid substitution and from these results

derive a set of synthetic gathers. Subsequently, I use the last version of the gather conditioning and the velocity function derived from the log modeling to predict the AVO classes involved in every one of the targets into the Oligocene Frio formations. The AVO performed in this project also consider the analysis of gradient and intercept by using of crossplot and a set of AVO attributes (A*B, Scaled Poison's Ratio Change: A+B, Fluid Factor), which will be generated both in 2D and 3D to identify and define the reservoir distribution.

Finally, once that the AVO analysis is performed, I carry out the LMR (Lamdha-Mhu-Rho) and Elastic seismic inversion to determine maps of properties, which will be described and discussed more widely in the next chapter. This with the main objective to reinforce the AVO analysis results, characterize and discriminate with more detail the lithological and reservoir conditions.

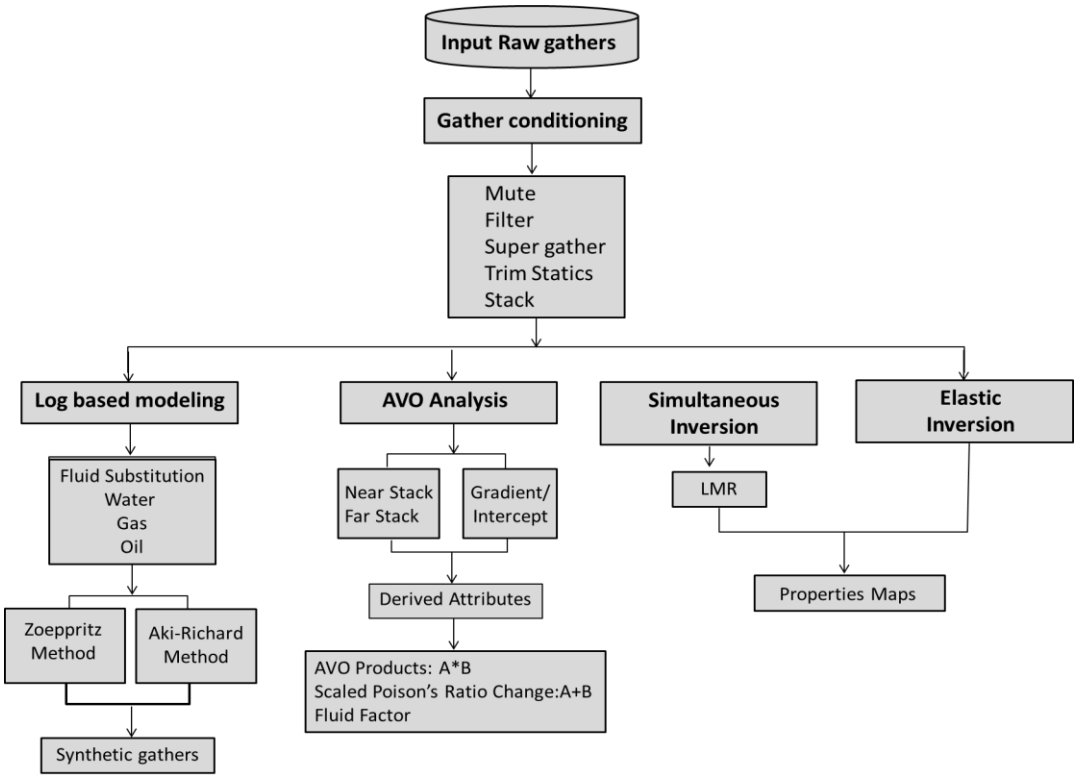

Figure 33*. Workflow considered to perform the AVO and seismic inversion analysis. Taken and modified from Hampson & Russell, February 2010.*

4.2. Theoretical Aspects of AVO

4.2.1. Seismic Waves

The AVO responses is dependent on the properties of P-wave velocity *(Vp)*, S-wave velocity *(Vs)* and density *(ρ)* in a porous rock, due it involves the matrix material, the porosity, and the fluids filling the pores. So this lead to two different types of velocities:

P-wave or compressional wave, which the direction of particle motion is in the same direction as the wave movement. Figure 34a

S-wave or shear wave, which the direction of particle motion is perpendicular to the wave movement. Figure 34b

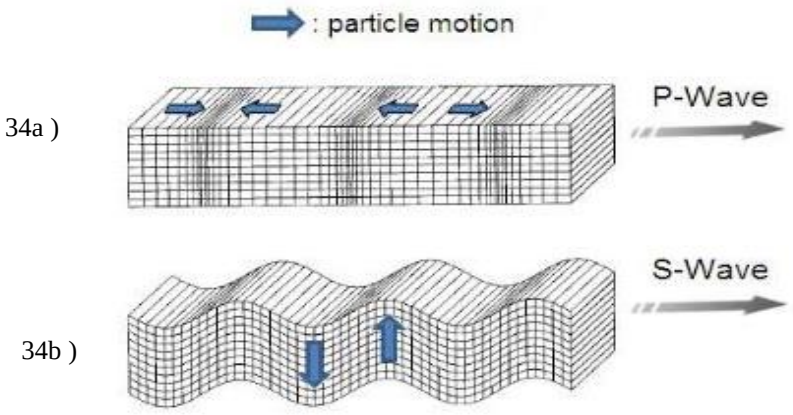

Figures 34a and 34b*. Seismic Waves Propagation. Taken from Park Seismic LLC, Shelton, Connecticut.*

The simplest expression of P-wave and S-wave by using the Lame's parameter is given as:

$$V_p = \sqrt{\frac{\lambda + 2\mu}{\rho}} \quad ; \quad V_S = \sqrt{\frac{\mu}{\rho}} \tag{3}$$

Where:

λ = the first Lame constant; μ = the second Lame constant; and ρ = density

Another way to express these functions is using the Bulk Modulus and Shear Modulus, which are given as:

$$V_p = \sqrt{\frac{k + 4/3\,\mu}{\rho}} \quad ; \quad V_S = \sqrt{\frac{\mu}{\rho}} \tag{4}$$

Where:

K = Bulk Modulus; μ = Shear Modulus; and ρ = density

4.2.2 Poisson's Ratio

Another parameter that is useful to see the relationship between V_P and V_S velocities is the Poisson's ratio, which is defined as the ratio of the fraction (or percent) of expansion divided for the fraction (or percent) of compression, for small volumes of these changes [Hampson & Russell et al. 2010], so the expression is given:

$$\sigma = \frac{\gamma - 2}{2\gamma - 2} \qquad \text{where:} \quad \gamma = \left(\frac{V_P}{V_S}\right)^2 \tag{5}$$

So this formula also can be expressed in different way, allowing derive V_P or V_S from σ, and is given by:

$$\gamma = \frac{2\sigma - 2}{2\sigma - 1} \tag{6}$$

The graph I, shows a plot between the Poisson's ratio and V_P/V_S ratio, which is very useful for the hydrocarbon detection.

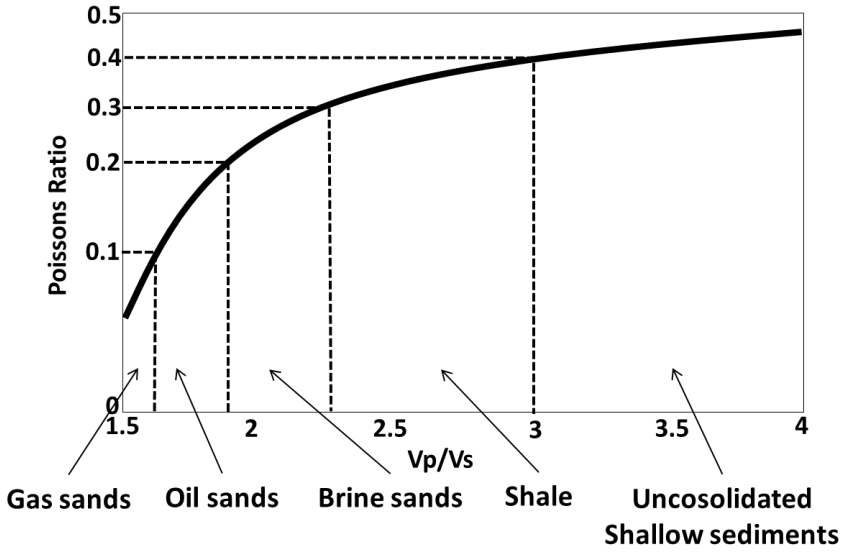

Graph I. *Plot Poisson's ratio vs Vp/Vs. Taken and modified from Per Avseth course NTNU 2012.*

So the values more representatives between the Poisson's ratio and *Vp/Vs* can be resume as:

$V_P/V_S = \sqrt{2}$, then $\sigma = 0$

$V_P/V_S = 1.5$ then $\sigma = 0.1$ (Gas case)

$V_P/V_S = 2$, then $\sigma = 1/3$ (Wet case)

$V_P/V_S = \infty$, then $\sigma = 0.5$ ($V_S = 0$)

4.2.3 Biot-Gassman Equation

In the AVO analysis three fundamental parameters are the estimation of V_P velocity, V_S velocity and density (ρ). However there are some factors which influence in the velocity of the rocks such as: the rock matrix, the porosity and type of fluid filling the pore space (figure 35). So to solve this problem Biot (1941) and Gassman (1951) derived an equation to the calculation of saturated Bulk modulus and Shear Modulus, for later use the conventional formulas for V_P, V_S and ρ estimation [Hampson & Russell et al. 2010].

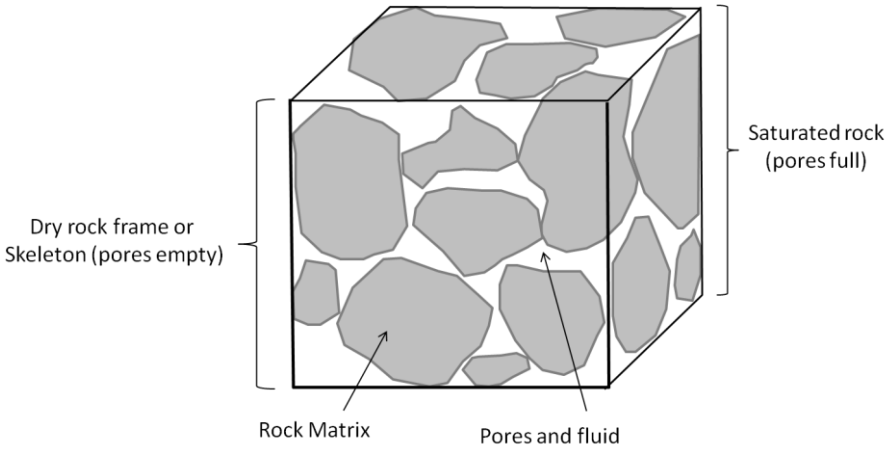

Figure 35. *Fluid saturated rock. Taken and modified from Hampson-Russell workshop 2010.*

So the Biot-Gassmann bulk modulus expression is given as:

$$K = K_{fr} + \frac{K_f}{\phi} + \frac{\left(1 - \frac{K_{fr}}{K_S}\right)^2}{1 + \frac{K_f}{\phi K_S}\left(1 - \phi - \frac{K_{fr}}{K_S}\right)} \qquad (7)$$

Where: K_{fr}: dry frame, K_S: rock matrix, K: saturated rock, K_{fl}: fluid, and ϕ: porosity.

And the V_P and V_S velocities can be now estimated by using the conventional V_P and V_S expressions given in the equations (4), and the formula for the density saturated rock.

$$\rho_{sat} = \rho_m(1-\phi) + \rho_w S_w \phi + \rho_{hc}(1-S_w)\phi \tag{8}$$

Where:

ρ_{sat}: saturated density rock, ρ_m: density matrix, ρ_w: water density, ρ_{hc}: hc density, S_w: water saturation and ϕ: porosity.

In the Biot-Gassmann equations, the shear modulus does not change for varying saturations at constant porosity, and the bulk modulus of the solid matrix, K_m can be taken directly of laboratory measures on drill core samples, being the typical values given as:

Sandstones: K_m: 37 GPa ; μ_m: 43 GPa; ρ_m: 2.65 g/cm^3
Shales: K_m: 20-25 GPa ; μ_m: 6-10 GPa; ρ_m: 2.60-2.66 g/cm^3
Chalk: K_m: 60-80 GPa ; μ_m: 27-32 GPa; ρ_m: 2.71 g/cm^3

The fluid bulk modulus can be calculated using the Reuss average equation given as:

$$\frac{1}{K_{fl}} = \frac{S_w}{K_w} + \frac{1-S_w}{K_{hc}} \tag{9}$$

Where:

K_{fl} = the bulk modulus of the fluid; K_w= the bulk modulus of the water; K_{hc}= the bulk modulus of the hydrocarbon.

And the typical values are: K_{gas} = 0.021 GPa, K_{oil}=0.79 GPa and K_w=2.38 GPa.

4.2.4 AVO Concept

The AVO is the geophysical term, which describes the amplitude variation with offset. This phenomenon is based on the relation between the reflection coefficients and angle of incidence. Commonly seismic data are registered as a function of offset, however there is a direct relation between angle and offset, which depends on velocities [Hampson & Russell et al. 2010]. The figure 36, shows CRP arrangement and its gather representation in function of offset before NMO correction.

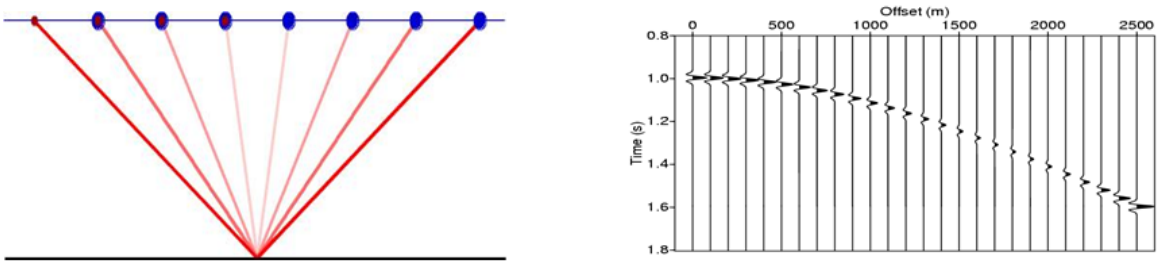

***Figure 36**. CRP arrangement and its gather representation. Taken from Per Avseth course NTNU 2012*

Conventional seismic surveys consider the coefficient reflection exclusively to compressional waves. When a compressional seismic wave arrives vertically at a horizontal interface, the amplitude of the reflected wave is proportional to the amplitude of the incoming wave [Hampson & Russell et al. 2010], so the expression for a normal incidence reflection and transmission can be expressed as:

$$R_S(0°) = R_{S0} = 0, \quad T_S(0°) = T_{S0} = 0, \tag{10}$$

$$R_P(0°)R_{P0} = R_{P0} = \frac{\rho_2 V_{p2} - \rho_1 V_{p1}}{\rho_2 V_{p2} + \rho_1 V_{p1}} \tag{11}$$

$$T_P(0°) = T_{P0} = \frac{2\rho_2 V_{p2}}{\rho_2 V_{p2} + \rho_1 V_{p1}} = 1 - R_{P0} \tag{12}$$

When a compressional seismic wave arrives obliquely the situation is more complicated. The compressional reflection coefficient is now a tortuous function of the angle of incidence, the densities, V_P and V_S of the two layers of contact. Zoeppritz derived the

amplitude of the reflected waves upon a plane interface, and amplitude of the reflected waves to the angle of incidence, using the conservation of stress and displacement across the layer boundary [Hampson & Russell et al. 2010], which gives four equations with four unknowns, expressed as:

$$\begin{bmatrix} R_P(\theta_1) \\ R_S(\theta_1) \\ T_P(\theta_1) \\ T_S(\theta_1) \end{bmatrix} = \begin{bmatrix} -\sin\theta_1 & -\cos\phi_1 & \sin\theta_2 & \cos\theta_2 \\ \cos\theta_1 & -\sin\phi_1 & \cos\theta_2 & -\sin\phi_2 \\ \sin 2\theta_1 & \frac{V_{P1}}{V_{S1}}\cos 2\phi & \frac{\rho_2 V_{S2}^2 V_{P1}}{\rho_1 V_{S1}^2 V_{P2}} & \frac{\rho V_{S2} V_{P1}}{\rho_1 V_{S1}^2}\cos 2\phi_2 \\ -\cos 2\phi_1 & \frac{V_{S1}}{V_{P1}}\sin 2\phi & \frac{\rho_2 V_{P2}}{\rho_1 V_{P1}}\cos 2\phi_2 & -\frac{\rho_2 V_{S2}}{\rho_1 V_{P1}}\sin 2\phi_2 \end{bmatrix}^{-1} = \begin{bmatrix} \sin\theta_1 \\ \cos\theta_2 \\ \sin 2\theta_1 \\ \cos 2\varphi_1 \end{bmatrix} \quad (13)$$

However although the Zoeppritz equations give an exact measure of the amplitude as an angle function, the equations themselves do not give an intuitive understanding of the AVO process for angles greater than zero degrees. So, a set of approximations were derived to reduce this problem.

4.2.5 Aki-Richards Equation

In 1980, Aki and Richards derived an algebraic expression of the Zoeppritz equations. They separated the equations into three reflections terms, each weaker than the previous term [Hampson & Russell et al. 2010].

$$R_P(\theta) = A + B\sin^2\theta + C\tan^2\theta\sin^2\theta \quad (14)$$

Where:

$$A = \frac{1}{2}\left(\frac{\Delta V_P}{V_P} + \frac{\Delta\rho}{\rho}\right), \quad B = \frac{1}{2}\frac{\Delta V_P}{V_P} - 4\left[\frac{V_S}{V_P}\right]^2\frac{\Delta V_S}{V_S} - 2\left[\frac{V_S}{V_P}\right]^2\frac{\Delta\rho}{\rho}, \quad C = \frac{1}{2}\frac{\Delta V_P}{V_P}$$

This approximation is considered the AVO equation, where A is called the intercept, B the gradient, and C the curvature.

4.2.6 Shuey's Equation

In 1985, Shuey derived another approximation of the Zoeppritz equations, rewriting the ABC equation by using V_P, ρ, and σ, taking into account that the gradient is different than that described by Aki-Richards [Hampson & Russell et al. 2010].

$$B = A\left[D - 2(1+D)\frac{1-2\sigma}{1-\sigma}\right] + \frac{\Delta\sigma}{(1-\sigma)^2} \tag{15}$$

Where: $$D = \frac{\Delta V_P / V_P}{\Delta V_P / V_P + \Delta_P / \rho}, \quad \sigma = \frac{\sigma_2 + \sigma_1}{2}, \text{ and } \Delta\sigma = \sigma_2 - \sigma_1$$

Assuming that σ=1/3 the previous equation can be simplify

$$B = A\left[D - 2(1+2(1+D)\frac{1}{2}\right] + \frac{9\Delta\sigma}{4} = 2.25\Delta\sigma - A \tag{16}$$

Leading to the intuitive version of the two-term AVO

$$R_P(\theta) = A + (2.25\Delta\sigma - A)\sin^2\theta \tag{17}$$

4.2.7 Fatti et al´s Formulation of Aki-Richards Equation

An third equivalent form of the Aki-Richards equation was formulated by Fatti et al. [Geophysics, September, 1994] and is written:

$$R_P(\theta) = C_1 R_P(o°) + C_2 R_S(0°) + C_3 \tag{18}$$

Where: $C_1 = 1 + \tan^2\theta$, $C_2 = -8K\sin^2\theta$, $C_3 = 2K\sin^2\theta - \frac{1}{2}\tan^2\theta$, $K = \left(\frac{V_S}{V_P}\right)^2$

$$R_P(0°) = \frac{1}{2}\left[\frac{\Delta V_P}{V_P} + \frac{\Delta\rho}{\rho}\right], \quad R\ (0°) = \frac{1}{2}\left[\frac{\Delta V_S}{V_S} + \frac{\Delta\rho}{\rho}\right], \quad R_d = \frac{\Delta\rho}{\rho}$$

The Fatti et al. formulation gives a way to extract quantitative information about the P and S reflectivity, which can be used for processes of pre-stack inversion.

4.2.8 AVO Cross Plotting

During the amplitude analysis has been shown that the hydrocarbons related with AVO (amplitude versus offset) anomalies, can show an increasing or decreasing amplitude variation with the offset [Castagna, et al. 1997]. So, the amplitude versus offset analysis is facilitated by crossplotting intercept (A) and gradient (B). However also has been observed the brine saturated sands and shale tend to have a very good marked trend, so this trend can be considered to help to distinguish the AVO anomalies associated with the hydrocarbons saturated sands or lithological changes [Castagna, et al. 1997].

In the oil industry to exist four main classifications for the AVO anomalies [Rutherford-Williams, 1989 and Castagna, 1997], which were developed taking into account the contrast in acoustic impedance between the targets sands and the surrounding shales.

According with this classification, gas sands class 1 have positive intercept and negative gradient. So they are characterized to be sands with higher impedance than shales around [Rutherford-Williams, 1989]. Gas sands class 2, have nearly the same impedance as the encasing shale. These gas sands very often present values of R_0 near zero [Rutherford-Williams, 1989]. Gas sands class 3, have lower impedance than the encasing shale with negative large magnitude values of R_0 [Rutherford-Williams, 1989]. Finally gas sands class 4, are characterized to be sands with low impedance, where their reflection coefficient decrease with increasing offset. This very often happen when, shear wave velocity in the sands is lower than in the overlying shale [Castagna, et al. 1997] (table 2).

Class 1	High Impedance sands with decreasing AVO
Class 2	Near-zero impedance contrast
Class 2p	Same as 2, with polarity change
Class 3	Low impedance sand with increasing AVO
Class 4	Low impedance sand with decreasing AVO

***Table 2**. AVO Classification by Rutherford - Williams, and Castagna, 1997. Taken and modified of Hampson & Russell course et al. 2010.*

The figures 37 and 38 show the generic curves at the top of the gas sands and the AVO cross plot classification respectively.

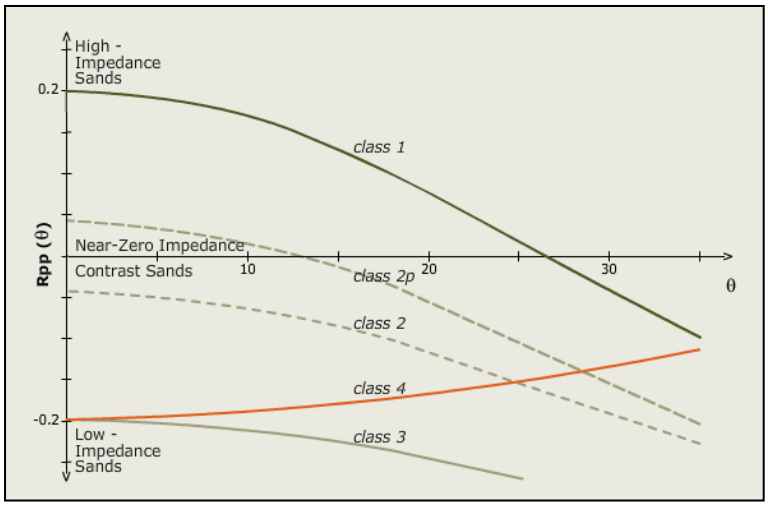

***Figure 37**. Generic AVO curves. Taken from Per Avseth course NTNU 2012.*

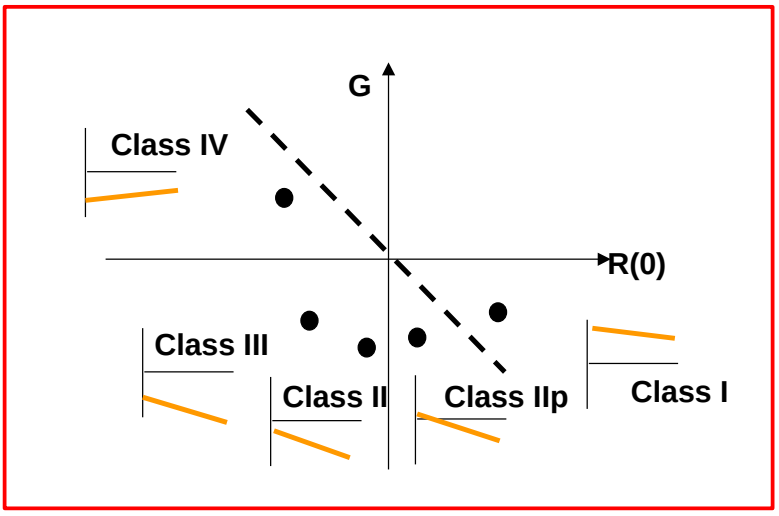

***Figure 38**. AVO crosplotting. Taken from Per Avseth course NTNU 2012.*

The AVO response differs with lithology, fluid and their combination, and hence by using AVO forward modeling will help to confirm the AVO response class, which can be followed by the AVO attributes analysis, leading to the interpreters to identify hydrocarbons zones [Hampson & Russell et al. 2010].

The raw A and B attributes are rarely used individually, so a set of additional attributes can be derived from them, being the most common the next.

- AVO Product: A*B
- Scaled Possion's Ratio Change: A+B
- Shear Reflectivity: A-B
- Fluid Factor

4.2.9 Product A*B

Most of the AVO anomalies has the form how is show in the figure below.

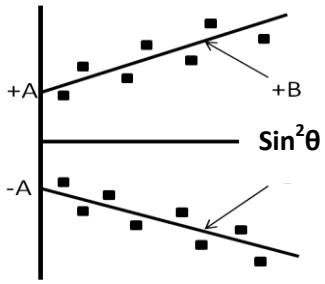

Taken from H&R workshop 2010

However in the product A*B, both the intercept (A) and gradient (B) are large numbers or "bright" with the same sign, due when we form the product A and B we get:

Top of sand: (-A)*(-B) = +AB

Base of sand: (+A)*(+B) = +AB

So these products give a positive "bright" response both in top and base of the reservoir [Hampson & Russell et al. 2010].

4.2.10 Scaled Poisson's Ratio Change: A+B Attribute

To explain this attribute, we can consider the Shuey's equation given in the equations (16). And if we assume the background Poisson's ratio $\sigma=1/3$ the equations (16) can be simplified as:

$$B = A\left[D - 2(1+D)\frac{1}{2}\right] + \frac{9\Delta\sigma}{4} = 2.25\Delta\sigma - A \quad \text{or} \quad A + B = 2.25\Delta\sigma \tag{19}$$

So the sum A+B is proportional to the change in Poisson's Ratio, which will be represented by a negative response at the top of the reservoir (decrease in σ) and a positive response at the base (increase in σ) [Hampson & Russell et al. 2010].

4.2.11 Fluid Factor Attribute

The fluid factor attribute is based on Castagna's mudrock equation, which is assumed to be true for non-hydrocarbons filled layers expressed as:

$$V_P = 1.16V_S + 1360 m/s \tag{20}$$

So from the previous expression we can derive the following equivalent equation:

$$\frac{\Delta V_p}{\Delta V_s} = 1.16 \rightarrow \Delta V_p = 1.16\Delta V_s \rightarrow \frac{\Delta V_p}{V_p} = 1.16\left(\frac{\Delta V_p}{V_p}\right)\frac{\Delta V_s}{V_s} \tag{21}$$

So the Fluid Factor attribute help to define zones, where Castagna's equation is not fulfilled, in other words potential hydrocarbons zones:

$$\Delta F = \frac{\Delta V_P}{V_P} - 1.16\left(\frac{V_S}{V_P}\right)\frac{\Delta V_P}{V_S} \quad \text{or} \quad \Delta F = R_p = R_p - 1.16\left(\frac{V_S}{V_P}\right)R_S \tag{22}$$

The AVO Fluid Factor commonly will show a strong deviation from Castagna's equations both the top and base of the reservoir [Hampson & Russell et al. 2010].

4.3. Gather Optimization

In this project I received a set of gathers previously pre-conditioned by the processing center of Western-Geco company, which consisted from geometry correction until final seismic migration, by passing previously for the implementation of filtering (SRME, Radon), sorting in CDP gathers and velocity analysis (figure 39). So in this project just was realized a quality control (post-conditioning) in the data to be sure that they had been conditioned correctly and there was not any residual artifact that could affect the result of AVO analysis.

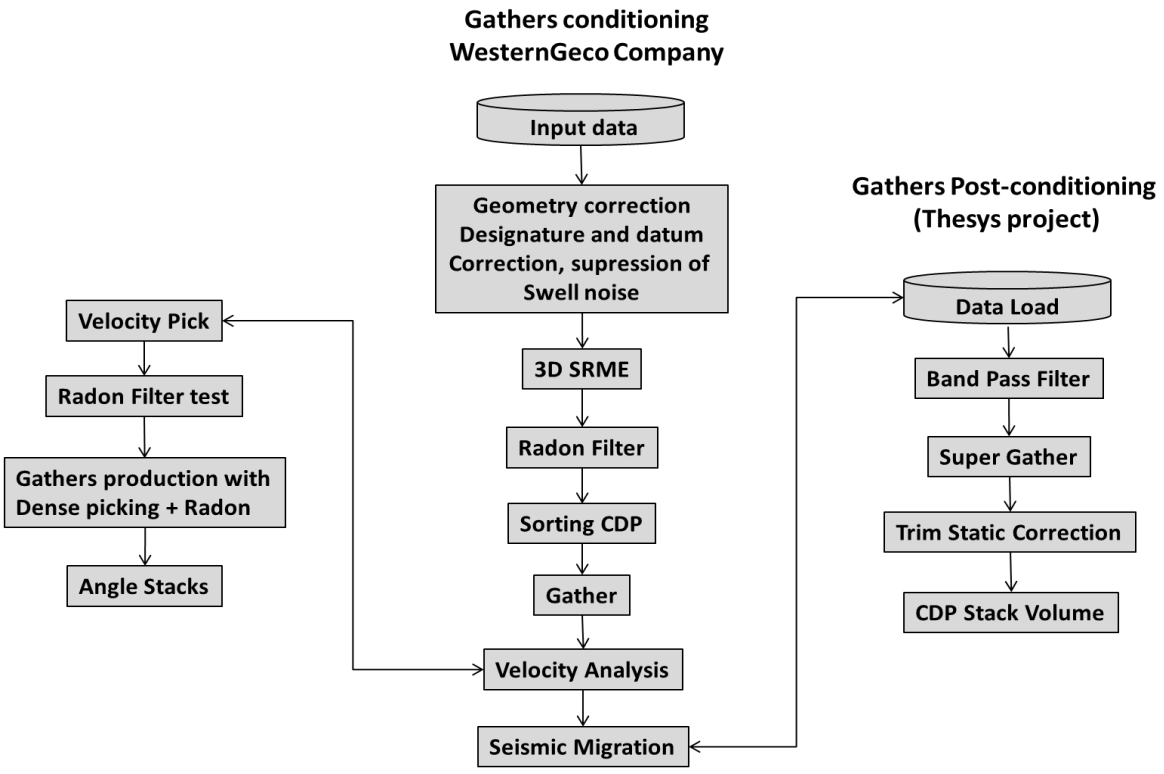

***Figure 39**. Workflow implemented by the Western-Geco company for the gathers conditioning and sequence of post-conditioning of gathers performed in the thesis project. Taken and modified from WesternGeco company-Pemex, December 2012; Hampson & Russell et al. 2010.*

The quality control (post-conditioning) consisted in a filtering application to remove the residual noise associated to high and low frequencies, application of super gather filter to remove residual noise, trim static correction to correct residual time alignment problems

and finally the construction of a CDP stack volume. The post-conditioning was performed considering two important points: (1) noise suppression and isolation of the reflectivity in the event of interest, and (2) not biasing or otherwise corrupting the reflectivity variation with offset.

In this project I received near of 200 Km^2 of pre-conditioning seismic gathers, which occupied around 1.4 TB in hard disk. These gathers came in SEG-Y format and came fragmented by a set of 5 gathers in 2D lines. Each line had a total seismic recording of 12 seconds and sample interval of 4 ms. The gathers were loaded in the Hampson & Russell program in coordinate UTM-15, taking into account the seismic study geometry to later merge them as a 3D volume to its subsequent analysis and implement. The figure 40 shows two gathers displayed in the inline 4012, which were loaded in the Hampson & Russell program.

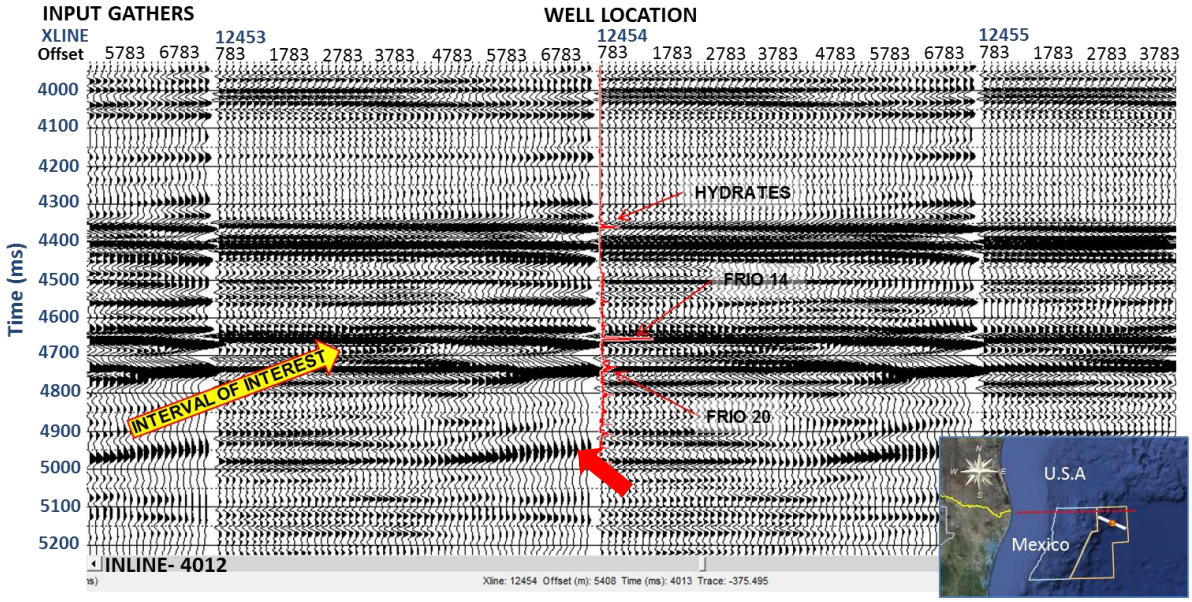

***Figure 40**. Initial seismic gather volume loaded in the Hampson & Russell program.*

As is evident in the input seismic gathers, the far traces show a slight distortion of the signal which was interpreted as noise of low frequency. To be sure and identify the frequency range of noise, a frequency spectrum was created in the line of well location (inline 4012). The frequency spectrum was extracted considering a seismic window along all recording seismic section and all range of xlines. The result of frequency spectrum

showed that exist a small range of signal below of 3 Hz, with a maximum frequency of 90 Hz and average maximum amplitude between 22 to 45 Hz. Under these parameters a band pass filter was designed and applied to remove all unwanted noise, mainly below of 3 Hz. Band pass filtering use a Fourier Transform to put the data in function of frequency domain. In the frequency domain, the output signal can be then expressed as a product between the input signal and the band pass filter [Landro et al. 2012].

$$G(f) = A(f) * H(f) \tag{23}$$

Where G(f) is the output signal, A(f) is the input signal and H(f) is the filter.

Thus, the band pass filter will remove all signals, taking into account both signal below and above of specified frequency. The figure 41 shows the result of band pass filter implementation, while the figure 42 shows the frequency spectrum before and after of filtering.

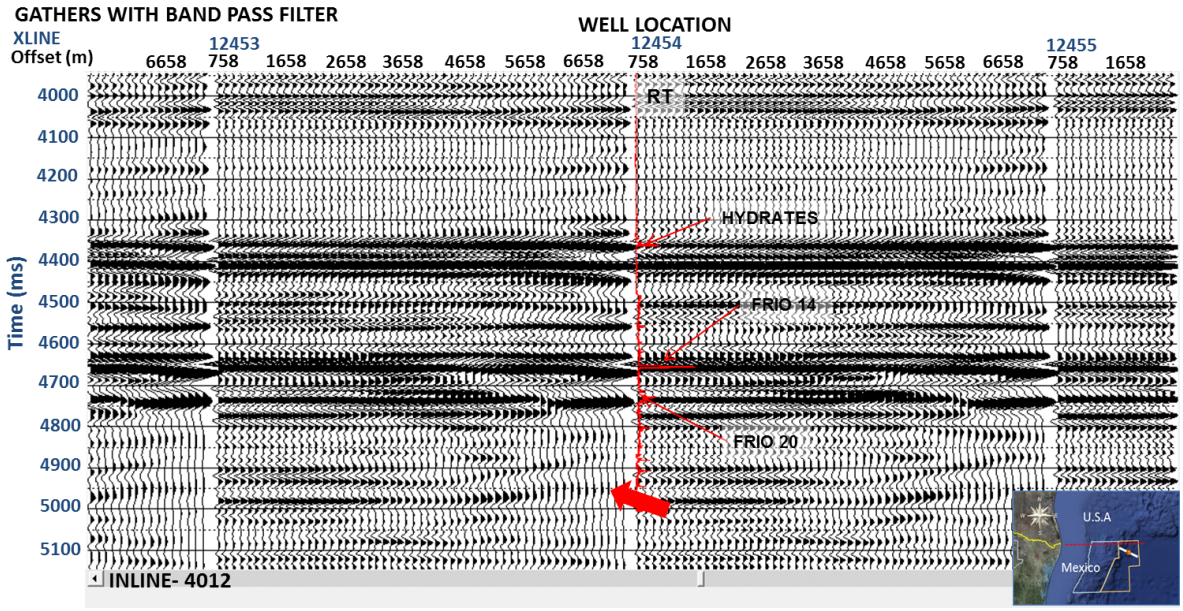

Figure 41. *Seismic gather displayed in the inline 4012, showing the results after band pass filter application, being evident the reduction of noise contained in far offsets.*

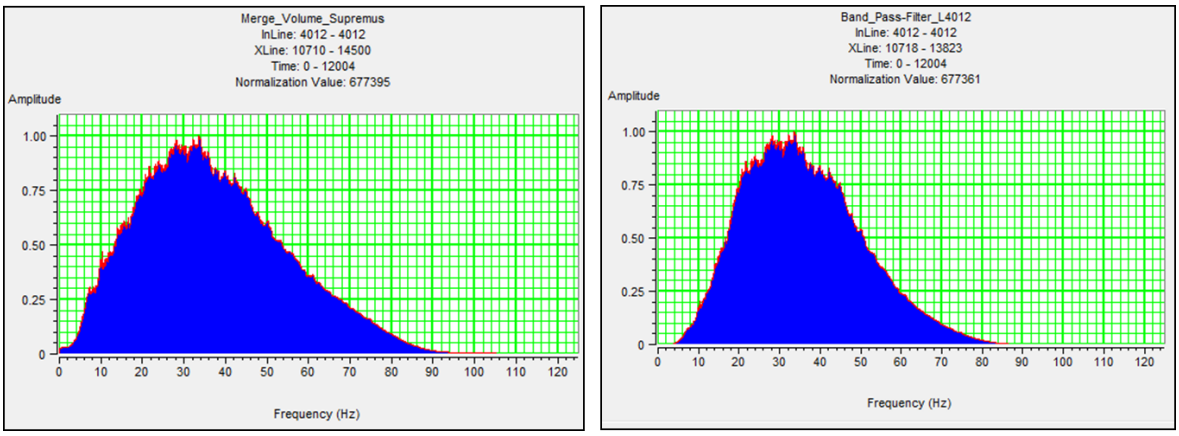

Figure 42. *Frequency spectrum before and after to be implemented the band pass filtering. In this figure we can also observe the noise suppression below and above of 3Hz and 90 Hz respectively.*

As is evident in the figures above, all unwanted signals below and higher than 3Hz and 90 Hz respectively were suppressed. The application of this filtering contributed to prevent false interpretations during the AVO analysis, caused by the presence of low frequency noise.

Once carried out the noise suppression at far offset, the next step was to apply a super gather filtering. The super gather or common offset stack was applied with the objective to remove the random noise and improve the signal to noise ratio. This filtering also is very effective at preserving offset-dependent amplitude variations and contributes to reduce the data volume. The way as the super gather works is creating a subset of input gathers and calculating a number of "super-gathers", which every trace represents a range of offsets. Therefore, it forms average CDP's to enhance the signal to noise ratio, by collecting adjacent CDP´s and adding them together [Hampson & Russell et al. 2010].

The figure 43, shows the result after to be implemented the super gather filtering. As is evident the super gather shows a slight improvement in the signal to noise ratio, resulting in a seismic section a bit cleaner and preserving better the amplitudes. In this case the difference is not so strong between the band pass filtering and super gather, due that the gathers were not so affected by random noise, however is notorious a slight increase of amplitude mainly in the gathers near to the well.

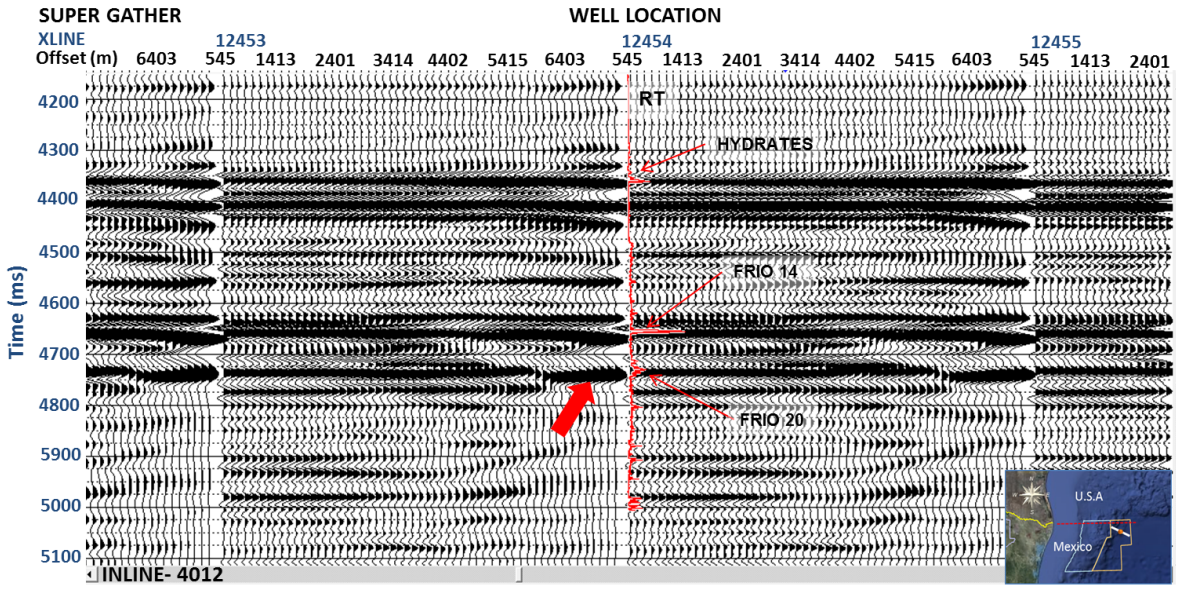

Figure 43. *Seismic gather displayed in the inline 4012, showing the result of super gather filtering. The super gather contributed to remove the random noise and to improve the signal to noise ratio, increasing slightly the amplitude in the events.*

Continuing with the workflow specified in the figure 39, I proceeded to perform a trim static correction. This filtering was implemented to correct the residual time alignment problems. According with the trim static theory, this correction attempts to determine an optimal shift, which will be applied each trace in a gather. The time shift is created by cross correlating in each trace by using a reference trace, usually the CDP stacked trace [Hampson & Russell et al. 2010].

After of several tests performed, the parameters that better adjust to carry out this correction was by using a constant time of 2200 ms, window length of 100 ms, maximum time shift of 25 ms and correlation window of 50 ms. The figure 44, shows the result of trim static correction, where is possible to observe how all the events are better aligned, which contributed positively during the AVO analysis.

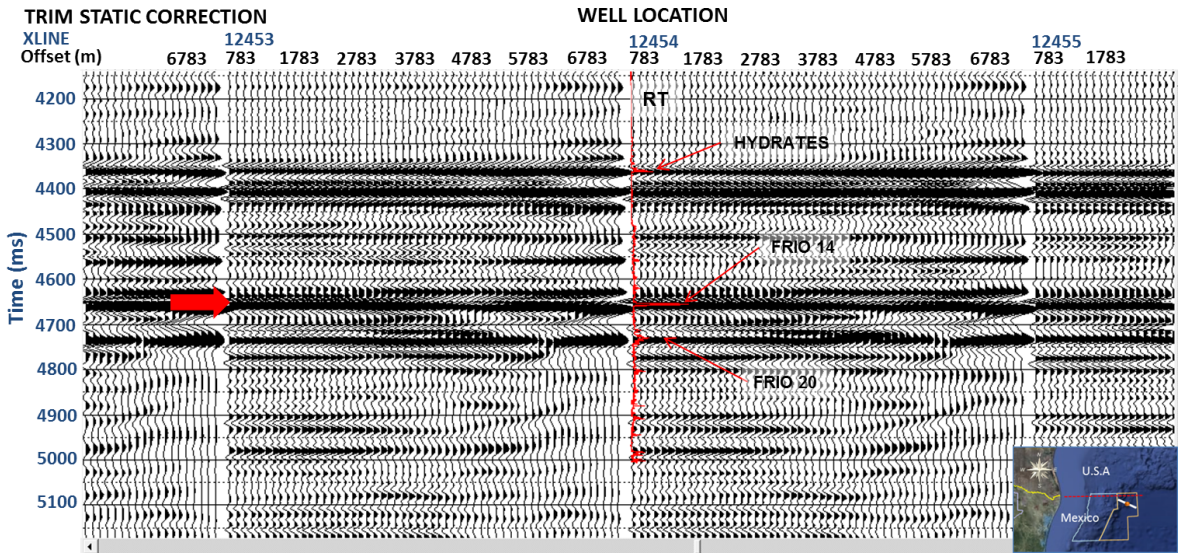

Figure 44. *Seismic gather displayed in the inline 4012, after to be performed the trim static correction, where is evident the better alignment of seismic events along of all interval of interest.*

Finally, I proceeded to perform the construction of a CDP stack. This process has as main function to stack all the traces which fall within the range limits, in other words the CDP stack will sum all traces of the gathers to generate a stacking volume [Hampson & Russell et al. 2010]. This process has as benefit to improve the signal to noise ratio and to obtain a stack volume, which was used to interpret important structural and stratigraphic features and display all AVO and seismic inversion results both 2D and 3D. The figure 45 shows the result of the CDP stack volume, being possible to observe all amplitude anomalies, and structural and stratigraphic features in the area of study.

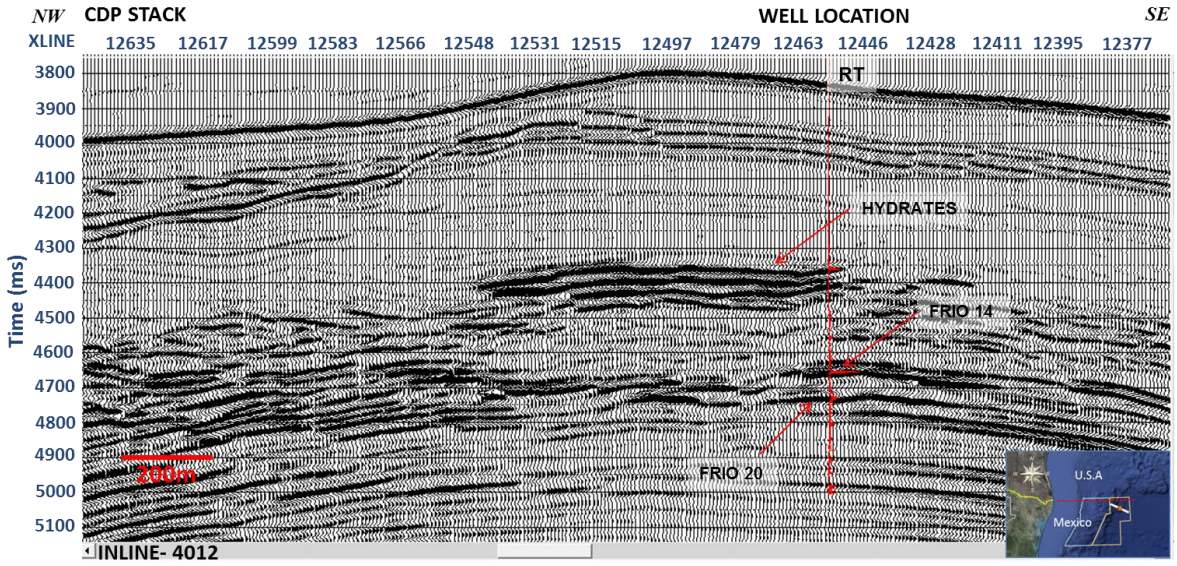

***Figure 45**. Seismic section displayed in the inline 4012, showing the result of the CDP stack. From this image is possible to observe the structural and stratigraphic features, as well as the amplitude anomalies contained in the interval of interest.*

4.4. AVO log Modeling

One of the most important challenges in this project was identify and predict the type of hydrocarbon associated to the reservoir and its relationship with the seismic response. One way to do it was by using a log based modeling. The log based modeling into the Hampson & Russell program, consisted in use shear velocity, compressional velocity and density as input logs, to later considering the Biot-Gassman theory to create different log responses assuming different type of fluids saturation in sand intervals. In this project I considered as fluid replacement: water saturation, gas saturation and oil saturation. These responses were compared with the original logs and from here, determine the type of log response more associated to the reservoir. Additionally, to obtain a better interpretation of log modeling, these also were supported by a crossplot V_P/V_S versus acoustic impedance, which contributed a better understanding of lithological distribution and fluid types determined by the log modeling. Once established the three different models, I proceeded to associate the log response to the seismic response, which was defined by the construction of synthetic gathers. The synthetic gathers were determined using the FRM (Fluid Replacement Module) application within Hampson & Russell program and using as input data the results

of log based modeling, and the implementation of Aki-Richards and Zoeppritz algorithms. Then, the synthetic gathers obtained were compared with the last version of conditioned gather (gathers with trim static correction). Thus, determine which log modeling result was more similar to the real gather.

The first step in the log modeling is the correlation between well logs and real seismic gather. To perform this, first was necessary the extraction of a wavelet around of the well. The extraction was performed taking into account a time window of 3500 to 3800 ms (interval of interest), and regarding a statistical wavelet with length of 100 ms, taper length of 25 ms and phase 0. After, the compressional sonic and density logs together with the extracted wavelet were used to estimate the reflectivity series and the synthetic trace. Finally, the synthetic trace was compared with seismic gather with trim static correction to its correct adjust and match. Thereby, one new P-sonic log corrected was created which I used for the subsequent analysis. The figure 46, shows the synthetic trace at zero offset (blue color), the compose trace (red color) and the real gather (black color). Hence, is possible to observe the good fit between the synthetic trace (blue color) and the real (black color).

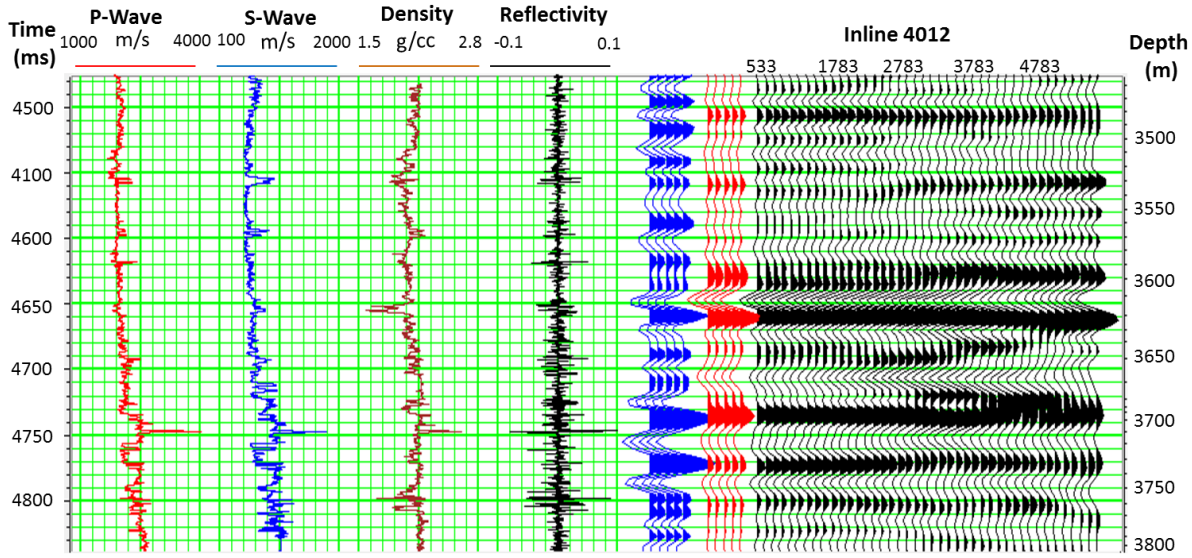

***Figure 46**. Result of correlation between well logs and real seismic gather with trim static correction. Where the blue traces represent the synthetic trace generated by logs, the red traces the composite real trace and the black traces the real seismic gather, showing a good correlation.*

Once done the log correlation, next step was to carry out the log based modeling assuming different fluid saturations in sand intervals. The log modeling performed in this project was based in the log modeling of shear wave, so first was necessary the construction of a new shear sonic log by using the Castagna´s mud rock equation (20), which is only valid for wet sands and shales. Then, the new shear sonic log is used as initial variable to subsequently, substitute different types of fluids in the sand intervals leaving fixed the compressional sonic and density logs. Thus, identify which type of fluid fit better with original logs, by observing variations in the shear sonic, Poisson´s ratio and V_P/V_S logs. Once the new shear sonic log was created, I replace the sand intervals assuming 100 % of water saturation using the FRM (Fluid Replace Modeling) module within the Hampson & Russell program, which calculate the velocity of sands saturated with water by using the Biot-Gassman theory and taking into account standard values to k modulus, μ modulus and density (ρ) and considering a matrix quartz sand (table 3).

Fluid	Mineral	Density (ρ) (g/cc)	Bulk modulus (k) (GPa)	Shear Modulus (μ) (GPa)
	Quartz sand	2.65	36.6	45
Water	-	0.97	2.5	45
Gas	-	0.05	0.04	45
Oil	-	0.58	0.4	45

***Table 3**. Rock physic values considered to estimate the new sonic velocities under different types of fluids.*

The figure 47 shows the result of the log modeling assuming water saturated sands. Hence is possible to observe that there is a reduction in the velocity of shear sonic log mainly in the sands Frio 14 and Frio 20, taking into account the log modeled represented by the curve in blue color. These sands also show a slight increase in the Poisson's ratio and V_P/V_S ratio, regarding the modeled curves in black and brown color respectively.

On the other hand, the sands in the interval Oligocene Frio 26 showed a very small reduction in shear velocity, while that Poisson's ratio and V_P/V_S ratio showed a small increase. The small difference in response between the water-saturated curve and the original curve, could point out that this interval may have very low hydrocarbon saturation.

The figure 48, shows a cross plot between acoustic impedance and V_P/Vs ratio, where is well defined the trend produced by water-saturated sands and shales.

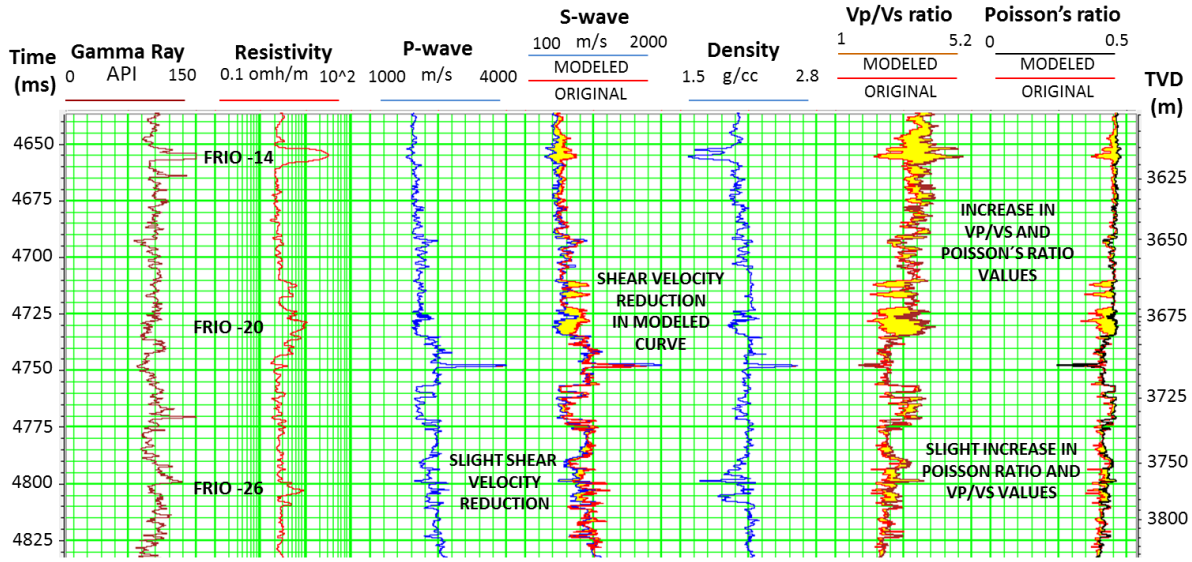

***Figure 47**. Result of log modeling assuming water-saturated sand, where is evident the reduction in shear wave velocity and the slight increase in the Poisson's ratio and V_P/V_S ratio.*

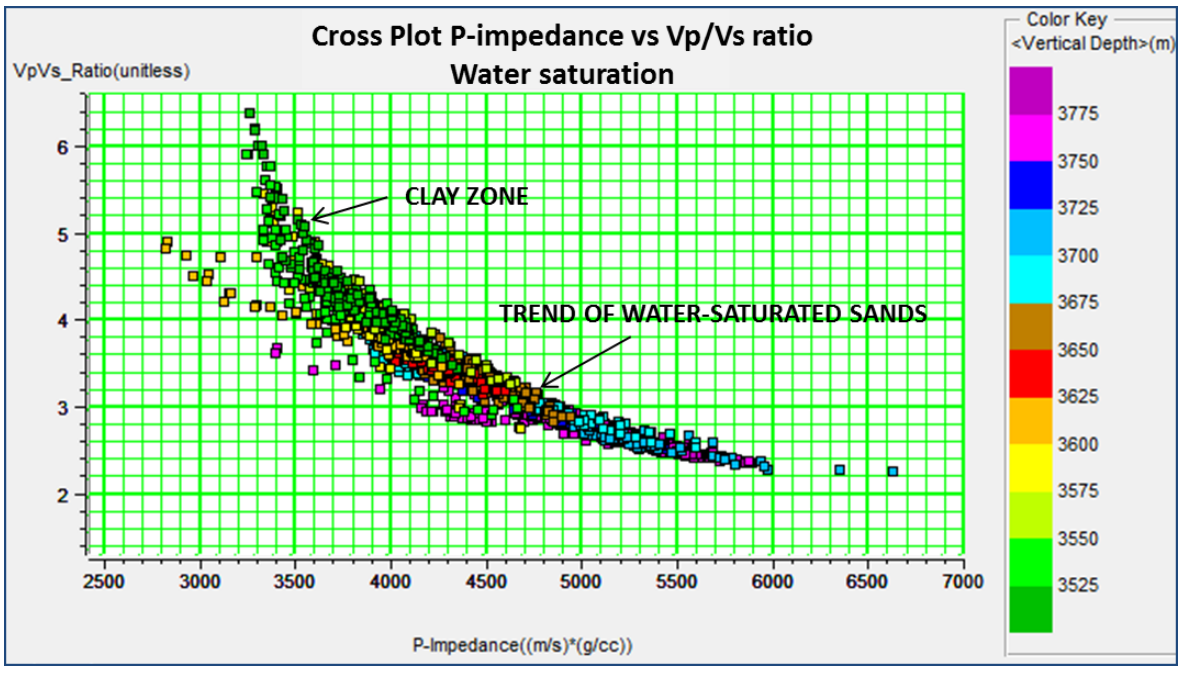

***Figure 48**. Cross plot P-impedance versus V_P/V_S ratio, where is evident the linear trend produced by the water-saturated sands and shales.*

Other important feature in the sands Oligocene Frio 20, is that from half interval to the top, the log modeling showed a shear velocity reduction when it was saturated by water, and from half interval to the base, the modeled curve did not show any change compared with original curve, which may is pointing out that the lower interval may be saturated by water in the original sand interval.

The log modeling assuming oil and gas saturation, were performed taking into account the same sand matrix and the same rock physics parameters used in the water saturation modeling. On the other hand, the rock physic parameters for oil and gas were also considered standard values which are represented in the table 3. The figure 49 shows the result of log modeling for gas-saturated sands. From this figure I observe how the shear velocity values increase for the intervals Oligocene Frio 20 and Oligocene Frio 26, being less evident for the sand Oligocene 14. Hence, also is possible to see how the Poisson's ratio and V_P/V_S ratio decrease significantly in each sand, so in this case is possible to assume that the sand intervals are not related with gas saturation due these no fit with the original curves, except for the sand Frio 14 which showed a slight reduction of shear velocity from the original curve.

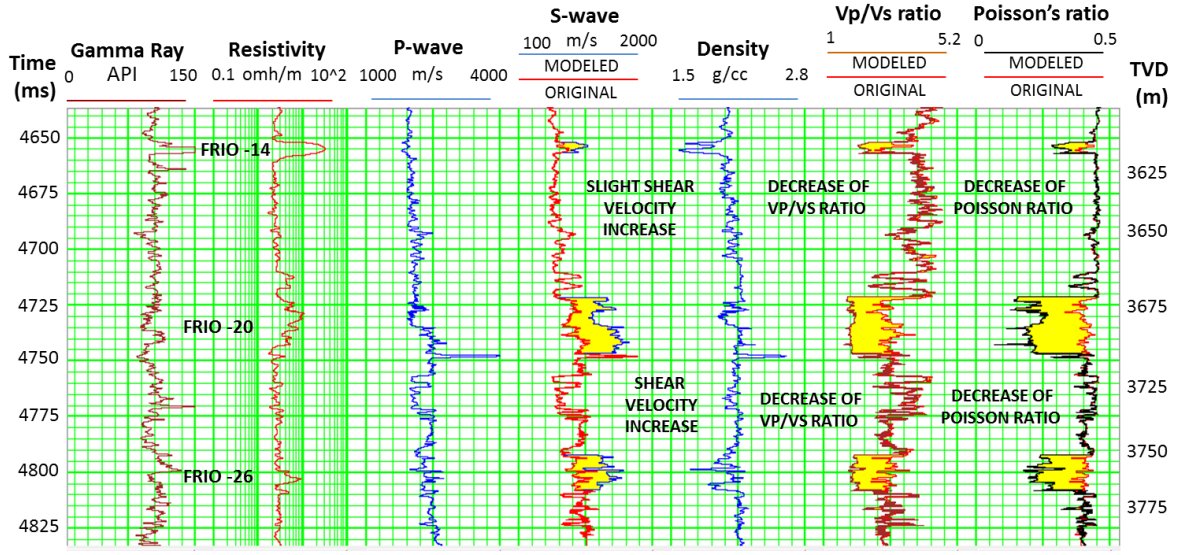

***Figure 49**. Result of gas-saturated sands modeling, showing an increase in the shear sonic log and reduction in Poisson's ratio and V_P/V_S ratio after of fluid replacement. Hence, also is evident that from these three intervals modeled, the sand Oligocene Frio-14 showed less change from the original curve, suggesting that it may be associated to gas saturation.*

On the other hand, the cross plot performed between Poison's ratio and acoustic impedance (figure 50) for gas saturated sands, showed the definition of three different zones: shales represented by green circle, wet sands represented by blue circle and the gas saturated sands represented by yellow circle. In this cross plot, is evident how the gas saturated sands are represented by low value of Poisson's ratio, while that their acoustic impedance value is distributed in a wider interval, which may points out that these sands have different degree of compaction and porosity, where high values of acoustic impedance indicates lower porosity and greater compaction. The shales zone showed low acoustic impedance values and high V_P/V_S ratio, while wet sands depicted V_P/V_S ratio values contained between shales and gas saturated sands with higher acoustic impedance values than shales.

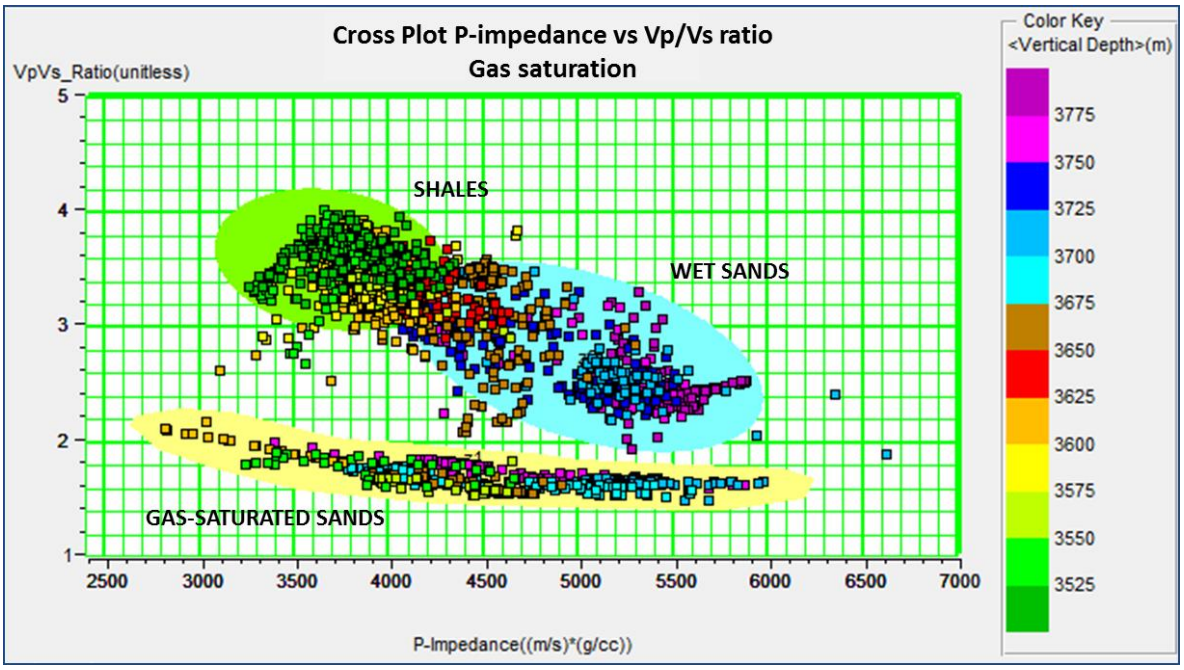

***Figure 50**. Cross plot performed for the gas saturated sands, showing three zones: shales (green circle), wet sands (blue circle) and gas saturated sand (yellow circle). Where is evident how the gas saturated sand are represented by lowest V_P/V_S ratio values.*

From log modeling performed for oil saturated sands (figure 51), I could observe how the sands Oligocene Frio 14 and Oligocene Frio 20 had a good fit with the original shear velocity log. However, for the Oligocene Frio 20 the fit was only regarding the upper part of this interval due that lower part showed better fit with the water saturated sand. These sands showed a decrease in Poisson´s ratio and the V_P/V_S ratio, being more evident in the

sands Oligocene Frio 20. On the other hand, the log modeling performed in Oligocene Frio 26, showed a higher increment of shear velocity that the original, which suggest that Oligocene Frio 26 may has lower oil saturation than the upper reservoirs. Is important point out that, in this modeling was considered 100 percent of oil saturation with the main target to observe how would be the log responses in ideal conditions of saturation (100 percent of saturation). The Oligocene Frio 26 sand also showed a decrease in Poisson's ratio and V_P/V_S ratio, however in that sense the sands Oligocene Frio 14 and Oligocene Frio 20 would be most representative for this modeling due they adjusted almost at 100 percent taking into account the original curves.

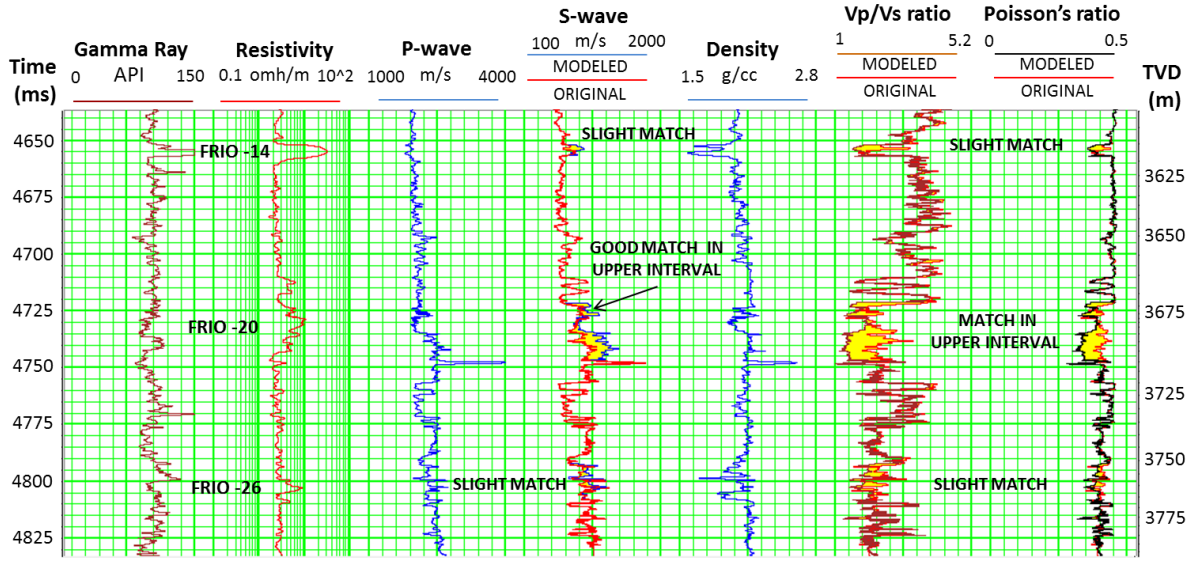

Figure 51. *Log modeling result in oil saturated sands conditions, showing how the upper sands (Frio 14 and Frio 20), fit almost perfectly with the results obtained by this modeling. Although the sand Oligocene Frio 26 did not fit a 100 percent with the log modeling, the difference between its shear curve modeled and the original is not significant, which may points out this sand has lower oil saturation than upper sands (Frio 14 and Frio 20).*

The figure 52 shows the cross plot V_P/V_S versus acoustic impedance for the oil saturated sand, being possible to define three representative zones: shales represented by green circle, wet sands represented by blue circle and the gas saturated sands represented by yellow circle. The cross plot shows that the oil saturated sand has a low V_P/V_S ratio value, however it is a bit higher than that derived for the model of gas saturated sands (figure 50). The wide distribution of acoustic impedance may be attributed once again to different degree of

compaction and porosity in the intervals along of well. On the other hand, the shales once more were represented by low acoustic impedance values and high V_P/V_S ratio. While wet sands also were represented by a higher V_P/V_S ratio that oil saturated sands but lower than shales, showing also a wide distribution in their acoustic impedance values.

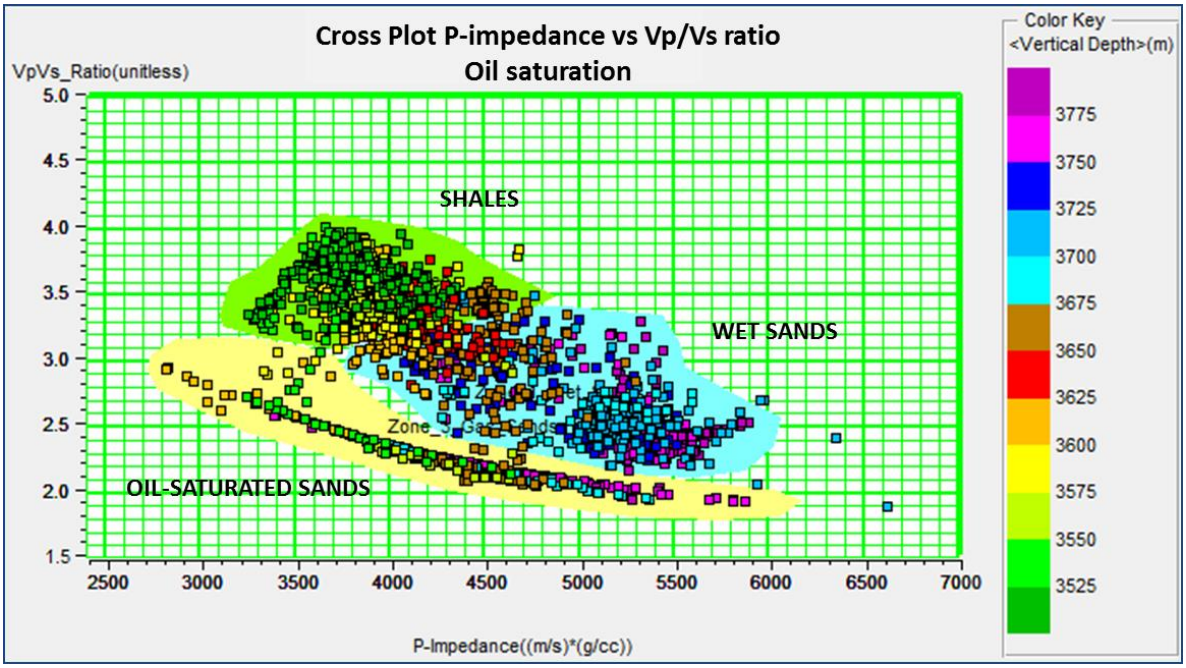

***Figure 52**. Cross plot performed for the oil saturated sands, showing three zones: shales (green circle), wet sands (blue circle) and oil saturated sand (yellow circle). Where is evident how the oil saturated sand are represented by lowest Vp/Vs ratio values than that represented by shales and wet sands, being also evident the wide distribution of their acoustic impedance values associated to lithology with different degrees of compaction and porosity.*

Once established the log modeling for each interval assuming of same percent and type of fluid saturation, the next step was to perform other log modeling but now assuming two types of fluid saturation in different intervals along of the well, to after be compared with the original logs. Thereby, I proposed a log modeling regarding gas saturation for the Oligocene Frio 14 and oil saturation for Oligocene 20 and Oligocene 26. This fluid saturation was proposed taking into account the results of previous log modeling, in addition of the petrophysical evaluation performed in the well (see appendix A). Once more to determine the rock matrix and the rock physic parameters of fluids were assumed standard values (table 3) and the Biot-Gassman theory. In addition to consider different

degree of saturation in each interval, where for the sand Oligocene Frio 14 was considered a 40% of gas saturation, while in the sands Oligocene Frio 20 and Oligocene Frio 26, were considered with 100% and 80% of oil saturation respectively. Is important highlight that to determine the correct saturation was necessary realize several tests until achieve the most appropriated saturation. The figure 53 shows the log modeling result after of fluid substitution. Hence, I could observe how the three sands modeled showed a good fit with original logs

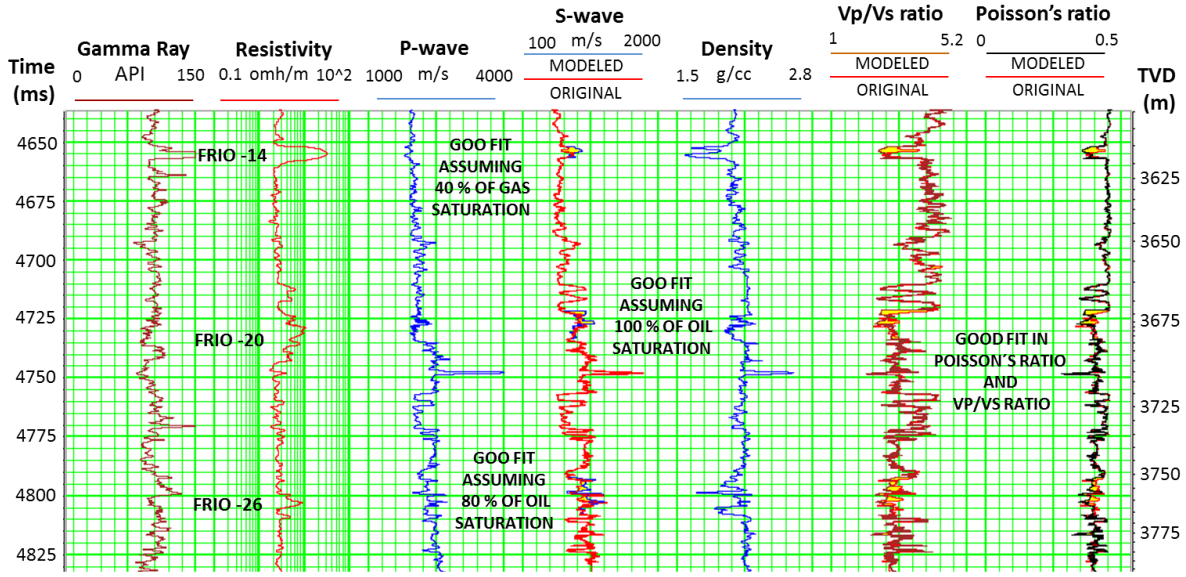

Figure 53*. Log modeling result assuming different fluids and degrees of saturation in each sands interval, where is evident the good fit between the original logs and modeled logs. In this modeling was assumed 40% of gas saturation for Oligocene Frio14, while for Oligocene Frio 20 and Oligocene Frio 26 were assumed 100% and 80% of oil saturation respectively.*

The cross plot V_P/V_S ratio versus acoustic impedance realized for this modeling (figure 54), helped to define four different zones: shales represented by the gray zone, wet sands represented by blue zone, oil saturated sands by green zone and yellow for gas saturated sands. Thereby, is evident how the gas saturated sands are associated with lower acoustic V_P/V_S ratio values, showing also a trend toward low values of acoustic impedance. The oil saturated sands also showed one well-defined trend with relative low V_P/V_S ratio. However, their acoustic impedance showed a trend toward higher values than gas saturated sands. On the other hand, the shales showed highest V_P/V_S ratio values and they were established in

zones with relatively low acoustic impedance. The water bearing sands were characterized by relatively high acoustic impedance values with a trend toward lower values and high values of V_P/V_S ratio.

The figure 55 shows the cross plot V_P/V_S ratio versus Poisson´s ratio performed for the original logs. Thereby, is evident how this cross plot also shows almost the same pattern of distribution for oil-gas saturated sands defined by log modeling. Therefore, may be interpreted that the percentage of saturation and types of hydrocarbons used in the modeling of oil-gas saturated sands may be representative of the real conditions of the reservoir.

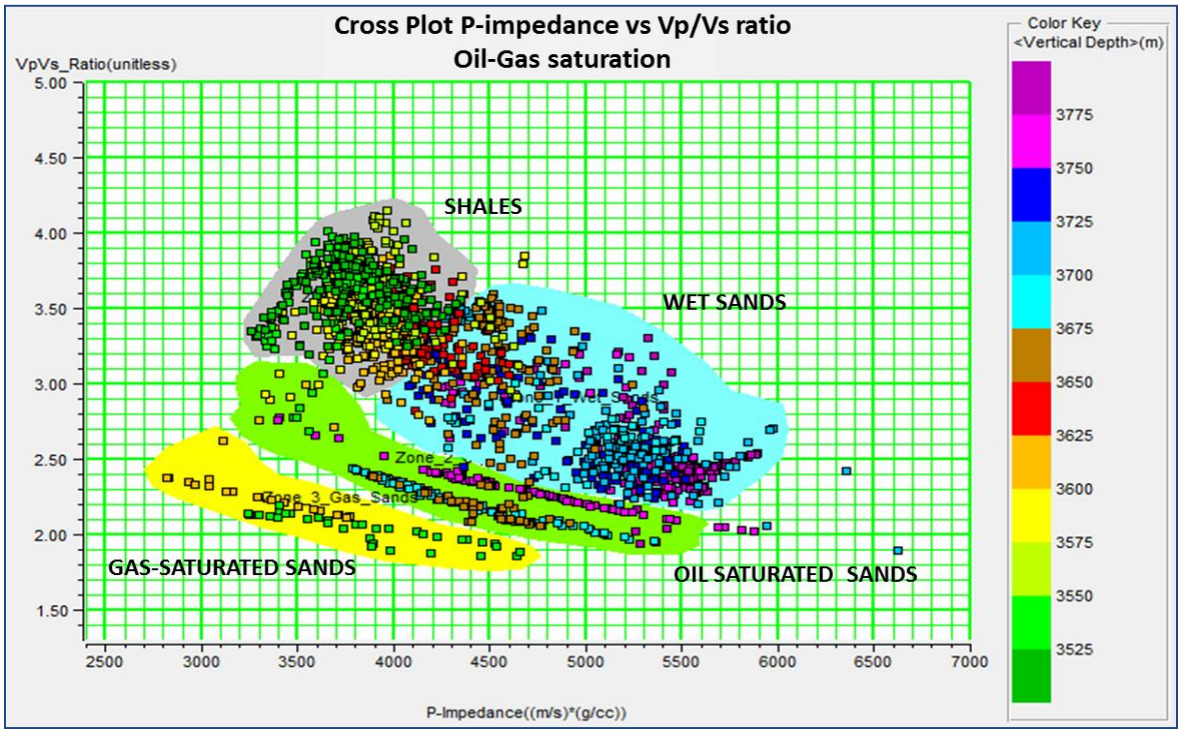

***Figure 54**, Cross plot of acoustic impedance versus Vp/Vs ratio performed for the oil-gas modeling, showing the definition of four zones of interest: shales represented by the gray zone, water bearing sand represented by blue zone, oil and gas represented by green and yellow color respectively.*

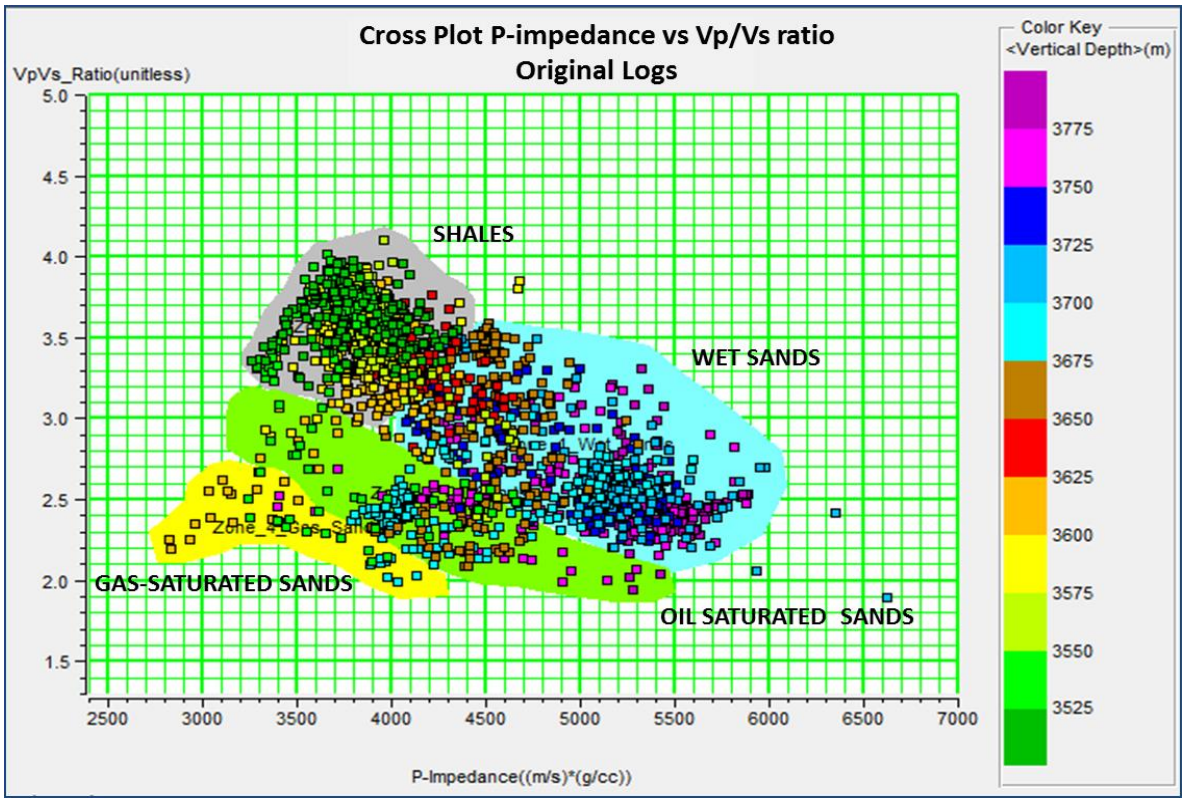

Figure 55. *Cross plot Vp/Vs versus Poisson's ratio performed in the original logs, showing the same zones pattern identified by the modeling of oil-gas saturated sands.*

Finally the last step performed in the log modeling was the generation of synthetic gathers. The synthetic gathers were realized for each log modeled with different fluids saturation (water saturation, gas saturation, oil saturation and gas-oil saturation) and taking into account Zoeppritz and Aki-Richards algorithms. The main target of synthetic gathers was to predict seismic gather response and their relationship with the logs response and fluids content in the reservoir. The synthetic gathers also helped to identify any artifact which could not have been properly corrected during the gathers conditioning step. The figures 56 and 57 show the result of synthetic gathers performed to each log modeled.

The result of synthetic gathers with water saturation in both algorithms Zoeppritz and Aki-Richards, showed a reduction in amplitude toward far offsets in all intervals modeled (Oligocene Frio 14, Oligocene Frio 20 and Oligocene Frio 26). Conversely, in the case of gas saturation the synthetic gathers showed an increase of amplitude toward far offsets,

mainly in the reflectors contained in intervals between 4500 ms to 4800 ms, being more evident in the upper reflectors (4500 ms – 4700ms).

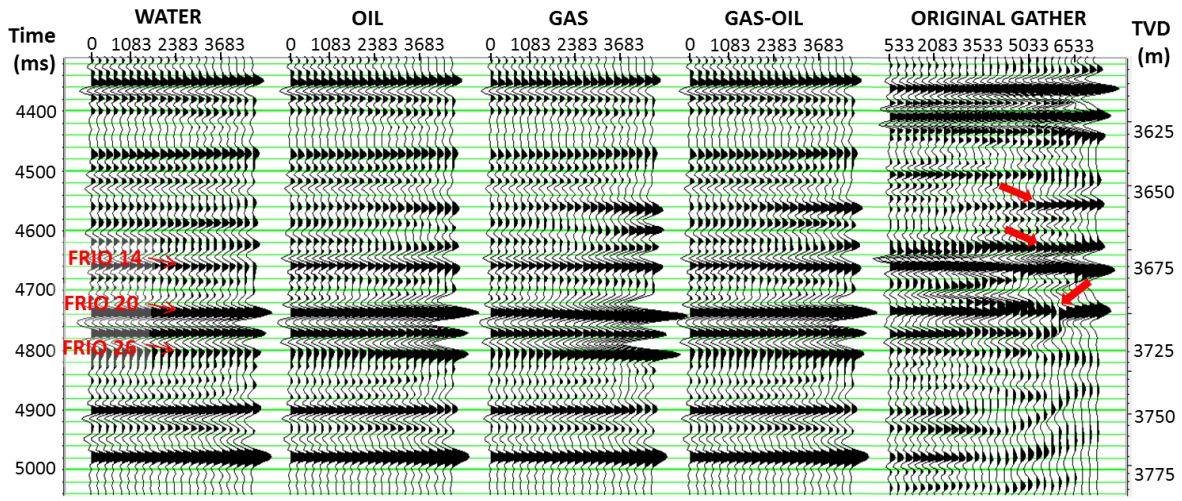

***Figure 56**. Synthetic gathers generated by using Zoeppritz algorithm.*

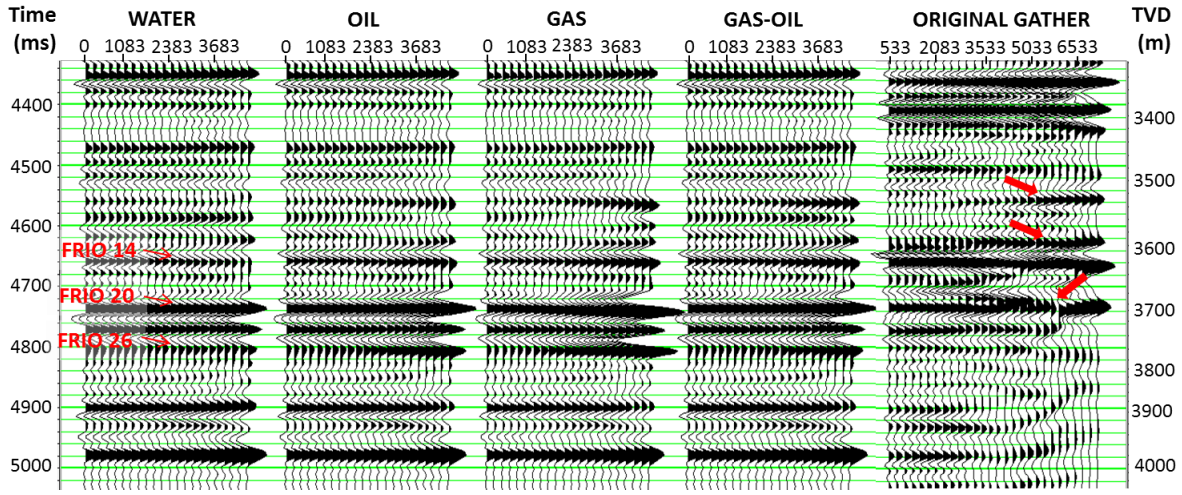

***Figure 57**. Synthetic gathers generated by using Aki-Richards algorithm.*

In the case of oil saturation, the synthetic gathers also showed an amplitude increase, but slightly minor than that expressed by gas saturation. When the synthetic gathers were compared with the original gather, I observed that synthetic gathers response associated to gas saturation fit better in the upper layers (4500 ms -5670ms). While the amplitudes located in ranges between 4720 ms to 4820 ms, the fit was slightly better with oil saturation. Thereby, I proceeded to perform the synthetic gather with gas-oil saturation. The

synthetic gather result assuming gas-oil saturation showed a better fit with the original gather in both methods. However, is evident that although both algorithms showed similar results, the synthetic gather of Zoeppritz adjusted slightly better with the original gather than Aki-Richard method, mainly in the upper intervals (4500 ms - 4700 ms). Other important feature defined during the synthetic gather implement was the identification of two reflectors that showed good AVO response, which were not associated to any target sand interval. One of these intervals is located at 4560 ms and another at 4620 ms just above of Oligocene Frio 14. Further, I could observe that in the original gather the amplitudes associated to Oligocene Frio 20 (4730 ms approximately) showed a slightly misfit at 5780 m in offset, which may represent a little problem during the AVO analysis.

From the log modeling and synthetic gathers results I can resume that these results helped to confirm and evaluate two main aspects; first the seismic and log responses associated with different type of fluid saturations, which were derived two types of reservoirs: one associated to gas (Oligocene Frio 14) and other associated to oil (Oligocene Frio 20 and Oligocene Frio 26); and second to predict and to have a better estimation of potential intervals to contain hydrocarbons and which could be confirmed during the AVO and seismic inversion analysis.

4.5. AVO pick and Gradient Analysis

Once realized the log modeling the next step was to perform the AVO analysis which had as main target, characterize the reservoir seismic response and its relationship with the seismic amplitude. This goal was achieved by interpreting cross plots gradient (A) versus intercept (B) in the real gathers and by using of AVO attributes (A*B, Poisson's scaled ratio, and R_P/R_S ratio). The AVO analysis in this project was performed in the CDP gathers with trim static correction. These gathers were transformed from CDP´s offset to CDP´s incident angles, by using the velocity field of P-wave obtained during the log modeling. The figure 58 shows the input gathers and their transformation to incident angles, where I could identify incident angles until 55 degrees, which was enough to perform the AVO analysis.

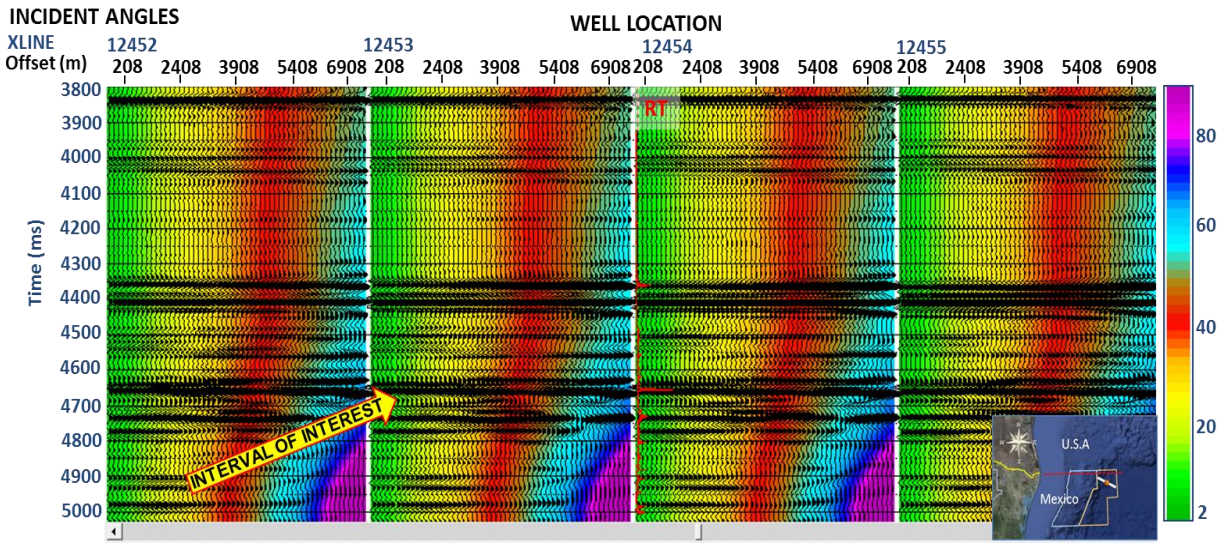

Figure 58. *Input seismic gathers and their conversion to incidence angle gathers by using of velocity function derived of log modeling. Thereby, is evident how after of transformation is possible to achieve angles until 55 degree in the area of interest.*

Once identified the range of incident angles and sure that they were large enough for the AVO analysis, I proceeded to perform the pick analysis, where to carry out this process first was necessary the correlation of some horizons focused in the intervals of interest and some reflectors with AVO response (horizons with increased amplitude with offset). So, under these assumptions were selected five horizons: Top of hydrates, Miocene 1, Miocene 2, Oligocene Frio14, and Oligocene Frio 20. The horizons Top of Hydrates, Miocene 1 and Miocene 2, were selected due these reflectors showed AVO response during the implementation of synthetic gathers and their names were selected according with their geological formation and lithological properties. The reflector located in the Oligocene Frio 26, was not considered for this analysis due it did not show AVO response during the synthetic gather implementation. This analysis was performed regarding incident angles of 50 degrees and the approximation of Aki-Richards. The figure 59 shows the pick analysis result of five reflectors selected around of well.

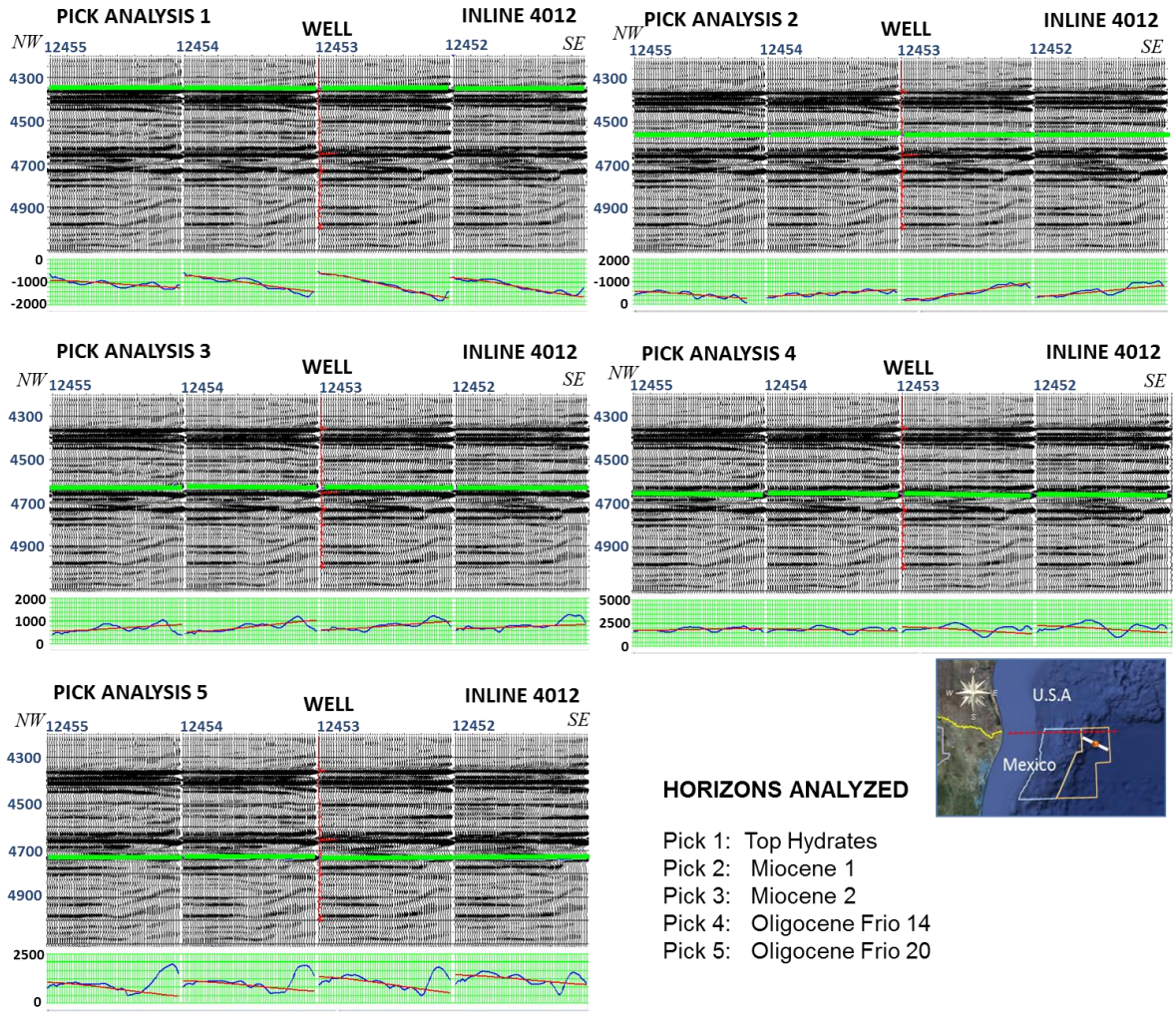

***Figure 59**, Result of pick analysis performed in five reflector selected around the well and which showed AVO response during the synthetic gather implementation.*

The Top of hydrates was picked taking into account a negative reflector (trough), where I could observe that the amplitude increased strongly with offset, mainly in areas toward west portion of well. Hence, is possible to deduct that the zone just below of possible presence of methane hydrates could be saturated by free gas. The presence of free gas and high compaction of methane hydrates often generate a strong contrast in acoustic impedance, which is manifested by a high amplitude response, negative reflection coefficient and change of polarity taking into account the sea bottom as reference. So this amplitude response due its characteristics may be associates with AVO class 3. The pick analysis 2, was developed over a reflector denominated “Miocene 1” due it is located into this geological formation and considering a positive reflector (pick). This reflector showed

an increase of amplitude with offset, mainly in the east portion of well. From this response I may suggest that the acoustic impedance for these sands may be smaller than shales surrounding. Therefore, is possible to expect an AVO a bit similar of that of methane hydrates, so an AVO class 3 was suggested also. The pick analysis developed in the reflector denominated “Miocene 2” was performed in a positive reflector (pick) and showed a very small increase of amplitude with offset, which suggest that acoustic impedance contrast between this sand and shales surrounding could be small or the sands could have low hydrocarbon saturation. However, due these sands did not show a polarity change and amplitude increase with offset once more could be expected an AVO class 3 associated with low hydrocarbon saturated sands or sands with very low compaction (loose material). The pick analysis in the Sand Oligocene Frio14 was performed in a positive reflector (pick) and showed a slight decrease of amplitude with offset, so this sands interval could have higher acoustic impedance than shales surrounding. The characteristics of reflectivity and gradient for these sands suggest an AVO class 1 or class 4. Finally the pick analysis realized in the sand Oligocene Frio 20, was performed in a positive reflector (pick), and showed a decrease of amplitude with offset a little stronger than the sand Oligocene Frio 14. Which points out these sands have higher acoustic impedance than shales surrounding. So, assuming these characteristic and taking into account the strong coefficient reflection response and decreasing of amplitude with offset an AVO class 1 was interpreted.

Once finished the pick analysis, I proceeded to perform a gradient analysis with more detail. The gradient analysis allowed to define and interpret better the types of AVO associated to each event analyzed during the pick analysis. The gradient analysis was performed taking into account one gather focused in the well and a cross plot gradient (B) versus intercept (A), which facilitated the AVO classification. The figures 60a, 60b, 60c, 60d and 60e show the result of gradient analysis. Hence, I could observe that AVO analysis performed in the top of hydrates, showed a negative reflection coefficient at normal incidence, which is increased with offset increasing. This AVO anomaly drops into the third quadrant, which according with the AVO theory it can be interpreted as AVO class 3, reinforcing the AVO interpretation performed during the Pick analysis.

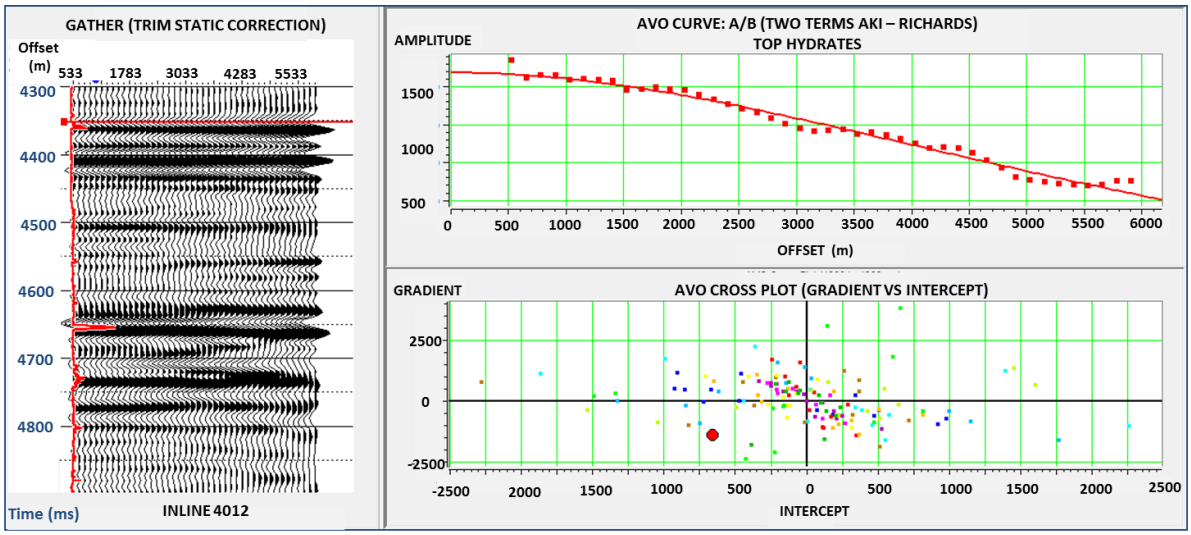

***Figure 60a**. Gradient analysis performed in Top of hydrates reflector, showing an AVO class 3 response, according with their gradient characteristics and cross plot results.*

The gradient analysis performed in the reflector denominated "Miocene 1", was realized over a pick reflector, showing a positive reflection coefficient at normal incidence which decreasing with offset increasing. This reflector also shows polarity change and the cross plot performed for this anomaly drops in the fourth quadrant, which suggest an AVO class 2.

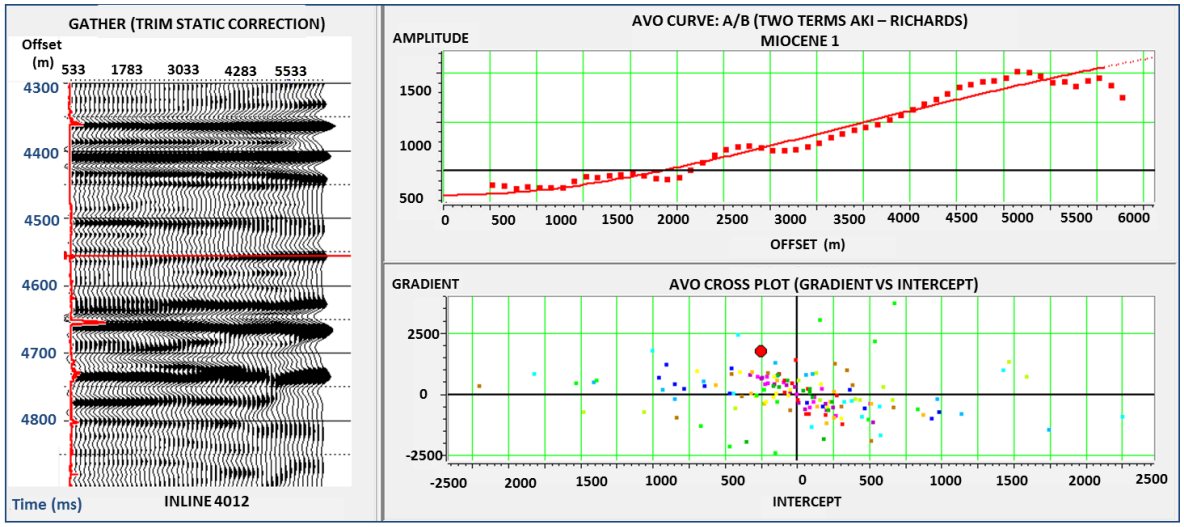

***Figure 60b**. Gradient analysis performed in the reflector "Miocene 1", showing an AVO class 2 response, according with their gradient characteristics and cross plot results,*

For the reflector “Miocene 2”, the gradient analysis showed a positive reflection coefficient at normal incidence, taking into account that the reflector was analyzed over a pick event. The amplitude anomaly showed an amplitude increase with offset increasing. The cross plot performed for this sand drop in the first quadrant, so an AVO class 3 was interpreted,

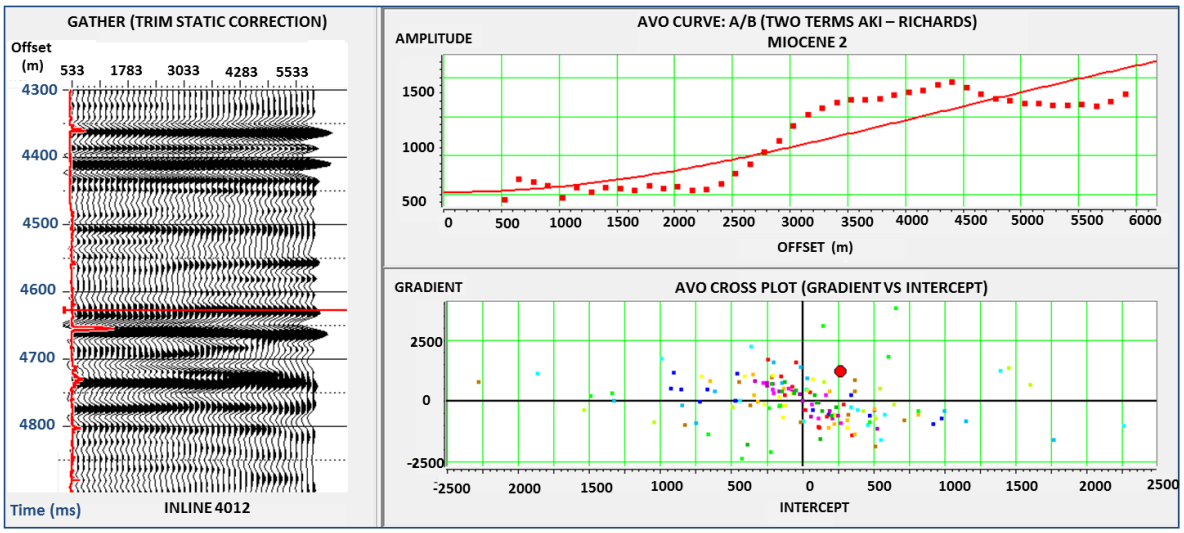

***Figure 60c**. Gradient analysis performed in the reflector “Miocene 2”, showing an AVO class 3*

The sand Oligocene Frio 14, was realized over a pick reflector and showed a positive reflection coefficient at normal incidence, which decrease with offset increasing. This amplitude anomaly drops in the top of second quadrant and closer of area of AVO class 2, so in this case an AVO class 4 may be derived.

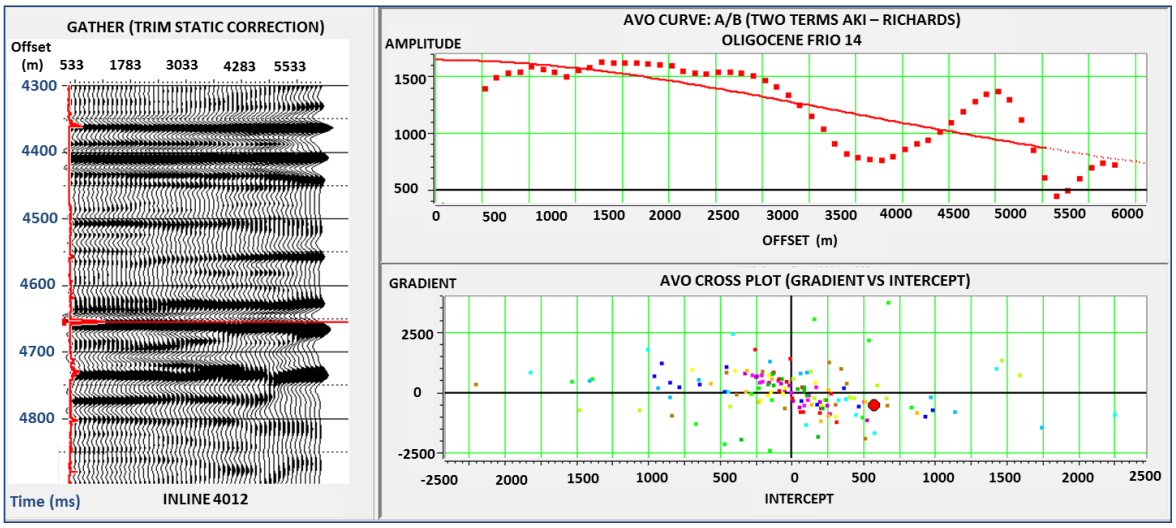

***Figure 60d**. Gradient analysis performed in the reflector Oligocene 14, showing an AVO class 4.*

Finally the gradient analysis performed in the sand Oligocene Frio 20 was realized over a pick reflector and showed a positive reflection coefficient with negative amplitude gradient. The amplitude anomaly dropped toward right portion of the second quadrant, so an AVO Class 1 was interpreted for this interval.

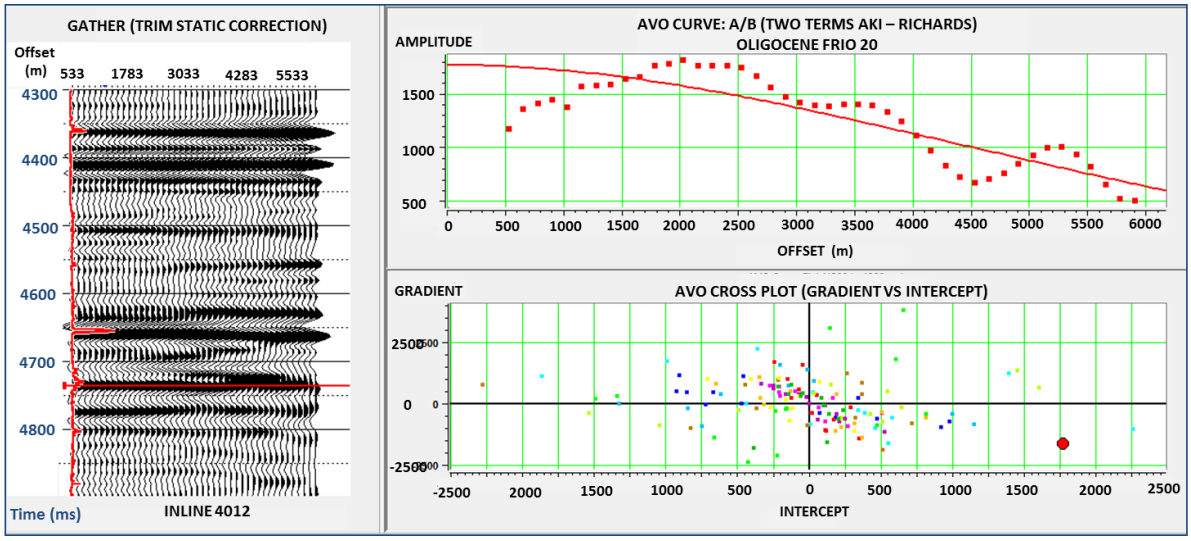

***Figure 60d**. Gradient analysis performed in the reflector Oligocene 20, showing an AVO class 1 response, according with their gradient characteristics and cross plot results*

,

4.6. AVO Attributes and Cross plot

Once finished the gradient analysis, the next step was to perform an AVO analysis by using attributes. This analysis helped to identify in an easy way amplitude abnormalities in the data, and contributed to determine if these abnormalities could be associated to the presence of fluids or lithologic changes. However, is important to highlight that the correct understanding and proper application of AVO attributes was essential to avoid creating false expectations during their analysis.

To carry out this process, the gathers with trim static correction and velocity function derived from the oil log modeling were used as input into the Hampson & Russell program. Therefore, in this project were performed three attributes A*B, Poisson's ratio scaled (A+B) and Fluid factor. The figure 61 shows the result of A*B attribute extracted from conditioning gathers.

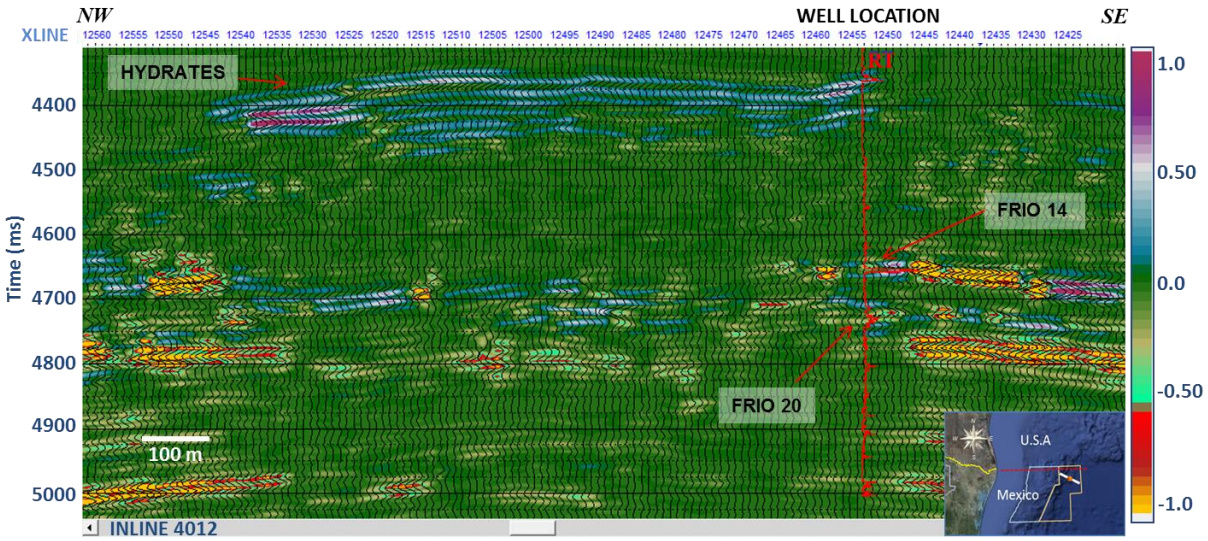

Figure 61. *Attribute A*B performed in the gathers with trim static correction, which shows positive anomalies associated to methane hydrates zone and along of the reflector associated with the Oligocene Frio 14, while sand Oligocene Frio 20 shows a slight negative amplitude toward its top.*

The attribute A*B, showed a set of positive anomalies mainly focus in the zone of methane hydrates and along of all reflector associated with the sand Oligocene 14, mainly in its top and base. These positive anomalies according with the A*B theory are very characteristic of AVO class 3, due product performed between the gradient and intercept taking into account both top and base for a reservoir associated with AVO class 3, always will give a positive result [Hampson & Russell et al. 2010]. On the other hand, the sand Oligocene Frio 20 shows a low negative anomaly, which may be interpreted as a different type of AVO and therefore may be associated a one different type of fluid or lithological change. This type of anomaly is also slight evident toward center of sand Oligocene Frio 14, which may is pointing out fluids or lithological characteristics similar in some zones of both intervals. In this attribute the reflector Oligocene Frio 26, Miocene 1 and Miocene 2 did not show anomaly response.

The next attribute derived in this project was the Poisson´s ratio scaled *(A+B)*. This attribute helped to have a better understanding of the anomalies identified in the attribute A*B. According with the algorithm of this attribute, the top of the reservoir is represented for a decreasing value of the Poisson's ratio, while base is represented by an increasing

value of the Poisson's ratio (see theory section) in intervals associated with hydrocarbon presence [Hampson & Russell et al. 2010]. The figure 62 shows the result of this attribute.

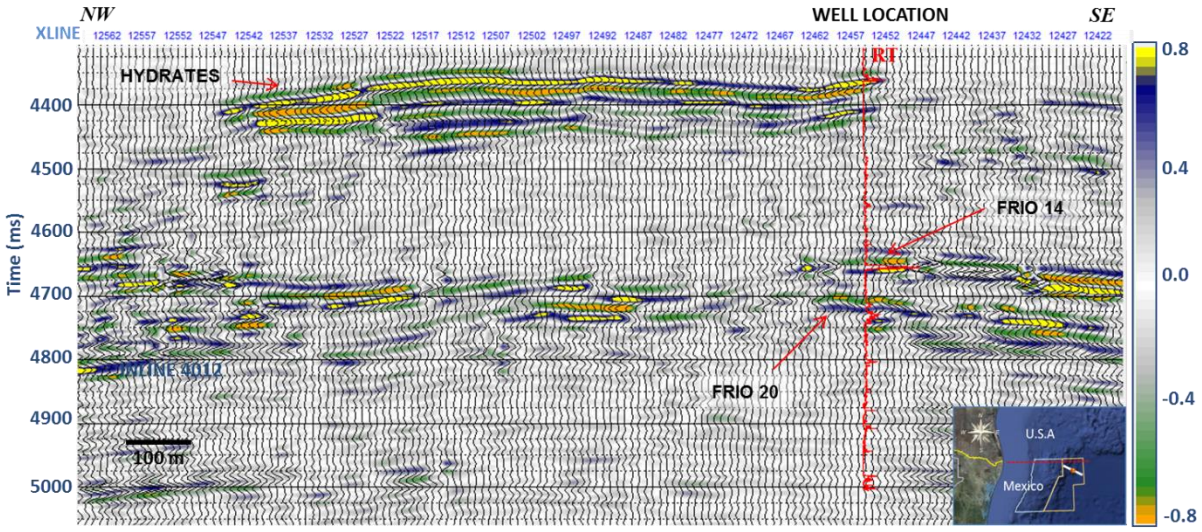

Figure 62. *Attribute of Poisson's ratio scaled performed in the gather with trim static correction, showing the couple of AVO anomalies represented by a negative poisson´s ratio in the top and positive poisson´s ratio in the base, reinforcing the interpretation of AVO anomalies identified by the attribute A*B.*

From this figure, I could observe how the amplitude anomalies now are more restricted toward the zones with hydrocarbon presence, which were also identified by the well. In this attribute is evident how the zone of hydrates is represented by a negative and positive Poisson´s ratio response. These couples of anomalies are more evident toward the western portion of the hydrates, and less evident toward their base. On the other hand, the Oligocene Frio 14, shows a negative Poisson´s ratio response in its top and a positive response in its base, extending toward its eastern portion and in fragmented blocks toward its western portion by the presence of normal faults. The sand Oligocene Frio 20 also shows a negative and positive Poisson´s ratio response mainly toward its top, being slightly distributed toward its eastern portion. The sand Oligocene Frio 26 once more does not show response. With this attribute I could have a better understanding of amplitude anomalies identified by the attribute A*B, and thus determine which anomalies are associated with the hydrocarbons presence and lithological changes.

Finally the last attribute performed in this project was the Fluid Factor attribute, this attribute was implemented with the objective to reinforce the interpretation derived from A*B and Poisson´s scaled ratio (A+B). The Fluid Factor attribute is characterized to be an attribute based in the Castagna´s mudrock equation, which according with the AVO theory the mudrock equation is only valid in areas where the shale and water are present. So in areas where this assumption is not fulfilled will be highlighted for a high amplitude anomaly, in other words hydrocarbon zones [Hampson & Russell et al. 2010]. The figure 63 shows the result of this attribute.

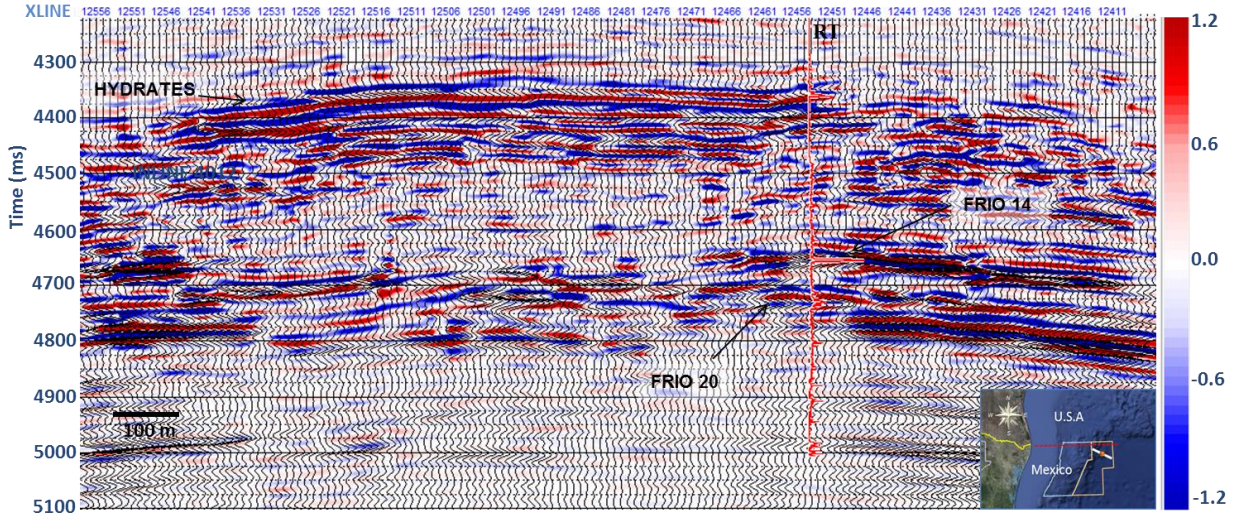

Figure 63. *Result of Fluid Factor attribute extracted in the gathers with trim static correction, showing zones with high amplitude, which some of them fit with the amplitude anomalies identified by the A*B and Poisson´s scaled ratio, mainly in the zones of hydrates and sands with hydrocarbons saturation identified by the well (Oligocene 14 and Oligocene 20).*

From this attribute, I could identify a set of anomalies of high reflectivity distributed toward the top of the structure. The top of hydrates shows a negative reflectivity, being slight stronger toward the western portion, which fit with interpretation realized in the A*B and Poisson´s ratio attributes. For sands Oligocene Frio 14 and Oligocene Frio 20, this attribute show a negative high reflectivity in the top and a positive reflectivity in the base, being a bit stronger and evident in the Oligocene Frio 14. Also is possible to observe that the high reflectivity anomaly for the sand Oligocene Frio 14, may be extended toward the center of structure. However, this reflectivity is attenuated due to the presence of hydrates in upper layers. On the other hand, there is other reflector that also shows a high reflectivity

response just below of the Oligocene Frio 26, which is also attenuated below of hydrates zone. However due this reflector shows a different response of reflectivity (positive reflectivity in the top, negative in medium and positive toward the base) compared with hydrocarbon zones, I can interpret this reflector with high amplitude as product of a lithological change, maybe associated at a high volcanic activity landward during this geological period (Upper Oligocene –Lower Miocene), which produced that pyroclastic material were transported basinward by the winds and deposited on these layers. So is possible that these layers have a big amount of volcanic ash and pyroclastic material producing this high reflectivity.

Once performed these attributes in cross sections, I proceeded to extract the same attributes by using time slices in the potential intervals with the objective to understand and interpret the AVO anomalies distribution and their relationship with the structure and reservoir rock. The figures 64a, 64b, 64c, 64d and 65a, 65b, 65c, 65d show the result of A*B, Poisson´s scale ratio, Fluid factor and Intercept performed in the sands Oligocene Frio 14 and Oligocene Frio 20 respectively. From the figure 64a, I could interpret that the A*B attribute showed a positive AVO anomaly, which looks to be delimited by fault blocks. This distribution of anomalies fit with positive AVO anomalies interpreted in cross section, which were interpreted as AVO class III. The figure 64b, shows a negative response of Poisson´s ratio, that adjust with the AVO anomaly interpreted in the top of this interval, which was represented by a negative Poisson ratio for the top of reservoir. The figure 64c, shows the result of Intercept attribute. In this attribute is possible to observe all the normal faults system located in the top of structure and its relationship with high amplitude anomalies. This faults system had been already described in the seismic interpretation chapter, which was interpreted as a normal faults system generated by gravitational collapse as a product of intense deformation. However, with this attribute I could interpret, which fault blocks may have more expectation to contain hydrocarbons and which fault blocks may be associated to reservoir rock distribution. Finally, I show the Fatti´s attribute in the figure 64d which was performed taking into account a seismic window of 50 ms below of the target horizon (Oligocene Frio 14). This attribute showed a positive anomaly of high reflectivity, which fit with the anomalies distribution determined by the other

attributes. So, this anomaly also could be interpreted as a possible distribution of hydrocarbons.

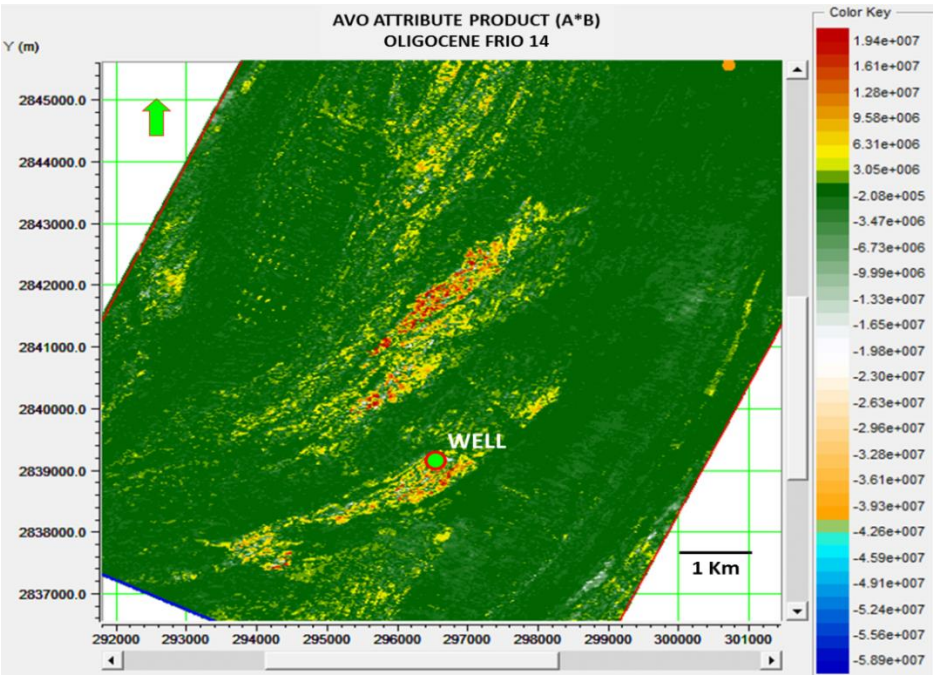

***Figure 64a**. AVO attribute of A*B extracted in the sand Oligocene Frio 14, showing a positive anomaly distribution in areas with possibilities to contain hydrocarbons.*

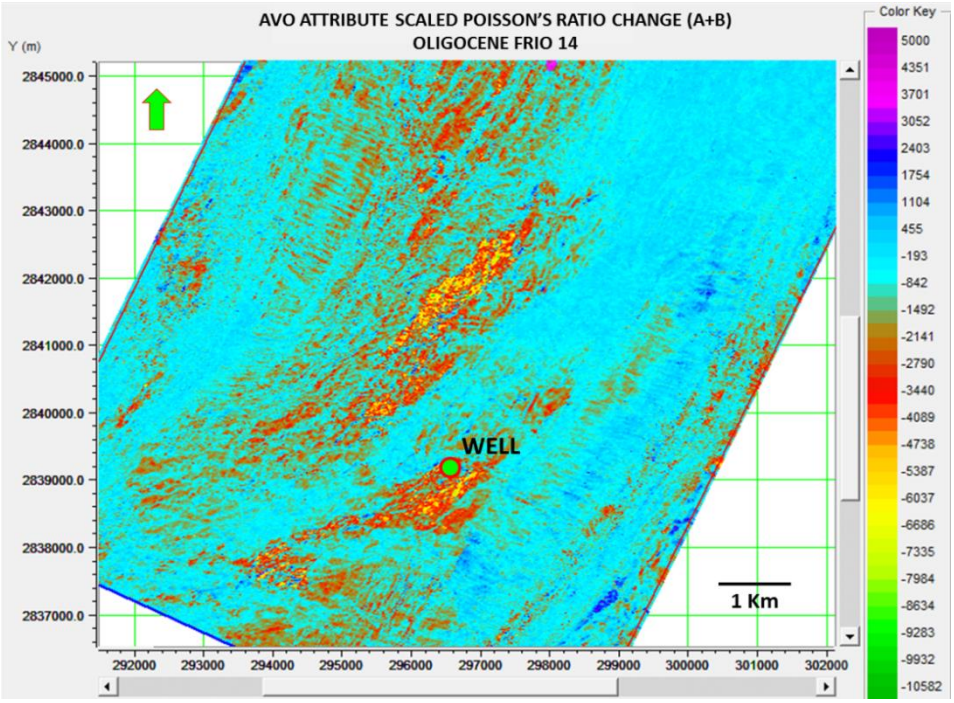

***Figure 64b**. AVO attribute of Poisson´s scaled ratio extracted in the sand Oligocene Frio 14, showing negative anomalies in potential areas to contain hydrocarbons*

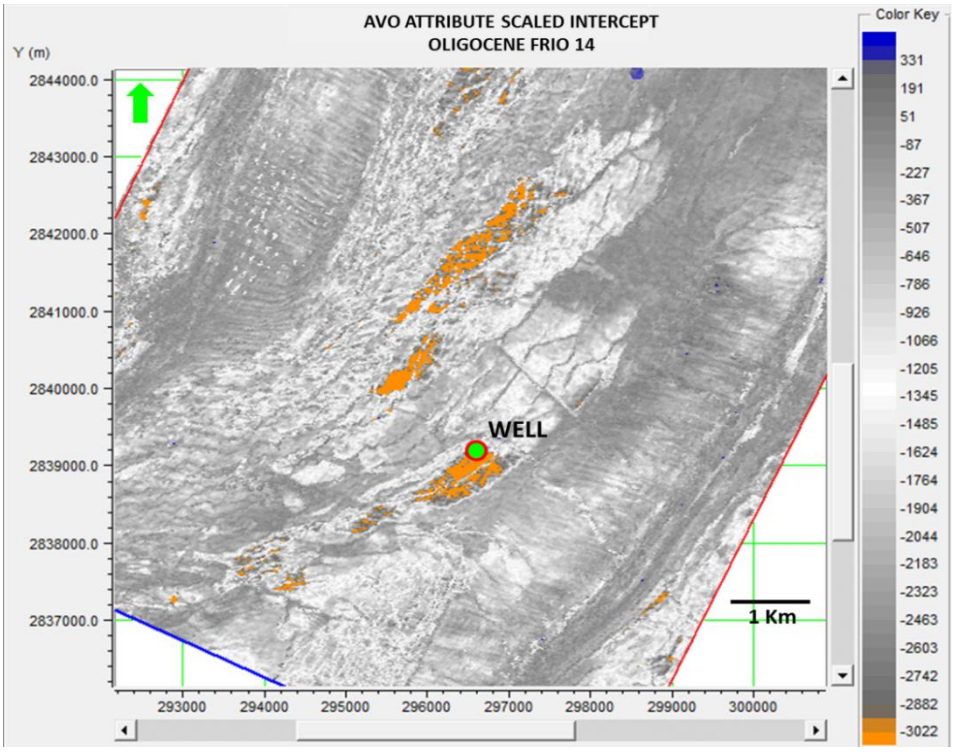

Figure 64c. *AVO attribute of Intercept extracted in sand Oligocene Frio 14, showing a normal faults system and negative anomalies associates to areas to contain higher hydrocarbon saturation.*

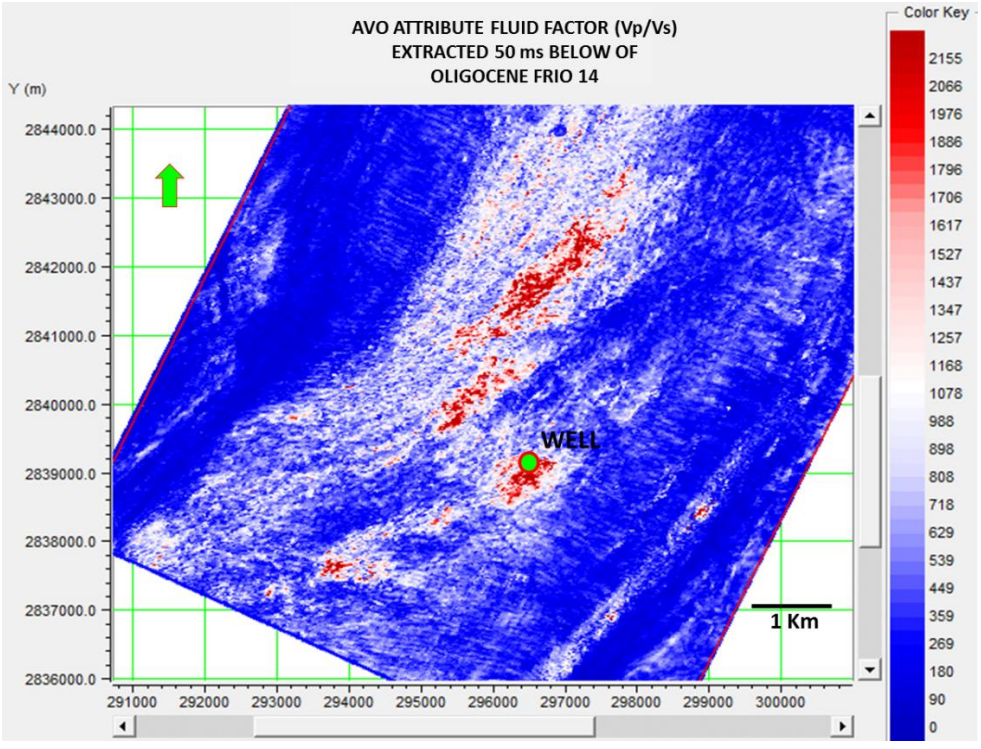

Figure 64d*. AVO attribute of Fluid Factor extracted in sand Oligocene Frio 14, showing a high reflectivity in potential zones to contain hydrocarbons.*

From figure 65a, I could observe that the attribute A*B shows a set of positive anomalies from medium to high amplitude. These anomalies create a channel pattern that cut the center of structure in orientation almost N-S. Along of this channel is evident that exist two zones with higher amplitude, which may be associated to higher hydrocarbon saturation, while that zones with medium amplitude may represent reservoir rock distribution. The figure 65b associated to the Poisson´s ratio attribute, shows a set of anomalies with the same geometry and amplitudes shown by the A*B attribute. In this case the high amplitudes represent negative values of Poisson´s ratio, which is associated with the presence of hydrocarbon according with its theory.

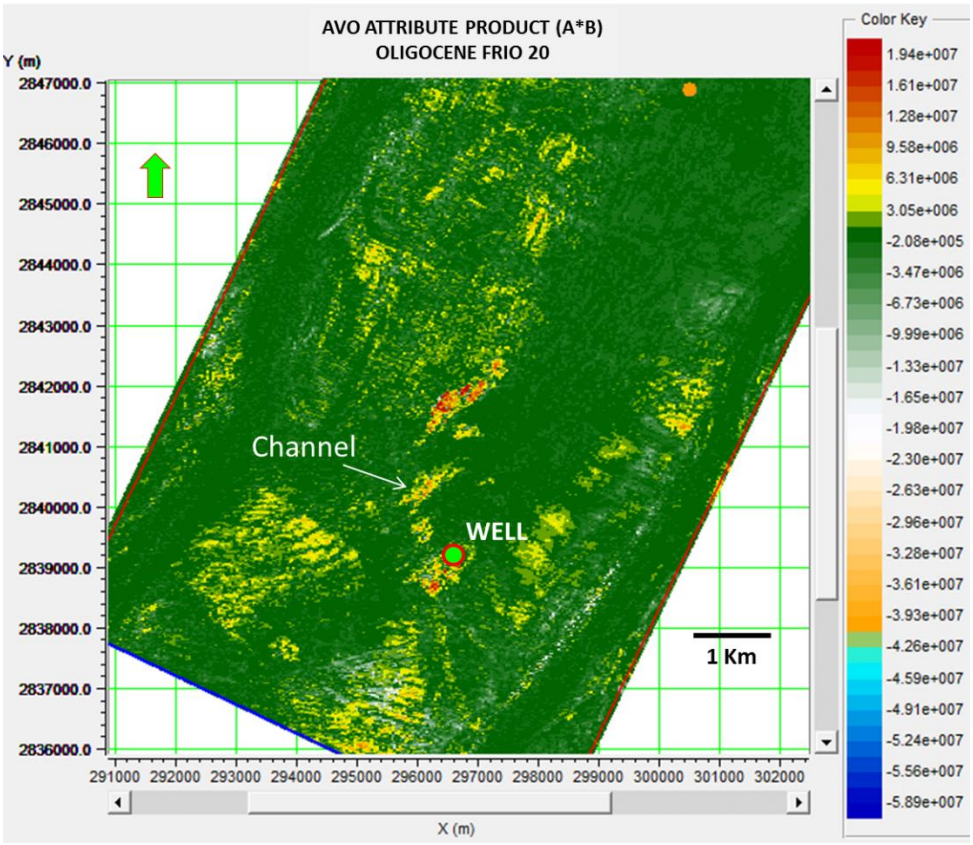

Figure 65a. *AVO attribute of product A*B extracted in the sand Oligocene Frio 20, showing a set of positive anomalies associated to channels facie with high expectation to contain hydrocarbons*

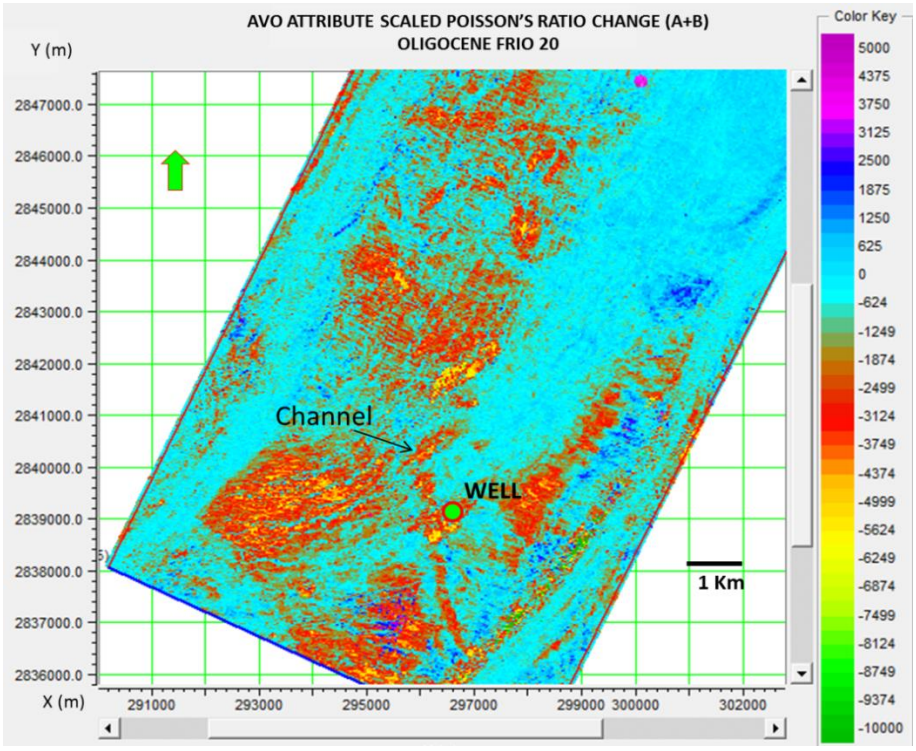

Figure 65b. *AVO Attribute of Poisson´s scale ratio, showing negative anomalies associated to channel system with high possibility to contain hydrocarbon saturation.*

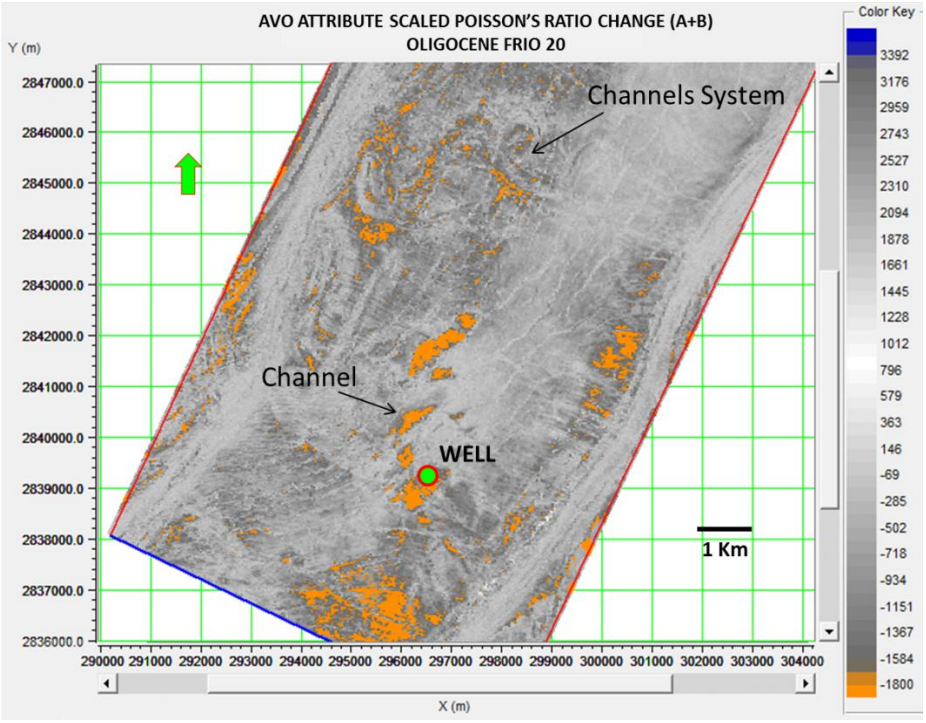

Figure 65c. *AVO attribute of Intercept, showing the distribution of channels system associated to negative amplitude anomalies in the center and north of structure*

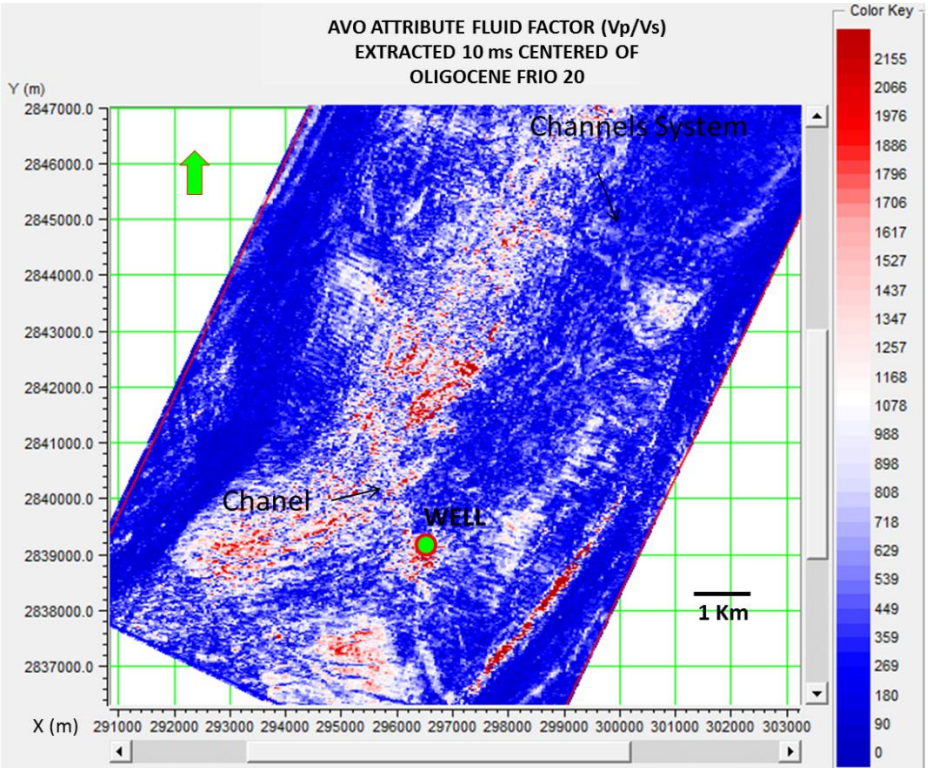

Figure 65d. *AVO attribute of Fluid Factor, showing anomalies with high reflectivity associated to channel facies in the center of structure.*

On the other hand, the result obtained by the Intercept attribute (figure 65c), shows a set of negative anomalies with high amplitude, mainly concentrated in the center and north of structure. This attribute helped to define the geometry of channels which represent the distribution of reservoir rock and potential areas to contain hydrocarbons. In addition, allowed define the faults pattern which interrupts the continuity of channels, producing a set of fragmented anomalies with high amplitude. Finally the Fluid Factor attribute (figure 65d), shows a set of anomalies with high reflectivity located in the center and north of structure, which coincide with the channels system and reservoir rock distribution previously identified by the other attributes.

Once extracted the AVO attributes in each horizon, I proceeded to generate an AVO cross plot along of well section by using the Poisson´s scale ratio attribute as reference. This cross plot was performed just in the interval of interest and taking into account the sands of Oligocene Frio 14 and Oligocene Frio 20. However, to perform this cross plot first was

necessary to establish a background trend. To establish this background an interval of shales was selected and plotted to later be used and integrated with the AVO cross plot focused in the interval of interest, allowing define and interpret better the AVO anomalies associated to lithological changes or hydrocarbon presence. The figure 66 shows the result of cross plot performed in the well section and the distribution of AVO anomalies contained in it.

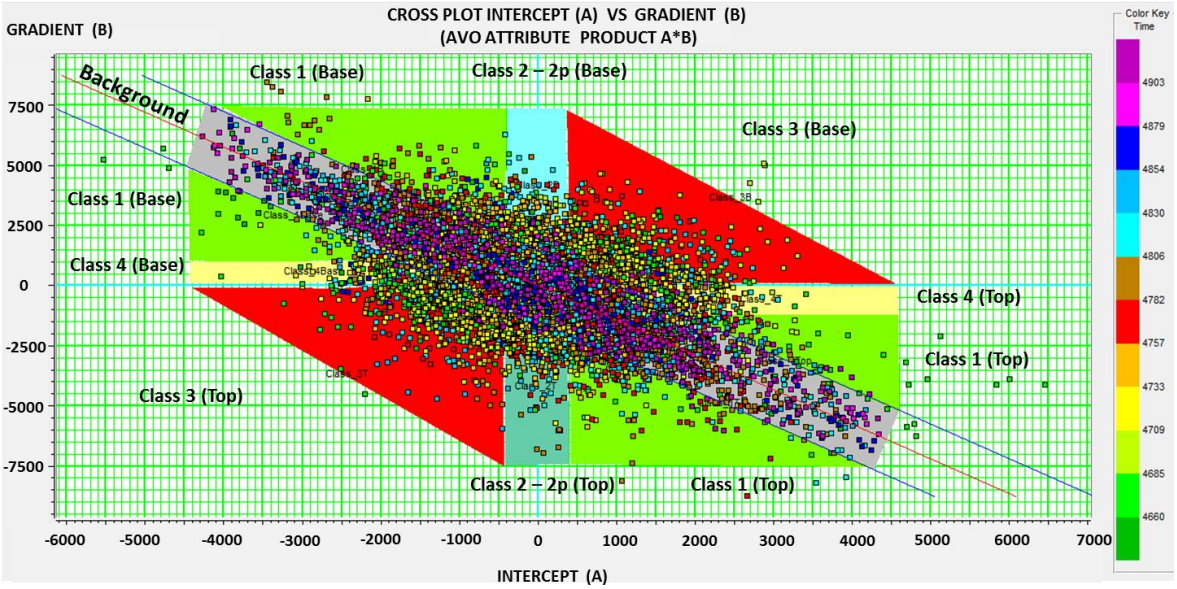

Figure 66*. Cross plot generated by using the Poisson´s scaled ratio as reference, showing the AVO anomalies distribution along of interval of interest.*

Finally, to establish in cross section the AVO anomalies distribution depicted by the cross plot, I proceeded to interpret such AVO anomalies taking into account the background trend, and the classification established by Rutherford and Williams, 1989 and Castagna, 1997. The figure 67, shows the representation in cross section of AVO interpretation realized in cross plot.

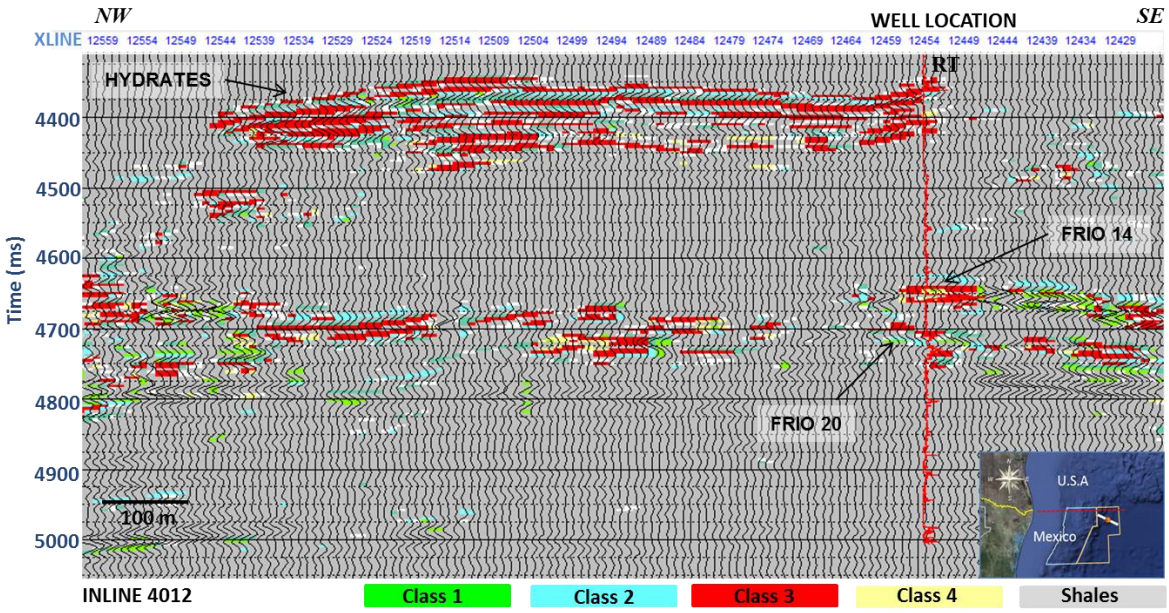

Figure 67*. Result of AVO represented in cross section. From this figure is evident that AVO class 3 is the most outstanding, mainly in the shallower reservoirs (hydrates zones and Oligocene Frio 14), followed by the AVO class 1 (associated to the upper interval of sand Oligocene Frio 20), while Classes 2 and 4 are distributed in small portions along of section.*

From figure 67, is evident how the AVO anomalies that most outstanding is the AVO class 3, which is concentrated in the shallow reservoirs associated with the methane hydrates and sands Oligocene Frio 14. Thereby, also is evident that toward deeper zones, mainly in the flanks of structure the most outstanding AVO is the class 1 where the sands Oligocene Frio 20 are located. On the other hand, the classes of AVO 2 and 4 are distributed in small portions mainly toward center of the structure. However, also is evident that these anomalies are attenuated by the presence of methane hydrates in shallower intervals. Therefore, taking into account this AVO analysis, the log modeling and well results is possible to have a relationship between the AVO classes and the hydrocarbon associated. Thereby, may be established that gas is the most common hydrocarbon and which is associated with AVO class 3, while oil may be represented mainly by AVO class 1 and sometimes for the rest of AVO classes (1 and 4).

4.7. Discussion and Results

I can conclude that the different interpretation techniques of AVO applied in this thesis work, allowed to describe and distinguish the different lithological composition and fluids contained in the reservoirs. On the one hand, the log modeling and synthetic gather performance allowed define the type of hydrocarbons and their relationship with the log and gather response, while that the pick and gradient analysis allowed define the type of hydrocarbons and their relationship with the amplitude response. On the other hand, with the AVO attributes application both in cross section and map, was possible to define spatially the lithological and hydrocarbons distribution. So, in based of the previous techniques applied I can describe the next results more briefly.

The results of log modeling obtained for the sand Oligocene Frio 14 showed a better fit with gas saturation. However the gas saturation for this interval was not higher than 40 percent. This sand also had a log response similar to original logs when it was saturated with 100 percent of oil. However to determine the correct fluid, was implemented a set of cross plot in this interval assuming different fluids saturations and compared with the cross plot of original logs and thus determine the correct fluid, in addition to consider the petrophysical evaluation .

On the other hand, the sands Oligocene Frio 20 and Oligocene Frio 26 showed a better fit with oil saturation, considering a saturation of 100 and 80 percent respectively. Other important feature defined by the log modeling, was that from 28 meters which constitute the sand Oligocene Frio20 (interval from 4700 to 4728) the lower part (interval from 4714 to 4728) showed a better fit with hundred percent of water saturation, while its upper part (interval from 4700 to 4714) showed a better fit with hundred percent of oil saturation, which highlight that only fifty percent of all sand interval may contain hydrocarbons.

The results of gradient analysis and AVO cross plot showed that the reservoirs Oligocene 14 and Oligocene 20 are associated to AVO class 3 and AVO class 1 respectively, while Oligocene Frio 26 did not show AVO response. On the other hand, the AVO analysis performed in the hydrates zones showed an AVO class 3, which point out that these areas

with high amplitude response may contain free gas saturation, in addition of presence of methane hydrates highly compacted, producing a strong contrast of acoustic impedance.

The result of AVO attributes analysis performed in the sands Oligocene Frio14 and Oligocene Frio 20, showed zones with high expectations to contain hydrocarbons due that they showed a high contrast of reflectivity between the sands with hydrocarbons and shales surrounding. The AVO attributes revealed also that the sands Oligocene Frio14, are associates a set of anomalies separated by normal faults, which makes this reservoirs has a strong structural influence. The AVO anomalies in this interval were more evident toward the center of structure and northern from the well. On the other hand, the Oligocene Frio20 showed a set of anomalies related with channel facies which cut transversally the structure. However these channel facies only showed AVO response in the channels closer to the well location. Thereby, I could conclude that the AVO analysis and the log based modeling was able to define the type of hydrocarbons involved in the reservoir and the geometry and distribution of reservoir rock associated at two different types of traps. However is important to highlight that to obtain these results, the correct gather conditioning and log edition, as well as the correct understanding of the cross plot and AVO attributes was essential.

V. SEISMIC INVERSION

5.1. LMR Inversion

Although the AVO analysis was able to define the potential areas to contain hydrocarbons, the seismic inversion contributed to know with more details the lithological characteristics and distribution of reservoir properties (porosity, lithology, saturations). In this work I performed two different types of seismic inversion: simultaneous inversion LMR and Elastic Inversion. The target of LMR inversion was to apply a methodology of seismic inversion which could complement and use the results obtained by the AVO analysis. So in that sense, with the seismic inversion LMR was possible to use the CDP´s gathers conditioned for the AVO analysis, which were inverted to extract the Lames´s parameters (λ and μ) and later converted in the form $\lambda\mu - \mu\rho$. Thereby, identify the distribution and potential areas to contain hydrocarbons and support the previous result delivered by the AVO. In addition, with this seismic inversion method was possible to obtain the elastic properties of the reservoir (density *(ρ)*, P-impedance *(Z_P)*, S-impedance *(Z_S)*, and V_P/V_S) and thus to know with more detail the reservoir conditions.

On the other hand, the elastic inversion was used as complement of LMR inversion as a secondary alternative, taking into account that the LMR works better in reservoir of gas and in this case I consider a reservoir with two different types of fluids (oil and gas) and two different types of stratigraphic traps.

In this chapter I begin with the description of the LMR inversion to later proceed to its application following a wok flow proposed by Hampson & Russell in 2010 for LMR method (figure 68). The first step in the work flow consisted in the conversion of CDP´s stack gathers to angle gathers. After I use the CDP´s angle gather, seismic horizons and input logs (V_P, V_S and density) to obtain an initial model. Once obtained the initial model I proceed to realize a pre-stack-inversion analysis to confirm the parameters to be used and thus, extract the correct wavelet taking into account far and near offsets. Then, I perform the LMR inversion with the established parameter and corresponding wavelets to obtain the

elastic properties of reservoir (P-impedances (Z_P), S-impedance (Z_S), density (ρ) and *Vp/Vs* ratio). Finally, I use the volumes V_P/Vs ratio and P-impedance (Z_P) to transform and produce the inverted volumes $\lambda\mu$ and $\mu\rho$.

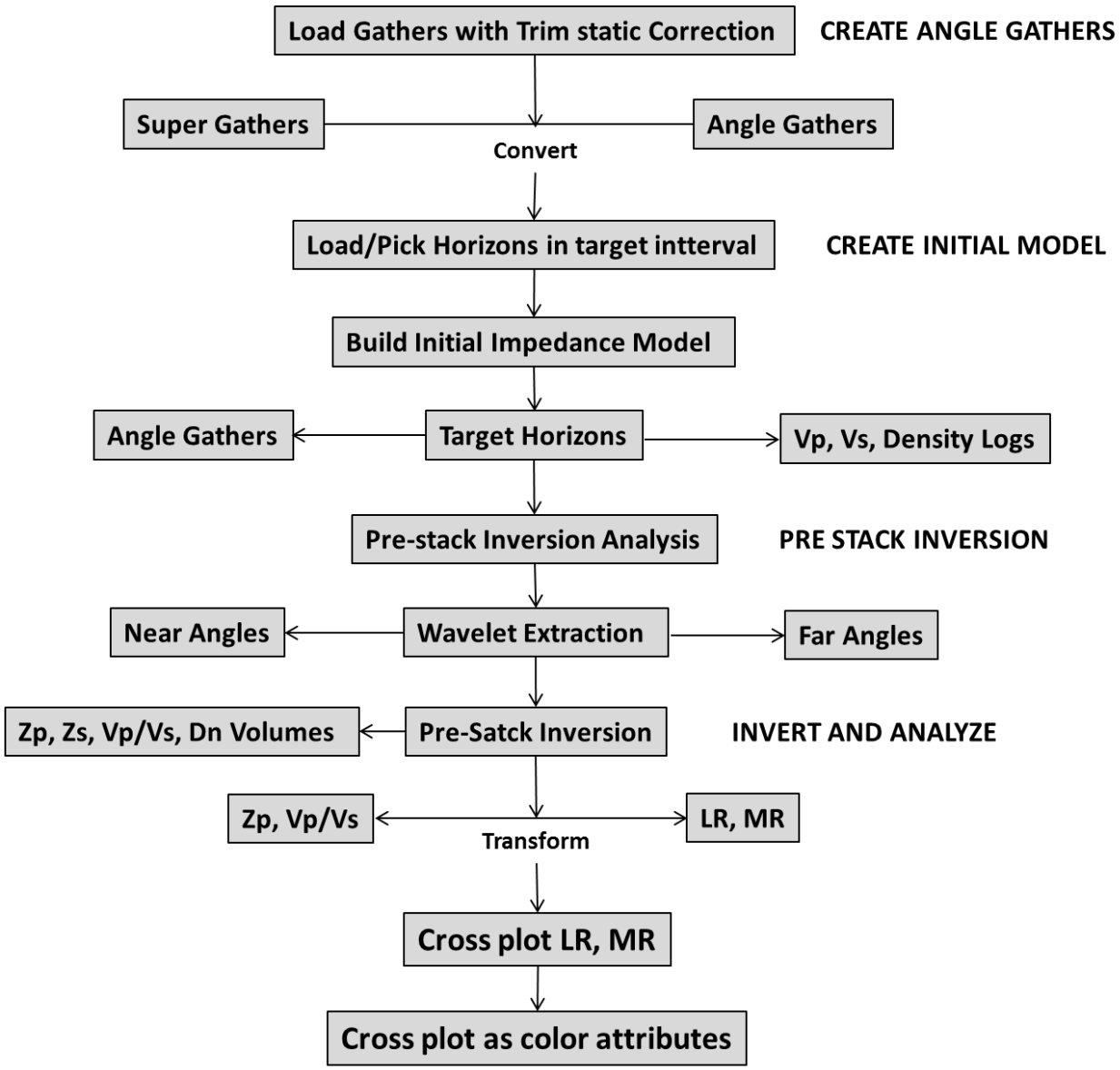

***Figure 68**. Workflow of seismic inversion LMR, which consist mainly of five main steps 1) the construction of initial model, 2) the pre-stack inversion model, 3) Perform of pre-stack inversion LMR, 4) Transformation to λρ and μρ domain and 5) crossplot to define hydrocarbon zones.*

5.1.1. Theoretical Background of Seismic Inversion

In the industry of Exploration and Production, several measures are based in the inversion process for their interpretation. The reason is simple, most of the seismic measurements used in seismic interpretation that include noises, and loss of energy cannot be solved with a unique signal. Hence, the seismic inversion is an alternative option which can be considered as a mathematical expression to estimate a response that verifies in function of observations and modifies until be acceptable [Barclay et al. 2008].

The inversion process can be considered as the inverse of forward modelling. This forward modelling often start with a model of subsurface properties, later simulates mathematically an experiment or physical process, which can be electromagnetic, acoustic, nuclear, chemical or optic. If modelling and assumptions are accurate, then the simulated response fits to the real data. The inversion process is frequently used for several disciplines in Exploration and Production, and it can be applied to several fields of searching with scales and levels of different complexity [Barclay et al. 2008].

The seismic inversion uses the arrival time and amplitude of seismic wave reflected in a reflection point in the subsurface, to later obtain the acoustic impedances of these reflector layers. This inversion method is often used in reservoir characterization to generate detailed models of subsurface properties [Barclay et al. 2008].

The first step of seismic inversion based in forward modelling, begins considering a model of layers with their depths, thickness, densities and velocities estimated from log of wells. The simplest modelling, which involve only velocities of compressional waves (P waves) and density, can be used to obtain by seismic inversion, the acoustic impedance of P waves. However, more than one type of rock with different reservoir quality and saturation can have the same P-wave impedance value. P-wave impedance represents the total effect of lithology, fluid and porosity [Hampson and Russell, 2006]. Consequently, it is difficult to separate the effect of these factors having only measurements of Z_P. To distinguish rocks types with the same Z_P but different lithology, porosity, or saturation, it is advisable to

introduce S-wave related properties. Adding S-wave information reduces the uncertainty in discriminating reservoir from non-reservoir rock

In the case of simple modelling, it combines with a seismic pulse to create a seismic trace modelled, called synthetic trace. The inversion process, takes a real seismic trace, removes the seismic pulse and creates a model of subsurface of trace (figure 69) [Barclay et al. 2008]. Most of inversion routines perform several iterations between the forwards modelling and inversion until get the better fit, trying to reduce the difference between the synthetic trace and the data.

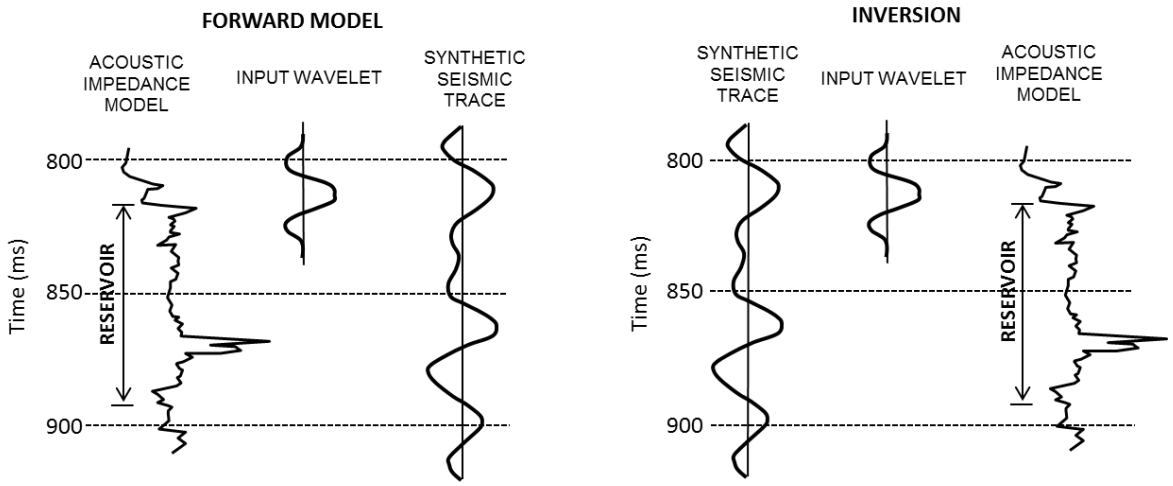

***Figure 69**. Modelling and inversion. The forward modelling (left), takes a model of subsurface acoustic impedance estimated from log of wells, combines with a seismic pulse (wavelet), and obtains as a result a synthetic seismic trace. The inversion (right) begins with a seismic trace recorded and removes the effect of a wavelet estimated, to create values of acoustic impedance in each sample of time. Taken and modified from Barclay et al. 2008*

In the practice, every one of these steps can be very complex and depend on the type of seismic data which are being inverted. In seismic data of vertical incidence, the creation of an initial model requires measurements of volumetric density obtained from density logs, and compressional velocities obtained from sonic logs, in the interval of interest. Then, the model of density - velocity is converted in a reflectivity model, which is represented by reflectivity between the amplitude of reflected wave and the amplitude of incident wave.

This parameter (reflectivity), relates with densities and velocities in each interface, trough of acoustic impedance contrast (2). The model resulting in depth scale is converted in a time model trough of velocities [Barclay et al. 2008].

The combination of the model in time scale with a seismic pulse creates a synthetic trace. Mathematically, this process is called "convolution" (1). The seismic pulse represents the energy generated by a seismic source. Then, is selected a model wavelet, which adjusted to characteristics of amplitude, phase and frequency of seismic data processed. The convolution between the seismic wavelet with the model of reflectivity gives a synthetic seismic trace, which represents the response of the subsurface [Barclay et al. 2008].

LMR Inversion

Today exist some methods which combine the AVO with the seismic inversion method to estimate the acoustic impedance of layers and thereby the properties of subsurface. One of these methods is the LMR inversion. The LMR method is an AVO inversion where CDP stack gathers are inverted to extract volumes of Lames's parameters (λ and μ), to later invert them in form $\lambda\rho - \mu\rho$. Goodway et al. (1997), believes that λ is very sensitive fluid indicator, so low values of these parameter could suggest hydrocarbons saturations. On the other hand, μ is more related as a matrix indicator, due it is insensitive to fluid saturation. In theory, sands will be associated with high values of μ, due the dominant mineral in the sand matrix is quartz, so it has a higher rigidity compare with shales. Therefore the combination of low values of $\lambda\rho$ and $\mu\rho$ suggest the presence of hydrocarbons bearing sand [Young et al. 2007].

The LMR inversion based on the Lame's parameters λ and μ, can be represented in function of ρ, taking into account the formulas for V_P and V_S described in the equation (3).

Therefore $$Z_S^2 = (\rho V_S)^2 = \mu\rho \quad (24)$$

and $$Z_P^2 = (\rho V_P)^2 = (\lambda + 2\mu)\rho \quad (25)$$

so $$\lambda\rho = Z_P^2 - 2Z_S^2 \quad (26)$$

5.1.2. LMR Inversion Analysis

The first step in the LMR inversion according with work flow depicted in figure 68, was the creation of an initial modeling. This modeling consisted first in the conversion of CDP gathers to CDP angle gathers by using of velocity function created during the gas – oil log modeling. Once obtained the angles gathers, I considered these gathers and three horizons focused in the interval of interest (Oligocene Frio14, Oligocene Frio20 and Oligocene Frio26), as well as the logs of density, shear sonic and compressional sonic as input parameters for build my initial model. The figure 70 depicts the gathers with trim static correction transformed to angle gathers, as well as the horizons and logs considered for the initial model construction.

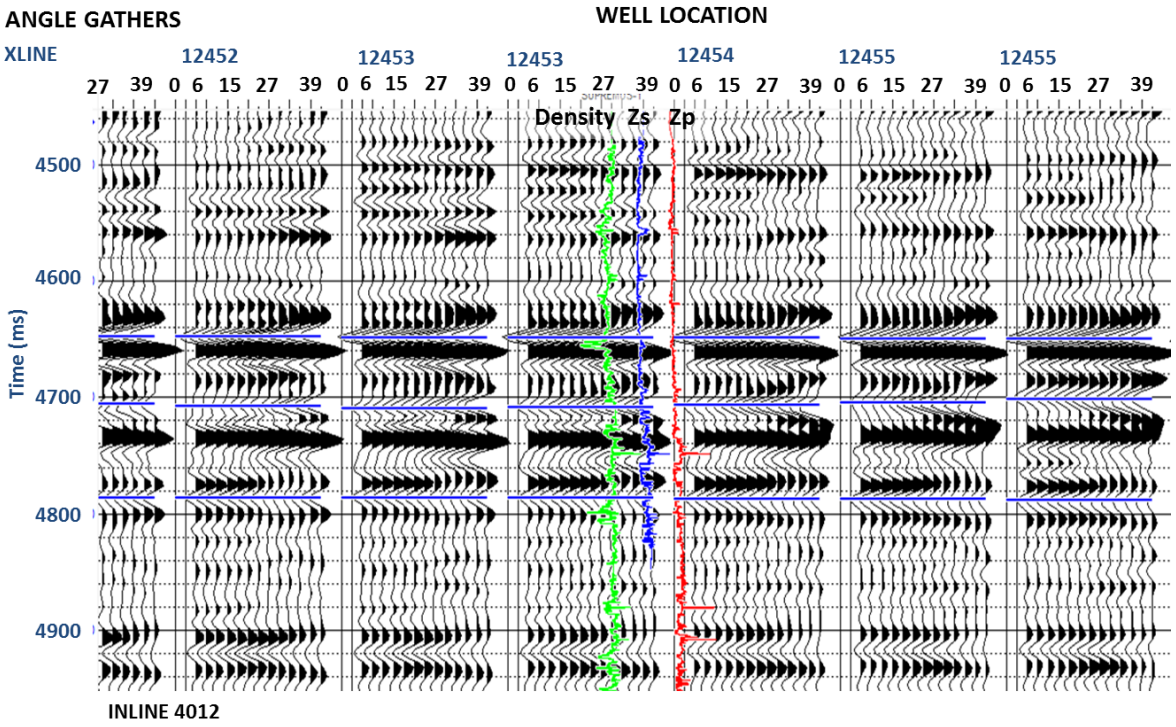

***Figure 70**. Angle gathers, seismic horizons and logs considered for the construction of pre-stack initial model, where the angle gathers show a maximum angle of 42 degrees*

From the figure 70, I could observe that maximum range of angles achieved for the CDP angle gathers was of 42 degrees, which was enough to perform the initial model. On the other hand, the input logs and horizons did not show any problem of noise and edition, so I proceeded to run the initial modeling. The figure 71 shows the result of the initial modeling. The initial modeling allowed obtain an initial acoustic impedance model taking into account the range of angles in the interval of interest, which will be used during the pre-stack analysis and final pre-stack seismic inversion. From this figure also is evident how the acoustic impedance increased according with depth, which may be considered as normal due to mechanical compaction.

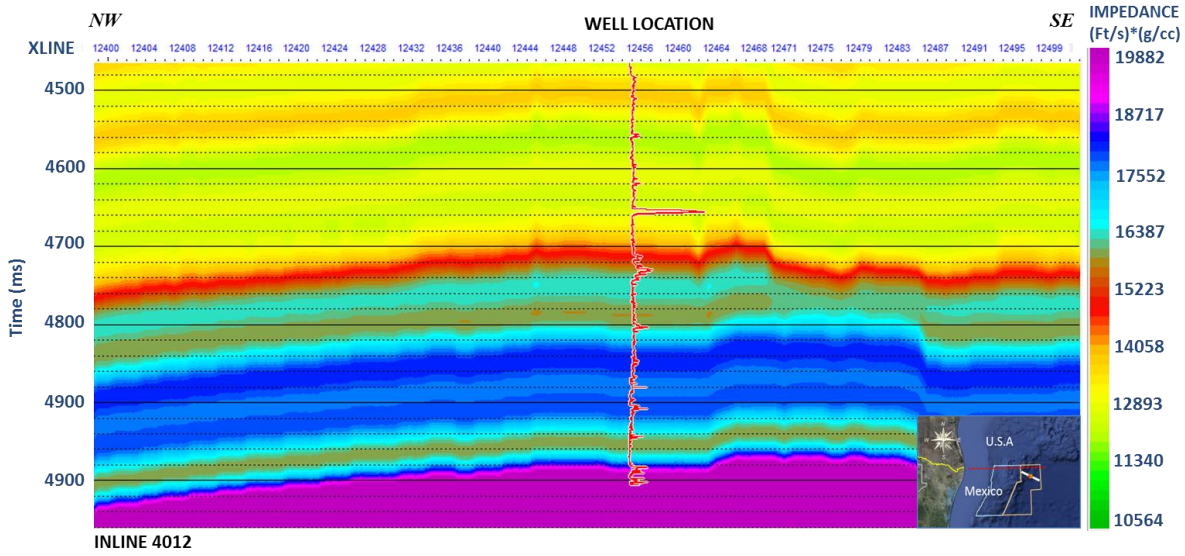

Figure 71. *Initial modeling of acoustic impedance performed for the pre-stack seismic inversion process.*

Once completed the initial modeling, a pre-stack inversion analysis was generated to confirm the inversion parameters and allow that program determines the proper scaling. To perform this, I use the initial modeling as input and two statistical wavelets extracted from the data. One extracted for near offset (0-21 degrees) and other for far offset (21-42 degrees). These wavelets were extracted, taking into account a seismic window of 350 ms focused in the interval of interest (4500 ms – 4850 ms). Also is important to mention that in this project the extraction of wavelet was performed with a maximum angle of 42 degrees, which was the maximum range of degrees achieved by the angle gathers.

The figure 72 shows the two wavelets extracted for near and far offsets, as well as their frequency spectrum. From this figure, I could observe that the wavelet extracted in near offset shows high amplitudes in frequencies around 35-45 Hz, while the wavelet extracted in far offset shows a wider range of high amplitude in frequencies between 25-45 Hz, so could be expected an improvement of amplitude response at far offset

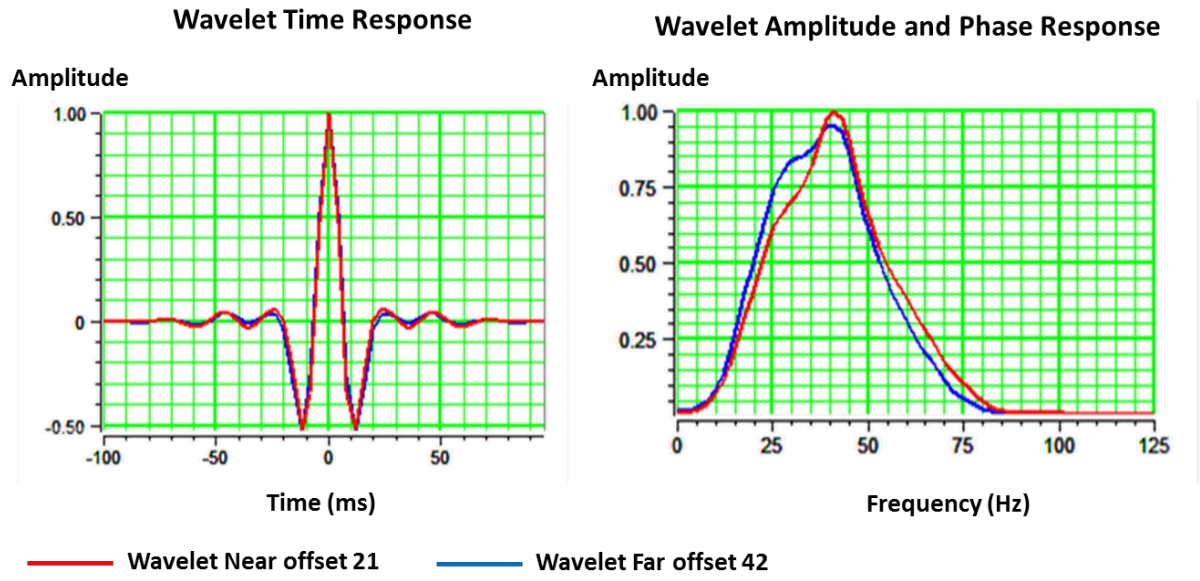

***Figure 72**, Result of wavelet extractions in near (0-21 degrees) and far offset (21-42 degrees).*

Once established the parameters for the initial model and the two wavelets extracted in near and far offsets, I proceeded to perform the pre-stack analysis. During this process the program calculated a set of regression coefficients for the acoustic impedance and density along of the well. These regression coefficients were corrected taking into account a slope that fits to values of density and acoustic impedance calculated by the program. The figure 73 shows the regressions coefficients calculated for the program for P-impedance (Z_P), S-impedance (Z_S) and density (ρ). Hence, is possible to see how the regressions curves show a good fit with the data after to be corrected manually.

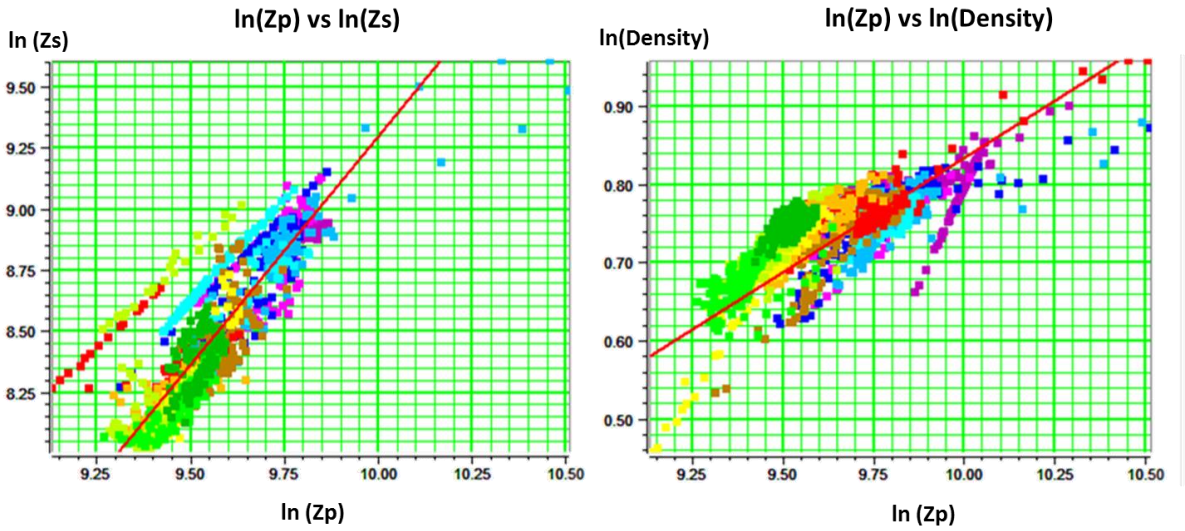

Figure 73*. Regression coefficients calculated for P-impedance (Zp), S-impedance (Zs) and density (ρ), showing a good fit with the regression lines after to be corrected manually.*

With the regression coefficient calculated, the program was able to process a trace inverted for P-impedance (Z_P), S-impedance (Z_S), density (ρ), and V_P/V_S ratio. The figure 74 shows the traces calculated by the program and their comparison with the real traces. From this figure is evident how each log traces calculated in the initial modeling (log traces in black color) and pre-stack analysis (log traces in red color) show a good match with the real log traces (log traces in blue color), which means that the input parameter are correct. On the other hand, the synthetic trace produced by the pre-stack inversion analysis showed almost a 98 percent of correlation with the real seismic traces, which was enough to perform the final inversion.

Finally once established the initial modeling and the pre-stack inversion analysis the final pre-stack inversion was performed taking into account as input the initial modeling result and the regression coefficient calculated for the P-impedance (Z_P), S-impedance (Z_S) and density (ρ). Thereby, a set of volumes inverted were generated such as P-impedance, S-impedance, density and V_P/V_S ratio, which are depicted in the figures 75, 76, 77 and 78.

The figure 75 depicts the density volume inverted, where is possible to identify three different packages of layers representing a geological unit with a specific range of density. These units of packages, according with the interpretation performed in the chapter 3

(seismic interpretation) are associated to different system of deposit along of geological time, where the upper unit was interpreted as Upper Miocene - Pliocene, the intermediate as Lower Miocene and the deeper as Upper Oligocene, which were assigned for this section as Unit 1, Unit 2 and Unit 3 respectively.

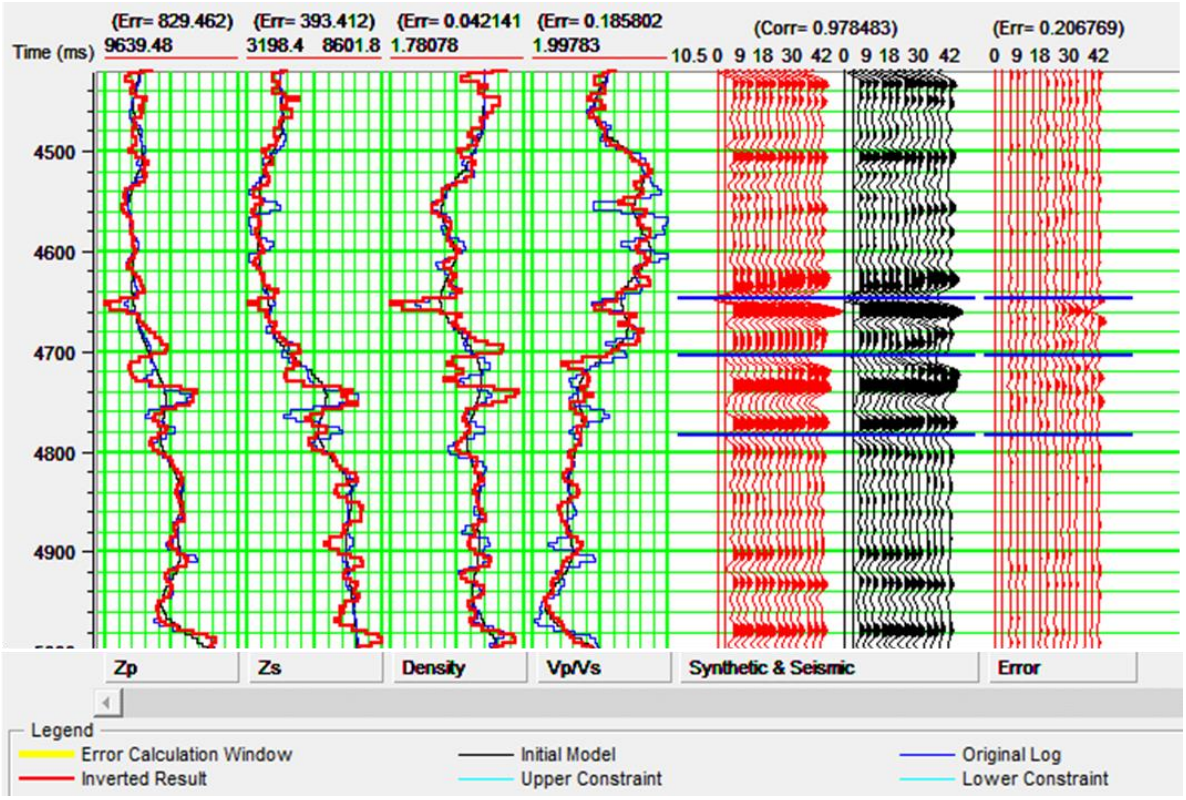

Figure 74*. Result of the pre-stack inversion analysis, showing a good fit between the initial inversion modeling, pre-stack inversion analysis and seismic trace correlation.*

The strong change in density shown in each stratigraphic unit could be interpreted as product of different lithological and mechanical composition in these units. In the stratigraphic unit 1, is possible to identify a zone with lower density associated to the anomalies distributed below of methane hydrates zone, mainly toward the base and weast portion of these bodies. While that in the stratigraphic unit 2, the zone with lowest density values is associated to the Oligocene Frio14 interval and slightly in the interval denominated "Miocene 1", which may be associated to the presence of fluids, regarding the AVO analysis. In the stratigraphic unit 3, is possible identify three layers with density reduction; one, in the top of the sand Oligocene Frio20 and other two in two layers around of sand Oligocene Frio26, being also more consistent throughout of structure.

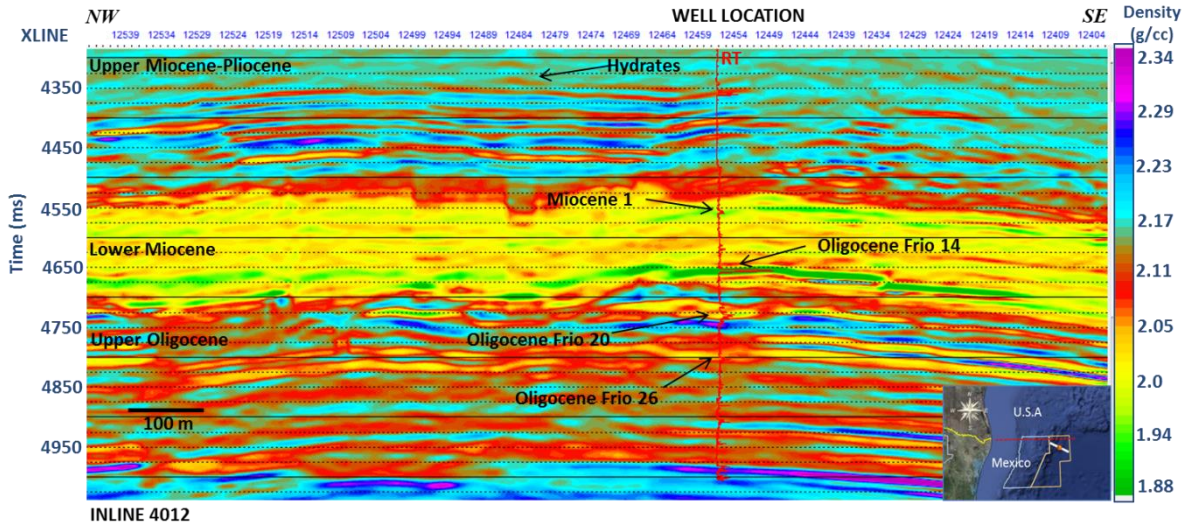

***Figure 75**. Density volume derived from the pre-stack seismic inversion.*

The figure 76, shows the inverted volume of V_P/V_S ratio. In this volume the stratigraphic unit 1 (Upper Miocene – Pliocene), shows a V_P/V_S reduction in the anomalies located below of methane hydrates zones. While that in stratigraphic unit 2 (Lower Miocene), is possible identify a V_P/V_S reduction in the sand Oligocene Frio14 and slightly in the interval denominated "Miocene 1". On the other hand, the stratigraphic unit 3 (Upper Oligocene) shows a slight reduction of V_P/V_S values toward the top of this stratigraphic unit and the area associated to the sand Oligocene Frio 20, although this is not well defined.

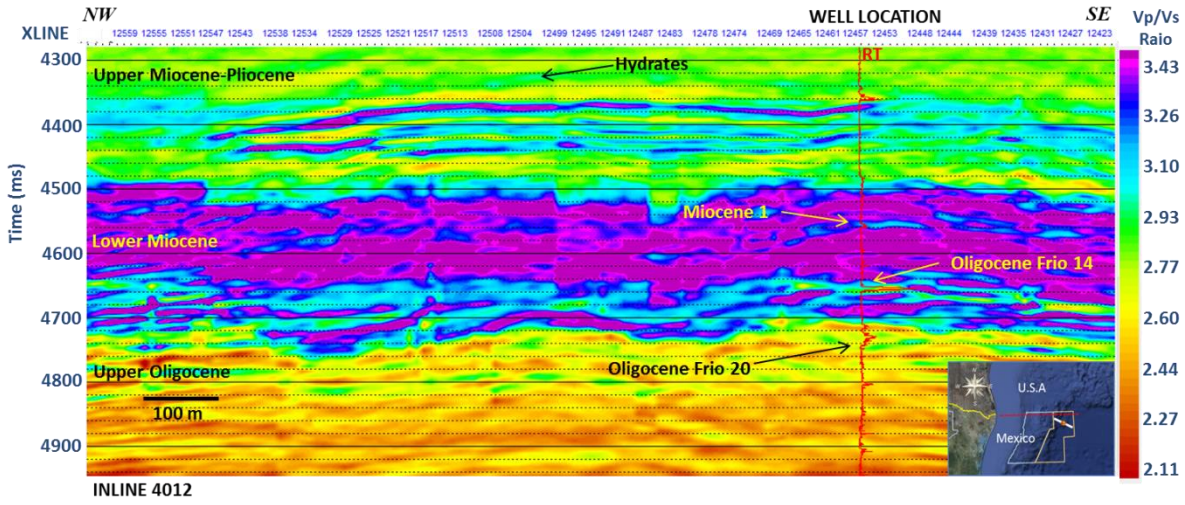

***Figure 76**. Inverted Volume of V_P/V_S ratio obtained as result of pre-stack seismic inversion.*

Finally the inverted volumes of S-impedance (Z_S) and P-impedance (Z_P) depicted in the figures 77 and 78, showed a response a bit similar mainly in the stratigraphic units 1 and 3. In the stratigraphic unit 1 (Upper Miocene – Pliocene) both volumes showed a reduction of acoustic impedances values in the top, west portion and base of the anomalies located below of hydrate methane zone, being more evident in the P-impedance (Z_P). For the stratigraphic unit 2 (Lower Miocene), the compressional acoustic impedance volume showed a reduction in the Oligocene Frio14 and slightly in the reflector "Miocene 1". This difference in responses may be pointing out a different degree of hydrocarbon saturation, being greater for the sand Oligocene Frio 14. In this unit the S-impedance (Z_S) showed a wider range of reduction compared with compressional impedance, which I interpret is associated to the presence of shales, being the response on shear acoustic impedance more sensitive for this lithology. On the other hand, for the stratigraphic unit 3 the interval that showed lower values in both Z_P and Z_S acoustic impedance was the Oligocene frio20 mainly in the top of this interval, although its base was represented by a high value, which I interpret is produced by the presence of water saturation in the reservoir. From these two volumes, is evident how the Z_S impedance volume was more sensitive to lithological changes, and Z_P impedance was more sensitive to fluid content defining better the intervals with more potential to contain hydrocarbons and water saturation.

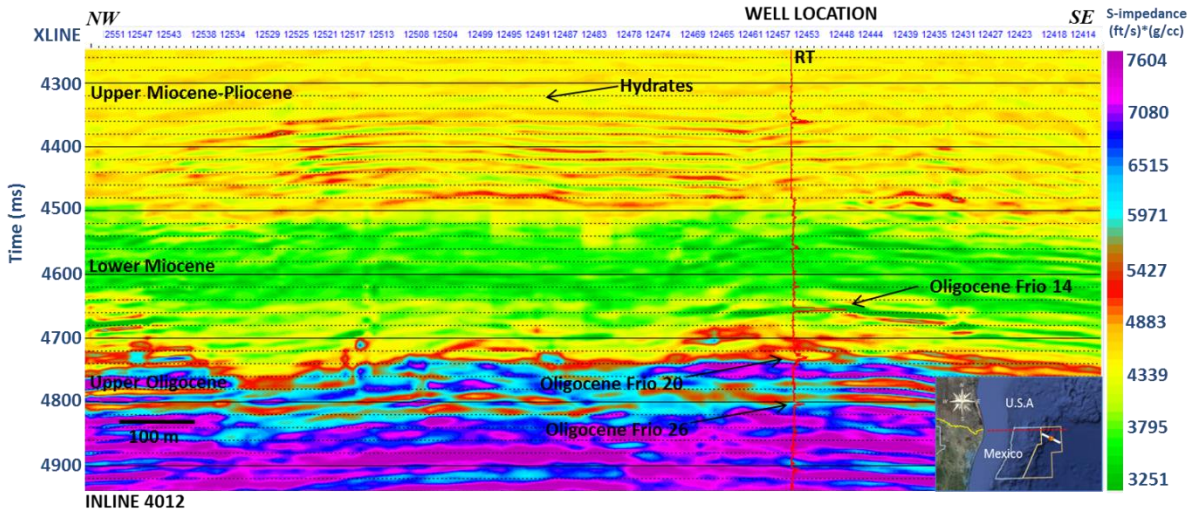

***Figure 77**. Result of pre-stack inversion for shear acoustic impedance (Z_S)*

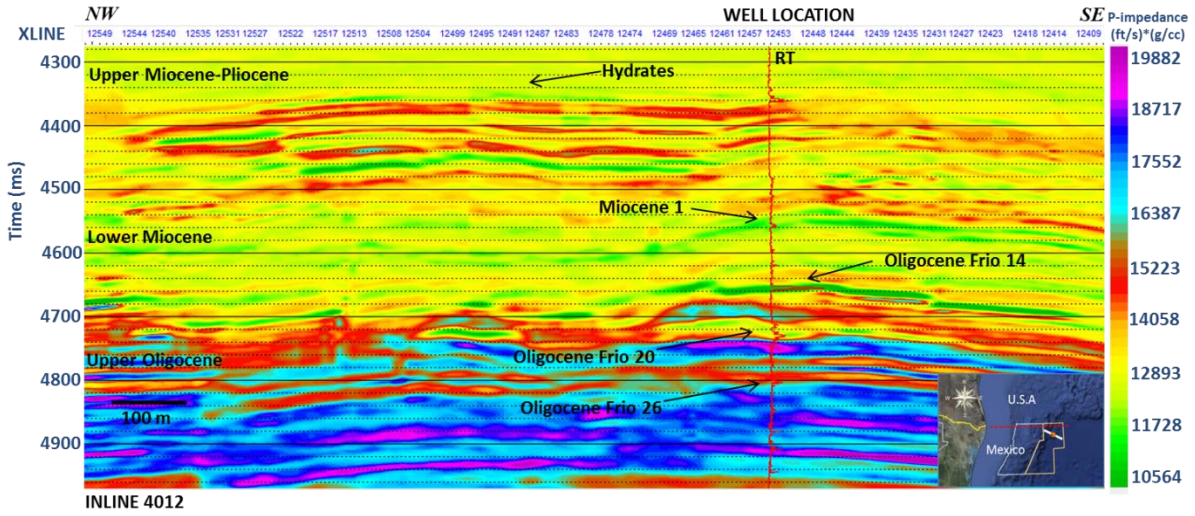

Figure 78. *Result of pre-stack inversion for compressional acoustic impedance (Zp)*

Once realized the pre-satck inversion, the next step was the transformation into LMR domain. To perform this, the volumes of P-impedance (Z_P) and V_P/V_S ratio were considered as input. Hence, the internal calculation generated for the program produces both volumes Lambda-rho and Mhu-rho which are represented in the figures 79 and 80 respectively. The Lamda-rho volume (figure 79) clearly shows the areas with low values in each stratigraphic unit. In the stratigraphic unit 1, this volume shows a reduction in the top, west portion and base of anomalies located below of methane hydrate zones, which may be produced by the presence of free gas with higher saturation. This result coincides somehow with the results of previous volumes (density (ρ), Z_P, Z_S, V_P/V_S ratio), which reinforce the interpretation derived for this unit. The stratigraphic unit 2, shows a strong reduction in Lamda-rho values in the sand Oligocene Frio14 and slightly in the sand "Miocene 1". These low values of Lamda-rho extend slightly toward the center of structure, being interrupted and displaced by the presence of normal faults. On the other hand, the stratigraphic unit 3, the zone that showed lower value was the sand Oligocene Frio 20, mainly in the top of this interval and a small portion toward the center of structure. Other feature that is important highlight in this sand is that in its lower interval, this sand showed a high increase of Lamda-rho values, which also is evident in other anomaly located in the center of structure. This increment of Lamda-rho may point out the presence of water saturation, taking into account the inverted volumes of density (ρ) and Z_P and the AVO analysis result.

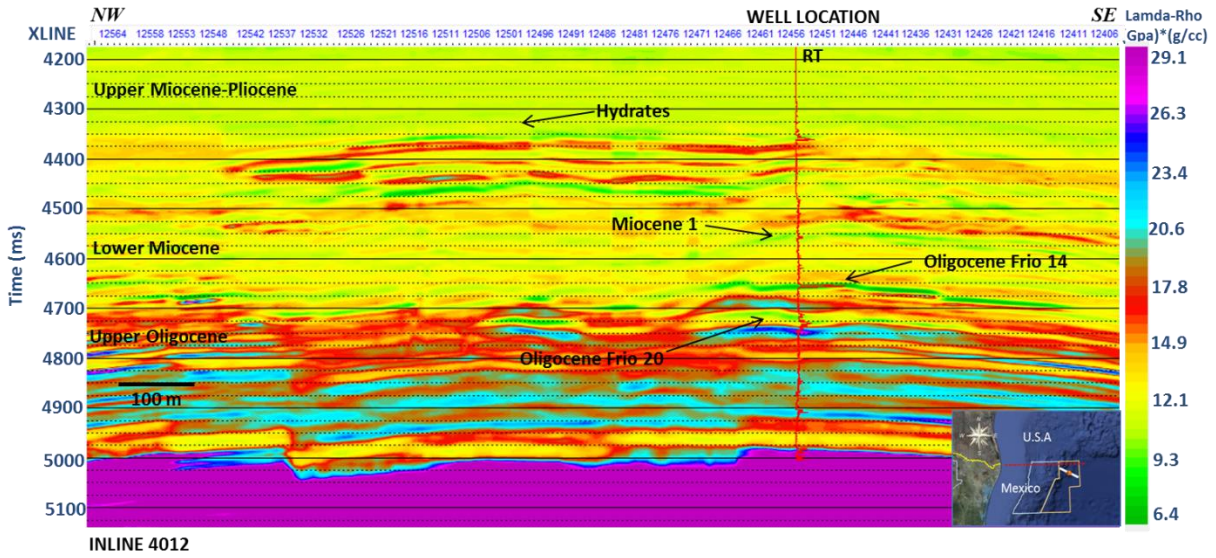

***Figure 79**. Volume obtained as a result of simultaneous inversion LMR, showing low values of Lamda-Rho associated to the possible presence of hydrocarbons.*

On the other hand, the Mhu-rho volume (figure 80), clearly shows the stiffness and compaction related with three different stratigraphic units interpreted in this section. The stratigraphic unit 1, is represented by a set of inhomogeneous layers with low values of Mhu-rho, which were deposited in laminar cycles due it shows slight alternations of deposit. The low values depicted in this stratigraphic unit may indicate low compaction and the presence of loose material. The stratigraphic unit 2, shows lowest values of Mhu-rho mainly toward the center of unit, which may point out this is the stratigraphic unit most shaly and homogeneous and representing the regional top seal for the sands Oligocene Frio 14 and Oligocene Frio 20 . On the other hand, the stratigraphic unit 3 shows highest Mhu-rho values, which point out this is the stratigraphic unit most compacted and sandy. Although the cyclic changes of Mhu-rho values also may point out presence of compacted shale between the sand layers. The Mhu-rho values are reduced toward the top of this unit, maybe associated to the presence of porous sands or less compacted.

Once interpreted and analyzed the volumes inverted LMR, the next step was to generate a cross plot between Mhu-rho and Lambda-rho, with the main purpose to have a better understand and analysis between fluids and lithological distribution in the reservoirs. The figure 81 shows the result of cross plot generated for Mhu-rho and Lambda-rho. This cross

plot clearly shows a linear trend toward lowest Lamda-rho and Mhu-rho values, which was interpreted as areas more porous and saturated by hydrocarbons. On the other hand, also is evident areas with relative high values of Mhu-rho and Lamda-rho, which were interpreted as less porous rocks and water saturated sands

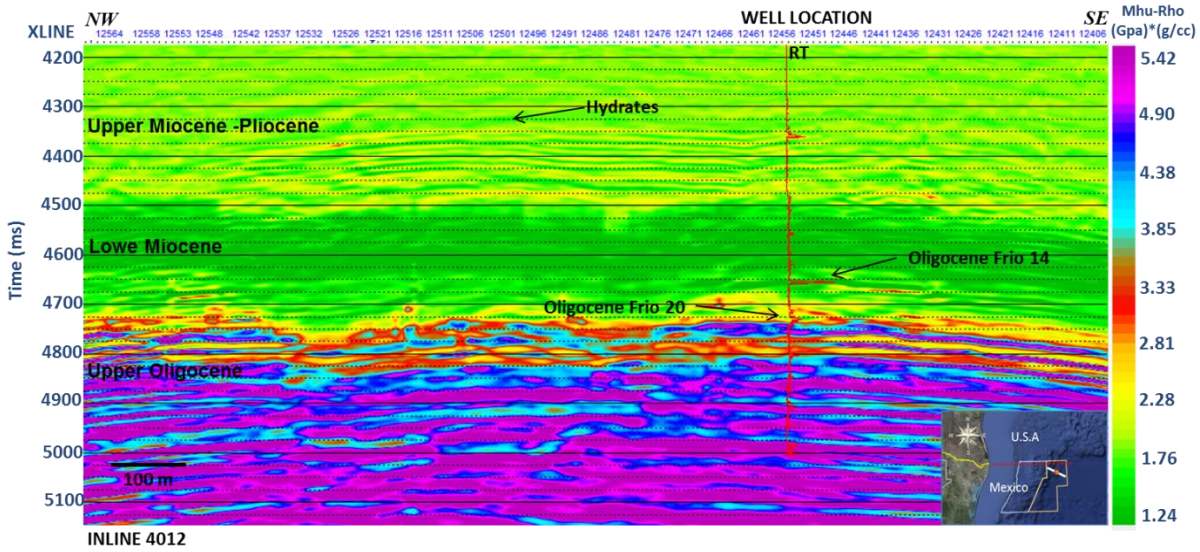

***Figure 80**. Volume obtained as a result of simultaneous inversion LMR, showing the values distribution of Mhu-Rho associated to lithological changes and compaction.*

The cross plot generated in the figure 81 also was represented in cross section, with the main target to highlight the areas with most expectation to contain hydrocarbons. The figure 82 shows the result of fluid distribution interpreted by the cross plot Lamda-rho vs Mhu-rho, where I could observe that the areas with higher possibilities to contain hydrocarbons are the Oligocene Frio14, hydrates zones and slightly in the Oligocene Frio 20. In this cross section also is evident that in the lower interval of the sand Oligocene Frio 20, the cross plot is showing areas with relative high values of Lamda-rho and Mhu-rho that was interpreted as water saturated sand, supporting the results derived by the log modeling and AVO analysis. However, is important highlight that cross plot Lamda-rho and Mhu-rho is not defining correctly the hydrocarbon presence associated to the Oligocene Frio20 sand. This may be due to the presence of two different types of hydrocarbons in the trend Lamda-rho and Mhu-rho. While Oligocene Frio14 is saturated by gas, the Oligocene Frio20 is saturated by oil, which could be manifested in distinct values of Lamda-rho and not be

represented correctly in the same trend. So, to solve this after will be applied other method of seismic inversion (Elastic Impedance) and which will be discussed later.

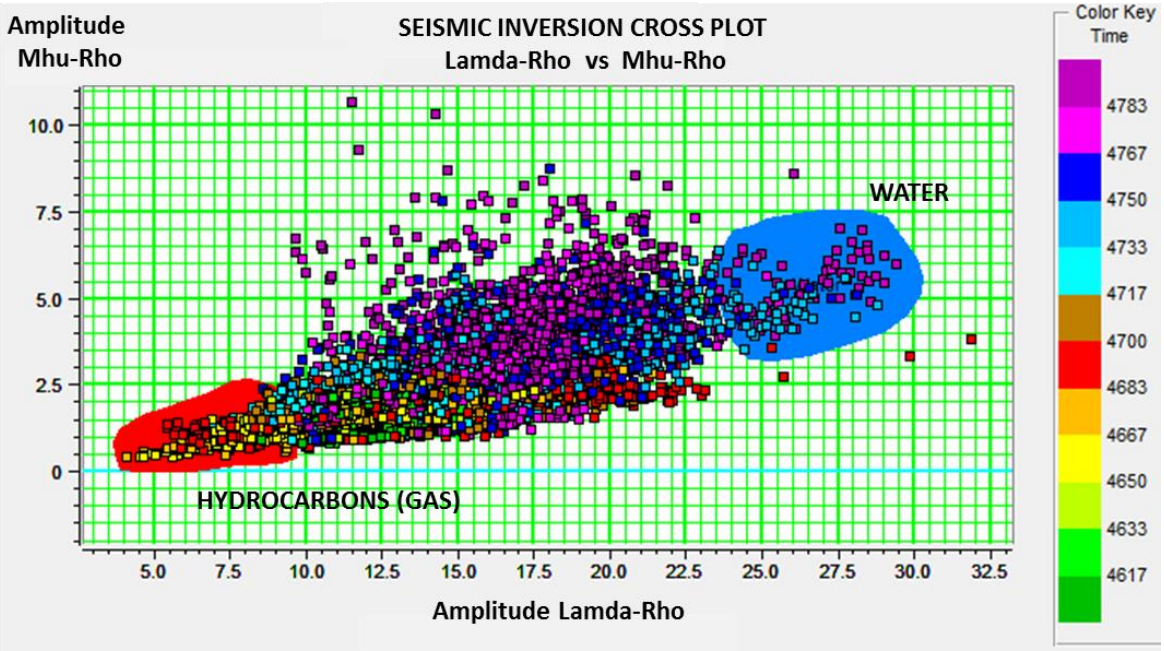

Figure 81. *Cross plot Lamda-rho versus Mhu-rho, showing the areas with high expectation to contain hydrocarbons and water saturated sands*

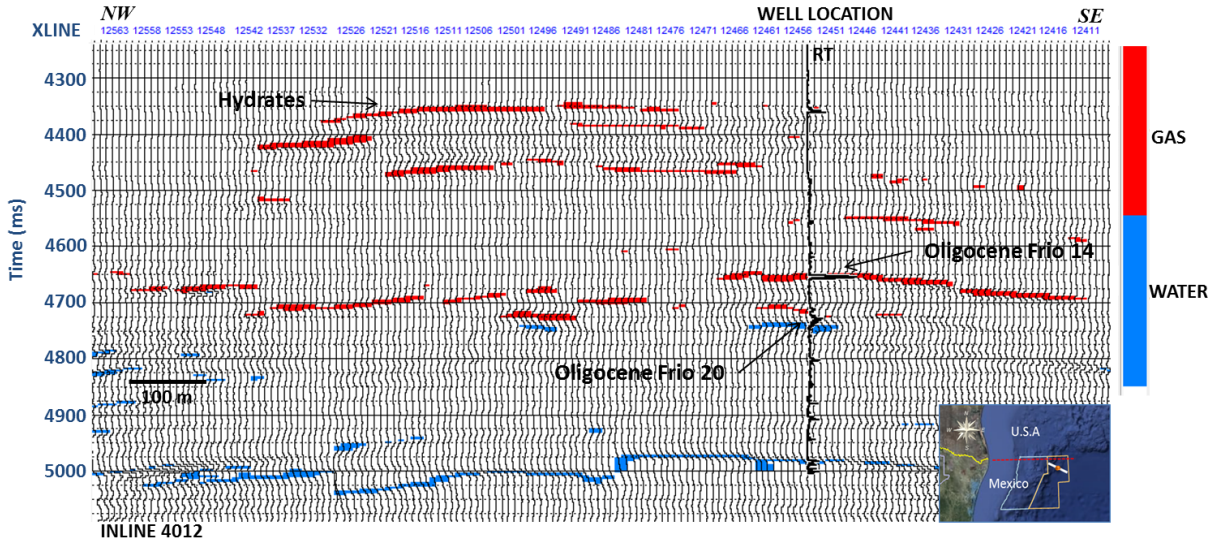

Figure 82. *Cross section showing the hydrocarbon distribution interpreted in the crossplot Lamda-Rho vs Mhu-Rho.*

Finally once performed the properties volumes and defined the areas with more potential to contain hydrocarbon, the next step was to represent the volumes result in each interval by using a set of attributes extracted in time slices

The figures 83a, 83b, 83c, 83d show four of the most representative maps of geological properties (density (ρ), P-impedance (Z_P), V_P/V_S ratio and Lamda-rho) derived of LMR inversion, and which were extracted in the sand Oligocene Frio14. Thereby, is evident how each attribute showed a reduction in their values towards the top of structure. These anomalies are limited by normal fault blocks generated by gravitational collapse in the crest of structure, which continue their distribution to the north of well. The integrated interpretation of these attributes represents the size and distribution of gas saturated sands taking into account the cross plot Lamda-rho and Mhu-rho, as well as the integration of log modeling result and AVO analysis. However, in some cases this set of anomalies also represent the rock reservoir distribution although in this sense these have slightly lower magnitudes that the areas with hydrocarbon saturation.

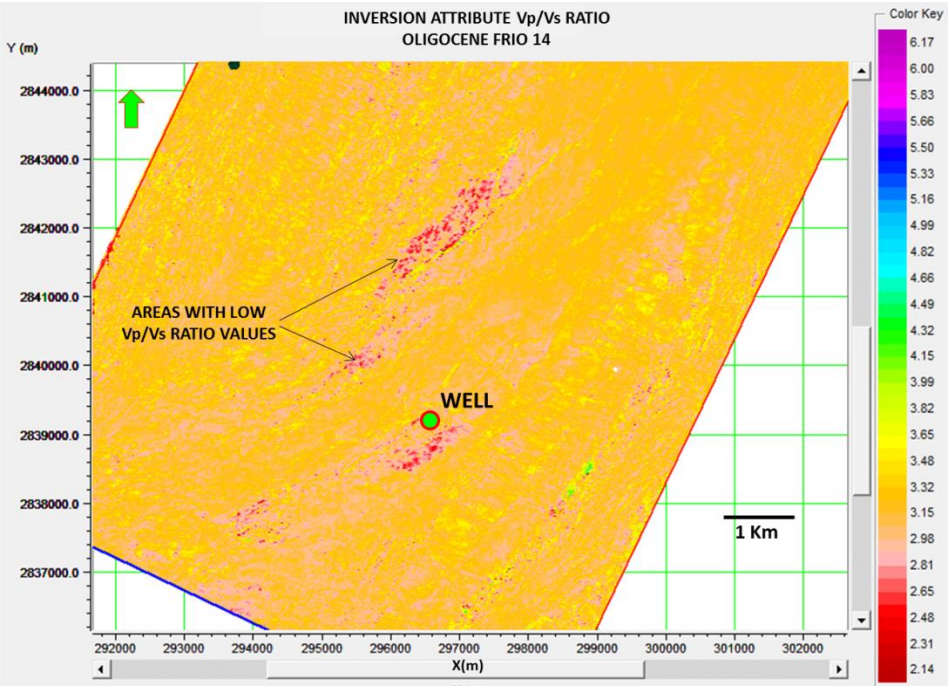

***Figure 83a**. Map of distribution of V_P/V_S ratio generated in the interval Oligocene Frio14, as a result of simultaneous inversion LMR.*

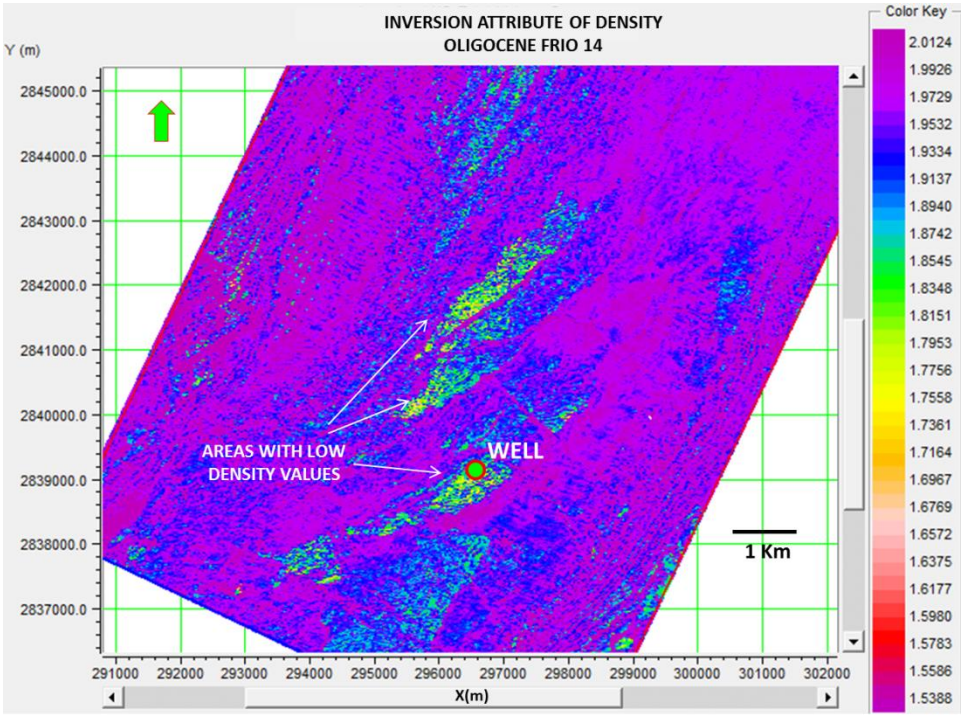

Figure 83b. *Map of distribution of Density generated in the interval Oligocene Frio14, as a result of simultaneous inversion LMR.*

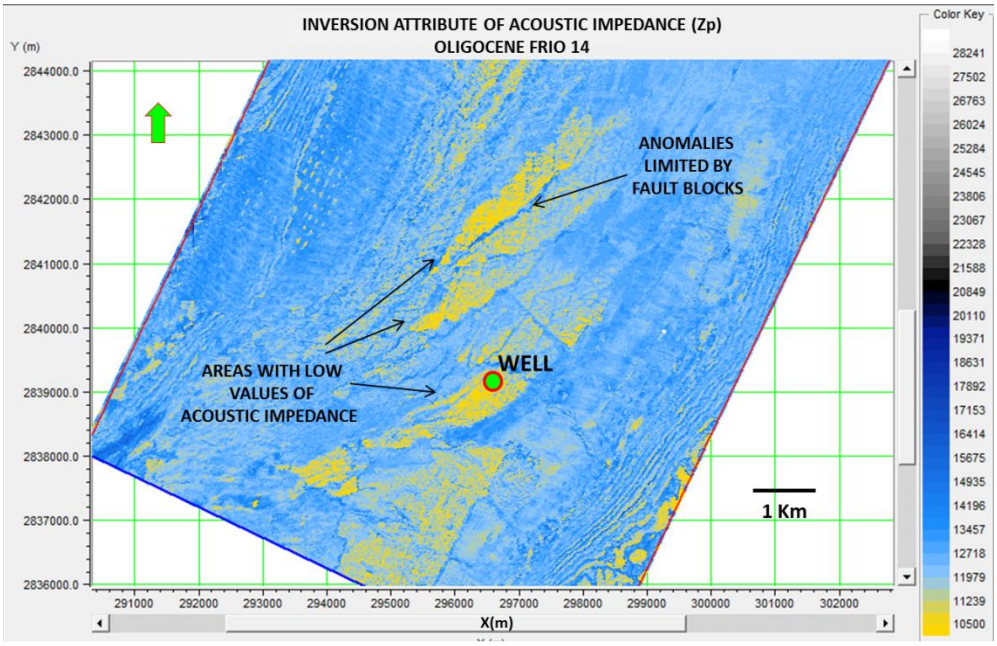

Figure 83c. *Map of distribution of Acoustic Impedance generated in the interval Oligocene Frio14, as a result of simultaneous inversion LMR.*

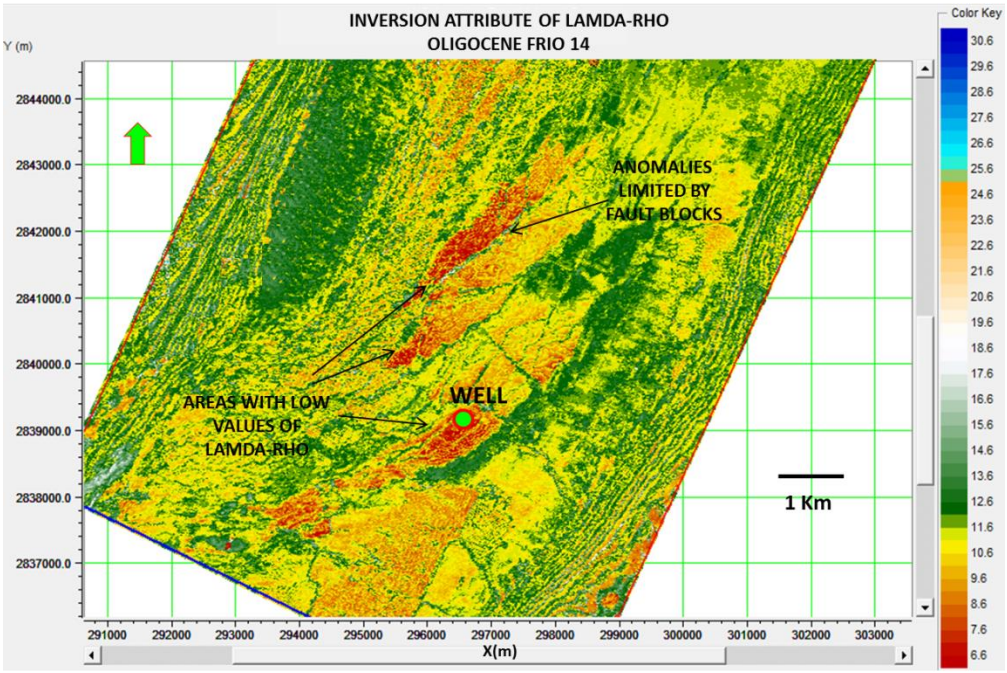

Figure 83d. *Map of distribution of Lamnda-Rho generated in the interval Oligocene Frio14, as a result of simultaneous inversion LMR.*

The figures 84a, 84b, 84c and 84d show the property maps (V_P/V_S, density (ρ), P-impedance (Z_P) and Lamda-rho) generated in the sand Oligocene Frio 20. Thereby, is also evident that although the V_P/V_S ratio does not show a significant reduction of their values the others attributes do, indicating the distribution of hydrocarbons. These anomalies follow the geometry of a channel system which comes across the structure in almost direction North-South, showing highest amplitude response towards the top of structure which could be associated a higher hydrocarbon saturation taking into account the integration of these attributes, log modeling result and AVO analysis. In the zones where Lamda-rho are relatively less low, these zones may be associated with the presence of reservoir rock, in other words porous sands but maybe with low hydrocarbon saturation.

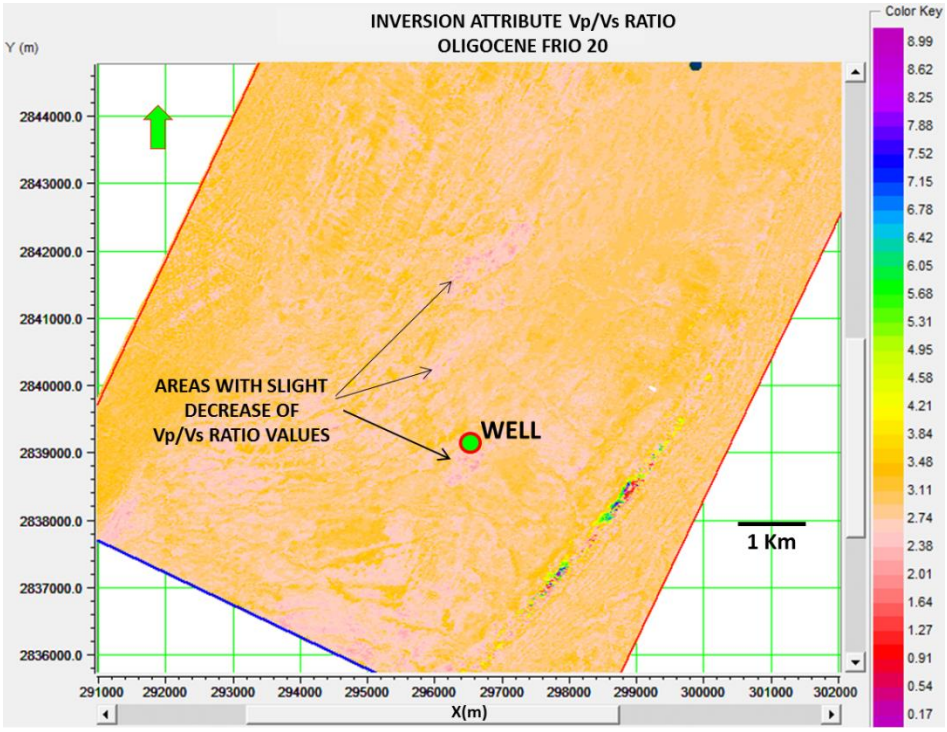

Figure 84a. *Map of distribution of V_P/V_S Ratio extracted in the interval Oligocene Frio20, as a result of simultaneous inversion LMR.*

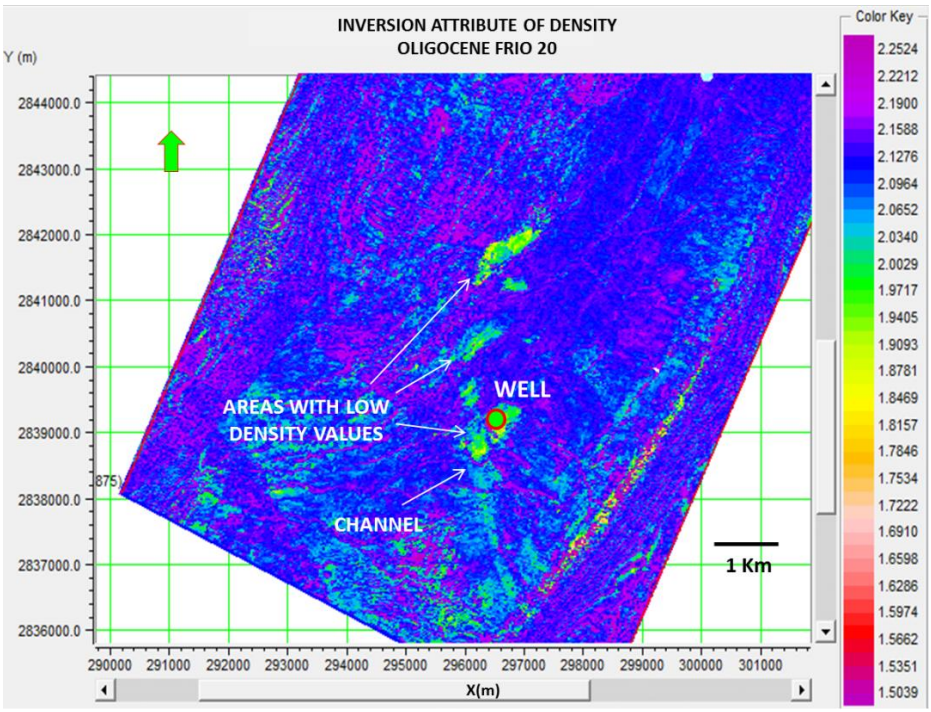

Figure 84b. *Map of distribution of Density extracted in the interval Oligocene Frio20, as a result of simultaneous inversion LMR.*

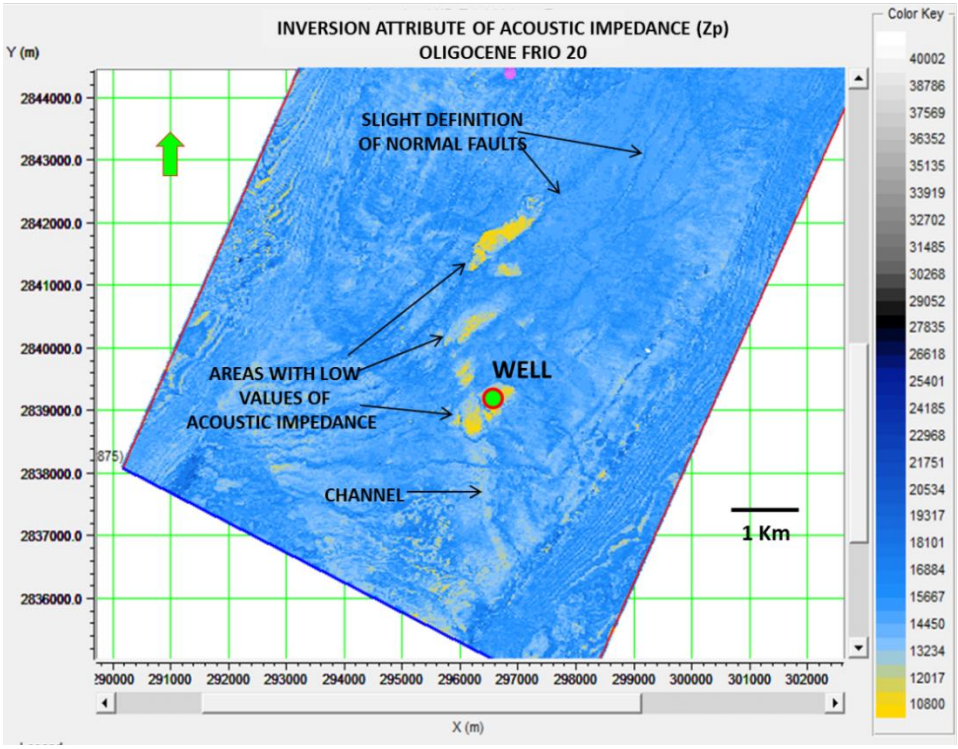

Figure 84c. *Map of distribution of Acoustic Impedance extracted in the interval Oligocene Frio20, as a result of simultaneous inversion LMR.*

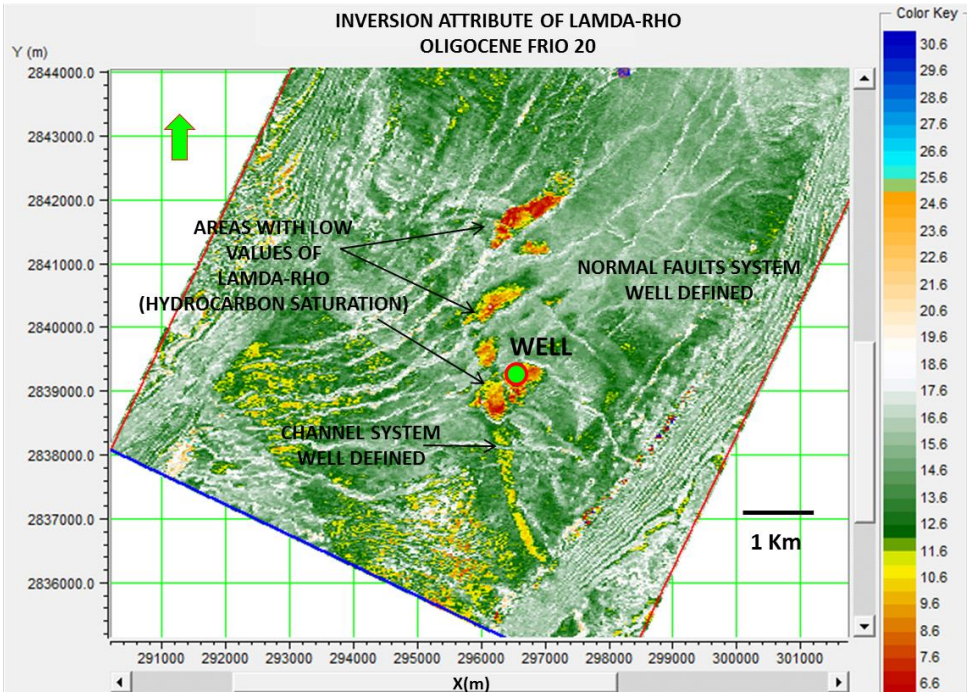

Figure 84d. *Map of distribution of Lamda-rho extracted in the interval Oligocene Frio20, as a result of simultaneous inversion LMR.*

5.2. Elastic Impedance Inversion

Once obtained the results of simultaneous inversion LMR the next step was to perform the Elastic Impedance inversion. This process consisted in the creation of elastic impedance volumes at specified angle ranges. To do this, first was necessary the calculus of Elastic Impedance logs to later be used them to create Elastic Impedance earth models and thus derive the final EI inversion volume. The figure 85 shows the workflow followed to realize this inversion method.

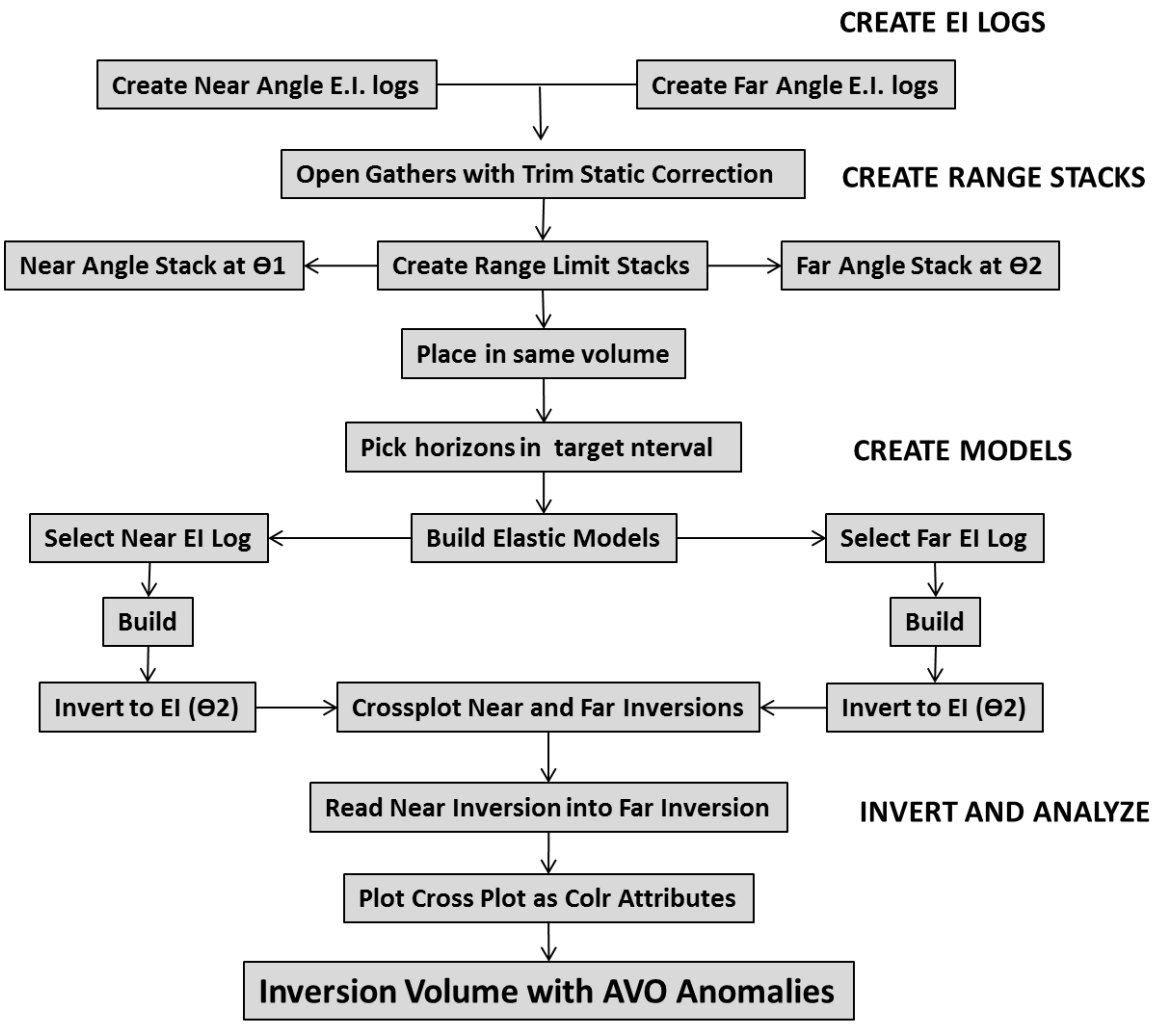

Figure 85*. Workflow performed during the implementation of elastic impedance inversion, which consisted of four main steps: the creation of EI logs, creation of range limited stacks, construction of EI model and finally the derivation of the final EI inversion volume*

5.2.1. Theoretical Backgrounds of Elastic Impedance Inversion

The most common limitation with conventional post-stack inversion is that it is only valid for a zero-offset experiment. So, if we want to apply a post-stack inversion in far offset the assumption is not valid anymore. In 1998 Connolly introduced a quantity called elastic impedance. Where the basic assumption behind of this concept is that, the reflection coefficients at non-zero incident angle should be expressed in the same way as for zero offset. The Connolly method is based on Shuey´s form of Aki-Richards equation (14), which can be used to invert data with AVO effect by using angle stacks for a range of incident angles (essentially a partial far-angle stack). The basic idea behind of Connolly method is that the reflection coefficient at non-zero incident angle should be written in the same way as for zero offset (2) [Landro et al. 2012].

$$R(\theta) = \frac{EI_i - EI_{i-1}}{EI_1 + EI_{i-1}} \tag{27}$$

Where:

EI_i =Elastic impedance; $R(\Theta)$ = Reflection coefficient to incident angle

Because the equation (2) is the same as (27), it means that if we use the conventional post-stack inversion at far offset stack, the quantity we get out is elastic impedance. In conventional post-stack inversion, a well tie is an import issue, due it links the well information with seismic data, allowing establish an explicit expression for elastic impedance as a function of acoustic parameters measured from a well log [Landro et al. 2012]. Based on Shuey´s form from Aki-Richard equation (14), Connolly derived the following expression for elastic impedance:

$$EI = V_P^{\left(1+\tan^2\theta\right)} V_S^{\,-8KSin^2\theta}\, \rho^{\left(1-4KSin^2\theta\right)} \tag{28}$$

Where:

V_P = P wave velocity; V_S = S wave velocity; ρ = density; $K=V_P^2/V_S^2$

The basic assumption in Connolly equation is that elastic impedance should play the same role for angle dependent reflectivity as acoustic impedance for zero offset reflectivity. If the condition is fulfilled is possible apply post stack inversion schemes on far offset stacks. So for an incident angle equal to zero, the elastic impedance is equal to the acoustic impedance [Landro et al. 2012].

5.2.2. Elastic Impedance Inversion Analysis

The first step in the EI inversion consisted in the generation of EI logs. These logs were created by using the compressional sonic, shear sonic and density logs as input in the Hampson & Russell program and taking into account the Connoly equation for elastic impedance (28). In this case, the EI logs were created regarding near and far offsets, where angles of 10 and 30 degrees were considered by each of these logs respectively. The figure 86 shows the results of EI logs both far and near offsets and their correlation with conventional logs (GR, Resistivity, P-wave, S-wave and density).

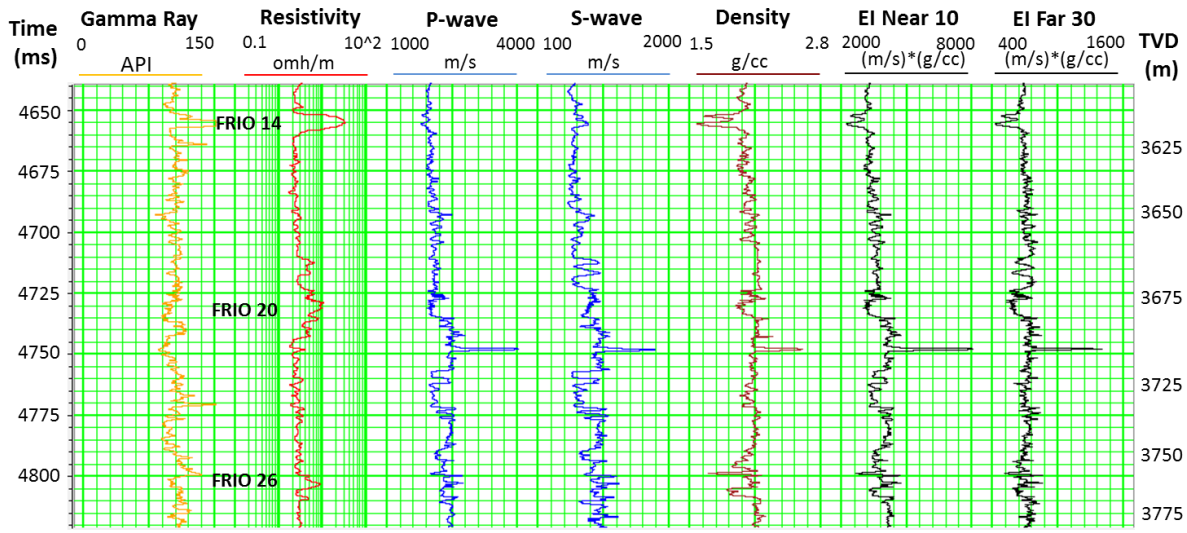

Figure 86. *EI logs derived for near (10) and far (30) offsets and using the Connoly equation. Thereby, is evident the reduction in elastic impedance values in the reservoir zones.*

Once created the EI logs the next step was to create the range limit stacks by using as input the CDP gathers with trim static correction and the velocity function derived from the log modeling. These CDP range limit stacks were created taking into account near and far

offsets of 10 and 30 degrees respectively such as the EI logs. The figure 87 shows the result of range limit stack gathers both near offset (figure 87a) and far offset (figure 87b). Hence, is evident that the amplitude response displayed to CDP stack gathers in far offset shows a cleaner section with slight increase of amplitude response mainly in the areas with possible presence of hydrocarbon (Oligocene Frio14, Oligocene Frio20 and hydrates zone).

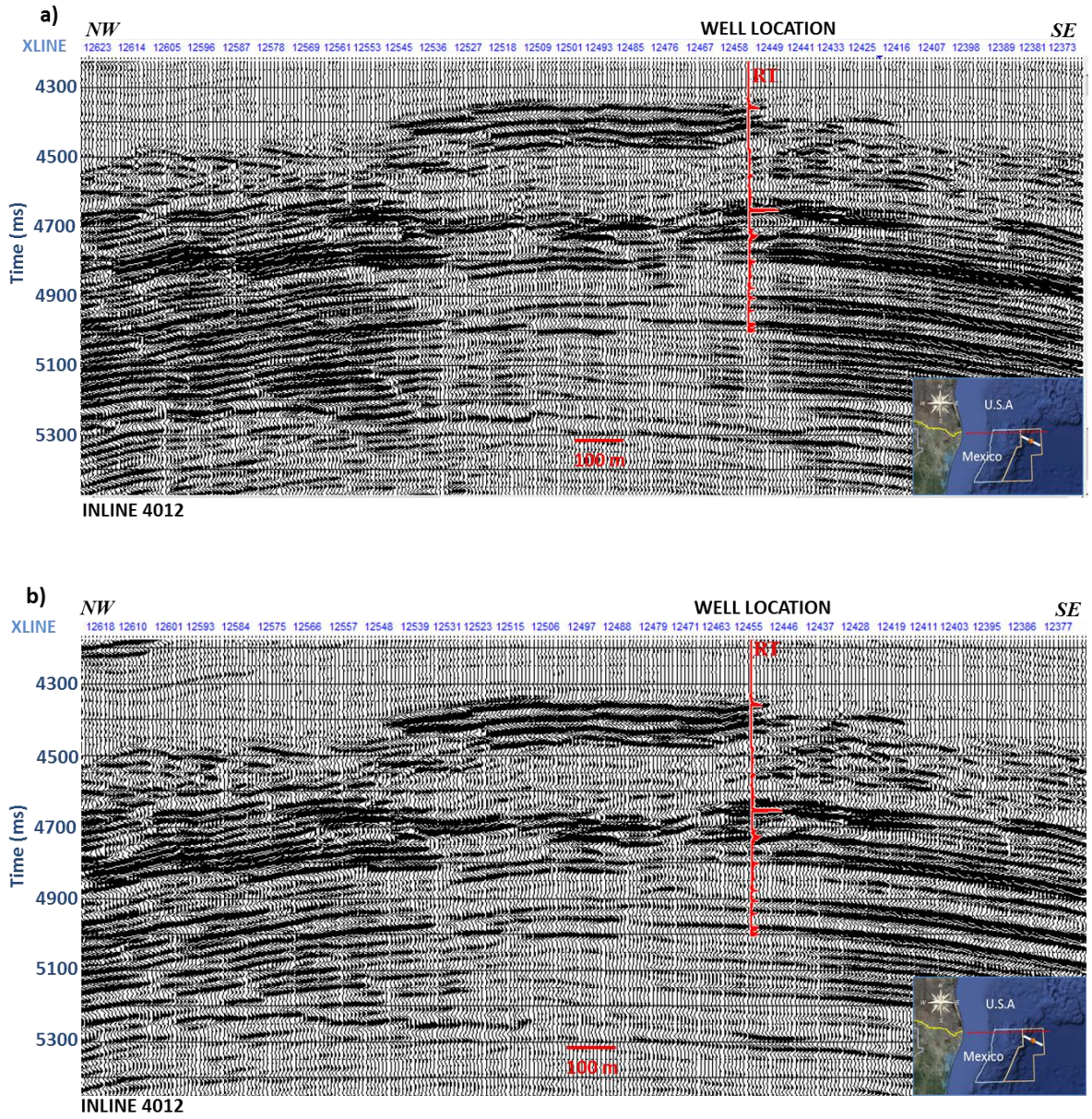

Figure 87*. Result of limit range stacks: a) near offset (10 degrees) and b) far offset (30 degrees), where is evident an improvement of the amplitude response for limit range stack in far offset.*

Once created the correct volumes of range limited stack in both near and far offsets, I use these volumes to build an initial EI model. This model was performed considering as input the range limited stack volumes (near and far offset), the EI logs and three horizons interpreted over the interval of interest (Oligocene Frio14, Oligocene Frio20 and Oligocene Frio26). Therefore, two initial EI models are crated one for near offset (10 degrees) and other for far offsets (30 degrees), which are depicted in the figure 88.

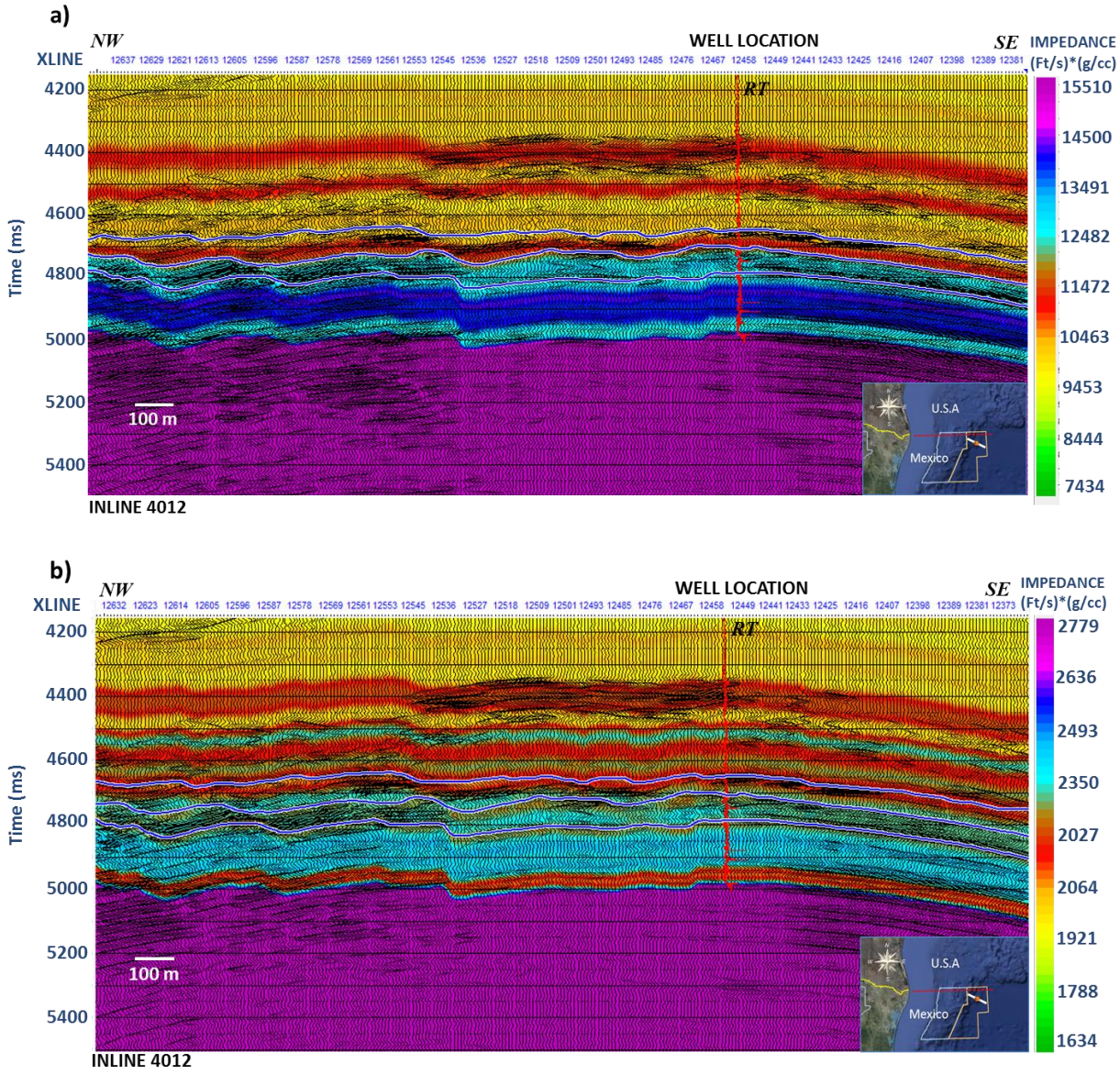

Figure 88*. Initial EI models; a) near offset (10 degrees) and b) far offset (30 degrees), where is evident a slight improvement in the EI definition for far offsets.*

From figure 88 is possible to observe how the initial model of EI established for far offset (88b) shows a better definition than the initial EI model in near offsets (88a), since this depicts a better contrast of EI values along all CDP gather stack. So, once established the initial models, I use these volumes to perform the final EI inversion and then two EI inversion volumes are generated; one for near offset (10 degrees) and other for far offset (30 degrees), which are depicted in the figure 89.

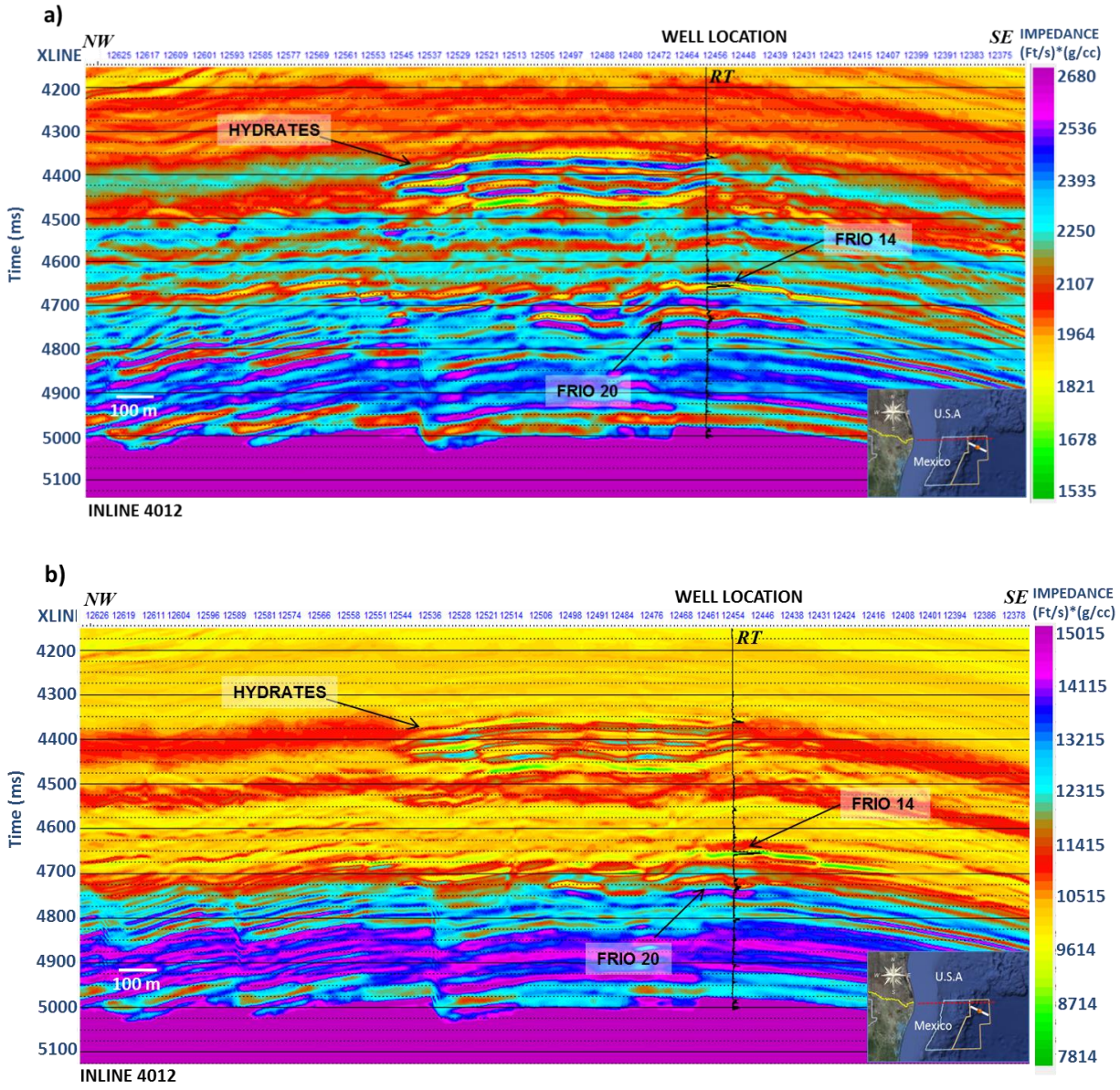

Figure 89*. Result of final EI inversion. a) EI inversion in far offsets and b) EI inversion in near offset. Hence, is evident the better definition of hydrocarbons zones in the results of EI inversion performed in far offset.*

From the figure 89 is evident that EI inversion result in far offset (30 degrees), shows a better definition than EI in near offset (10 degrees). Thereby, I observe how the top, base and west portion of anomalies distribution located just below of methane hydrate zone depict a EI value reduction associated to the presence of free gas. On the other hand, the Oligocene Frio14 also depicts a strong reduction of EI, which is distributed towards the center of structure. This distribution is more evident in the EI inversion result in far offset, which I consider is produced by the presence of gas. In the sand Oligocene Frio 20, I can interpret the possible presence of two types of fluids due it shows two different values in its top and base. The top of Oligocene Frio 20 is represented by a low value of EI, while its base is represented by high value, which I interpret is produced by the presence of oil and water respectively, regarding the values manifested in this inversion and AVO results. Finally, in the Oligocene Frio 26 I do not observe a considerable EI reduction, so this interval may be considered how a zone with a very reduced presence or absence of hydrocarbons.

To have a better understanding of fluids distribution in the EI volumes, I proceeded to perform a cross plot focused in the interval of interest, using as input data the inversion volume results in near and far offsets. The figure 90 shows the cross plot result.

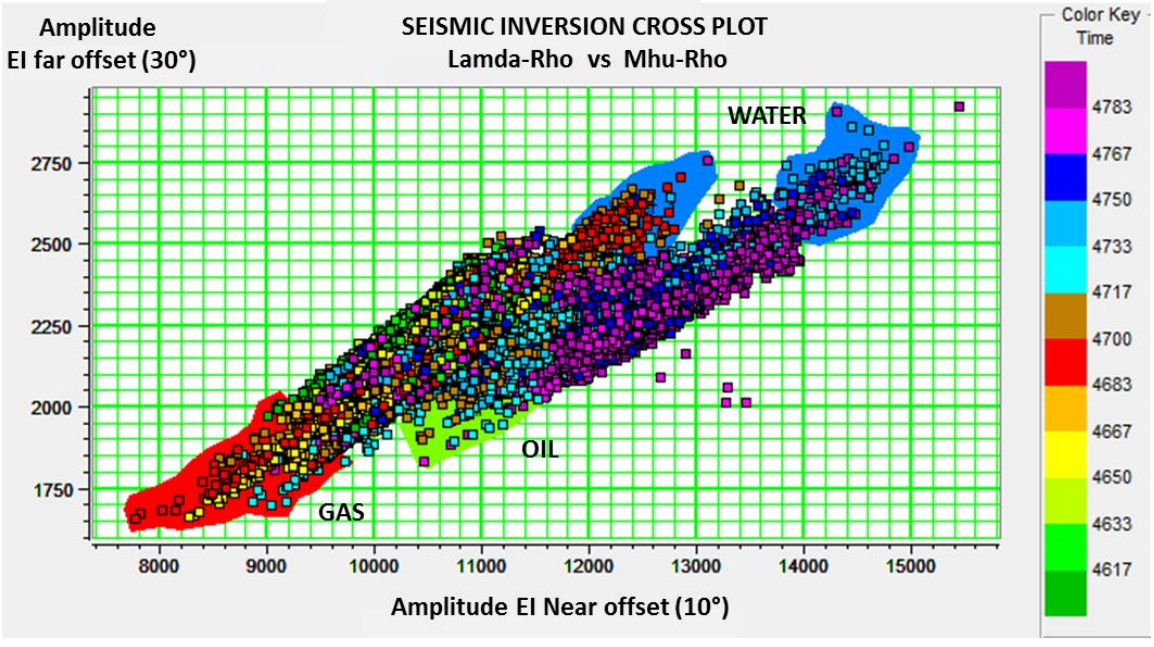

***Figure 90**. Cross plot of EI in near offset vs EI in far offset, showing two trends related to two types of fluids.*

The cross plot depicted in the figure 90 shows two trends with different distribution of EI. Hence, is clear that one these trends tend to be towards lower values of EI, which is represented by the polygon in red color. This area was associated to the sand Oligocene Frio14, and due its lower values of EI this area was interpreted as gas presence. The other zone with low EI values defined by the green polygon represents the area associated to the sand Oligocene Frio20, which was interpreted as oil. Finally, to have a better interpretation of this cross plot, I proceeded to represent this interpretation in a cross section where was possible observe their distribution along of well section (figure 91).

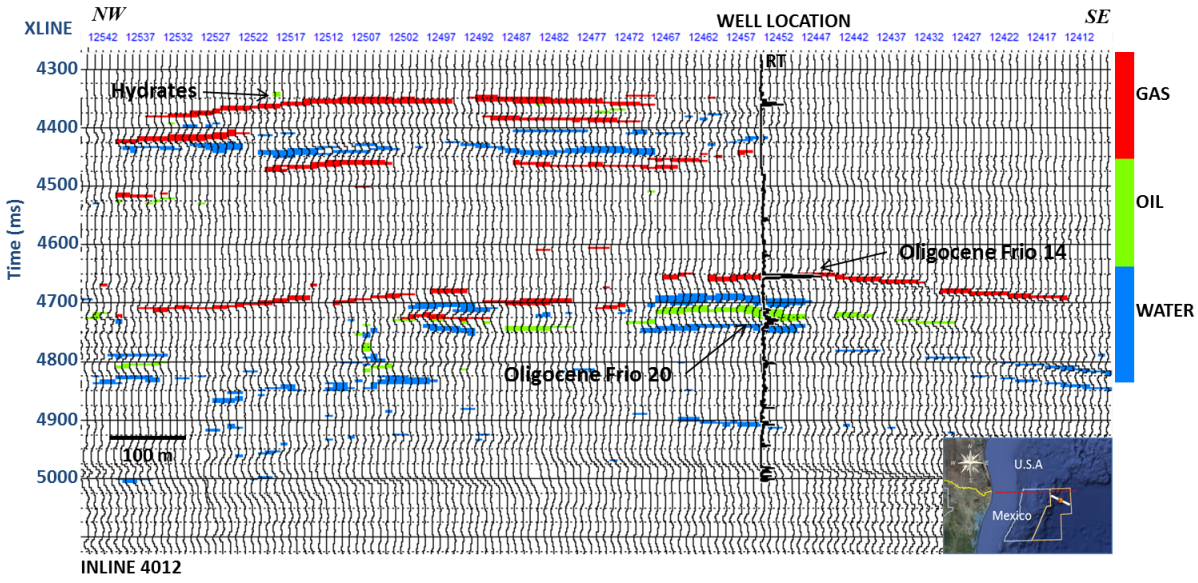

Figure 91. *Cross section representing gas and oil distribution interpreted and defined for the Oligocene Frio14, Oligocene Frio 20 and Hydrates zone.*

From this cross section, I could observe how the hydrocarbon zones defined by the cross plot fit very good with the hydrocarbon areas defined by the log modeling and AVO analysis, being possible to differentiate more clearly the areas associated to the presence of gas, oil and water.

Once interpreted and defined the types of hydrocarbons and their distribution in cross section, I proceeded to perform the extraction of these attributes by using the technique of time slices focused in the two main targets (Oligocene Frio14 and Oligocene Frio20). These extractions were performed using as input the EI volume in far offset, which depicted better

results and using a seismic windows of 5 ms and 10 ms for the horizons Oligocene Frio14 and Oligocene Frio20 respectively (figures 92a and 92b).

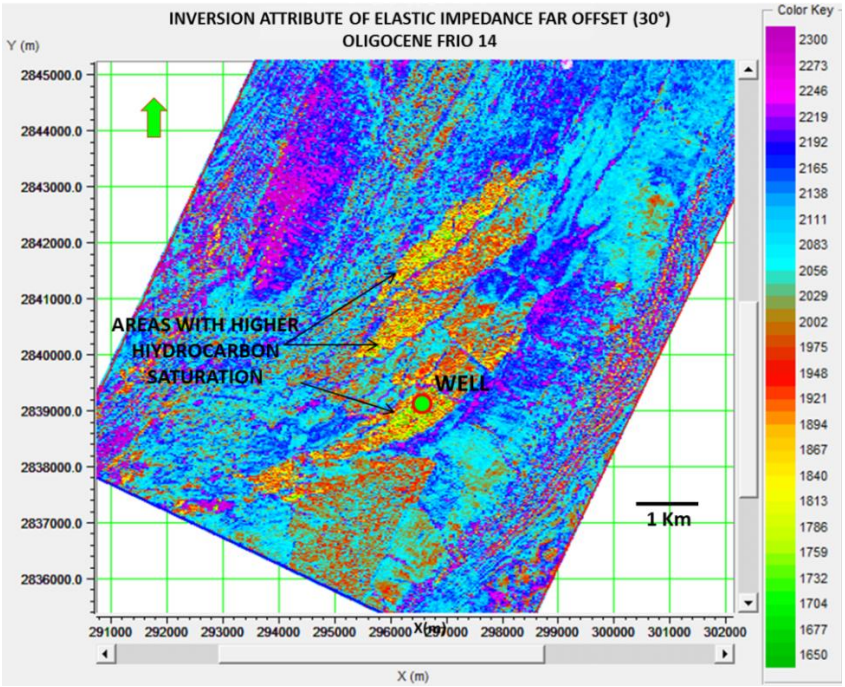

Figure 92a. *Extraction of Elastic Impedance inversion in far offset performed in the Oligocene Frio14, showing the areas with higher hydrocarbon saturation.*

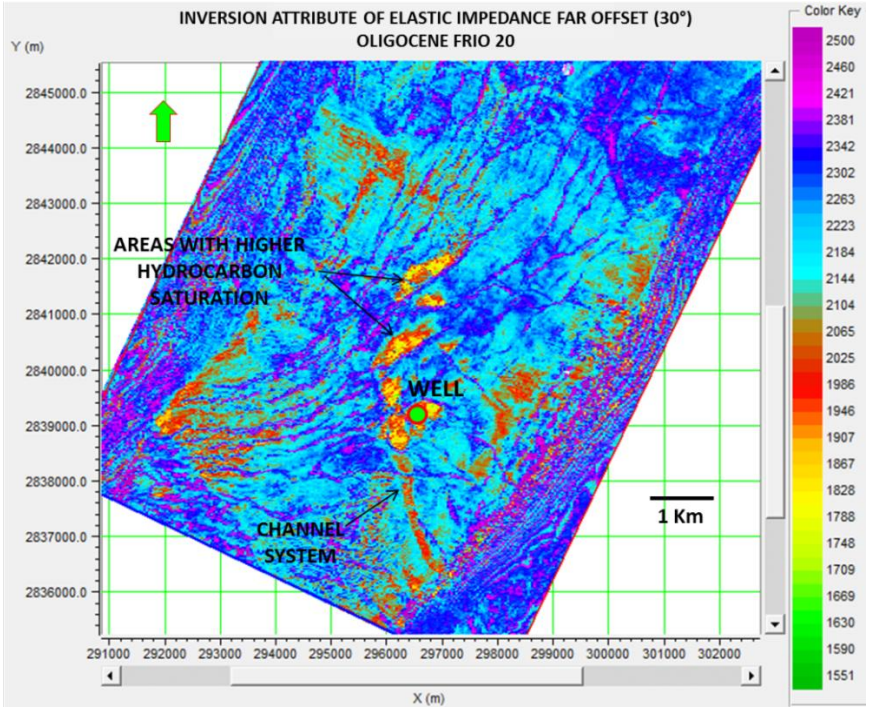

Figure 92b. *Extraction of Elastic Impedance inversion in far offset performed in the Oligocene Frio 20, showing a channel system and zones with higher hydrocarbon saturation.*

From figures 92a and 92b, I could observe how the extraction derived for both intervals (Oligocene Frio14 and Oligocene Frio20) allowed represent the areas associated with reservoir rock distribution, and areas with higher hydrocarbon saturation and their relationship structural and stratigraphic in each reservoir. While the sand Oligocene Frio 14 shows a reservoir limited by a system of normal faults that separate the reservoir in several blocks, the sand Oligocene Frio 20 shows a reservoir rock distribution defined by channels system, which also are interrupted by the same system of normal faults and showing lower values of EI in areas with higher hydrocarbon saturation.

5.3. Discussion and Results

The implement and execution of two methodologies of seismic inversion in this project allowed define and characterize the seismic and geological properties associated at two reservoirs located into Upper Oligocene defined as Oligocene Frio 14 and Oligocene Frio 20.

The seismic inversion result delivered for the sand Oligocene Frio 14 was represented by a set of anomalies associated to the presence of hydrocarbon saturation and reservoir rock distribution. The areas with high hydrocarbon saturation for this interval were defined by reduced values of Lambda-rho and EI in far and near offset. These anomalies with low values were defined in sands around of the well, and toward the top of the structure, being limited and displaced by the presence of normal faults, and which continue their distribution to the north of structure. On the other hand, the cross plot Lambda-rho vs Mhu-rho and EI in far offset vs EI in near offset, also contributed to define correctly the gas distribution for this reservoir, which showed a gradient toward lower values, allowing its correct separation and definition.

The sand Oligocene Frio 20, also showed a set of anomalies with high amplitude associated to a channels system, which comes across the structure in almost direction North-South, showing lower values of Lambda-rho and EI towards the top of structure pointing out higher hydrocarbon saturation. In zones of the channel where Lamda-rho is relatively less low, were associated with the presence of reservoir rock, with absent or low hydrocarbon

saturation. Other important aspect manifested in this interval was the presence of two different types of fluids due it shows two different values of Lamda-Rho and EI in its top and base. On the one hand, its top showed a low value of EI and Lamda-rho, while its base was represented by high value and which were interpreted as presence of oil and water respectively. The water saturation also was defined in the property volumes of Z_P and density (ρ) depicted by an increment in their values, as well as in each cross plot performed in this interval, being defined by a gradient toward high values of Lamda-rho and EI. However in this interval the LMR inversion could not define correctly the presence of oil, mainly during the implement of cross plot Lamda-rho vs Mhu-rho and its representation in cross section, which may be due to the presence of two different types of hydrocarbons dropping in the same trend Lamda-rho and Mhu-rho, no allowing differentiate and define the oil zone characterized by a slight lower Lamda-rho value than gas and the same type of reservoir rock manifested by the same value of Mhu-rho. Therefore, to solve this situation the EI inversion was implemented, allowing distinguish correctly one trend to each type of fluid, in addition of the areas with water saturation.

Finally, a last important aspect since the geological point of view was that the inverted volume Mhu-rho could determine the seismic response related with different geological environments associated to the reservoirs. First, the stratigraphic unit 1 was represented by a set of inhomogeneous layers with low values of Mhu-rho, which were deposited in laminar cycles due it showed slight alternations of deposit. The low values depicted in this stratigraphic unit, was interpreted as sediment with low compaction and presence of loose material. The stratigraphic unit 2, which showed lowest values of Mhu-rho mainly toward the center of unit, was interpreted as the stratigraphic unit most shaly and homogeneous and representing the regional top seal for the sands Oligocene Frio 14 and Oligocene Frio 20. Finally the stratigraphic unit 3, which showed highest values of Mhu-rho, which was interpreted as the most compacted and sandy zone. However, cyclic changes of Mhu-rho depicted in this unit, also was interpreted as the presence of compacted shale between the sand layers.

CONCLUSIONS

The Integration of different methods and techniques of seismic interpretation allowed the correct definition and reservoir characterization of one deep water Prospect located in the Perdido Fold Belt Area, taking into account its features structural, stratigraphic and characteristics of reservoir. Thereby, that several geological models have been derived, considering their relationship with the reservoir rock distribution and hydrocarbons involved. So, since the seismic interpretation point of view, I can conclude and determine several important aspects:

- The age of deformation related with the main structure was interpreted as Upper Oligocene – Lower Miocene, according with their syn-kinematic deposits and regional geological events involved. Although there is evidence that deformation continues till recent (sea bed deformation).
- In younger layers (lower Miocene), was interpreted a shallow linked system (extension – contraction) in the western portion of structure with detachment in shaly sequences deposited in the upper Oligocene, which was generated as product of unstable sediments deposited during Lower Miocene and the late deformation occurred during the Miocene – Pliocene. The late deformation also produced the generation of gravitational sliding characterized by slumps and debris flows
- Overlying Lower Miocene sequences was defined the presence of a set of high amplitude anomalies, generated as product of a contrast in acoustic impedance between methane hydrates and free gas saturated sands.
- The structural and stratigraphic analysis allowed define two main types of combined traps: one characterized by an anticline structure limited by reverse faults in the flanks, showing in its top a normal faults system generated by a gravitational collapse as a product of the intense folding occurred during the Oligocene. This type of trap also showed a set of high amplitude anomalies related with lobular sediments deposited in facies of talud and proximal basin. The second type of trap also was characterized by the same structural domain but associated to the presence

of submarine channels system with variable amplitude and geometry well defined, which were truncated by a normal faults system generated in the top of structure.

On the other hand, the log modeling and AVO analysis performed in this work, also delivered important information related to the type of hydrocarbons associated with the reservoir rock distribution and trap, being possible to conclude the next points.

- The log modeling result showed that exist two types of hydrocarbons in the reservoirs defined by the seismic interpretation: one associated to gas (target Oligocene Frio 14 and methane hydrates zone) and other associated to oil (target Oligocene Frio 20). Where, the target Oligocene Frio 20 also showed to be saturated by water in its lower interval.
- Although the results of synthetic gathers performed in the target reservoirs showed a good result applying both Aki- Richard and Zoepprittz algorithms, the Zoeppritz algorithm was slightly better than the other, allowing not only to define the correct fluid contained in the reservoirs but also the presence of an residual noise in far offsets associated with the sand Oligocene Frio 20, which was taken into account during the AVO analysis.
- To obtain the most accurate results during the log modeling, the correct log edition, the integrated analysis of cross plots associated to different saturations and fluids, as well as the petrophysical evaluation was key to obtain better results.
- The results of gradient analysis and AVO cross plot showed that the reservoirs Oligocene 14 and Oligocene 20 are associated to AVO class 3 and AVO class 1 respectively. On the other hand, the AVO analysis performed in the anomalies below of hydrates zones showed an AVO class 3, which support the interpretation that these areas with high amplitude response may contain free gas saturation, in addition of presence of methane hydrates compacted.
- The integrated analysis of AVO attributes (A*B, Poisson scaled ratio, and Fluid Factor), allowed define not only the reservoir rock distribution but also the areas with most expectation to contain hydrocarbons in each interval analyzed due these

showed a high contrast of response between the sands with hydrocarbons, reservoir rock distribution and shales surrounding.

Finally, with the implementation of two seismic inversion methodologies was possible to define and characterize the seismic and geological properties associated to the different types of reservoirs involved in this project, allowing derive the next conclusions.

- The hydrocarbon saturation zones related with the amplitude anomalies in the sands Oligocene Frio 14 and Oligocene Frio 20, were defined by areas with reduced values of their inverted volumes of Lambda-rho and EI in far and near offsets, as well as by use of cross plots Lamda-rho vs Mhu-rho and EI in far offset vs EI in near offset.
- The seismic inversion results performed in the sand Oligocene Frio 20, could determine the presence of two different types of fluids. One associated to the presence of oil, which showed low values in the inverted volumes of Lambda-Rho and EI in far and near offsets. And other associated to the presence of water, which was represented by high values, mainly in the inverted volumes of EI (Elastic impedance), Lamda-rho, P-impedance (Z_P) and density (ρ), which was also manifested by the cross plot EI in far offset vs EI in near offset.
- In the Oligocene Frio 20, the LMR inversion could not define correctly the presence of oil for this reservoir, mainly in the cross plot Lamda-rho vs Mhu-rho and its representation in cross section. Thereby, that the use of EI inversion was necessary as additional inversion method to solve this situation, generating better results.
- The inverted volume Mhu-rho could determine the seismic response related with three different geological environments defined during the seismic interpretation section. First, the stratigraphic unit 1, which manifested relatively low values of Mhu-rho associated to sediments with low compaction and loose material. The stratigraphic unit 2, which showed lowest values of Mhu-rho interpreted as the presence of shale and the stratigraphic unit 3, with highest values of Mhu-rho, which was interpreted as the most compacted and sandy zones.

REFERENCES

Barclay F., Bruun A., Camara A., Cooke A., Cooke D., Godfray R., Lowden D., McHugo S., Ozdemir H., Pickering S., González F., Herwanger J., Volterrani S., Murineddu A., Rasmussen A. and Roberts R., *2008, Inversion Sísmica: Lectura entre Líneas*., Oilfield Review., Perth, Australia Occidental, Australia., Pemex, Tampico, Tamaulipas México., Aberdeen, Escocia., Gatwick, Inglaterra., Pemex, Reynosa Tamaulipas, México., Houston, Texas, E.U.A., Stavanger, Noruega., Calgary, Alberta, Canada, 44-48

Castagna J., Swan H., 1997, *Principles of AVO crossplotting*., University of Oklahoma, Norman, Oklahoma and ARCO Exploration and Production Technology, Plano, Texas., The Leading Edge, 1-6

Chiburis E., Leaney S., Franck C., Leaney S., McHugo S., Skidmore C., 1993, *Hydrocarbon Detection with AVO*., Seismic Report, Houston Texas, 42

Collet T., Lewis R., Uchida T., 2000, *El Creciente Interés en los Hidratos de Gas*., United States Geological Survey., Denver, Colorado, EUA., Oilfield Review, 47-53

Connolly P., 1999, *Elastic Impedance*., BP Amoco, Houston, Texas, US., The Leading Edge, 438-446

Grandmann S., Beaumont C. and Albertz M., 2008, *Factors Controlling the Evolution of the Perdido Fold Belt, Northwestern Gulf of Mexico, Determined from Numerical Models*., Tectonics. Vol. 28, 1-5

Grandmann S., Beaumont C., 2009, *The Evolution of the Perdido Fold Belt in the Context of Salt Tectonic of Northwestern Gulf of Mexico-Insight from Numerical Modelling*., Tirrenia, Italy., AAPG Hedberg Conference, 1-4

Hampson-Russell., 2010, *AVO workshop CGG-Veritas*., CGG Veritas Company, Houston Texas, 26-38, 114-115, 120, 136, 253-255, 262, 292.

Landro M., 2012, *Seismic Data Acquisition and Imaging*., University of Science and Technology, Trondheim, Norway, 51, 93, 94

Mackenzi, W., 2003, *Trident Reserves*., US Gulf of Mexico (Deep Water) Upstream Service, 1-5

Mackenzi, W., 2003, *Baha Reserves*., US Gulf of Mexico (Deep Water) Upstream Service, 3

Mackenzi, W., 2003, *Great White Reserves*., US Gulf of Mexico (Deep Water) Upstream Service, 1-5

Manson E., Chapin M., Steffens Gary E., 2005, Great White Prospect and the Perdido Fold Belt New-Petroleum Province in Ultra Deep Water, Alaminios Canyon, Gulf of Mexico., shell Deep Water Exploration., Houston, Texas, US, 27-28

Pemex., 2010, *Estudio de Plays Detalle Cinturon Subsalino 2D PSDM*., Coordinacion Area Perdido., Poza Rica, Veracruz, México, 16, 20-23.

Pemex., 2009, Estudio de Plays Sector Subsalino (Mioceno-Oligoceno)., Coordinacion Area Perdido., Poza Rica, Veracruz, México, 34-39

Pemex., 2008, *Estudio de Plays Area Perdido.*, Coordinacion Delta del Bravo - Area Perdido., Poza Rica, Veracruz, México, 13-15

Pemex., *2002, Informe Final de Estudio Marino Sísmico Maximo 3D.*, Proyecto de Inversion Area Perdido. Vol 1., Poza Rica, Veracruz, México, 2, 12, 19, 85, 86, 87, 90

Russell B., Hendly K., 2001, *Fluid Properties Discrimination with AVO, a Biot Gassman Perspective*., Hampson-Russell Software Ltd., Houston Texas, 61

Young K., Tatham R., 2007, *Lambda-Mhu-Rho Inversion as a Fluid and Lithologic Discriminator in the Columbus Basin, Offshore Trinidad*., Dept. of Geologycal Science Jackson School of Geoscience, University of Texas-Austin., SEG San Antonio, Annual Meeting, 214

Yuping S., Yunguang T., Tianqi W., Guanpo C., Jian L., 2010, *AVO Attribute Interpretation and Identification of Litholgical Traps by Prestack Elastic Parameter Inversion.,* A Case Study in K Block, South Turgay Basin., Petro China Reserve Institute of

Petroleum Exploration & Development Northwest Lanshou Gansu., SEG Denver Annual Meeting, 439

Schlumberger., 2012, *Petrel Geophysics Course*., Petrel Training Course NTNU., Trondheim, Norway, 165-217

Trudgill B., Rowan M., Fiduk Carl., Weimer P., Gale P., Korn B., Phair R., Gafford W., Roberts G., Dobbs S., 1999, *The Perdido Fold Belt, Northwestern Deep Gulf of Mexico, Part 1: structural Geometry, Evolution and Regional Implications*., AAPG Bulletin V.83. No.1, 90-92

Zhang H., James R., 2001, *A Review of AVO Analysis*. CREWES Research Report, 360

APPENDIX A

During the chapter 3 (seismic interpretation) and chapter 4 (AVO analysis), I use the results of petrophysical evaluation as complement to define the main targets to follow and select the type of hydrocarbons to be implemented during the log modeling. So, according with this petrophysical evaluation the reservoir Oligocene Frio 14 is constituted by gas, while the Oligocene Frio 20 is constituted by gas and oil, and which showed porosity ranges of 25% -28% and permeability of 284 mD respectively.

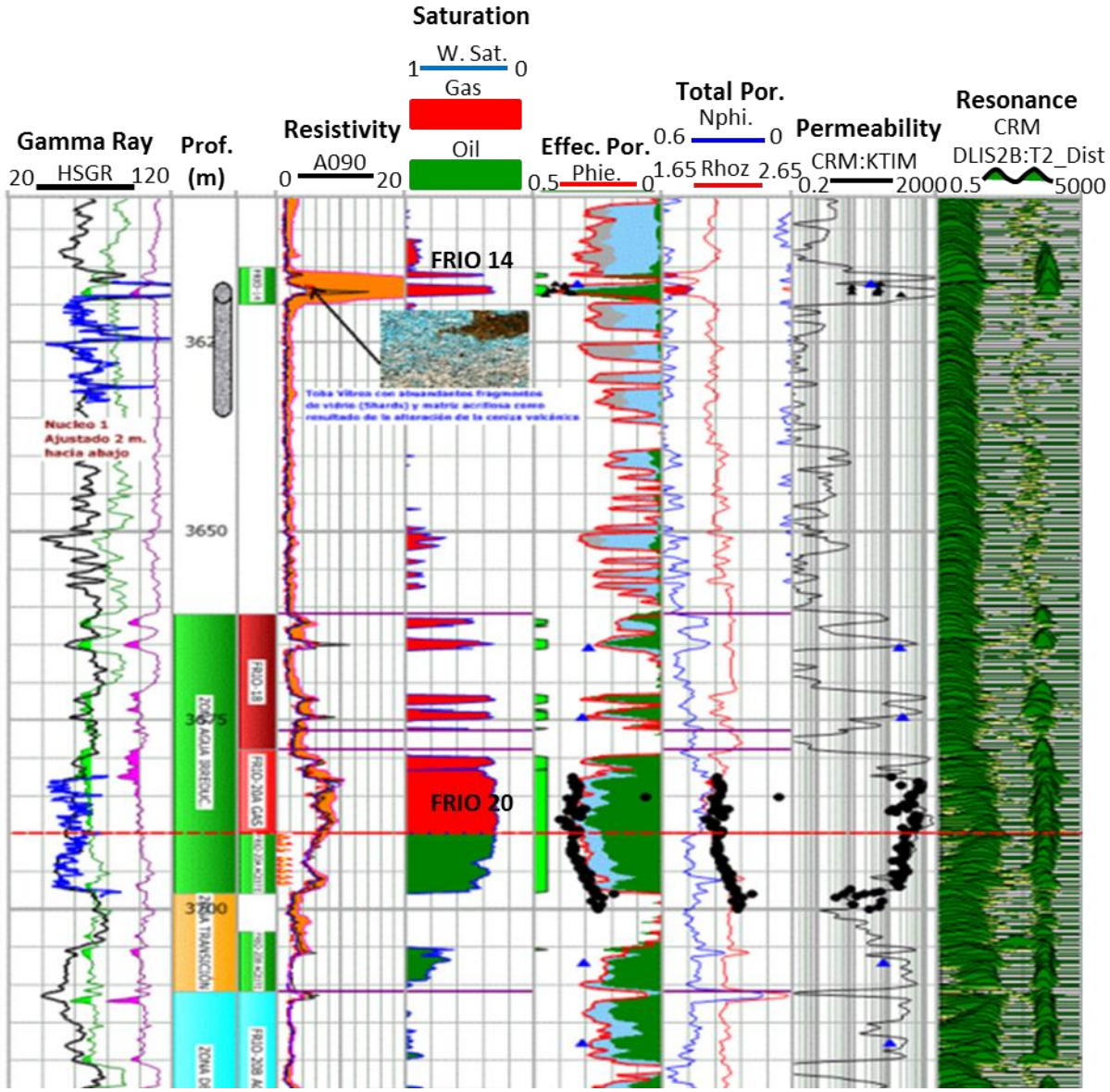

APPENDIX B

For the application of Elastic Impedance the derivation of equation (22) Based on Shuey´s form from Aki-Richard equation (14), the Connolly equation (28) can be derived as next:

$$R(\theta) = A + B\sin^2\theta + C\sin^2\theta\tan^2\theta \qquad (14)$$

Where

$$A = \frac{1}{2}\left(\frac{\Delta V_P}{V_P} + \frac{\Delta\rho}{\rho}\right)$$

$$A = \frac{\Delta V_P}{2V_P} - 4\frac{V_S^2}{V_P^2}\frac{\Delta V_S}{V_S} - 2\frac{V_S^2}{V_P^2}\frac{\Delta\rho}{\rho}$$

$$C = \frac{1}{2}\frac{\Delta V_P}{V_P}$$

and where

$$\overline{V_P} = \left(V_P(t_i) + V_P(t_{i-1})\right)/2$$

$$\Delta V_P = V_P(t_i) - V_P(t_{i-1})$$

$$\frac{V_S^2}{V_P^2} = \left(\frac{V_S^2(t_i)}{V_P^2(t_i)} + \frac{V_S^2(t_{i-1})}{V_P^2(t_{i-1})}\right)\Big/2$$

and similar for the other variables (NB. For ease of notations, the "bars" will be omitted from the average V_P^2/V_S^2 ratios.)

Is necessary a function f(t) which has properties analogous to acoustic impedance, such that reflectivity can be derived from the formula given below for any incidence angle θ

$$R(\theta)\frac{f(t_i) - f(t_{i-1})}{f(t_i) + f(t_{i-1})}$$

Call this function EI (elastic impedance), and use the alternative log derivation for reflectivity which is accurate for small to moderate changes in impedance;

$$R(\theta) \approx \frac{1}{2}\frac{\Delta EI}{EI} \approx \frac{1}{2}\Delta \ln(EI)$$

And so,

$$\frac{1}{2}\Delta \ln(EI) = \frac{1}{2}\left(\frac{\Delta V_P}{\overline{V_P}} + \frac{\Delta \rho}{\rho}\right) + \left(\frac{\Delta V_P}{2\overline{V_P}} - 4\frac{V_S^2}{V_P^2}\frac{\Delta V_S}{\overline{V_S}} - 2\frac{V_S^2}{V_P^2}\frac{\Delta \rho}{\overline{\rho}}\right)\sin^2\theta + \frac{1}{2}\frac{\Delta V_P}{\overline{V_P}}\sin^2\theta\tan^2\theta$$

Substituting K for V_P^2/V_S^2 and rearranging

$$= \frac{1}{2}\left(\frac{\Delta V_P}{V_P}\left(1+\sin^2\theta\right) + \frac{\Delta \rho}{\overline{\rho}}\left(1-4K\sin^2\theta\right) - \frac{\Delta V_S}{V_S}8K\sin^2\theta + \frac{\Delta V_P}{V_P}\sin^2\theta\tan^2\theta\right)$$

but $\sin^2\tan^2\theta = \tan^2\theta - \sin^2\theta\tan^2\theta$, so

$$= \frac{1}{2}\left(\frac{\Delta V_P}{\overline{V}_P}\left(1+\tan^2\theta\right) - \frac{\Delta V_S}{V_S}8K\sin^2\theta + \frac{\Delta \rho}{\overline{\rho}}(1-4K\sin^2\theta)\right)$$

Note that ha we used only the first two terms of (7), then the above and following expressions differ only by changing the *tan²Θ* to *sin²Θ.* We substitute again Δlnx for Δx/x;

$$\Delta \ln(EI) = (1+\tan^2\theta)\Delta \ln(V_P) - 8K\sin^2\theta\Delta \ln(V_S) + (1-4K\sin^2\theta)\Delta \ln(\rho)$$

now if we make K constant we can take all terms inside the Δs

$$= \Delta \ln\left(V_P^{(1-\tan^2\theta)}\right) - \Delta \ln\left(V_S^{8K\sin^2\theta}\right) + \Delta \ln\left(\rho^{(1-4\sin^2\theta)}\right)$$

$$= \Delta \ln\left(V_P^{(1-\tan^2\theta)}V_S^{8K\sin^2\theta}\rho^{(1-4\sin^2\theta)}\right)$$

And finally integrating and getting the exponentiate and setting the integration constant to zero, we obtain the EI [Connolly et al. 1999].

$$EI = V_P^{(1-\tan^2\theta)}V_S^{8K\sin^2\theta}\rho^{(1-4\sin^2\theta)} \qquad (28)$$